Flavour Tagging in Hadronic B_s^0 Decays for the ATLAS Experiment at the Large Hadron Collider

Dissertation

zur Erlangung des akademischen Grades

Doktor der Naturwissenschaften

an der

Fakultät für Mathematik, Informatik und Physik

der

LEOPOLD FRANZENS UNIVERSITÄT INNSBRUCK

eingereicht von

Mag. rer. nat. Patrick Jussel

im Februar 2011

"I was born not knowing and have had only a little time to change that here and there."

- Richard P. Feynman

Abstract

The determination of the initial b quark content of neutral B mesons using various techniques of flavour tagging has been studied for the ATLAS experiment at the Large Hadron Collider at CERN near Geneva. This work mainly focuses on opposite side soft muon flavour tagging on the hadronic decay channels $B_s^0 \to D_s^- \pi^+$ and $B_s^0 \to D_s^- a_1^+$ with $D_s^- \to \phi(K^+, K^-)\pi^-$ and $a_1^+ \to \rho^0(\pi^+, \pi^-)\pi^+$. These hadronic decay channels will be used for the measurement of the B_s^0 oscillation frequency Δm_s. This study has been performed on fully simulated and reconstructed Monte Carlo data sets.

Multi muon trigger scenarios have been evaluated to be prepared for data taking at design luminosities. A flavour tagging software has been developed and implemented into the ATLAS Athena software framework. The probabilities for wrong tags P_w have been evaluated to be $(22.30^{+0.56}_{-0.55})$ % for $B_s^0 \to D_s^- \pi^+$ and $(23.31^{+0.56}_{-0.55})$ % for $B_s^0 \to D_s^- a_1^+$, the tagging power has been found to be 0.303 ± 0.005 for $B_s^0 \to D_s^- \pi^+$ and 0.281 ± 0.005 for $B_s^0 \to D_s^- a_1^+$. The sources of wrong tags have been identified and its kinematic dependencies studied in detail. Based on multivariate methods combining kinematic variables, a software for the calculation of a per-event wrong tag fraction has been developed and validated.

Zusammenfassung

In dieser Arbeit wurden verschiedene Methoden zur Bestimmung der Flavour neutraler B Quarks bei der Entstehung für das ATLAS Experiment am Large Hadron Collider am CERN bei Genf untersucht. Das Hauptaugenmerk dieser Arbeit liegt auf der Bestimmung der B_s^0 Flavour in den hadronischen Zerfallskanälen $B_s^0 \to D_s^- \pi^+$ und $B_s^0 \to D_s^- a_1^+$ mit $D_s^- \to \phi(K^+, K^-)\pi^-$ und $a_1^+ \to \rho^0(\pi^+, \pi^-)\pi^+$ durch ein gegenüberliegendes niederenergetisches Myon. Die beiden hadronischen Zerfallskanäle werden für die Messung der B_s^0 Oszillationsfrequenz benötigt. Diese Arbeit wurde mit vollständig simulierten und rekonstruierten Monte Carlo Daten durchgeführt.

Für die Datennahme bei Design-Luminosität wurden verschiedene Multi-Myonen Triggerszenarios untersucht. Eine Software zur Bestimmung des Flavour Tags wurde entwickelt und in das ATLAS ATHENA Framework implementiert. Die Wahrscheinlichkeiten für einen falschen Flavour Tag P_w wurden ermittelt: $(22.30^{+0.56}_{-0.55})$ % für $B_s^0 \to D_s^- \pi^+$ und $(23.31^{+0.56}_{-0.55})$ % für $B_s^0 \to D_s^- a_1^+$. Die Tagging Power ist 0.303 ± 0.005 für $B_s^0 \to D_s^- \pi^+$ und 0.281 ± 0.005 für $B_s^0 \to D_s^- a_1^+$. Die verschiedenen Quellen eines falschen Flavour Tags wurden identifiziert und ihre kinematischen Abhängigkeiten im Detail studiert. Im Zuge dieser Arbeit wurde eine multivariate Analysesoftware verwendet, mit Hilfe derer verschiedene Variablen so kombiniert werden, dass eine Per-Event Wahrscheinlichkeit für einen falschen Flavour Tag bestimmt werden kann.

Contents

CHAPTER

ONE

Introduction and Motivation

The adventurous history of Particle Physics is a story of remarkable success, affected by an exemplary interplay between theory and experiment. Some of the most impressive ideas have been regarded as not measurable at all...

> *"I've done a terrible thing today, something which no theoretical physicist should ever do. I have suggested something that can never be verified experimentally"*
>
> \- Wolfgang Pauli [102]

... whereas some experimental results messed up the understanding of Particle Physics at that time. One beautiful example of this interplay is the discovery of parity violation. The measurement of pionic kaon decays lead C.N.Yang and T.D.Lee to their famous theorem about parity violation in the β-decay [115], which in return has been experimentally tested within a few month by C.S.Wu and her co-workers [152]. The list of particles theoretically predicted at first and later on discovered in experiments is long. One of the most famous examples is the discovery of the $W^{\pm}$ and Z^{0} bosons by the UA1 and

UA2 experiments at the Super Proton Synchrotron SPS at the European Organisation for Nuclear Research CERN in Geneva. At Fermilab near Chicago the heavy flavour quarks *bottom* and *top* predicted by theory have been discovered, as well as the *tau* neutrino.

Currently the success story of Particle Physics continues. The experiments unraveling the secrets of matter and its interaction over the years became larger and more precise, driving the instrumentation and technology to the very cutting edge. One can compare the advancing measurements in Particle Physics to the corresponding experiments in Astrophysics. In both fields scientists were and still are building machines, which uncover physical phenomena, searching for the frontiers of our universe on small and big scales alike:

> *"We find them smaller and fainter, in constantly increasing numbers, and we know that we are reaching into space, farther and farther, until, with the faintest nebulae that can be detected with the greatest telescopes, we arrive at the frontier of the known universe."*
>
> - Edwin Powell Hubble

The Large Hadron Collider LHC is the next generation machine in Particle Physics, enabling physicists to push the boundaries of our understanding of the world. The LHC has started operation in 2009, in the first year a large number of collision events have been recorded (see e.g. Figure 1.1). The plans of the particle physicists with the LHC are ambitious. One of the biggest puzzles of modern science is the origin of mass. The experiments at the LHC are designed to detect the Higgs boson, a particle emerging from the Higgs Mechanism, which generates masses for the two massive $W^{\pm}$ and Z^0 as well as for bosons for quarks and leptons. Apart from that, the experiments at the LHC have the capability to measure a wide range of physical phenomena beyond the Standard Model of Particle Physics. Many groups around the world hope to discover so-called supersymmetric particles. Further topics amongst many cover grand unified theories, extra dimensions, technicolor or string models.

Alongside the discovery of new particles and phenomena, the four experiments at the LHC are designed to perform a large number of precision measurements, confining the parameters of the Standard Model of Particle Physics or eventually uncovering hints for physics beyond the Standard Model. Measurements of the QCD properties of the proton-proton collisions itself are planned. Most parameters of the Standard Model will be measured at higher precision and the properties and decays of the heavy quarks *bottom* and *top* will be determined.

> *"There are two possible outcomes: if the result confirms the hypothesis, then you've made a measurement. If the result is contrary to the hypothesis, then you've made a discovery."*
>
> \- Enrico Fermi

Within the physics of the *bottom* quark, scientists are trying to solve the big puzzle of the asymmetry between matter and anti-matter in our universe. Without a few exceptions due to radioactivity and collisions of cosmic rays with the matter on our earth, no occurrence of anti-particles have been found. Looking deep into the universe with satellite experiments, no evidence for regions consisting of anti-matter have been found so far. In the Standard Model of Particle Physics the asymmetry between particles and anti-particles is explained by $\mathcal{CP}$ violation. However, regarding the current understanding of the big bang, matter and anti-matter have been produced in equal amounts. The $\mathcal{CP}$ violation in the Standard Model of Particle Physics is too small to explain the asymmetry observed in our universe.

At the ATLAS experiment, $\mathcal{CP}$ violation will be measured in decay channels of the the neutral B_s^0 meson, e.g. in the gold-plated decay channel $B_s^0 \to J/\psi\phi$ with $J/\psi \to \mu^+\mu^-$ and $\phi \to K^+K^-$. As the B_s^0 meson and its anti-particle $\bar{B}_s^0$ are oscillating with the frequency Δm_s[1], one crucial ingredient for this measurement is the identification of the B_s^0 flavour at production time and at decay time. In the measurement of $\mathcal{CP}$ violation the parameter Δm_s is used as one key parameter. While Δm_s already has been measured by the Fermilab experiments CDF and DØ, this value will be measured with high precision at the LHC. At the ATLAS experiment this measurement is planned to be performed with hadronic decay channels, in which the final state explicitly is related to the flavour at decay time, as e.g. $B_s^0 \to D_s(\phi\pi)\pi$.

This thesis focuses on the determination of the initial flavour of the B_s^0 meson, using the technique of flavour tagging. In Chapter 2 the theory on which this work is based is outlined. In Chapter 3 the underlying experimental environment, the LHC and the ATLAS detector, are described. Chapter 4 is dedicated to the Monte Carlo techniques and event reconstruction used by the author to create and reconstruct the required Monte

[1] The oscillation between the two flavour eigenstates B_s^0 and $\bar{B}_s^0$ has the frequency Δm_s, the mass difference between the two mass eigenstates of the B_s^0 meson.

Carlo data samples. The various observables relevant for flavour tagging as well as possible flavour tagging methods are introduced in Chapter 5. In Chapter 6 the trigger used in this thesis is discussed. Furthermore, various trigger scenarios have been studied in detail by the author in order to understand all effects of the trigger on flavour tagging. Finally, in Chapter 7 the reconstruction and results of soft lepton flavour tagging on the two hadronic decay channels $B_s^0 \to D_s^- \pi^+$ and $B_s^0 \to D_s^- a_1^+$ are presented. A detailed background analysis has been performed and multivariate analysis techniques have been used to develop an per-event wrong tag fraction.

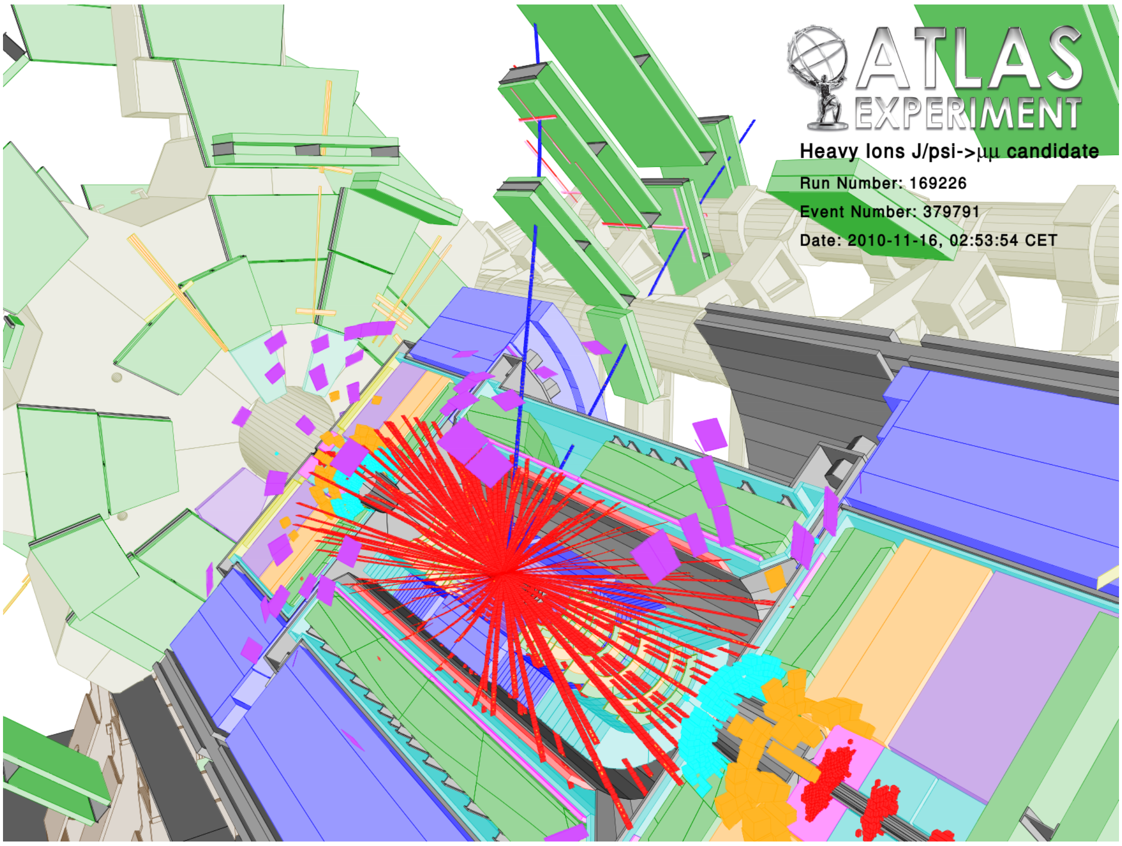

Figure 1.1: Event display of a heavy ion collision with a candidate of the decay $J/\psi \to \mu^+\mu^-$. The event passes the selection requirements for J/ψ candidates in [36]. Figure taken from the event displays on [20].

CHAPTER

TWO

Theoretical Background

In the following chapter the theory on which this work is based on is summarised. In the beginning, the Standard Model of Particle Physics will be introduced, followed by a short introduction into $\mathcal{CP}$ violation and a few comments on various topics from the field of B Physics, which are useful as background to this thesis. Excellent textbooks like [54, 96, 120, 122, 129] give a more elaborate introduction into the field of Particle Physics.

2.1 The Standard Model of Particle Physics

Particle Physics deals with the science of the fundamental components of matter and the interactions between them. Up to date the most accurate and best understood model is the so-called Standard Model of Particle Physics, a relativistic quantum field theory [92–94, 134, 149]. Accurate lectures on QED and QCD can be found in [131, 132].

Within the Standard Model, matter is made out of fermions with spin 1/2 in units of $\hbar$, obeying the Fermi-Dirac statistics. Fermions can be categorised into quarks and

Matter Type	Generations I	II	III	Electric charge
Leptons	$\begin{pmatrix} e^- \\ \nu_e \end{pmatrix}$	$\begin{pmatrix} \mu^- \\ \nu_\mu \end{pmatrix}$	$\begin{pmatrix} \tau^- \\ \nu_\tau \end{pmatrix}$	-1 0
Quarks	$\begin{pmatrix} u \\ d \end{pmatrix}$	$\begin{pmatrix} c \\ s \end{pmatrix}$	$\begin{pmatrix} t \\ b \end{pmatrix}$	$+2/3$ $-1/3$

Table 2.1: The three generations of fermions, divided into quarks and leptons. Electrons, muons and tau-leptons have an electric charge of -1 in units of the elementary charge, whereas their corresponding neutrinos are neutral. The *up*-type quarks have an electric charge of $+2/3$, the *down*-type quarks $-1/3$.

leptons, the building blocks of all matter around us. These particles can be organised in three generations, as shown in Table 2.1.

Each generation or family consists of two doublet of fermions. A quark doublet contains one up-type quark with charge $+2/3$ and one down-type quark with charge $-1/3$, charge in units of the elementary charge e. Quarks can interact via the strong, weak and electromagnetic force. A leptonic doublet contains an electron-, muon- or tau-lepton with charge -1, and associated a neutrino with charge 0. The charged leptons interact weakly and electromagnetic, while the neutral leptons can only interact weakly. Each particle has its anti-particle.

In the Standard Model, the interactions between the fermions are described by fundamental gauge interactions, mediated by gauge vector-bosons following the Bose-Einstein statistics, with spin 1 in units of $\hbar$:

- electromagnetic interaction: one gauge boson, photon γ
- weak interaction: three gauge bosons, $W^{\pm}$, Z^0
- strong interaction: eight gluons

The Standard Model is a relativistic quantum field theory based on symmetry groups. The Standard Model Lagrangian is invariant under the local gauge transformation from the symmetry group describing the strong, weak and electromagnetic forces, written as

$$SU(3)_C \otimes SU(2)_L \otimes U(1)_Y. \tag{2.1}$$

The group $SU(3)_C$ is the symmetry group generating the strong interaction. The force is mediated by an octet of gluons. The strong interaction conserves the colour quantum number, which is the strong equivalent of the electromagnetic charge.

The tensor product of the two symmetry groups $SU(2)_L \otimes U(1)_Y$ generates electromagnetic and weak interaction. The vector bosons mediating the electroweak force are the massless photon γ and the bosons $W^{\pm}$ and Z^0, which are themselves massive particles. The electroweak interaction conserves the weak hypercharge.

Within the Standard Model, the mass of electroweak bosons is generated by the spontaneous symmetry breaking mechanism, introducing a scalar particle, the so-called Higgs boson H [99]. While not measured at present state, the discovery of the Higgs boson is one of the main physics tasks of the Large Hadron Collider LHC and its experiments.

In the following sections some concepts of the Standard Model of Particle Physics are outlined.

2.1.1 Quantum Electrodynamics

The simplest gauge example of a relativistic quantum field theory is the Quantum Electrodynamics QED with its underlying unitary symmetry group $U(1)$.

Considering the Lagrangian density of the Dirac equation

$$\mathcal{L} = i\bar{\psi}\gamma^{\mu}\partial_{\mu}\psi - m\bar{\psi}\psi, \tag{2.2}$$

with the standard Dirac gamma matrices γ^{μ}, m, the mass of the fermion, the indices $\mu = 0, ..., 3$ and the spin 1/2 fermion written as Dirac spinor is

$$\psi = \begin{pmatrix} \psi_R \\ \psi_L \end{pmatrix}, \quad \bar{\psi} = \psi^{\dagger}\gamma^0. \tag{2.3}$$

The unitary group $U(1)$ has one generator $\alpha(x)$:

$$\psi \to e^{-i\alpha(x)}\psi. \tag{2.4}$$

While the mass term $m\bar{\psi}\psi$ is invariant under a local $U(1)$ transformation, the derivative in the first term of (2.2) breaks this invariance as $\partial_\mu \alpha(x) \neq 0$. In order to keep the invariance, a covariant derivative D_μ has to be introduced adding a vector field A_μ:

$$\partial_\mu \to D_\mu = \partial_\mu - iqA_\mu, \tag{2.5}$$

where the A_μ transforms under $U(1)$ in the following way:

$$A_\mu \to A_\mu + \frac{1}{q}\partial_\mu A_\mu. \tag{2.6}$$

The introduction of the new vector field leads to the desired invariance of the first term of the Lagrangian (2.2):

$$D_\mu \psi \to D_\mu \psi' = e^{-i\alpha(x)} D_\mu \psi. \tag{2.7}$$

The requirement of invariance under a local $U(1)$ transformation introduces a vector field, which can be identified as the physical photon field. Therefore, the field strength tensor has to be added to the Lagrangian leading to the final Lagrangian of Quantum Electrodynamics

$$\begin{aligned} \mathcal{L} &= \bar{\psi}\left(i\gamma^\mu D_\mu - m\right)\psi - \frac{1}{4}F_{\mu\nu}F^{\mu\nu} \\ &= \bar{\psi}\left(i\gamma^\mu \partial_\mu - m\right)\psi - \frac{1}{4}F_{\mu\nu}F^{\mu\nu} + q\bar{\psi}\gamma^\mu A_\mu \psi, \end{aligned} \tag{2.8}$$

where $F_{\mu\nu} = \partial_\mu A_\nu - \partial_\nu A_\mu$ is the gauge invariant field strength tensor of the photon field. Due to the form of the covariant derivative D_μ in (2.5) the coupling of the form $q\bar{\psi}\gamma^\mu A_\mu \psi$ can be identified, where q represents the strength of the coupling, the charge of the particle.

The requirement of gauge invariance forbids the introduction of a mass term of the type $m^2 A_\mu A^\mu/2$, hence the photon is required to be massless in QED.

Leptons	Quarks	t_3
$\begin{pmatrix} \nu_e \\ e^- \end{pmatrix}_L \begin{pmatrix} \nu_\mu \\ \mu^- \end{pmatrix}_L \begin{pmatrix} \nu_\tau \\ \tau^- \end{pmatrix}_L$	$\begin{pmatrix} u \\ d' \end{pmatrix}_L \begin{pmatrix} c \\ s' \end{pmatrix}_L \begin{pmatrix} t \\ b' \end{pmatrix}_L$	+1/2 -1/2
$e_R^-,\ \mu_R^-,\ \tau_R^-$	$u_R,\ d'_R,\ c_R,\ s'_R,\ t_R,\ b'_R$	0

Table 2.2: Left-handed fermion doublets and right-handed fermion singlets with their assigned weak isospin.

2.1.2 Electroweak Theory

For the construction of the electroweak theory, some experimental ingredients have to be taken into account. Regarding the chirality, no right-handed neutrinos have been observed. The measurements indicate only left-handed neutrinos and right-handed anti-neutrinos. Next, while under weak interactions the flavour of leptons is conserved, this is not valid for quarks, for example in the weak decay of hadrons like the kaon $K^\pm$. Another experimental result is the non-zero mass of the weak bosons $W^\pm$ and Z^0, while the photon is massless.

All those ingredients have to be taken care of and will be used in this chapter in order to design the electroweak theory.

In the first part, the Glashow-Salam-Weinberg Model of the electroweak symmetry group $SU(2)_L \otimes U(1)_Y$ is described. In the second part, the Higgs mechanism is used for the generation of the bosons masses.

2.1.2.1 The Glashow-Salam-Weinberg Model

The symmetry group for the weak interaction is $SU(2)_L$, where L denotes the chiral component of the fermion field which is involved in this interaction. In Table 2.2 the fermions are listed as left-handed fermion fields, as weak isospin doublet and as right-handed fermion singlets taking into account the non-existence of right-handed neutrinos. In the left-handed scheme, the members of a doublet have a charge difference of 1. Therefore a transition within one doublet has the charge ± 1. The weak interaction conserves the lepton number.

Like in the case of QED, the $SU(2)$ gauge symmetry starts with the Lagrangian of the free fermions without any field, but this time the high-energy limit will be used in order to avoid a mass term. The masses of fermions will be discussed later in this chapter. Therefore, the Lagrangian for the fermions can be written as

$$\begin{aligned}\mathcal{L} &= i\bar{\psi}\gamma^\mu\partial_\mu\psi \\ &= i\bar{\psi_L}\gamma^\mu\partial_\mu\psi_L + i\bar{\psi_R}\gamma^\mu\partial_\mu\psi_R,\end{aligned} \tag{2.9}$$

where the fermion spinor $\psi = \psi_L + \psi_R$ is the sum of the left- and right-handed spinors. Note, neutrinos only exist as left-handed particles.

We require the left-handed part to be invariant under a transformation $U(x)$ of the group $SU(2)_L$:

$$\begin{aligned}\psi_L \to \psi_{L'} &= U(x)\psi_L \\ &= e^{\frac{ig}{2}\vec{\tau}\vec{\beta}(x)}\psi_L,\end{aligned} \tag{2.10}$$

where $\vec{\tau}$ is the vector of the Pauli matrices (generators of the $SU(2)$ group) and the vector $\vec{\beta}(x)$ indicates the dependence on space-time of the transformation. Analogous to (2.5) for the QED, the gauge invariance can be maintained by introducing three new vector fields W_μ^ν associated to three vector bosons W^1, W^2 and W^3 into the covariant derivative

$$\partial_\mu \to D_\mu^{SU(2)} = \partial_\mu + \frac{ig}{2}\vec{\tau}\vec{W}_\mu. \tag{2.11}$$

Substituting the derivative ∂_μ of the left-handed part in (2.9) with the covariant derivative, we get an additional term in the Lagrangian:

$$\mathcal{L}_w = -\frac{g}{2}\bar{\psi_L}\gamma^\mu\vec{\tau}\vec{W}_\mu\psi_L. \tag{2.12}$$

For the unification, the invariance under a transformation $U(1)$ is required on both, the left- and right handed terms in (2.9). In order to keep $\mathcal{L}_{L+R}$ invariant under a transformation $U(1)$, one additional gauge field B_μ is introduced in the covariant derivative:

$$\partial_\mu \to D_\mu^{U(1)} = \partial_\mu + \frac{ig'}{2} Y B_\mu. \tag{2.13}$$

Now we apply the weak covariant derivative from $SU(2)_L$ in (2.11) only on the left-handed part in (2.9) and the covariant derivative from $U(1)_Y$ in (2.13) on both terms, the left-handed and the right-handed part. We receive a new Lagrangian invariant under a transformation $SU(2)_L \otimes U(1)_Y$:

$$\begin{aligned}\mathcal{L} = & -i\bar{\psi_L}(\gamma^\mu \partial_\mu + i\frac{g}{2}\gamma^\mu \vec{\tau}\vec{W}_\mu + i\frac{g'}{2}\gamma^\mu Y B_\mu)\psi_L \\ & - i\bar{\psi_R}(\gamma^\mu \partial_\mu + i\frac{g'}{2}\gamma^\mu Y B_\mu)\psi_R. \end{aligned} \tag{2.14}$$

For a proper description of the four physical vector bosons $W^\pm$, Z^0 and the photon, the four gauge fields in $\vec{W}^\mu$ and B^μ have to be written as

$$W_\mu^\pm = \frac{1}{\sqrt{2}}(W_\mu^1 \mp W_\mu^2), \tag{2.15}$$

$$A_\mu = W_\mu^3 \sin\Theta_w + B_\mu \cos\Theta_w, \tag{2.16}$$

$$Z_\mu = W_\mu^3 \cos\Theta_w - B_\mu \sin\Theta_w. \tag{2.17}$$

The weak mixing angle or Weinberg angle Θ_w is defined as

$$\cos\Theta_w = \frac{g'^2}{\sqrt{g^2 + g'^2}}. \tag{2.18}$$

In terms of the couplings the electromagnet charge e can be written as

$$e = g' \sin\Theta_w = g\cos\Theta_w. \tag{2.19}$$

With those ingredients, the final Lagrangian of the electroweak interaction can be written as

$$\mathcal{L}_w = -gW_\mu^\pm\, j_\pm^\mu + eA_\mu j_{em}^\mu - Z_\mu\, \frac{e}{\sin\Theta_w \cos\Theta_w} j_{NC}^\mu. \tag{2.20}$$

The first term in (2.20) describes the charged current interaction of the $W^{\pm}$ bosons, coupling to electrons and neutrinos in the form $j_{+}^{\mu} = \bar{\psi}_{\nu L}\gamma^{\mu}\psi_{eL}$ and $j_{-}^{\mu} = -\bar{\psi}_{eL}\gamma^{\mu}\psi_{\nu L}$. The second component describes the electromagnetic interaction of the photon field A_{μ} on electrons in the form $j_{em}^{\mu} = \bar{\psi}_{eL}\gamma^{\mu}\psi_{eL} + \bar{\psi}_{eR}\gamma^{\mu}\psi_{eR}$. The last term describes the neutral current interaction of the neutral Z^0 vector boson in the form $j_{NC}^{\mu} = \bar{\psi}_{\nu L}\gamma^{\mu}\psi_{\nu L} - \bar{\psi}_{eL}\gamma^{\mu}\psi_{eL} + \sin^2 \Theta_w j_{em}^{\mu}$.

2.1.2.2 The Higgs Mechanism

The gauge invariance implies, that all the spin-1 gauge bosons have zero mass. However, the $W^{\pm}$ and the Z^0 bosons have non-zero masses, discovered by the UA1 and UA2 collaborations at the SPS. Therefore it is necessary to introduce additional mass terms of the type $\frac{1}{2}m^2\phi_{\mu}\phi^{\mu}$. In the Standard Model of Particle Physics the mechanism of spontaneous symmetry breaking is used to generate these masses [81, 98, 99].

A complex, scalar $SU(2)$ doublet field, the Higgs field, is introduced as

$$\Phi = \sqrt{\frac{1}{2}} \begin{pmatrix} \eta_1 + i\eta_2 \\ \eta_3 + i\eta_4 \end{pmatrix}, \tag{2.21}$$

assuming a self-interacting potential $V(\Phi)$ in the Lagrangian of the form

$$\begin{aligned} \mathcal{L}_{\mathcal{H}} &= (D^{\mu}\Phi)^{\dagger}(D_{\mu}\Phi) - V(\Phi) = \\ &= (D^{\mu}\Phi)^{\dagger}(D_{\mu}\Phi) - \mu^2\Phi^{\dagger}\Phi - \lambda(\Phi^{\dagger}\Phi)^2. \end{aligned} \tag{2.22}$$

Requiring $\lambda > 0$ with $\mu^2 > 0$ leading to a potential with one unique minimum, spontaneous symmetry breaking would not occur. However, requiring a negative value of $\mu^2 < 0$ leads to a surface as shown in Figure 2.1 (a), or as a cross section through the centre in (b). In this case, the potential has a ring of absolute minima at

$$\Phi^{\dagger}\Phi = v_0^2 = -\frac{\mu^2}{2\lambda}. \tag{2.23}$$

On the manifold of the minimum potential $V(\Phi)$ the potential is invariant under a $SU(2)$ transformation. However, one direction can be chosen in order to remove three out of the four field components of the complex doublet field Φ into three massless Goldstone

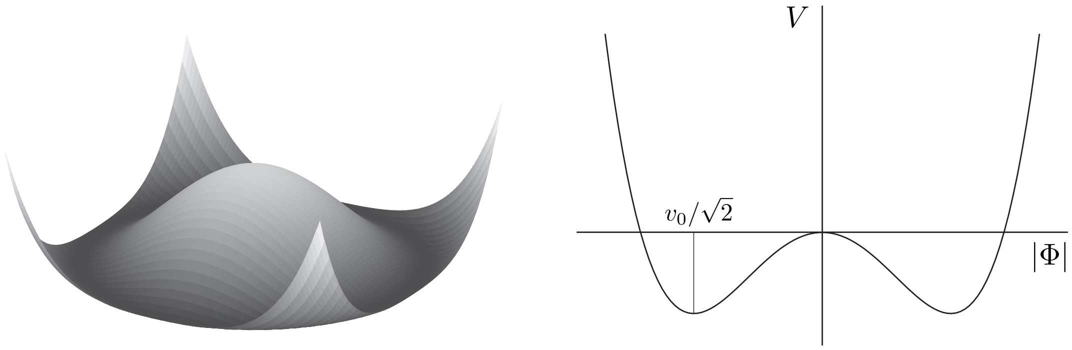

(a) (b)

Figure 2.1: The Higgs potential $V(\Phi)$ with $\mu^2 < 0$ and $\lambda > 0$. As illustrated in (a), the potential has the form of a Mexican-hat, the minimum of the potential is located on a ring. Figure (b) shows a cross section through the centre of the potential, illustrating the minimum of the potential $V(\Phi)$ at $v_0/\sqrt{2}$.

bosons and one physical Higgs field. With Φ expanded around one local minimum $\eta_1 = \eta_2 = \eta_4 = 0$ and $\eta_3 = v_0$

$$\Phi = \sqrt{\frac{1}{2}} \begin{pmatrix} 0 \\ v_0 + h(x) \end{pmatrix} \tag{2.24}$$

and the covariant derivative in $SU(2) \otimes U(1)$ from (2.11) and (2.13)

$$\partial_\mu \to D_\mu = \partial_\mu + \frac{ig}{2} \vec{\tau} \vec{W}_\mu + \frac{ig'}{2} Y B_\mu \tag{2.25}$$

in the Lagrangian (2.22), the following kinetic terms for the spin-1 bosons $W^\pm$ and Z^0 as written in (2.15) and (2.17) can be obtained:

$$\mathcal{L}_{W/Z} = \frac{g^2 v_0^2}{8} W_\mu^+ W^{+\mu} + \frac{g^2 v_0^2}{8} W_\mu^- W^{-\mu} + \frac{(g^2 - g'^2) v_0^2}{8} Z_\mu Z^\mu . \tag{2.26}$$

By comparing these terms with a typical boson mass term of the form $\frac{1}{2} m^2 A_\mu A^\mu$, the coupling of the $W^\pm$ and Z^0 bosons to the non-zero expectation value of the Higgs field gives us a mass ratio between these two bosons:

$$\frac{m_W}{m_Z} = \cos \Theta_w = \frac{1}{m_Z} \cdot \frac{g v_0}{2} . \tag{2.27}$$

From the four initial fields in (2.21), three Goldstone bosons have become longitudinal polarised modes of the massive gauge bosons, while the fourth field remains as massive, scalar Higgs boson with mass

$$m_{\mathcal{H}} = 2v_0\sqrt{\lambda}, \tag{2.28}$$

which cannot be predicted by the other parameters of the Standard Model of Particle Physics. The measurement of the Higgs boson mass poses one of the main tasks in order to complement all parameters of the Standard Model and to fully understand the mass generation of the heavy gauge bosons.

2.1.3 Quantum Chromodynamics

Quantum Chromodynamics (QCD) describes the strong interaction between particles which carry a colour charge, namely quarks and gluons. Quarks and gluons often are referred as partons. Bound states of quarks are called hadrons, colour-neutral states of a quark and an anti-quark called mesons, or alternatively three (anti)-quarks described by QCD called baryons. Beside the coupling of the partons in hadrons, the strong interaction is responsible for the binding of baryons in nucleons.

The theory is based on the gauge symmetry $SU(3)_C$, where C indicates the three colour charges r, g and b. Each quark, independent of its flavour (u, d, s, ...), carries a colour charge. The generators of the $SU(3)$ group are the eight gauge bosons, gluons. They have a zero electric charge, comparable to photons, but they couple to the colour charge. As shown in experiments (e.g. [15]) with charmonium ($c\bar{c}$) and bottomium ($b\bar{b}$), the strong interaction is flavour independent.

In QCD the Dirac spinor for a quark q of flavour $f \in \{u, d, s, c, b, t\}$ written as $\psi_f = (q_f^1, q_f^2, q_f^3)$, where the indices $\{1, 2, 3\}$ correspond to the colours $\{r, g, b\}$, has to be considered. Analogous to the QED, a Lagrangian similar to (2.2) for the free quark can be built:

$$\mathcal{L} = \sum_f \bar{\psi}_f (i\gamma^\mu \partial_\mu - m_f)\psi_f. \tag{2.29}$$

This Lagrangian is invariant under a global $SU(3)$ transformation $U(x)$ in the colour space:

$$\begin{aligned}\psi_f \to \psi_f' &= U\psi_f \\ &= e^{-ig_s\frac{\lambda^a}{2}\theta_a}\psi_f,\end{aligned} \tag{2.30}$$

where g_s is the coupling strength of the strong interaction, the Gell-Mann matrices λ^a with $a \in \{1, 2, ..., 8\}$ are the eight generators of the $SU(3)$ algebra and θ_a is an arbitrary 8-vector. The Gell-Mann matrices follow the commutation relation

$$[\lambda^a, \lambda^b] = 2if^{a,b,c}\lambda^c, \tag{2.31}$$

where $f^{a,b,c}$ is the real and antisymmetric structure functions of the $SU(3)$ group.

The requirement for local gauge invariance by substituting the constant θ_a by a space-time dependent $\theta_a(x)$ does not hold, but like in QED the derivative has to be substituted by a modified covariant derivative

$$\partial^\mu \to D^\mu = \partial^\mu + ig_s\frac{\lambda^a}{2}G^a_\mu, \tag{2.32}$$

where the gluon fields G^a_μ transform as

$$G'^\mu_a = U(x)G^\mu_a = G^\mu_a + \partial^\mu + g_s f^{abc}\theta_b(x)G^\mu_c. \tag{2.33}$$

Introducing the corresponding gluon field strength tensor

$$G^{\mu\nu}_a(x) = \partial^\mu G^\nu_a - \partial^\nu G^\mu_a + g_s f^{abc}G^\mu_a G^\nu_a \tag{2.34}$$

leads to the local $SU(3)_c$ invariant full Lagrangian of the QCD

$$\mathcal{L} = \sum_f \bar{\Psi}^\alpha_f(i\gamma^\mu D_\mu - m_f)\Psi^\alpha_f - \frac{1}{4}G^{\mu\nu}_a G^a_{\mu\nu}, \tag{2.35}$$

which can be written in the following terms:

$$\mathcal{L} = \sum_f \bar{q}_f \alpha (i\gamma^\mu \partial_\mu - m_f) q_f^\alpha - \frac{1}{4}(\partial^\mu G_a^\nu - \partial^\nu G_a^\mu)(\partial_\mu G_\nu^a - \partial_\nu G_\mu^a)$$
$$- g_s G_a^\mu \sum_f \bar{q}_f^\alpha \gamma_\mu \left(\frac{\lambda^a}{2}\right)_{\alpha\beta} q_f^\beta$$
$$- \frac{g_s}{2}(\partial^\mu G_a^\nu - \partial^\nu G_a^\mu) G_\mu^b G_\mu^c - \frac{g_s^2}{4} f^{abc} f_{ade} G_b^\mu G_c^\mu G_\mu^d G_\mu^e. \qquad (2.36)$$

2.1.3.1 Confinement and Asymptotic Freedom

Due to the non-abelian character of the symmetry group $SU(3)_c$, next to the kinetic term of the quarks and gluons in the first line of (2.36) and the colour interaction between quarks and gluons in line two, the third line represents the gluon self-interaction as shown in Figure 2.2. This special feature leads to two important properties of the QCD: confinement and asymptotic freedom.

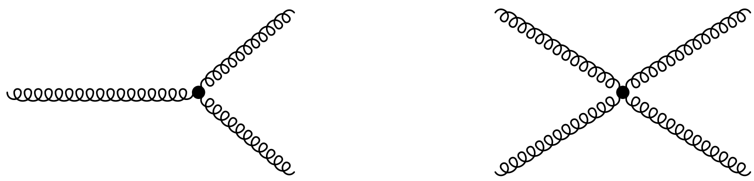

(a) (b)

Figure 2.2: Gluon self-interaction due to the non-abelian character of the $SU(3)_c$ allows the interaction between three (a) or four (b) gluons.

First, coloured particles are postulated to exist only in confined colour-singlet states, i.e. hadrons. This behaviour is called *colour confinement*. Therefore, quarks are bound in colour-singlet states, either as a baryon B or as a meson M:

$$B = \frac{1}{\sqrt{6}} \epsilon_{a,b,c} \left| q^a, q^b, q^c \right\rangle \qquad (2.37)$$
$$M = \frac{1}{\sqrt{2}} \delta_{a,\bar{a}} \left| q^a \bar{q}^{\bar{a}} \right\rangle, \qquad (2.38)$$

where $a, b, c \in \{1, 2, 3\}$ (according to r, g and b). Confinement implies, that no free quarks can be observed, which is in accordance to current measurements. Due to confinement also gluons cannot be found free, however bound multi-gluon states or glueballs are not forbidden in theory.

The second striking property of QCD is *asymptotic freedom* [95], describing the interaction between quarks at short distances less then 0.1 fm. With decreasing distance the strong interaction weakens, hence the partons can move nearly non-interacting within those short spacings. Due to asymptotic freedom, within the boundaries of a hadronic state, the partons can move nearly without interaction.

Combining the two regimes of confinement and asymptotic freedom gives the current understanding of the interaction between two quarks: at small distance, two quarks are strongly bound as hadrons. The binding energy increases with the distance between the two quarks, rendering the possibility for new particles to be created in the colour field.

2.1.3.2 The Strong Coupling Constant α_s

Perturbative calculations of scattering amplitudes are straightforward at the lowest order tree level. Considering higher orders in the coupling constant $\alpha_s = g_s^2/4\pi$ introduces Feynman diagrams containing loops of bosons and fermions, which leads to divergencies. The isolation and removing of these divergences, using the techniques of renormalisation, introduces a scale parameter μ with the dimension of mass, given by the point, where the removing of the divergent terms was performed. For large values of the transferred 4-momentum Q^2, the coupling constant can be written as

$$\alpha_s(Q^2) = \frac{\alpha_s(\mu^2)}{1 + \alpha_s(\mu^2)\frac{33-2n_f}{12\pi}\log|Q^2/\mu^2|}, \tag{2.39}$$

where n_f denotes the number of quark flavours involved ($n_f = 6$) and $\alpha_s(\mu)$ the strong coupling constant at the scale value, e.g. $\alpha_s(M_Z^0) = 0.118$ (here: $n_f = 5$, as the *top*-quark mass is much larger than m_Z). Written in other terms, α_s becomes

$$\alpha_s(Q^2) = \frac{12\pi}{(33 - 2n_f)\log(Q^2/\Lambda_{QCD}^2)}, \tag{2.40}$$

where the scale $\Lambda_{QCD} \approx 200$ MeV can be seen as the boundary between colour confined bound states and asymptotic free partons. For Q^2 values much larger than Λ_{QCD}, in the regime of asymptotic freedom, the coupling is small and perturbative calculations can be used, whereas at small Q^2 the quarks and gluons are bound within hadrons.

In Figure 2.3 the running coupling constant α_s is shown as a function of Q. For values of α_s with a large 4-momentum transfer $Q \to \infty$ or, in other words, small distances, the coupling clearly shows the behaviour of asymptotic freedom. However, despite the perturbative results for these calculations show a plausible behaviour at small energies, the perturbative theory is not valid anymore at $Q \approx 1GeV$.

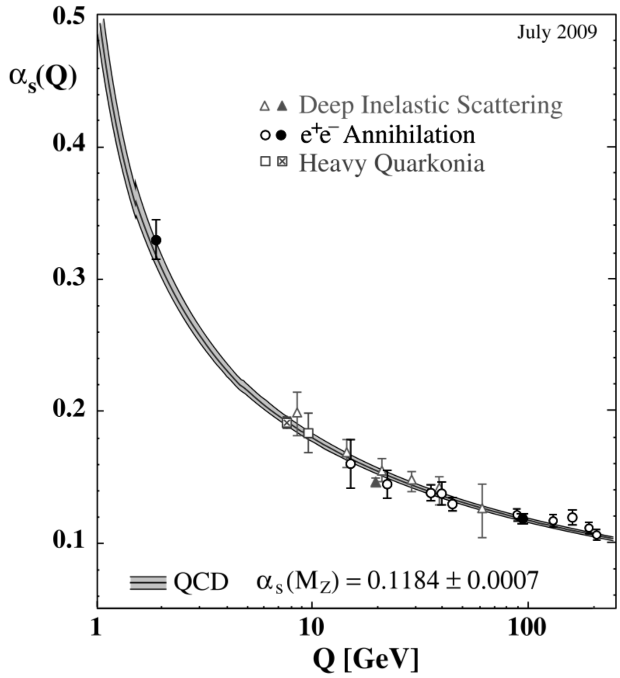

Figure 2.3: Summary on the measurements of the running coupling constant α_s. This figure is taken from [53].

2.2 Physics at the Large Hadron Collider

In hadron collisions at the Large Hadron Collider LHC dense clouds of protons collide at high energies, producing new particles in deep inelastic scattering events. Due to the proton structure at high energies, these kind of events have a complex structure, outlined in the following Chapter 2.2.1. Especially the production of heavy quark pairs, crucial for this thesis, is discussed in Chapter 2.2.2.

2.2.1 Proton Proton Collisions

In order to understand the collision of two protons, the internal structure of hadrons at high energies has to be understood. A detailed review can be found in [62].

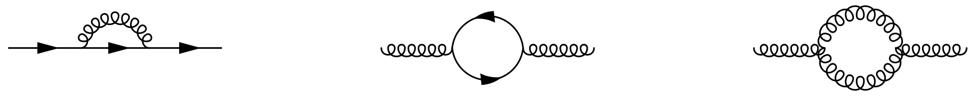

(a) (b) (c)

Figure 2.4: Lowest order quantum fluctuations in QCD. There exists no analogous interaction in QED to the gluon-gluon interaction shown in (c), whereas the emission and subsequent absorption of gluons in (a) and the $q\bar{q}$ pair production and subsequent annihilation are analogue to fluctuations in QED.

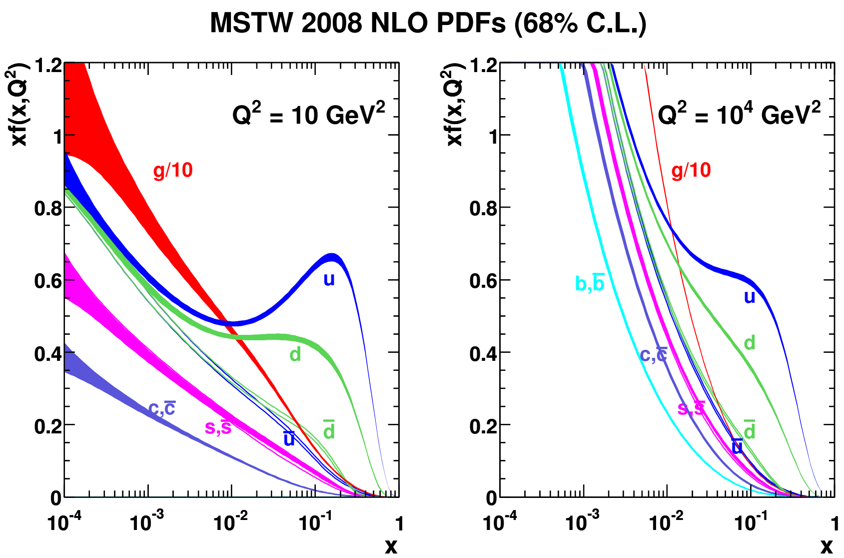

Figure 2.5: Parton distribution functions for two different energies $Q^2 = 10\ \mathrm{GeV}^2$ and $Q^2 = 10^4\ \mathrm{GeV}^2$. The gluon is downscaled. This figure is taken from [121] (MSTW 2008 NLO PDFs), plot by G. Watt.

At high energies, the proton cannot be considered as a simple three-quark state, but rather as a complex and highly dynamic superposition of a sea of gluons and quark-antiquark pairs around three valence quarks. The mechanisms of these additional partons have been established in QCD (Chapter 2.1.3) and in first order can be explained by asymptotic freedom. The short distance between the partons give rise to loops as shown in Figure 2.4, leading to the complex structure of the proton.

The hadrons momentum is added up by the sum of the partons momenta. Parton density functions (PDFs) $f_i(x, Q^2)$ describe the probability to find a parton i with a fraction x (Bjorken-x) of the protons longitudinal momentum. The inner structure of

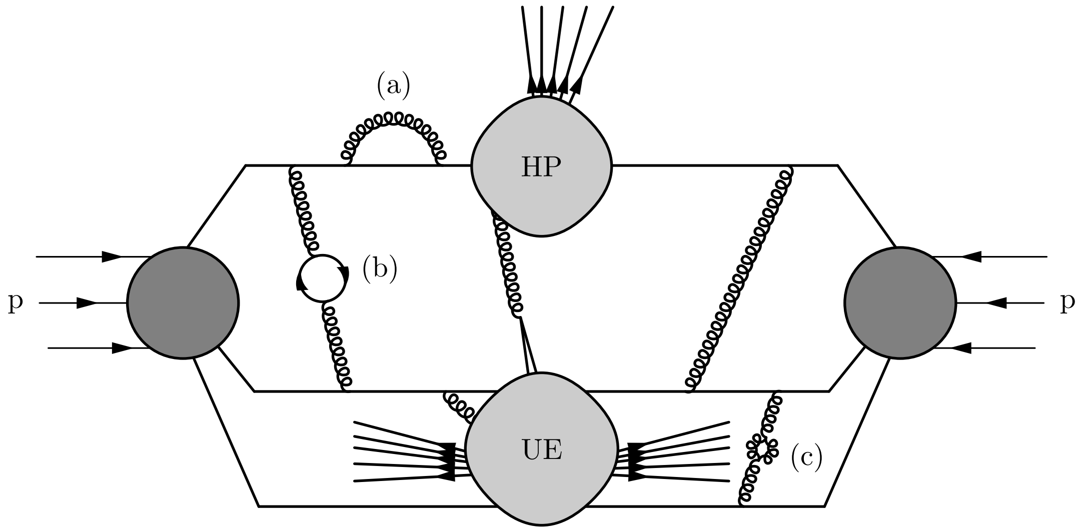

Figure 2.6: A schematic drawing of a typical proton-proton collision with hard inelastic scattering: one hard process (HP) creates particles with high transverse momentum p_T, while the other partons (gluons and quarks) within the proton cloud create particle jets with small p_T, the so-called underlying event (UE).

a high energy nucleon can be probed by deep inelastic scattering of a lepton with the nucleon by the processes $ln \to lX$. As shown in Figure 2.5 from the MSTW 2008 NLO, at low x the gluons $g/10$ dominate. Remark, the gluon is downscaled by a factor of 10. The distributions of the u- and d-quarks at high x are higher than the distributions of their corresponding anti-particles due to the valence quarks in the proton.

2.2.1.1 Hard Process and Underlying Event

Consequently, the collision of two protons cannot only be described by the interaction of two valence quarks, but the collision rather looks like a complicated event as shown in a simplified form in Figure 2.6. The process of prior physics interest is a hard process HP, in which two partons have a large energy transfer, enabling them to leave the confinement of the two protons. However, various additional processes take place during such a collision. The primary debris in such a collision is summarised as underlying event UE, which is often defined as all outgoing particles in one proton collision except the products of the hard process. The underlying event leads to predominantly soft scattering of the remaining partons into showers with large pseudorapidity, i.e. into the very forward direction.

The partons created in both, the hard process and the underlying event, loose energy through radiation in a cascade of parton emissions, creating parton showers. As soon as

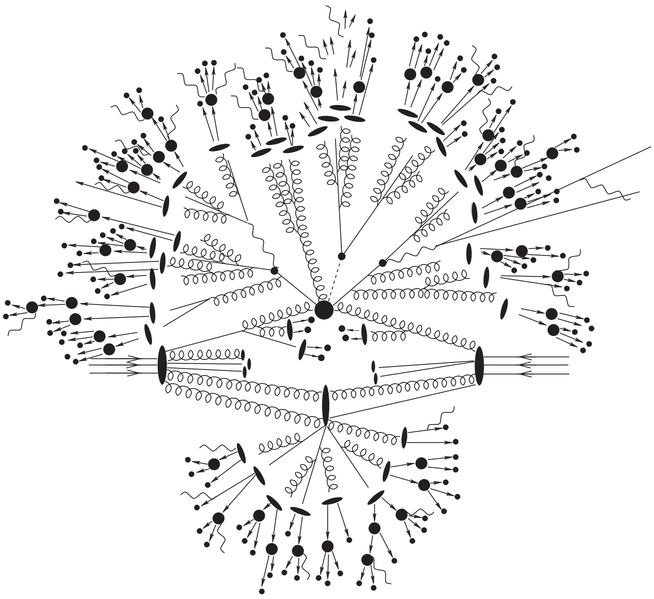

Figure 2.7: Illustration of a proton proton collision and the subsequent process of fragmentation and hadronisation. Adapted from [112].

the partons have lost most of their energy, due to confinement quarks and gluons recombine to colour singlet states. This process is called hadronisation. Hadrons containing b- and/or $\bar{b}$ quark(s) are called B hadrons,

In Figure 2.7 a proton proton collision is illustrated, starting from the collision of the two parton clouds, creating both, an underlying event and particles from a hard process, and finally undergoing fragmentation and hadronisation.

2.2.1.2 Pile-up

At the Large Hadron Collider, not just two protons collide, but two bunches of protons interact in the centre of the ATLAS experiment. It is very unlikely to have more than one event with a high p_T hard scattering process in one bunch crossing. However, with increasing luminosity the number of minimum bias events without any high p_T contribution increases, referred to as pile-up events. At a low luminosity of $\mathcal{L} = 10^{33}$ cm^{-2}s^{-1} the number of minimum bias events in one bunch crossing is expected to be 2.3, at the LHC design luminosity of $\mathcal{L} = 10^{34}$ cm^{-2}s^{-1} 23 minimum bias events per bunch crossing are expected.

2.2.2 Heavy Flavour Production at the Large Hadron Collider

The total cross section of $pp \to X$ has been calculated in [63], the $b\bar{b}$ production in $pp \to bbX$ is discussed at leading order in [126], higher order corrections are discussed in [63].

The hard process responsible for the production of particles and jets in the preferred direction perpendicular to the beam pipe is a $2 \to 2$ scattering of two partons. The production of heavy quark pairs occurs mainly through the QCD processes as shown in leading order in Figure 2.8.

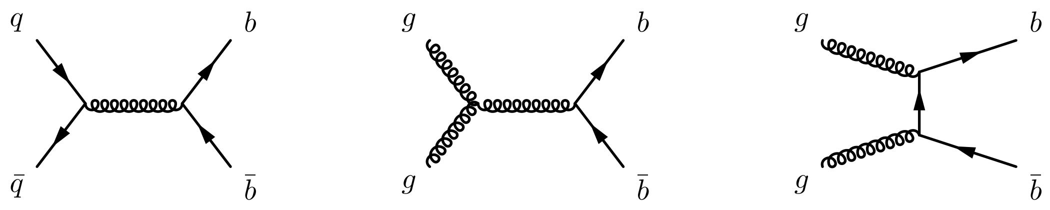

(a) (b) (c)

Figure 2.8: Leading order heavy flavour creation in hard QCD processes responsible for $b\bar{b}$ production in proton-proton collisions: quark-antiquark annihilation (a), gluon-gluon fusion (b) and gluon-splitting (c).

At leading order, the main $b\bar{b}$ production processes in proton collisions are quark-antiquark annihilation (a), gluon-fusion (b) and gluon-splitting (c). Hence, the production of heavy flavours is very sensitive on the gluon content as well as the valence- and sea-quark content, correspondingly the PDFs described in Chapter 2.2.1 have to be investigated properly. At the LHC the dominant process for the heavy quark pair production is gluon-fusion.

The $b\bar{b}$ production cross section can be calculated by summing over all possible configurations of the leading order diagrams, taking into account all possible states for the incoming particles (flavours, colours, spins and momenta). The total cross section can be written as

$$\sigma_{b\bar{b}}(\sqrt{s}, m_b^2) = \sum_{i,j} \int_{x_1} \int_{x_2} dx_1 dx_2 f_i(x_1, \mu^2) f_j(x_2, \mu^2) \times \hat{\sigma}_{ij}(\hat{s} = x_1 x_2 s, m_b^2, \mu^2), \qquad (2.41)$$

where $\hat{\sigma}_{ij}$ is the cross section for one QCD process of two partons i and j into a $b\bar{b}$ pair, and $f_{i/j}$ the PDF of the corresponding parton. At the LHC at a centre of mass

b hadron	in $Z^0 \to b\bar{b}$	at Tevatron	combined
B^+, B^0	$(40.2 \pm 0.9)\%$	$(33.2 \pm 3.0)\%$	$(40.0 \pm 1.2)\%$
B_s^0	$(10.5 \pm 0.9)\%$	$(12.2 \pm 1.4)\%$	$(11.5 \pm 1.3)\%$
B baryons	$(9.0 \pm 1.5)\%$	$(21.4 \pm 6.8)\%$	$(8.5 \pm 2.1)\%$

Table 2.3: The fractions of B hadrons in $Z^0 \to b\bar{b}$ decays, in $p\bar{p}$ collisions at $\sqrt{s} = 1.8$ TeV and the combined results [125].

energy of $\sqrt{s} = 14$ TeV, the $b\bar{b}$ pair production cross section is estimated to be of the order 500 μb, as shown in Figure 2.9. Accordingly one out of 100 collision events contain a $b\bar{b}$ pair. At the LHC design luminosity of $\mathcal{L} = 10^{34}$ cm^{-2}s^{-1} this cross section corresponds to a $b\bar{b}$ production rate of 500 kHz, by far exceeding even the first level trigger rate of 75 kHz at ATLAS (see Chapter 3.9).

The fractions of weakly decaying B hadrons have been measured in the decays $Z^0 \to b\bar{b}$ at the experiments and in $p\bar{p}$ collisions at $\sqrt{s} = 1.8$ TeV at the Tevatron. The results, summarised in [125], are shown in Table 2.3.

In proton-proton collisions with a $b\bar{b}$ pair, the two resulting B hadrons predominantly are produced in the forward direction, i.e. they have small angles with respect to the initial proton momentum. However, as shown in Figure 2.10, the acceptance for the measurement of B hadron pairs at ATLAS is above 34%. The figure shows the flight direction of the two B hadrons and the acceptance of the two LHC experiments ATLAS and LHCb. The angles are converted into pseudorapidity[2] η, where $\eta = 0$ corresponds to the plane perpendicular to the initial proton momentum. While the layout of the ATLAS experiment primarily aims at the detection of particles perpendicular to the beam axis, the quasi-hermetic design allows this excellent B hadron acceptance.

2.3 CP Violation and B_s Mixing

In the following, the physics processes of B_s^0 mixing and $\mathcal{CP}$ violation in B physics are introduced in Chapter 2.3.2 and Chapter 2.3.3, respectively. Within the Standard Model

[2] More details on pseudorapidity in Chapter 3.2

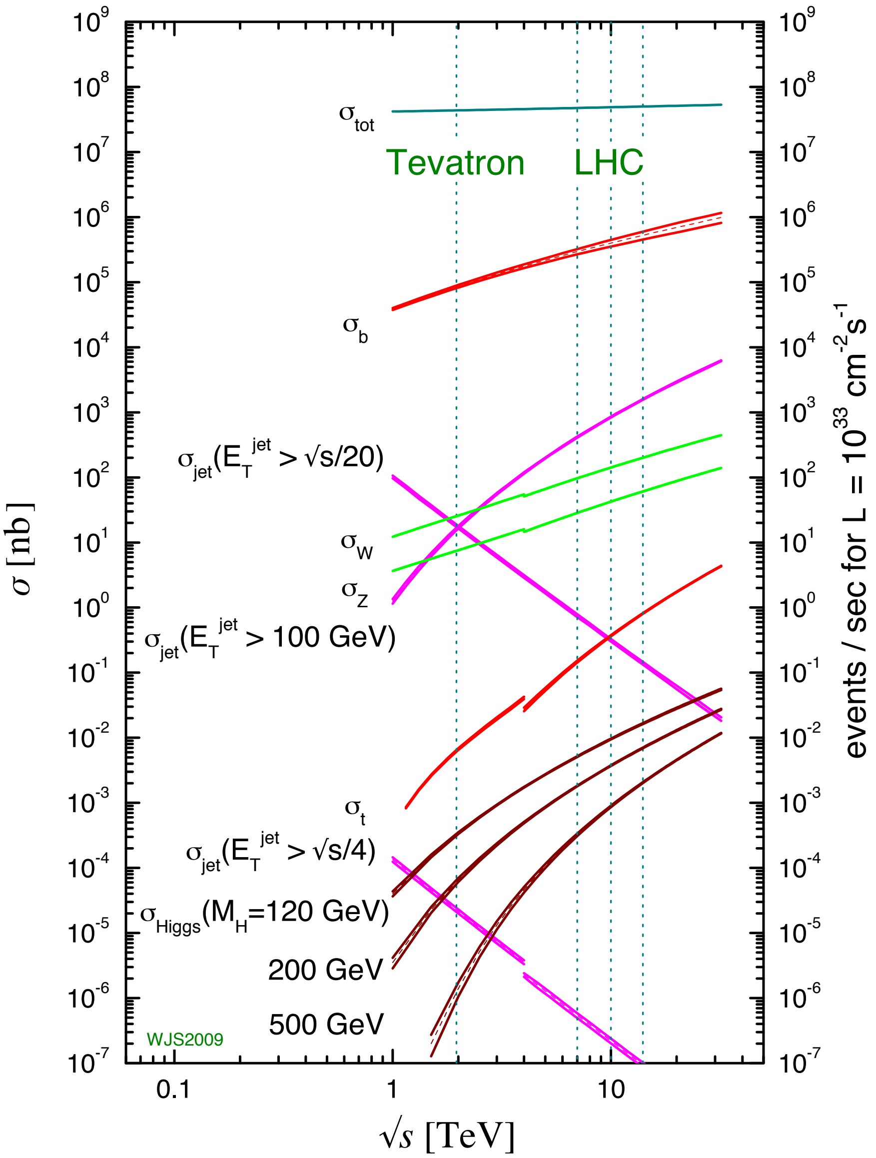

Figure 2.9: Standard Model calculations for the total cross section in proton-(anti)proton collisions at Tevatron and at the LHC as a function of the centre-of-mass energy. The inclusive $b\bar{b}$ production cross section, increasing with the collision energy, is estimated to be two orders of magnitude below the total cross section. The Figure is taken from [62], updated plot (2009) by J. Stirling.

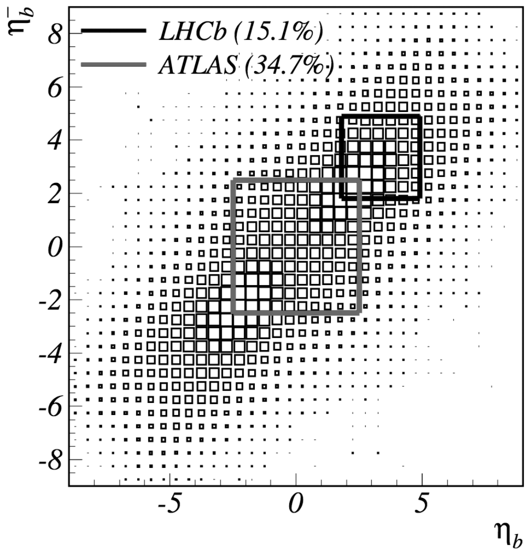

Figure 2.10: Pseudorapidity distribution of two B hadrons created in a hadronic $b\bar{b}$ pair event. Superimposed, the two squares display the acceptances of ATLAS and LHCb experiments. Figure adapted from [154], based on a simulation with PYTHIA [139]

of Particle Physics both, mixing and $\mathcal{CP}$ violation, are described by the Cabibo-Kobayashi-Maskawa matrix, which will be discussed in Chapter 2.3.1. A detailed description of the CKM matrix can be found in [66, 100].

2.3.1 The Cabibo-Kobayashi-Maskawa Matrix

In the theoretical framework of electroweak coupling, the interaction does not couple to the mass eigenstates of the quarks, but rather to a linear combination of *up*-type u, c, t or *down*-type d, s, b quarks. The usual convention denotes the *down*-type quarks as mixed gauge eigenstates, however this choice is arbitrary. The set of electroweak eigenstates can be written as

$$\begin{pmatrix} d' \\ s' \\ b' \end{pmatrix} = V_{CKM} \begin{pmatrix} d \\ s \\ b \end{pmatrix}, \tag{2.42}$$

where V_{CKM} in detail is written as

$$V_{CKM} = \begin{pmatrix} V_{ud} & V_{us} & V_{ub} \\ V_{cd} & V_{cs} & V_{cb} \\ V_{td} & V_{ts} & V_{tb} \end{pmatrix}. \tag{2.43}$$

The complex 3×3 matrix V_{CKM} is called Cabibbo-Kobayashi-Maskawa (CKM) matrix [61, 111]. The coupling strength of a charged current transition of e.g. a *down*-type quark d into an *up*-type quark u of the type $u \to dW^-$ is proportional to the corresponding matrix element V_{ud}.

Using the methods of the CKMFitter group, the current world average of the magnitudes of the CKM matrix elements fitted by the UTFit- and CKMFitter Collaboration [55, 67] are:

$$V_{CKM} = \begin{pmatrix} 0.974(19 \pm 22) & 0.22(50 \pm 10) & 0.003(59 \pm 16) \\ -0.22(56 \pm 10) & 0.973(34 \pm 23) & 0.04(15^{+10}_{-11}) \\ 0.008(74^{+26}_{-37}) & -0.040(70 \pm 10) & 0.9991(33^{+44}_{-43}) \end{pmatrix}. \tag{2.44}$$

2.3.1.1 CKM Matrix in Standard Parametrisation

The CKM matrix is unitary, which corresponds to the absence of flavour changing neutral currents (FCNC) processes at tree level in the electroweak theory. The requirement for unitarity reduces the number of 18 parameters of the complex 3×3 matrix to nine, three rotational Euler angles and six complex phases. It can be shown, that five of these six angles are not observable and therefore can be eliminated into one global phase. In general, for an $N \times N$ quark mixing matrix, the number of Euler angles is $\frac{1}{2}N(N-1)$ and the number of complex phases is $\frac{1}{2}(N-1)(N-2)$. Therefore, for the CKM matrix, the three Euler angles are denoted as Θ_{12}, Θ_{13} and Θ_{23}, the complex $\mathcal{CP}$ violating phase is written as δ.

These four parameters can be used to give the standard parametrisation [69] as e.g. advocated by the Particle Data Group PDG [125]:

$$V_{CKM} = \begin{pmatrix} c_{12}c_{13} & s_{12}c_{13} & s_{13}e^{-i\delta} \\ -s_{12}c_{23} - c_{12}s_{23}s_{13}e^{i\delta} & c_{12}c_{23} - s_{12}s_{23}s_{13}e^{i\delta} & s_{23}c_{13} \\ s_{12}s_{23} - c_{12}c_{23}s_{13}e^{i\delta} & -c_{12}s_{23} - s_{12}c_{23}s_{13}e^{i\delta} & c_{23}c_{13} \end{pmatrix} \tag{2.45}$$

where $c_{ij} = \cos\Theta_{ij}$ and $s_{ij} = \sin\Theta_{ij}$. The main advantage of this parametrisation emerges when forcing all but one angle Θ_{ij} to zero. Assuming $\Theta_{13} = \Theta_{23} = 0$ and $\Theta_{12} = \Theta_C$, where Θ_C is the Cabibbo angle, the resulting CKM matrix becomes

$$V_{CKM} = \begin{pmatrix} \cos\Theta_C & \sin\Theta_C & 0 \\ -\sin\Theta_C & \cos\Theta_C & 0 \\ 0 & 0 & 1 \end{pmatrix}, \tag{2.46}$$

the mixing matrix for the first two quark families, initially introduced in [61] in the absence of the heavy flavours b and t.

However, experimental measurements reveal the hierarchical structure of the three mixing angles:

$$s_{12} = 0.22 >> s_{23} = \mathcal{O}(10^{-2}) >> s_{13} = \mathcal{O}(10^{-3}) \tag{2.47}$$

2.3.1.2 CKM Matrix in Wolfenstein Parametrisation

Taking the hierarchy of the measured values in (2.44) into account, one realises that the diagonal elements are close to one, while the off-diagonal elements become smaller with increasing distance to the diagonal. The Wolfenstein parametrisation [151] uses this hierarchy by introducing an alternative parametrisation:

$$\begin{aligned} s_{12} &= \lambda \\ s_{23} &= A\lambda^2 \\ s_{13}e^{-i\delta} &= A\lambda^3(\rho - i\eta). \end{aligned} \tag{2.48}$$

Expanding the matrix (2.45) as a series in powers of the small value λ up to $\mathcal{O}(\lambda^3)$, the CKM matrix becomes

$$V_{CKM} = \begin{pmatrix} 1 - \frac{\lambda^2}{2} - \frac{\lambda^4}{8} & \lambda & A\lambda^3(\rho - i\eta) \\ -\lambda & 1 - \frac{\lambda^2}{2} & A\lambda^2 \\ A\lambda^3(1 - \rho - i\eta) & -A\lambda^2 + \frac{1}{2}A\lambda^4(1 - 2(\rho + i\eta)) & 1 - \frac{A^2\lambda^4}{2} \end{pmatrix}. \tag{2.49}$$

Note, that the element V_{ub} still is the exact value without any higher order contribution.

In the Wolfenstein parametrisation the suppression of transitions between the quark families becomes obvious in powers of λ. While transitions within one family are of the order $\lambda^0 = 1$, transitions between the adjacent families V_{us}, V_{cd} (V_{ts}, V_{cb}) are of the order λ^1 (λ^2), and the transition from the heavy flavour quarks t and b to the light quarks d and u are suppressed by a factor of λ^3.

2.3.1.3 Unitary Triangles

As stated before, the CKM matrix is a unitary matrix. Therefore the matrix elements have to fulfil the equation

$$V_{CKM}V_{CKM}^{\dagger} = \mathbb{1} = V_{CKM}^{\dagger}V_{CKM}, \tag{2.50}$$

where $\mathbb{1}$ is the identity 3×3 matrix. This relation can be written in a total of 18 equations, dealing with the line j and row k. The six diagonal equations ($i = k$) are equal one, representing the normalisation. From the twelve remaining equations, six are identical to the other six by swapping i and k, giving us a total of six orthogonality relations:

$$V_{ud}{V_{ub}}^* + V_{cd}{V_{cb}}^* + V_{td}{V_{tb}}^* = 0 \tag{2.51}$$
$$V_{ud}{V_{us}}^* + V_{cd}{V_{cs}}^* + V_{td}{V_{ts}}^* = 0 \tag{2.52}$$
$$V_{us}{V_{ub}}^* + V_{cs}{V_{cb}}^* + V_{ts}{V_{tb}}^* = 0 \tag{2.53}$$
$${V_{ud}}^*V_{cd} + {V_{us}}^*V_{cs} + {V_{ub}}^*V_{cb} = 0 \tag{2.54}$$
$${V_{ud}}^*V_{td} + {V_{us}}^*V_{ts} + {V_{ub}}^*V_{tb} = 0 \tag{2.55}$$
$${V_{cd}}^*V_{td} + {V_{cs}}^*V_{ts} + {V_{cb}}^*V_{tb} = 0 \tag{2.56}$$

These equations can be interpreted as triangles in the complex plane, each term representing one side of the triangle. In the Wolfenstein parametrisation, the three sides of the triangles (2.52), (2.53), (2.54) and (2.56) strongly vary in length (between $\mathcal{O}(\lambda)$ and $\mathcal{O}(\lambda^5)$), hence they are squashed. However, the side length of the triangles (2.51) and (2.55) are of the same lowest order of $\mathcal{O}(A\lambda^3)$, neglecting higher order terms they are identical. The triangles can be rescaled by dividing the equations with $V_{cd}{V_{cb}}^* = {V_{us}}^*V_{ts} = A\lambda^3$. They can be written as

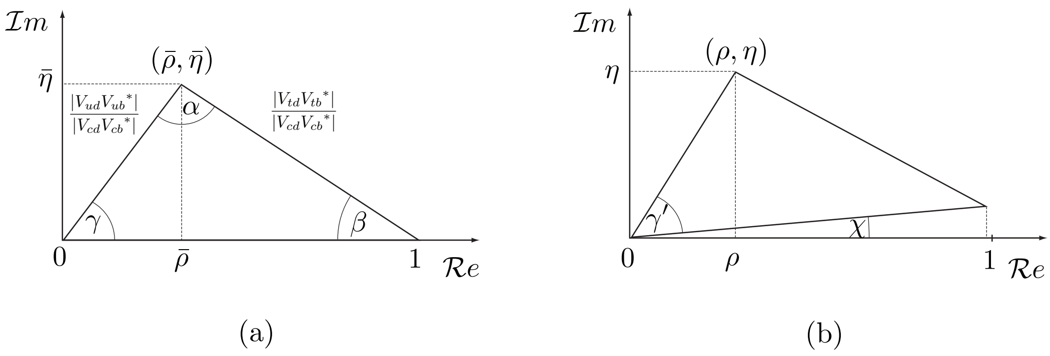

Figure 2.11: The two unitary triangles of the CKM matrix, the triangle (2.57) corresponding to (a), the triangle (2.58) to (b).

$$\frac{V_{td}V_{tb}{}^*}{V_{cd}V_{cb}{}^*} + \frac{V_{cd}V_{cb}{}^*}{V_{cd}V_{cb}{}^*} + \frac{V_{ud}V_{ub}{}^*}{V_{cd}V_{cb}{}^*} = 0 \tag{2.57}$$

$$\frac{V_{ud}{}^*V_{td}}{V_{us}{}^*V_{ts}} + \frac{V_{us}{}^*V_{ts}}{V_{us}{}^*V_{ts}} + \frac{V_{ub}{}^*V_{tb}}{V_{us}{}^*V_{ts}} = 0 \tag{2.58}$$

$$(1-\rho-i\eta) + (-1) + (\rho+i\eta) = 0 \tag{2.59}$$

The equation shown in (2.59) is often referred as *the unitarity triangle*. Taking into account the higher order terms $\mathcal{O}(\lambda^5)$ introduces additional terms, the two triangles (2.57) and (2.58) are no more identical. More detailed calculations in higher order can be found in Appendix A. By introducing a new set of parameters defined as

$$\begin{aligned} \bar{\rho} + i\bar{\eta} &= -\frac{V_{ud}V_{ub}{}^*}{V_{cd}V_{cb}{}^*} \\ &= (\rho + i\eta)(1 - \lambda^2/2) \end{aligned} \tag{2.60}$$

the triangle (2.57) in Figure 2.11 (a) can be aligned with the real axis. However, as shown in Figure 2.11 (b), the higher order terms in the triangle (2.58) introduce a small angle $\chi = \lambda^2\eta$ between the real axis and the base of the triangle. This angle can be probed through certain $\mathcal{CP}$-violating processes.

The three angles of the Unitary Triangle α, β and γ (or in an alternative nomenclature ϕ_1, ϕ_2 and ϕ_3) in Figure 2.11 (a) are

$$\alpha = \phi_2 = \arg\left(-\frac{V_{td}{V_{tb}}^*}{V_{ud}{V_{ub}}^*}\right) \tag{2.61}$$

$$\beta = \phi_1 = \arg\left(-\frac{V_{cd}{V_{cb}}^*}{V_{td}{V_{tb}}^*}\right) \tag{2.62}$$

$$\gamma = \phi_3 = \arg\left(-\frac{V_{ud}{V_{ub}}^*}{V_{cd}{V_{cb}}^*}\right). \tag{2.63}$$

As shown by Jarlskog [103, 104], all six unitary triangles (2.51)-(2.56) have an identical area of the order $\mathcal{O}(10^{-5})$, half of the Jarlskog Invariant J, which can be expressed in terms of the CKM matrix elements:

$$J = s_{12}s_{23}s_{13}c_{12}c_{23}c_{13}^2 \sin\delta. \tag{2.64}$$

2.3.1.4 Measuring the Unitary Triangle

Despite the Unitary triangle just is a graphical interpretation of the CKM matrix, the precise measurement of its sides and angles is an excellent test for the Standard Model. Deviations from a closed triangle would be a strong indicator for physics beyond the current Standard Model.

Assuming unitary of the CKM matrix ($\alpha+\beta+\gamma = 180°$), the $\mathcal{CP}$ violation is described by a single global phase and a total of three quark generations, the apex of the triangle has to be measured as precise as possible. Under these assumptions and using the Unitary Triangle as shown in Figure 2.11 (a), the aim is to constrain the apex of the triangle, taking into account as many measurements as possible. All measurements should agree with each other, contradictions are indicators for physics beyond the Standard Model.

Currently two main working groups perform global fits of the Unitary Triangle: while the UTFit collaboration [55] is using a Bayesian statistics model, the CKMFitter collaboration [68] uses a frequentist approach.

Both collaborations use the parameters listed in Table 2.4. A large number of experiments and collaborations contributed for the measurement of these parameters, as the B-factories BaBar [39] and Belle [49], the two major Tevatron experiments CDF and DØ, CLEO [148] and the LEP experiments as well as experiments for kaon physics. Future results from the LHC experiments and Super-B factories are expected to further increase the number of measurements, further increasing the precision.

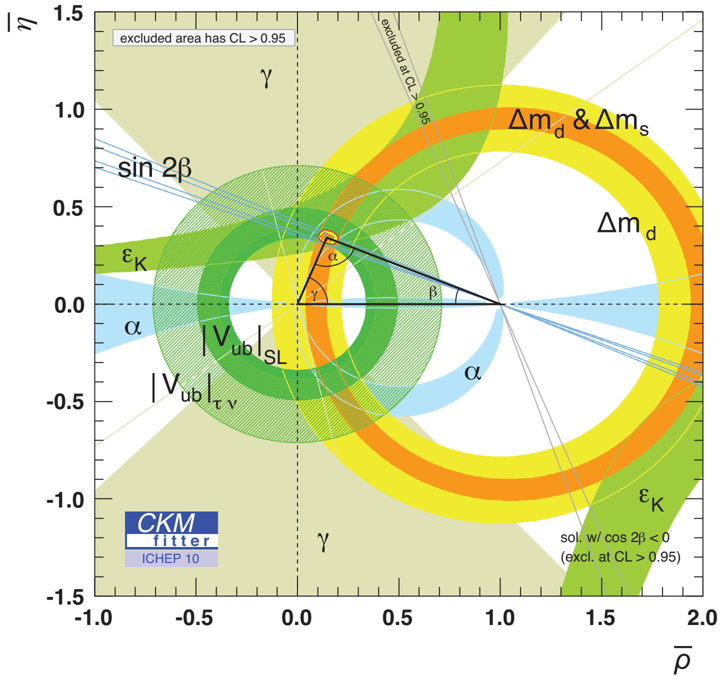

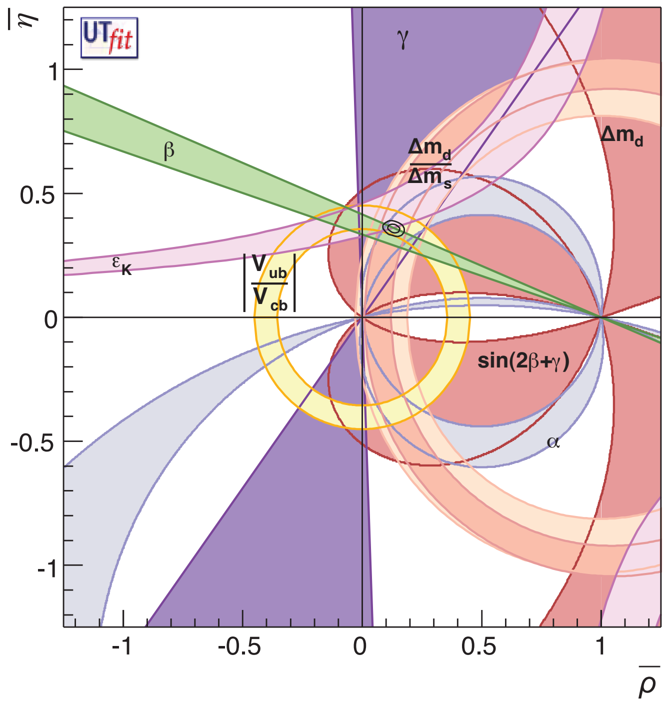

Figure 2.12: Current constraints on the Unitary Triangle in the ($\bar{\rho}$,$\bar{\eta}$) plane, including the most recent inputs in the global CKM fits as of summer 2010. Top figure provided by the CKMFitter collaboration [68], bottom figure provided by the UTFit collaboration [55], both presented at the ICHEP 2010.

Parameter	Value[a]	Experimental Method
$\vert V_{ud}\vert$	0.97425 ± 0.00022	superallowed nuclear β-decays, neutron β-decay and pion β-decay
$\vert V_{us}\vert$	0.2252 ± 0.0009	semileptonic kaon decays, e.g.: $K_L^0 \to \pi e \bar{\nu}_e$, $K_L^0 \to \pi\mu\bar{\nu}_\mu$, $K_L^\pm \to \pi^0 e\bar{\nu}_e$, ...
$\vert V_{ub}\vert$	$(3.89 \pm 0.44) \times 10^{-3}$	inclusive $B \to X_u l \bar{\nu}_l$, exclusive $B \to M l \bar{\nu}_l$ with $M = \pi, \rho, \omega, \eta$
$\vert V_{cd}\vert$	0.230 ± 0.011	di-muon production in DIS of neutrinos and anti-neutrinos, semileptonic charme decays: $D \to K l \bar{\nu}$, $D \to \pi l \bar{\nu}$
$\vert V_{cs}\vert$	1.023 ± 0.036	
$\vert V_{cb}\vert$	$(40.6 \pm 1.3) \times 10^{-3}$	inclusive semileptonic b decays to charm, exclusive $B \to D^{(*)} l \bar{\nu}_l$
Δm_d	0.507 ± 0.005 ps^{-1}	time dependent analysis of $B_d^0 - \bar{B}_d^0$ decay channels
Δm_s	17.77 ± 0.12 ps^{-1}	time dependent analysis of $B_s^0 - \bar{B}_s^0$ decay channels
α	$(89.0^{+4.4}_{-4.2})^\circ$	time dependent $\mathcal{CP}$ asymmetries in $b \to u\bar{u}d$: $B_d^0 \to \pi^+\pi^-$, $B_d^0 \to \rho^+\rho^-$, $B_d^0 \to \rho^\pm\pi^\mp$
β	$\sin 2\beta = 0.673 \pm 0.023$	$b \to c\bar{c}s$ decays ($B_d^0 \to charmonium + K_{S,L}^0$): $B_d^0 \to J/\psi K_S^0$, $B_d^0 \to \psi(2S)K$, ...
γ	$(73^{+22}_{-25})^\circ$	interference of $b \to c\bar{u}s$ and $b \to u\bar{c}s$: $B^- \to D^0 K^-$ / $B^- \to \bar{D}^0 K^-$
ϵ_K	$(2.228 \pm 0.011) \times 10^{-3}$	Indirect $\mathcal{CP}$ violation in $K^0 - \bar{K}^0$ mixing

Table 2.4: Input parameters for the Unitary Triangle fit [55, 68], the world average values and experimental methods used for the measurement of those parameters.

[a] Values taken from Particle Data Group [125]

Parameter	Fit results CKMFitter	Fit results UTFit
λ	0.22543 ± 0.00077	0.22545 ± 0.00065
A	$0.812^{+0.013}_{-0.027}$	0.8095 ± 0.0095
$\bar{\rho}$	0.144 ± 0.025	0.132 ± 0.02
$\bar{\eta}$	$0.342^{+0.016}_{-0.015}$	0.358 ± 0.012

Table 2.5: Results of the two Unitary Triangle fits, left by the CKMFitter group [68], right by the UTFit collaboration [55].

The measured values of the six CKM matrix elements $|V_{ud}|$, $|V_{us}|$, $|V_{ub}|$, $|V_{cd}|$, $|V_{cs}|$ and $|V_{cb}|$ are used in the fits, experimentally measured by the methods briefly described in Table 2.4. The $B^0_{d,s} - \bar{B^0_{d,s}}$ oscillation frequencies $\Delta m_{d,s}$ are proportional to the *top* matrix elements as

$$\Delta m_f \sim |V_{tf} V_{tb}|^2, \quad f = d, s. \tag{2.65}$$

The two parameters Δm_d and Δm_s are the main ingredients constraining the length of triangle side $|V_{td}V^*_{tb}|/|V_{cd}V^*_{cb}|$ in Figure 2.11 (a). In addition to the sides of the triangle the three angles α, β and γ are measured by various B meson decays. The $K^0 - \bar{K^0}$ $\mathcal{CP}$ violation parameter ϵ_K leads to an approximately hyperbolic constrain on the triangles apex.

The result of the current Unitary Triangle fits by the CKMFitter collaboration and the UTFit collaboration (ICHEP 2010) are shown in Figure 2.12. The fit results for the two collaborations are summarised in Table 2.5. They both are in good agreement with each other and with the Standard Model expectations.

2.3.2 B_s oscillations

For the determination of the initial flavour of a decaying B meson, flavour tagging is the method of choice. Therefore a short introduction into the topic of B^0_s mixing is presented.

There are two neutral B^0 mesons, the two flavour eigenstates $B^0_d = |\bar{b}, d\rangle$ and $B^0_s = |\bar{b}, s\rangle$ and their anti-particles. Like the neutral kaon system, the two B mesons appear as a superposition of a particle and an anti-particle, $B^0 - \bar{B}^0$ with $B^0 = (B^0_d, B^0_s)$. In

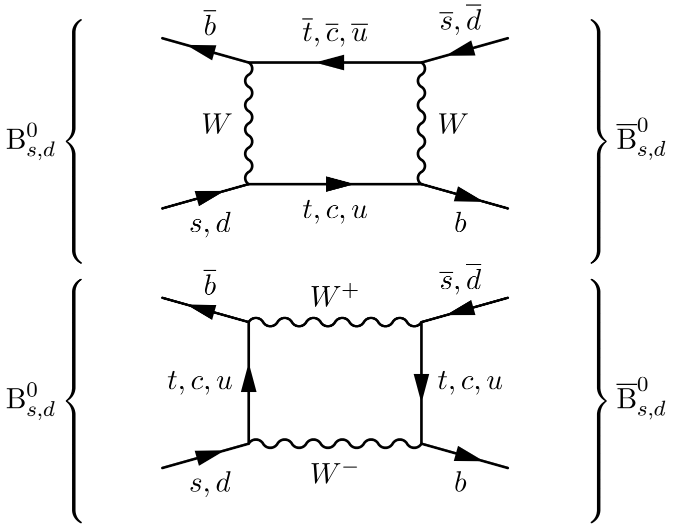

Figure 2.13: Leading order box diagrams for the oscillation of a $B^0_{s,d}$ meson in its anti-particle.

the further discussion the indices d and s are left out for the sake of simplicity, as the calculations for both neutral B mesons are the same. In the Standard Model neutral meson mixing in lowest order is described as box diagrams as shown in Figure 2.13, built by two W bosons and two *up*-type quarks. Because of the large magnitude of the V_{tb} matrix element, the contributions of the two lower mass quarks *up* and *charm* can be neglected as shown in [136]. Due to this phenomenon an initial pure B^0 or $\bar{B}^0$ state has to be treated as a time dependent linear combination of B^0 or $\bar{B}^0$ states.

We assume CPT conservation in the following discussion. To describe the propagation of neutral B mesons with time, the particles have to be written as their mass eigenstates, the light $|B_L\rangle$ and the heavy $|B_H\rangle$, which can be written as linear combinations of the flavour eigenstates in the form

$$|B_H(t)\rangle = p(t)|B^0_q\rangle - q(t)|\bar{B}^0_q\rangle \tag{2.66}$$

$$|B_L(t)\rangle = p(t)|B^0_q\rangle + q(t)|\bar{B}^0_q\rangle. \tag{2.67}$$

If CPT is violated in B meson mixing [109], a third complex parameter z has to be introduced in the form $p \to p\sqrt{1 \mp z}$ and $q \to q\sqrt{1 \pm z}$ in the equations (2.66) and (2.67). In the following discussion we assume that the CPT symmetry holds and therefore we can set $z = 0$, consequently the parameters p and q fulfil the normalisation

$$|p(t)|^2 + |q(t)|^2 = 1. \tag{2.68}$$

The time evolution of a propagating particle is described by an effective 2×2 time-independent Hamiltonian

$$\mathcal{H} = \mathbf{M} - \frac{i}{2}\mathbf{\Gamma}, \tag{2.69}$$

where $\mathbf{M}$ is the mass matrix and $\mathbf{\Gamma}$ is the decay matrix. The effective hamiltonian $\mathcal{H}$ describes the evolution of the time dependent mixing parameters p and q:

$$\mathcal{H}\begin{pmatrix} p(t) \\ q(t) \end{pmatrix} = \begin{pmatrix} M_{11} - \frac{i}{2}\Gamma_{11} & M_{12} - \frac{i}{2}\Gamma_{12} \\ M_{21} - \frac{i}{2}\Gamma_{21} & M_{22} - \frac{i}{2}\Gamma_{22} \end{pmatrix}\begin{pmatrix} p(t) \\ q(t) \end{pmatrix}. \tag{2.70}$$

Due to Hermeticity the off-diagonal matrix elements simplify to $M_{12} = M_{21}^*$ and $\Gamma_{12} = \Gamma_{21}^*$, and due to *CPT* conservation the diagonal elements are $M_{11} = M_{22} = M_0$ and $\Gamma_{11} = \Gamma_{22} = \Gamma_0$, leading to

$$\mathcal{H} = \begin{pmatrix} M_0 - \frac{i}{2}\Gamma_0 & M_{12} - \frac{i}{2}\Gamma_{12} \\ M_{12}^* - \frac{i}{2}\Gamma_{12}^* & M_0 - \frac{i}{2}\Gamma_0 \end{pmatrix}. \tag{2.71}$$

In total, the eigenvalues calculated out of (2.70) are given by

$$\lambda_{L,H} = \left(M_0 - \frac{i}{2}\Gamma_0\right) \pm \frac{q}{p}\left(M_{12} - \frac{i}{2}\Gamma_{12}\right) \tag{2.72}$$

and p and q can be written as

$$\left(\frac{q}{p}\right)^2 = \frac{M_{12}^* - \frac{i}{2}\Gamma_{12}^*}{M_{12} - \frac{i}{2}\Gamma_{12}}. \tag{2.73}$$

It is useful to introduce the mass difference of the two eigenstates $|B_H\rangle$ and $|B_L\rangle$ as the difference of the real parts of the eigenvalues in (2.72):

$$\Delta m = \mathcal{R}e(\lambda_H - \lambda_L) = M_H - M_L = 2|M_{12}|. \tag{2.74}$$

The mass difference is positive by definition. The average mass of the mixed quark system $B^0 - \bar{B}^0$ is

$$m = \frac{m_H + m_L}{2} = M_0. \tag{2.75}$$

Furthermore, it is convenient to define similar expressions for the decay widths of the two mass eigenstates. Taking into account the imaginary part of the eigenvalues, the difference of the decay width of the two mass eigenstates is defined as

$$\Delta\Gamma = -2\mathcal{I}(\lambda_H - \lambda_L) = \Gamma_H - \Gamma_L = \frac{4\mathcal{R}e(M_{12}\Gamma^*_{12})}{\Delta m} \tag{2.76}$$

and the average decay width is

$$\Gamma = -2\mathcal{I}m(\lambda_H - \lambda_L) = \frac{\Gamma_H + \Gamma_L}{2} = \Gamma_0. \tag{2.77}$$

While Δm is positive by definition, the sign of the difference in the decay width has to be measured experimentally. In the case of K mesons $\Delta\Gamma$ is negative and for D mesons $\Delta\Gamma$ is positive. Standard Model calculations predict a negative value for B mesons.

With all those ingredients the time evolution of an initial pure flavour eigenstate $|B^0\rangle$ can be written in the following way:

$$|B^0(t)\rangle = g_+(t)|B^0\rangle + \frac{p}{q}g_-(t)|\bar{B}^0\rangle \tag{2.78}$$
$$|\bar{B}^0(t)\rangle = g_+(t)|\bar{B}^0\rangle + \frac{p}{q}g_-(t)|B^0\rangle, \tag{2.79}$$

where $g_+(t)$ and $g_-(t)$ are the time dependent probability amplitudes of an initial flavour eigenstate $|B^0\rangle$ or $|\bar{B}^0\rangle$ to be observed after time t with the same flavour (g_+) or with the opposite flavour (g_-):

$$g_\pm(t) = \frac{1}{2}\left[e^{-i(M_0 - \frac{1}{2}\Gamma_0)t} \pm e^{-i(M_{12} - \frac{1}{2}\Gamma_{12})t}\right]. \tag{2.80}$$

From Equation 2.78 and 2.79 the probability for the measurement of one of the states $|B^0_q(t)\rangle$ or $|\bar{B}^0(t)\rangle$ at a time t from an initial pure flavour eigenstate $|B^0(t)\rangle$ is

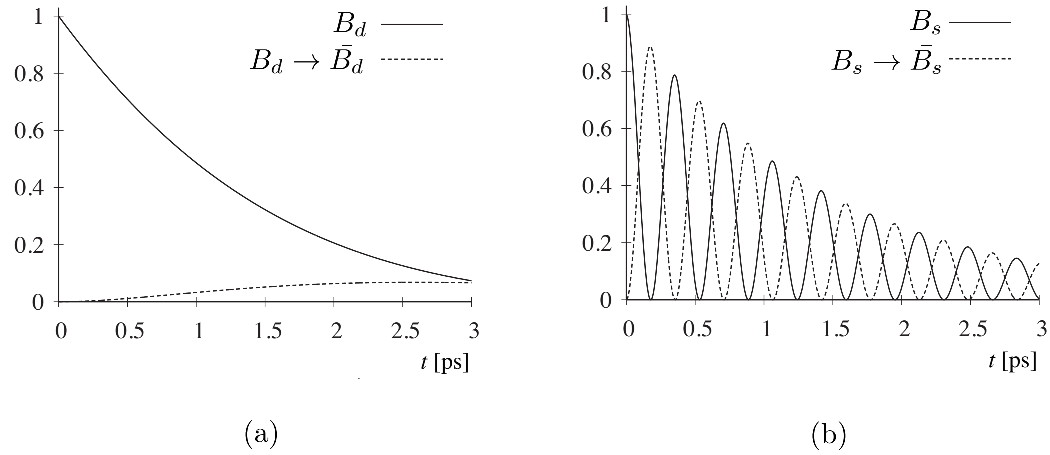

Figure 2.14: The time dependent probability for an initial flavour eigenstate B_q^0 meson to be observed as B_q^0 or its anti-particle, $\bar{B}_q^0$. In (a) this probability is shown for the B_d^0 meson, in (b) for B_s^0 with the current measured values for Γ_q and Δm_q as presented by the Particle Data Group PDG [136].

$$\mathcal{P}(t)(B^0 \to B^0) = |\langle B^0|B^0(t)\rangle|^2 = |g_+(t)|^2 \tag{2.81}$$

$$\mathcal{P}(t)(B^0 \to \bar{B}^0) = |\langle \bar{B}^0|B^0(t)\rangle|^2 = \left|\frac{p}{q}\right| |g_-(t)|^2, \tag{2.82}$$

where the time dependent probability distribution is

$$|g_\pm(t)|^2 = \frac{e^{-\Gamma t}}{2}\left[\cosh\left(\frac{\Delta\Gamma t}{2}\right) \pm \cos\left(\Delta m t\right)\right]. \tag{2.83}$$

The last term in (2.83) describes the time dependent oscillation between the two flavour eigenstates $|B_q^0\rangle$ and $|\bar{B}_q^0\rangle$ with the oscillation frequency Δm_q of the two neutral mesons B_q^0 $(q = d, s)$. In Figure 2.14 the time dependent probability corresponding to (2.83) of an initial B_q^0 meson to be observed as B_q^0 or as $\bar{B}_0^0$ is shown with the current world average values of experimentally measured $\Delta m_{d,s}$ and $\Gamma_{d,s}$, listed in Table 2.6. Some measurements in which flavour tagging methods are crucial for are described in the following paragraphs.

The mass difference Δm_q can be studied in two experimental ways. An indirect method is the measurement of the time integrated mixing probability, which is defined as

Parameter	B_d^0	B_s^0
$m_q[\text{ MeV}]$	5279.50 ± 0.30	5366.3 ± 0.6
$\Delta m_q[\text{ ps}^{-1}]$	0.507 ± 0.005	17.77 ± 0.12
$\tau_q[\text{ ps}]$	1.525 ± 0.009	$1.472^{+0.024}_{-0.026}$
$\Delta\Gamma_q[\text{ ps}^{-1}]$	SM: $\mathcal{O}(10^{-3})$	$0.062^{+0.034}_{+0.037}$
x_q	0.774 ± 0.008	26.2 ± 0.5
χ_q	0.1872 ± 0.0024	0.49927 ± 0.00003

Table 2.6: World average results of various parameters of the two neutral B mesons systems, B_d^0 and B_s^0, taken from the Particle Data Group PDG [136]. No direct evidence for a non negligible $\Delta\Gamma_d$ has been found, yet.

$$\chi(B_q^0 \to \bar{B}_q^0) = \frac{\int |\langle \bar{B}_q^0 | B_q^0(t)\rangle|^2 dt}{\int |\langle B_q^0 | B_q^0(t)\rangle|^2 dt + \int |\langle \bar{B}_q^0 | B_q^0(t)\rangle|^2 dt} \tag{2.84}$$

$$= \frac{x_q^2 + y_q^2}{2(x_q^2 + 1)}, \tag{2.85}$$

where the two dimensionless parameters x_q and y_q are defined as

$$x_q = \frac{\Delta m_q}{\Gamma_q} \tag{2.86}$$

$$y_q = \frac{\Delta\Gamma_q}{2\Gamma_q}. \tag{2.87}$$

The parameter x_q is the ratio of oscillation and decay rate, therefore describing the likelihood of oscillations before the decay. In Figure 2.15 the integrated mixing probability is shown as a function of the mixing parameter x_s under the assumption $x_q \gg y_q$, which is valid for neutral B mesons, but not for kaons. For the B_d^0 meson, with $x_d = 0.774 \pm 0.008$, the integrated probability of $\chi_d = 0.1872 \pm 0.0024$ allows a good measurement of Δm_d. The first results measuring B_d^0 mixing, using a time integrated method, were independently reported by the ARGUS collaboration [19] and the UA1 collaboration [145] in 1986. As the integrated probability converges already at small values to the theoretical maximum of $\chi = 0.5$, the large oscillation frequency in the B_s^0 system, resulting in $x_s = 26.2 \pm 0.5$ does not allow a proper measurement of Δm_s with this method.

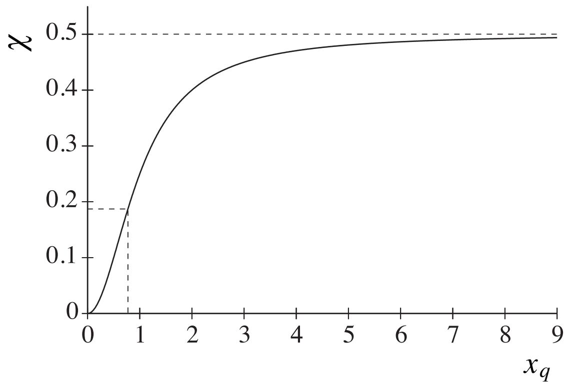

Figure 2.15: The time integrated mixing probability as defined in (2.85) as a function of $x_q = \Delta m_q/\Gamma_q$. The dotted line at $x_d = 0.771$ displays the measured $\chi_d = 0.1872 \pm 0.0024$ for B_d^0 mesons. For the B_s^0 meson with $x_s = 26.2 \pm 0.5$ the integrated probability already is close to the maximum $\chi_s = 0.49927 \pm 0.00003$. Values taken from PDG [125].

A direct measurement of the oscillation frequency Δm_q is a time dependent analysis of the probability distribution by measuring the proper lifetime of B_q mesons and their mixing state. In order to measure this distribution, both, the initial and the final state of the B_q^0 meson, have to be measured. The final state can be measured by analysing the flavour specific decay products of the B_q^0 meson, the initial state has to be determined by methods of flavour tagging.

The combined results of the measurements of Δm_d are shown in Figure 2.16, compiled by the Heavy Flavour Averaging Group HFAG for the Particle Data Group PDG.

The first and so far only measurement of Δm_s, considered by the HFAG, has been peformed by the CDF collaboration in 2006 [65], resulting in

$$\Delta m_s = 17.77 \pm 0.10(\text{stat}) \pm 0.07(\text{syst})\ \text{ps}^{-1}. \tag{2.88}$$

Within the Standard Model, the lifetime difference $\Delta\Gamma = \Gamma_H - \Gamma_L$ is expected to be of the order $\mathcal{O}(10^{-2}) \cdot x_q$. For the B_d^0 meson this value is of the order $\mathcal{O}(10^{-3})$, negligible small. However, for the B_s^0 meson a global fit including data from ALEPH, DELPHI, DØ and CDF by the HFAG in absence of $\mathcal{CP}$ violation results in

$$\Delta\Gamma_s = 0.062^{+0.034}_{+0.037}. \tag{2.89}$$

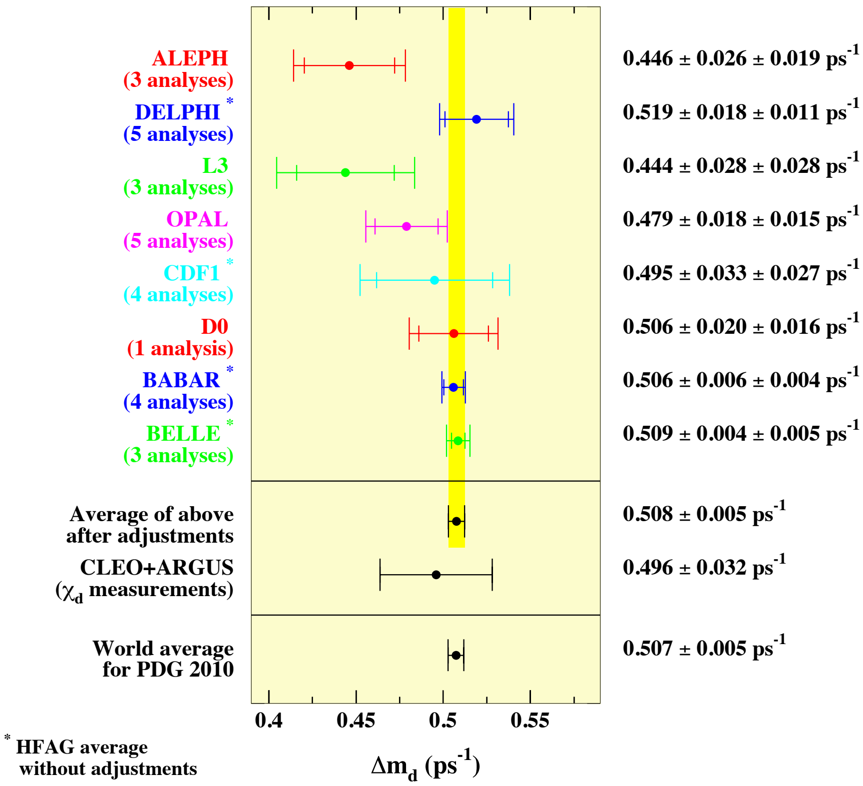

Figure 2.16: Averaged measurements of Δm_d of LEP and Tevatron experiments, the B factories BaBar and Belle and the χ_d measurements of CLEO and ARGUS converted into a Δm_d measurement, giving $\Delta m_d = 0.507 \pm 0.005$ [44].

2.3.3 CP Violation in the neutral B system

$\mathcal{CP}$ violation has been introduced as a complex phase in the CKM matrix in Chapter 2.3.1. Up to now, $\mathcal{CP}$ violation has been found in weak interactions of neutral K mesons and B mesons. In the kaon system indirect $\mathcal{CP}$ violation has been discovered in 1964 [70]. In 1999 direct $\mathcal{CP}$ violation has been discovered by the NA48 collaboration at CERN [124] and the KTeV experiment at Tevatron [113]. In 2001 the B factories BaBar and Belle observed $\mathcal{CP}$ violation in the B sector [38, 48]. In addition to mixing and $\mathcal{CP}$ violation in the K and B systems, evidence for $D^0 - \bar{D}^0$ mixing has been found [41, 51], whereas $\mathcal{CP}$ violation has not been observed, yet. The main problem in the measurement of charm mixing is long oscillation time compared to the short lifetime of the D mesons.

While there are measurements of asymmetries with untagged mesons revealing $\mathcal{CP}$ violation, in most measurements both, the initial and final state of the mesons, need to be known. Therefore the upcoming sections gives a short outline on $\mathcal{CP}$ violation [11, 79, 109] in the neutral B system: $\mathcal{CP}$ violation in the decay of B mesons, also known as direct $\mathcal{CP}$ violation, $\mathcal{CP}$ violation in mixing and $\mathcal{CP}$ violation in the interference of mixing and decay, the latter two known as indirect $\mathcal{CP}$ violation.

2.3.3.1 CP Violation in the decay

Direct $\mathcal{CP}$ violation can be observed in neutral mesons as well as in charged mesons. However, with regard to flavour tagging, only neutral mesons are of interest. For the direct $\mathcal{CP}$ violation in the decay of a B meson, the time dependent decay amplitudes of the process $B^0 \to f$ are:

$$\begin{aligned} A_f &= \langle f|\mathcal{H}|B^0\rangle, \quad \bar{A}_f = \langle f|\mathcal{H}|\bar{B}^0\rangle, \\ A_{\bar{f}} &= \langle \bar{f}|\mathcal{H}|B^0\rangle, \quad \bar{A}_{\bar{f}} = \langle \bar{f}|\mathcal{H}|\bar{B}^0\rangle, \end{aligned} \tag{2.90}$$

where f is a multiple particle final state and $\bar{f}$ its $\mathcal{CP}$ conjugate. The effect of the $\mathcal{CP}$ operator on the initial and final states can be written as:

$$\begin{aligned} \mathcal{CP}|f\rangle &= e^{i\xi_f}|\bar{f}\rangle, \quad \mathcal{CP}|B^0\rangle = e^{i\xi_B}|\bar{B}^0\rangle, \\ \mathcal{CP}|\bar{f}\rangle &= e^{-i\xi_f}|f\rangle, \quad \mathcal{CP}|\bar{B}^0\rangle = e^{-i\xi_B}|B^0\rangle, \end{aligned} \tag{2.91}$$

where ξ_B and ξ_f are arbitrary phases. Assuming $\mathcal{CP}$ invariance, the decay amplitudes are of the same magnitude and have an arbitrary phase:

$$|\bar{A}_{\bar{f}}| = e^{i(\xi_f - \xi_B)} A_f. \tag{2.92}$$

Deviations from the above relation are called direct $\mathcal{CP}$ violation, resulting in

$$\left|\frac{\bar{A}_{\bar{f}}}{A_f}\right| \neq 1. \tag{2.93}$$

Direct $\mathcal{CP}$ violation has been observed the first time in 1999 by the NA48 collaboration [124] and the KTeV experiment [113] in the decay of kaons into two pions. In the B system $\mathcal{CP}$ violation has been measured in the decay channel $B_d^0 \to K^+\pi^-$, using the following asymmetry:

$$\mathcal{A}_{\mathcal{CP}}^{dir} = \frac{\Gamma(\bar{B}_d^0 \to K^+\pi^-) - \Gamma(\bar{\bar{B}}_d^0 \to K^-\pi^+)}{\Gamma(\bar{B}_d^0 \to K^+\pi^-) + \Gamma(\bar{\bar{B}}_d^0 \to K^-\pi^+)}. \tag{2.94}$$

This asymmetry was first measured by BaBar [40] and Belle [50] in 2004. The current world average measured value is $\mathcal{A}_{\mathcal{CP}}^{dir}(B_d^0 \to K^+\pi^-) = -0.098 \pm 0.013$ [125].

2.3.3.2 CP Violation in B mixing

As shown in the previous chapter, the mass eigenstates of neutral B mesons are superpositions of the two flavour eigenstates B^0 and $\bar{B}^0$, shown in (2.66) and (2.67), introducing the two parameters p and q. The $\mathcal{CP}$ transformation on the flavour eigenstates introduces an aribtrary phase ξ:

$$\mathcal{CP}|B^0\rangle = e^{i\xi}|\bar{B}^0\rangle, \qquad \mathcal{CP}|\bar{B}^0\rangle = e^{-i\xi}|B^0\rangle. \tag{2.95}$$

It can be shown, that the off-diagonal matrix elements in (2.70) fulfil the relation

$$M_{21} = M_{12}e^{2i\xi}, \qquad \Gamma_{21} = \Gamma_{12}e^{2i\xi}, \tag{2.96}$$

and due to hermeticity of both $\mathbf{M}$ and $\mathbf{\Gamma}$ in (2.69)

$$M_{12}^* = M_{12}e^{2i\xi}, \qquad \Gamma_{12}^* = \Gamma_{12}e^{2i\xi}. \tag{2.97}$$

Inserting these relations into Equation (2.73) gives a condition for $\mathcal{CP}$ invariance in the B meson mixing:

$$\left|\frac{q}{p}\right| = 1 \quad \Leftrightarrow \quad \mathcal{H} = \mathcal{H}^{\mathcal{CP}}. \tag{2.98}$$

$\mathcal{CP}$ violation in mixing is well known and has been observed in semi-leptonic decays of the K^0 mesons. This indirect $\mathcal{CP}$ violation has not been measured yet in the B sector, which could become possible by the measurement of the asymmetry

$$\mathcal{A}_{\mathcal{CP}}^{indir} = \frac{\Gamma(\bar{B}^0 \to l^-\bar{\nu}X) - \Gamma(B^0 \to l^+\nu X)}{\Gamma(\bar{B}^0 \to l^-\bar{\nu}X) + \Gamma(B^0 \to l^+\nu X)} = \frac{1-|q/p|^4}{1+|q/p|^4}. \tag{2.99}$$

As $1-|q/p|^2$ is expected to be small in the B_d^0 system ($\simeq \mathcal{O}(10^{-3})$) and even smaller in the B_s^0 system ($\lesssim \mathcal{O}(10^{-4})$), indirect $\mathcal{CP}$ violation in the B system is expected to be very small. Recent results from the two B factories BaBar and Belle on B_d^0 mesons have been combined and yield $|q/p|_d = 1.0002 \pm 0.0020$. There are no results on the B_s^0 mesons yet.

2.3.3.3 Mixing induced CP Violation

If neither of the two above types of $\mathcal{CP}$ violations occurs in a decay, $\mathcal{CP}$ violation could arise from the interference between mixing and the decay. Assume a decay without mixing of the type $B^0 \to f$ and a decay with mixing of the type $B^0 \to \bar{B}^0 \to f$. Notice the requirement of decays into a common final state from both, B^0 and $\bar{B}^0$. In such a scenario, while both, mixing and the decay, separately are $\mathcal{CP}$ invariant, the interference term generates an additional complex parameter describing $\mathcal{CP}$ violation:

$$\lambda_f = \frac{q}{p}\frac{\bar{A}_f}{A_f}. \tag{2.100}$$

If $\mathcal{CP}$ is conserved, two conditions for λ_f on the absolute value and the complex phase are

$$\lambda_f = \frac{1}{\lambda_{\bar{f}}} \tag{2.101}$$

$$\arg(\lambda_f) + \arg(\lambda_{\bar{f}}) = 0 \tag{2.102}$$

Since the condition in equation (2.102) is arising from the interference of the phases from mixing and decay amplitudes, a violation of this condition is called mixing induced $\mathcal{CP}$ violation. In Figure 2.17 two examples of such interferences are shown for the B_s^0 system.

For the measurement of mixing induced $\mathcal{CP}$ violation the time dependent asymmetry $\mathcal{A}_{\mathcal{CP}}(t)$ can be written as

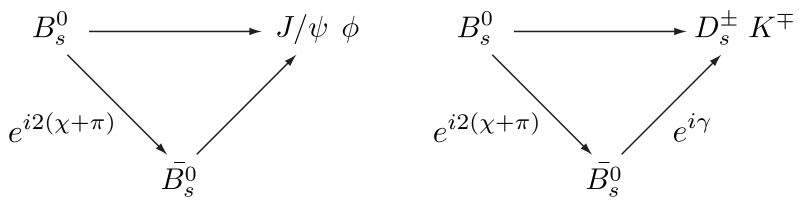

Figure 2.17: Illustration of interfering decay paths in the decays $B_s^0 \to J/\psi\phi$ and $B_s^0 \to D^\pm K^\mp$ and the resulting phase differences.

$$\begin{aligned}\mathcal{A}_{\mathcal{CP}}(t) &= \frac{\Gamma_f(B^0(t) \to f) - \Gamma_{\bar{f}}(B^0(t) \to f)}{\Gamma_f(t) + \Gamma_{\bar{f}}(t)} \\ &= \frac{(1-|\lambda|^2)\cos(\Delta m t) + 2\mathcal{I}m(\lambda_f)\sin(\Delta m t)}{(1+|\lambda|^2)\cosh(\frac{\Delta\Gamma t}{2}) + 2\mathcal{R}e(\lambda_f)\sinh(\frac{\Delta\Gamma t}{2})}.\end{aligned} \tag{2.103}$$

As shown in the left illustration in Figure 2.17, this asymmetry can be used to measure the weak mixing phase ϕ_s. In addition, by measuring the decay channel $B_s^0 \to D^\pm K^\mp$, angle γ of the unitary triangle could be measured.

The decay channel $B_s^0 \to J/\psi\phi$ with $J/\psi \to \mu^+\mu^-$ and $\phi \to K^+K^-$, the so-called gold-plated decay channel, is of special interest at ATLAS. This channel has a clean experimental signature and a straightforward di-muon trigger allows easy triggering. A detailed angular analysis of the decay products allows the extraction of various independent parameters:

- the mass and decay lifetime of B_s^0
- the mixing paramter $\Delta\Gamma_B$
- the weak mixing phase $\phi_s = -2\chi = -2\eta\lambda$

As B_s^0 is a pseudo-scalar and J/ψ and ϕ both are vector mesons, with a statistical approach the three decay amplitudes in this decay (two $\mathcal{CP}$ even and one $\mathcal{CP}$ odd) can be disentangled by analysing the decay angles defined in Figure 2.18. Fits of the Unitary Triangle, in which the Standard Model of Particle Physics is assumed, predict a very small B_s^0 mixing phase of $\phi_s \sim 0.04$ radians [116]. However, physics beyond the Standard Model could introduce additional contributions from new processes in the box diagram deviating the expected value. Therefore, the decay channel $B_s^0 \to J/\psi\phi$ is regarded as a good candidate for measuring effects of physics beyond the Standard Model.

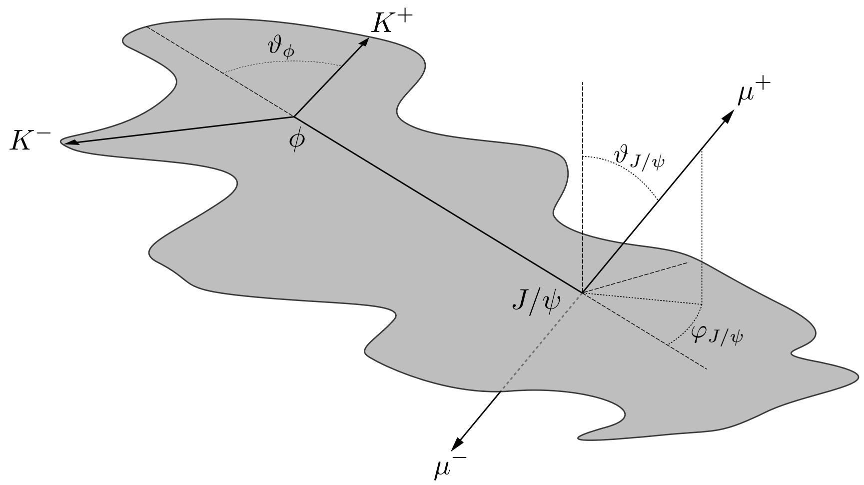

Figure 2.18: Angles of the decay $B_s^0 \to J/\psi(\mu^+\mu^-)\phi(K^+K^-)$ in the B_s^0 rest frame.

CHAPTER

THREE

The ATLAS Detector and the Large Hadron Collider

The ATLAS detector (A Large Toroidal LHC Apparatus) is one out of four detectors at the Large Hadron Collider (LHC). The LHC at CERN is a proton proton collider extending the frontiers of high energy physics to a new level in multiple aspects.

Chapter 3.1 will give an overview on the LHC, the LHC detectors and the proton beams. After a short introduction in the coordinate system and the nomenclature in Chapter 3.2, the ATLAS detector will be discussed in detail in the Chapters 3.3 to 3.8, with a special focus on the detector components crucial for this thesis. The detector components will be described, starting from the Inner Detector following the particles track to the very outer Muon Chambers. Finally, the trigger system and the data storage will be explained in the Chapters 3.9 and 3.10.

3.1 The Large Hadron Collider

The LHC [52, 59, 60, 85, 130] works as an accelerator and storage ring for proton-proton collisions rather than proton-anti-proton collisions. Therefore the LHC consists of two rings with counter-rotating beams. The LHC is constructed in the 26.7 km circular tunnel of the Large Electron-Positron Collider (LEP) [117] at the European Organisation for Nuclear Research (CERN) in Geneva, Switzerland. The tunnel is built in a depth between 50 m and 175 m, the ATLAS detector is built in a cavern 75 m underground.

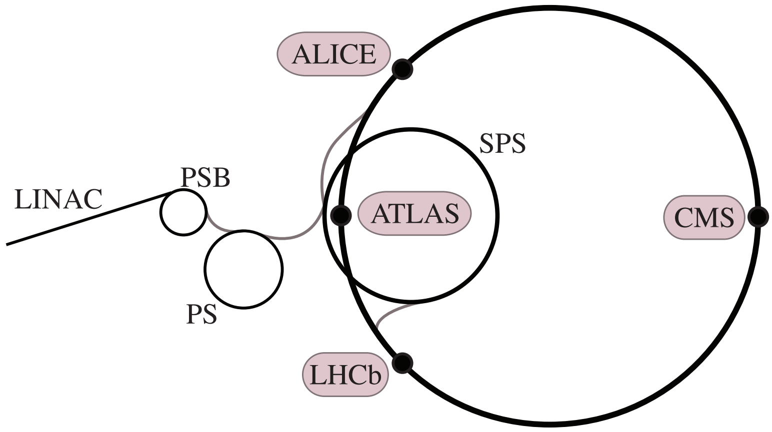

Figure 3.1: Schematic Overview of the Large Hadron Collider. Protons accelerate sequently, starting at the LINAC, going through the PSB, PS and SPS entering the LHC at an energy of 450 MeV. More details can be found in [52].

In the LHC bunches of protons are injected from the Super Proton Synchrotron (SPS) with an energy of 450 MeV and then accelerated using a system of eight superconducting cavities per beams. A schematic overview of the proton acceleration chain is shown in Figure 3.1. The proton energy is determined by the given curvature of the LHC tunnel and the maximum field of the dipole magnets responsible for bending the beam. Cooled to a temperature of 1.9 K (superfluid helium) the magnets deliver a nominal field of 8.33 T, providing a beam energy of 7 TeV or proton-proton collisions at a centre of mass energy of $\sqrt{s} = 14$ TeV. Compared to the centre of mass energy of 1.96 TeV for proton-anti-proton collisions at Tevatron, the sensitivity for new physics increases significantly.

Bending, steering and focusing of the proton beam is controlled with over 9000 magnets. The 1232 dipole magnets responsible for the bending are supported by multipole corrector magnets (sextupoles, octupoles and decapoles) to stabilise the beam. The 392 main quadrupole magnets and the associated corrector magnets (dipoles, sextupoles and octupoles) are responsible for the beam focus. The final focusing of the beams around the four interaction points is caused by dedicated high aperture triplet quadrupoles.

Along with the beam energy the second parameter crucial for the LHC is the luminosity, which in principle defines the number of collisions per time interval for a given cross section. A high luminosity can be reached by colliding beams with a high number of protons per beam on a small area with a high frequency. Luminosity can be expressed by the following term:

$$\mathcal{L} = \frac{N_b^2 n_b f_{rev}}{4\pi\sigma_x^*\sigma_y^*} F, \tag{3.1}$$

where N_b is the number of protons per bunch, n_b is the number of bunches per beam, f_{rev} is the revolution frequency and $\sigma_{x,y}^*$ the RMS of the transverse beam size at the interaction point in x- and y-direction. Often the beam size is written as a product of the two beam parameters, the transverse beam emittance that corresponds to the phase space covered by the beam ε and the betatron function β^*. Due to the crossing angle at the interaction point Θ_c the luminosity is decreased by the geometric luminosity reduction factor F:

$$F = \left(1 + \left(\frac{\Theta_c \sigma_z}{2\sigma^*}\right)^2\right)^{-\frac{1}{2}}, \tag{3.2}$$

where σ_z is the RMS of the bunch length in beam direction and σ^* the RMS of the transverse beam size. At design luminosity F gives a reduction of $\sim 16\%$. LHC will be running at peak design luminosity of $\mathcal{L} = 10^{34}$ cm^{-2}s^{-1}, with $n_b = 2808$ bunches per beam, each bunch consisting of approximately 1.15×10^{11} protons and a bunch crossing interval of 25 ns. The main beam parameters are listed in Table 3.1.

The overview of the LHC and its experiments is shown in Figure 3.2. Four main detectors have been installed at the four interaction points: the two general purpose detectors ATLAS and CMS (Compact Muon Solenoid) [71], located at the two opposite points of the LHC, Point 1 and 5 respectively, LHCb (Large Hadron Collider beauty) [118] at Point 8 and ALICE (A Large Ion Collider Experiment) [16] at Point 2. Around the interaction

Parameter	Value
Beam Energy	7 TeV / $\gamma_{rel} = 7461$
Injection Energy	450 MeV / $\gamma_{rel} = 480$
Luminosity	10^{34} cm^{-2}s^{-1}
Number of bunches	2808 out of 3564 spaces
Protons per bunch	1.15×10^{11}
Relativistic gamma factor γ	7461
Bunch spacing	24.95 ns
Beam current	0.584 A
RMS Bunch length	7.55 cm
RMS beam size σ^* in pipe	~ 0.2 mm
RMS beam size σ^* at Point 1	16.7 μm
Crossing angle Θ_c at Point 1	285 μrad

Table 3.1: Beam parameters of the Large Hadron Collider for proton-proton collisions [60].

points of ATLAS and CMS the two smaller detectors LHCf (Large Hadron Collider forward) [119] and TOTEM (Total Elastic and diffractive cross section measurement) [144] have been installed.

The two high luminosity experiments ATLAS and CMS are general purpose detector. While the main motivation of the two experiments is to unravel the electroweak symmetry breaking and to discover the Higgs boson, the two collaborations cover a broad range of searches within the standard model and beyond. Examples are the discovery of supersymmetric particles and remnants of dark matter, CP violation, heavy flavour physics and the precision measurement of standard model parameters.

From the detector principle ATLAS and CMS both are detectors covering most of the 4π solid angle around the interaction point. The main emphasis in both experiments are collisions with a high transverse momentum transfer. They are constructed to detect and identify particles produced in 14 TeV proton-proton collisions. ATLAS and CMS are able to detect, identify and absorb electrons and pions up to an energy of 1 TeV and measure the momenta of 1 TeV muons.

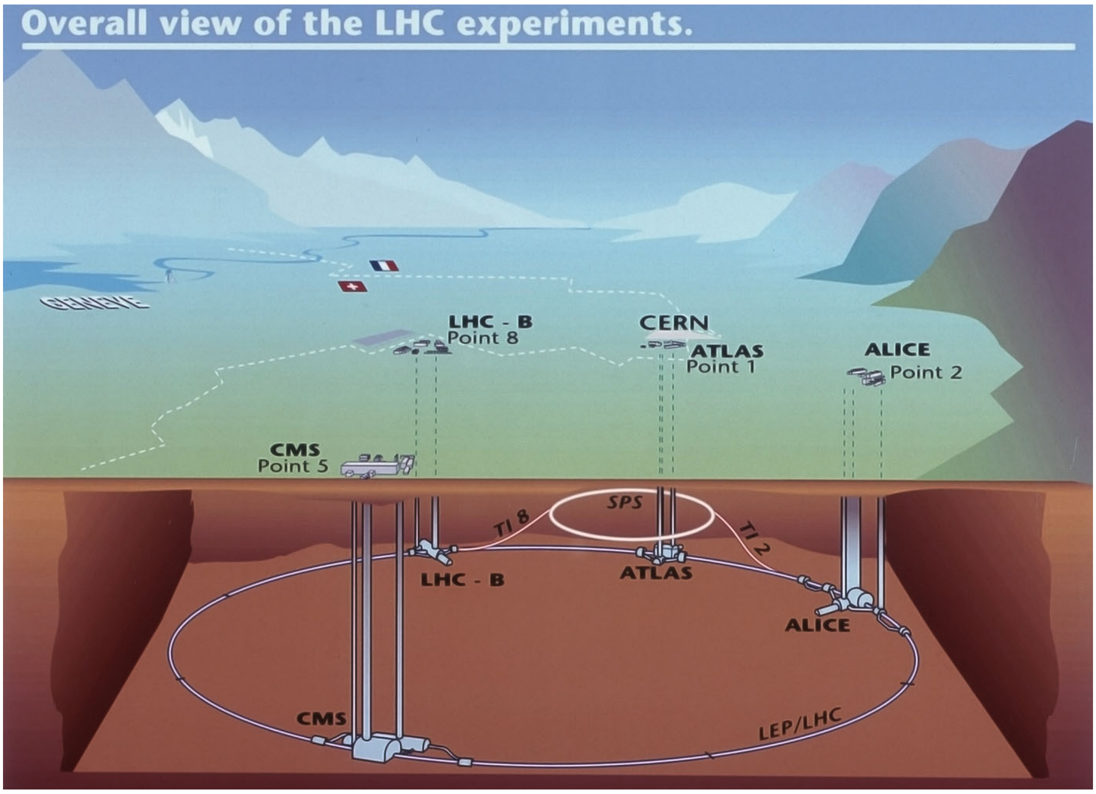

Figure 3.2: Overview of the Large hadron collider and the four main experiments. The depths of the tunnels varies in the range of 50 m − 175 m, the diameter of the ring is approximately 8.6 km.

One major difference between the two experiments is the choice of the magnet system and, in conjunction with this choice, the muon system. The CMS collaboration decided to use a single large-scale 4 T solenoid, which provides an excellent momentum resolution in the Inner Detector, enclosed in a 12000 t return yoke with embedded muon chambers. The drawback of this layout is the reduced space for the calorimeter inside the coil and limited performance for stand-alone muon reconstruction and triggering. ATLAS uses a small 2 T solenoid for the tracking system and a huge toroidal magnetic system for the muon spectrometer, which allows a stand-alone muon reconstruction over a large polar angle with a high momentum resolution. On the downside the toroid system is large scale an very expensive. The difference in the layout has a large impact on the size and mass of the two experiments: with a length of 46 m and a diameter of 22 m at a mass of 7000 t ATLAS is considerable larger but lighter than the CMS with a length of 22 m, a diameter of 15 m and a mass of 12500 t.

A second major difference is the choice of calorimeter. CMS uses a homogeneous $PbWO_4$ scintillating crystal calorimeter, giving a special emphasis on an excellent energy resolution and lateral segmentation. The ATLAS experiment uses a LAr-Pb sampling calorimeter with a lower energy resolution, a comparable excellent lateral segmentation and an additional longitudinal segmentation, providing the needed e/γ separation. The energy resolutions of the electromagnetic and hadronic calorimeters of the two detectors are shown in Figure 3.3.

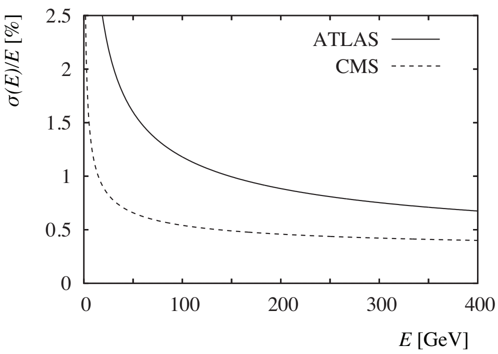

(a)

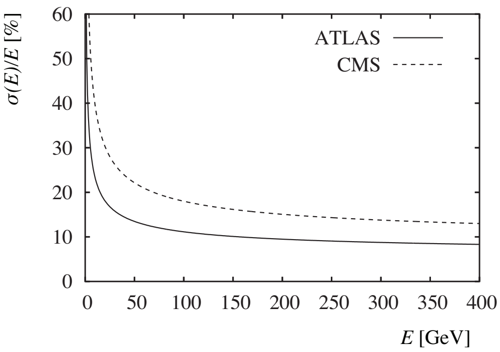

(b)

Figure 3.3: Energy measurement resolution in the calorimeter σ_E/E for the two detectors ATLAS and CMS. Figure (a) shows the resolution of the electromagnetic calorimeter, Figure (b) for the hadronic calorimeter.

The ALICE detector is a general purpose heavy ion detector, devoted to the sector of strong interactions, the QCD, especially the investigation of strong interacting matter and quark gluon plasma under very high energy density and temperature. The heavy ion runs at LHC mainly are dedicated to the collision of lead ions $^{208}_{82}\mathrm{Pb}^{82+}$, but collisions of lighter ions and proton nucleus collisions are planned, too. With the dipole field of 8.33 T the lead ions will collide at an energy of 2.76 TeV per nucleon or a centre of mass energy of 1150 TeV with a nominal luminosity of 10^{27} cm^{-2}s^{-1}. While heavy ion collisions mainly concentrate on the ALICE experiment, ATLAS and CMS both will study heavy ion collisions at the same luminosity.

A completely different kind of experiment is the LHCb detector, which aims at heavy flavour physics. The scientific program places special emphasis physics with hadrons containing b quarks like CP violation, rare B hadron decays and physics beyond the Standard Model. In contrary to the other main experiments LHCb is not covering the 4π solid angle around the interaction point, but it is built as a single arm detector in forward direction.

The TOTEM experiment aims for the measurement of the total proton-proton cross-section with a luminosity independent method. The experiment is partly integrated into the CMS detector and complemented by additional detectors placed about 147 m and 220 m from the interaction point. This layout gives a pseudo-rapidity range of $|3.1| \leq \eta \leq |6.5|$ allowing a detailed measurement of elastic and diffractive scattering into the very forward direction close to the beam pipe, to study the proton structure. In Figure 3.4 the typical range in pseudo-rapidity and in polar angle is shown for the ATLAS detector (a) and for the TOTEM experiment.

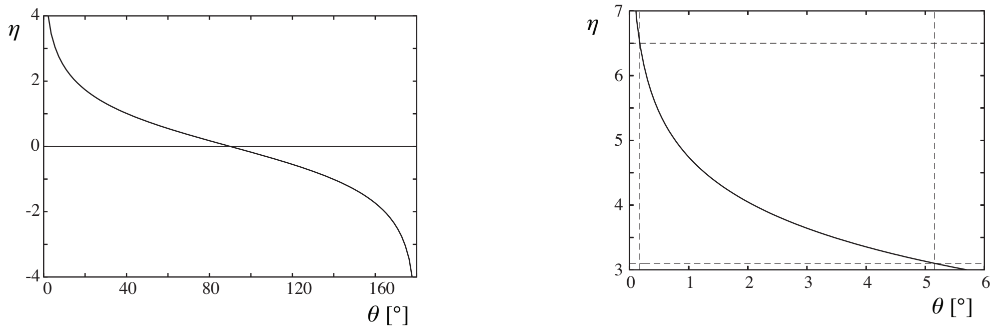

(a) (b)

Figure 3.4: Pseudo-rapidity η shown as a function of the polar angle Θ. In Figure (a) the pseudo-rapidity is shown for the typical range in the ATLAS detector, Figure (b) shows the close angles in the TOTEM experiment, illustrated with the dashed line.

The LHC*f* experiment, built ±140 m around Point 1 (ATLAS detector), covers a pseudo-rapidity of $|\eta| \geq 8.4$. Neutral particles scattered into the very forward direction will be detected for a data taking time of a few month, until the luminosity exceeds 10^{30} cm^{-2}s^{-1}. These measurements will allow the calibration of hadron interaction models of cosmic rays at extremely high energy up to a laboratory equivalent of 10^{17} eV.

3.2 Coordinate System and Nomenclature

Since the coordinate system and various observables are repeatedly used in this work, this chapter describes the most common used. The ATLAS experiment uses a right handed coordinate system, with the z-axis pointing along the LHC beam pipe, and the plane perpendicular to the beam pipe defines the x-y-plane. The positive x-axis is pointing from the interaction point towards the centre of the LHC, the positive y-axis is going upwards. The positive side of the z-axis is pointing towards the side A (direction Geneva) of the ATLAS detector, while negative z-values are assigned to the side C (direction Jura). Side B consequently is defined as the plane where $z = 0$.

Due to the cylindrical symmetry of the ATLAS detector, the use of cylindric coordinates (φ, θ and R) is useful. In this coordinate system the transverse distance to the z-axis is defined as the radius R. The azimuthal angle ϕ is measured around the beam axis, starting with $\varphi = 0$ on the x-axis and $\varphi = \pi/2$ on the y-axis. Usually the azimuthal angle is defined within $\varphi \in [-\pi, \pi]$. The polar angle θ is defined within $\varphi \in [0, \pi]$, where $\theta = 0$ is on the positive z-axis. In terms of the particles momentum components p_x, p_y and p_z, the two angles φ and θ can be written as:

$$\tan \phi = \frac{p_x}{p_y} \tag{3.3}$$

$$\tan \theta = \frac{\sqrt{p_x^2 + p_y^2}}{p_z}. \tag{3.4}$$

A more convenient way to express the polar angle θ is to use the pseudo-rapidity, which either can be expressed in terms of the polar angle or in terms of the particles momentum:

$$\eta = -\ln\left(\tan\left(\frac{\theta}{2}\right)\right) = -\frac{1}{2}\ln\left(\frac{|\vec{p}| - p_z}{|\vec{p}| + p_z}\right). \tag{3.5}$$

While the pseudo-rapidity is invariant under a Lorentz transformation, in the high energy limit of massless particles ($E >> mc^2$) the pseudo-rapidity becomes equal to the rapidity

$$y = \frac{1}{2}\ln\left(\frac{E - p_z}{E + p_z}\right), \tag{3.6}$$

which is Lorentz invariant under longitudinal boost. In addition, for the x-y-plane, η is equal to zero, in beam direction η goes to $\pm\infty$ which corresponds to $\theta = 0$ and $\theta = \pi$.

The direction of a particle can be described in the pseudo-rapidity-azimuthal space. As sketched in Figure 3.5 the difference in the direction of two particles can be defined in η and φ as ΔR:

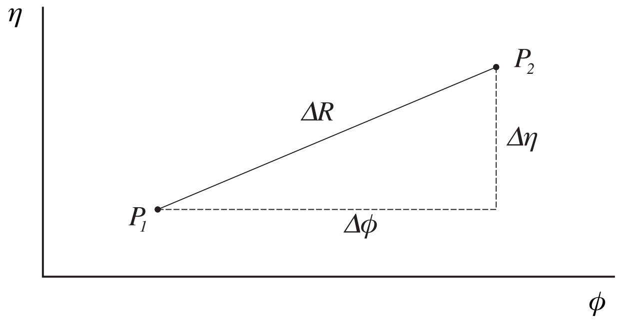

Figure 3.5: The tracks of two particles P_1 and P_2 in the η-φ-space and the distrance ΔR between them.

$$\Delta R = \sqrt{\Delta\eta^2 + \Delta\varphi^2}. \tag{3.7}$$

In hadron collisions, the trajectory of a particle is defined by various kinematic variables. The projection of the initial particles momentum p on the x-y-plane is defined as the transverse momentum p_T and the projection on the z-axis corresponds to the longitudinal momentum p_L. In the same manner the energy E can be split into the two components E_T and E_L. The transverse distance of the trajectories closest approach to the beam axis is defined as the transverse impact parameter d_0. Accordingly, the distance along the z-axis to the closest approach to the interaction point is defined as longitudinal impact parameter z_0.

3.3 The ATLAS Detector - Overview

The ATLAS detector is a general purpose detector located at Point 1 (see Figure 3.2) in a depth of approximately 80 m. An overview of the ATLAS detector layout is shown in Figure 3.6.

The detector layout consists of detector components arranged in layers concentrically around the collision point, as illustrated in Figure 3.7. The layer closest to the interaction point is the Inner Detector, dedicated to the measurement of charged particle tracks, allowing the reconstruction of the particles charge, momentum and production vertex. In Chapter 3.5 the components of the Inner Detector are described in more detail. The next two layers are designed to measure the energy deposit of electrons and photons, the

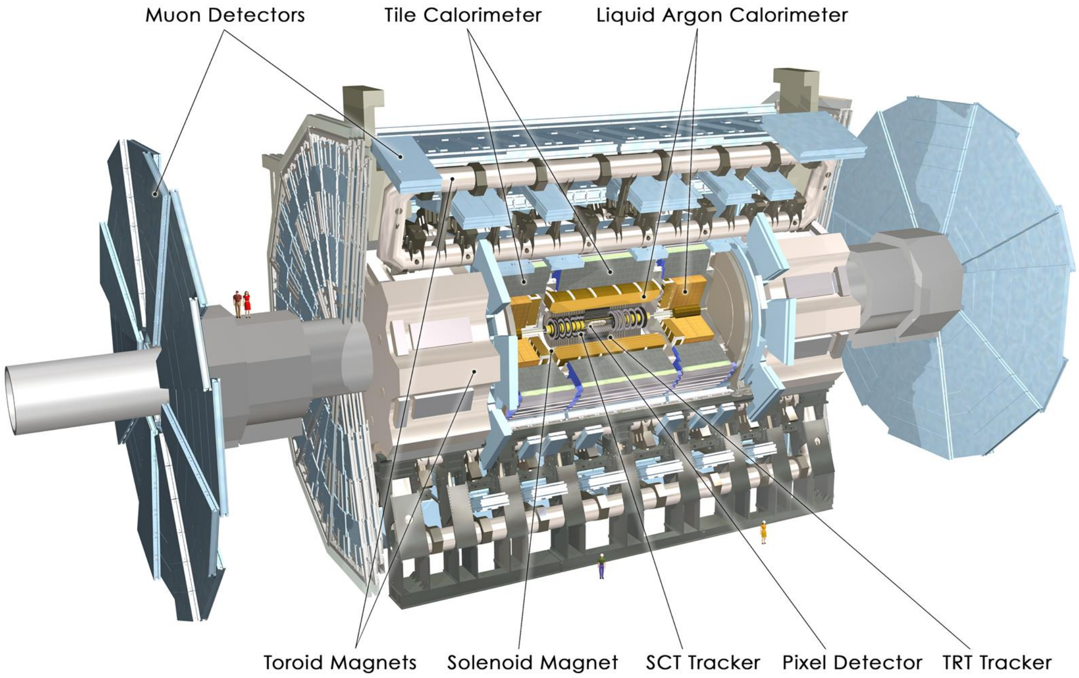

Figure 3.6: Schematic Overview of the ATLAS Detector

electromagnetic calorimeter, and of hadrons in the hadronic calorimeter. The various calorimeter types are described in Chapter 3.6. The outermost layer is the muon spectrometer, which is responsible for the large size of of the ATLAS detector. In the muon spectrometer, described in Chapter 3.7, the muons momentum can be measured at high precision. Within the Standard Model the only particles considered as stable, which are not accessible with those layers, are neutrinos, which can only be measured indirectly by evaluating the missing transverse Energy $E_{T,miss}$.

The elaborated Magnet System, responsible for the bending of charged particles in the Inner Detector and in the Muon System is described in Chapter 3.4. In Chapter 3.9 the event selection and the trigger system are detailed, and in Chapter 3.10 the data acquisition is summarised.

3.4 Magnetic System

The outer dimension of the ATLAS detector is dominated by the huge magnetic system AtlasMagnetSystemTDR with a diameter of 22 m and a length of 26 m. In total, the magnetic system consists of four magnets: the Central Solenoid CS [24, 153], the Barrel Toroid BT [42] and two End-cap Toroids ECT [25], arranged as shown in Figure 3.8.

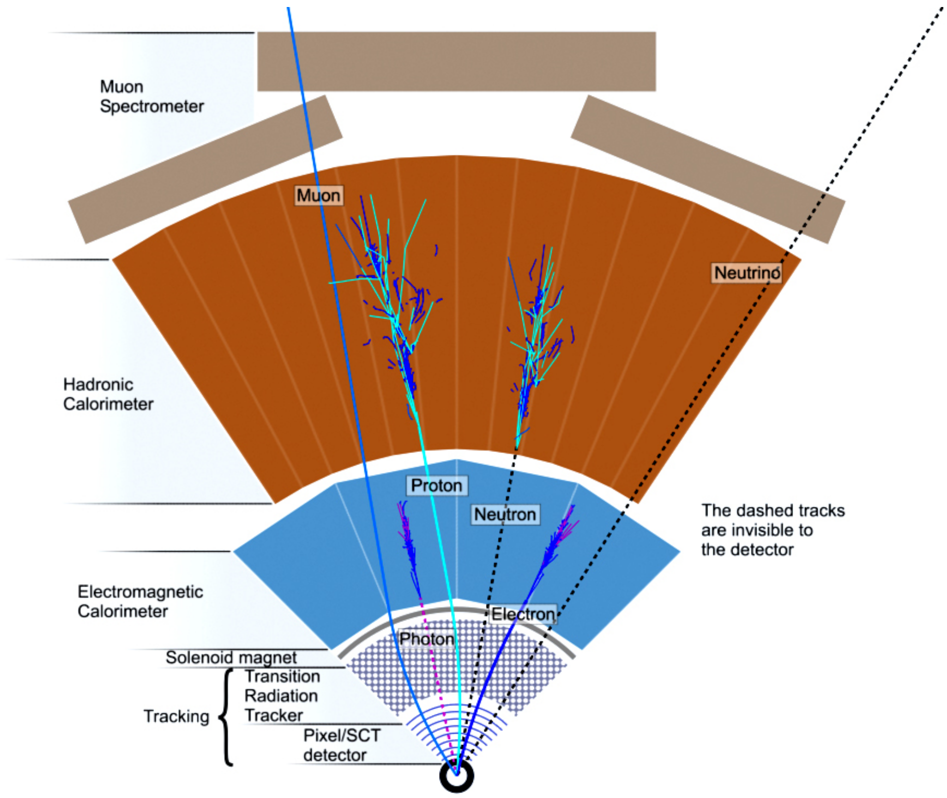

Figure 3.7: Event cross section in the ATLAS detector. Charged tracks from protons, electrons and muons create signals in the Inner Detector, photons, electrons and hadrons deposit their energy in the calorimeter. Muons create tracks through the whole detector cross section, and muons can only be detected as missing transverse energy.

With a length of 5.8 m and a diameter of 2.5 m, the CS is placed inside the calorimeter, embedding the Inner Detector with an axial magnetic field of 2 T, bending charged particles into the $R - \varphi$ plane. In order to minimise interactions of the particles with the detector material, the thickness of the solenoid has to be kept as low as possible. Too many interactions would have a negative influence on resolution of the energy measurement. The magnetic field of the CS is created by a single layer of $NbTi$ superconducting magnet winding at a temperature of 4.5 K, embedded into an Al support cylinder. The CS is integrated into the cryostat of the LAr electromagnetic calorimeter, minimising the need for additional support material. For particles traversing the magnet at normal incidence the material contributes with a radiation length of 0.66 X_0. The distance to the Barrel Toroid is large enough, so that the toroidal field does not influence the solenoidal central field of the CS. However, unlike the BT the magnetised steel of the tile calorimeter and its support girders influence the magnetic field of the CS in the order of 4 %. The calorimeter and its girders work as a partial return yoke for the magnetic flux lines.

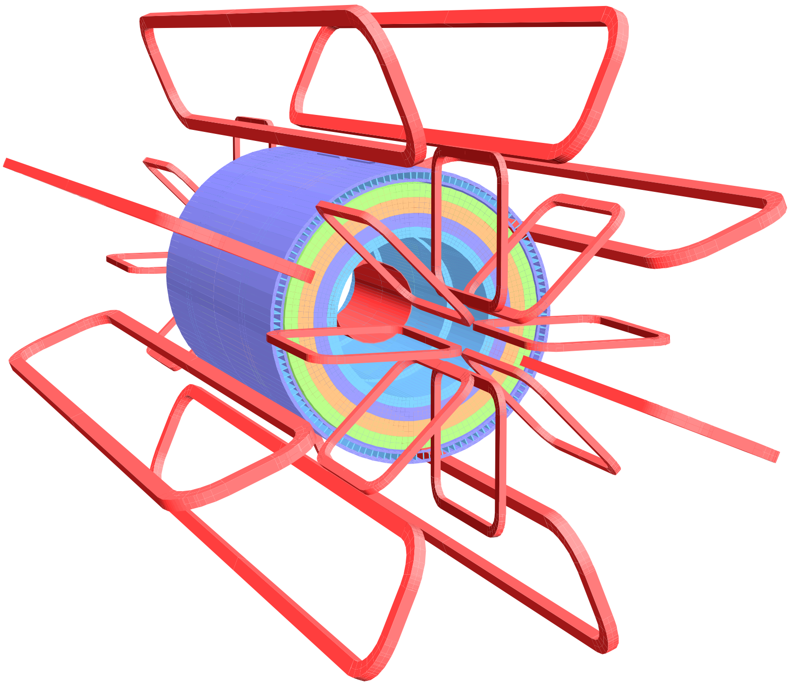

Figure 3.8: Schematic overview on the geometry of the Central Solenoid embedded in the tile calorimeter steel. The eight Barrel Toroid coils, with the end-cap coils interleaved are shown in red. [33]

In the outermost part of the detector, the muon system, the particle tracks are bent in a more complex magnetic system. The outer magnetic system consists of three air-core toroids, one large Central Toroid with a magnetic field of 0.5 T and two End-cap Toroids with a field of 1 T. The three toroidal magnets provide a magnetic field configuration in which the field lines mostly are orthogonal to the particles trajectories. As shown in Figure 3.8 each toroidal system consist of eight superconducting coils cooled to 4.5 K. The BT covers the pseudo-rapidity range of $|\eta| < 1.6$, the two ECTs the range between $1.4 < |\eta| < 2.7$. In the region between $1.4 < |\eta| < 1.6$ the BT overlaps with the ECTs. In order to provide a good bending power in this interface region, the ECTs are rotated by an angle of $\pi/4$ in the $R - \varphi$ plane with respect to the BT.

3.5 Inner Detector

The innermost part of a typical particle detector, the Inner Detector, is constructed to measure the tracks of all charged particles. In the case of the LHC at design luminosity an estimated number of 1000 particles emerge from the collision point every 25 ns within $|\eta| <$

2.5. These extreme conditions dictate detector elements fulfilling several characteristics, like materials able to handle extreme radiation conditions, a high space point granularity in order to separate all tracks even close to the collision point and fast electronics to keep up with the high collision rate. Figure 3.9 shows an overview of the ATLAS Inner Detector.

The decay time of B mesons (except onia states) has a life time of the order $\tau = \mathcal{O}(10^{-12}\text{ s})$ giving an average flight distance of $c\tau = \mathcal{O}(100\ \mu\text{m})$. These short distances need a precise reconstruction of both, the primary and and the secondary vertices. The precision of the vertexing depends on the reconstruction of all individual tracks, demanding a high number of layers, each with a large granularity and high precision. In addition, the short decay time of B mesons require a space point as close as possible to the primary pp vertex. In the ATLAS detector the layer closest to the collision point, the so called b-layer, still is at a radius of 50.5 mm.

Particles passing through the Inner Detector permanently interact with the detector material, not only providing the desirable signal, but on the other side suffering from diffraction. Therefore, adding additional layers of detectors on one hand side improve the tracking and vertexing, on the other hand the additional detector and electronics material decrease the tracking precision. Furthermore, the maximum tracking precision and efficiency is constrained by the financial budget available.

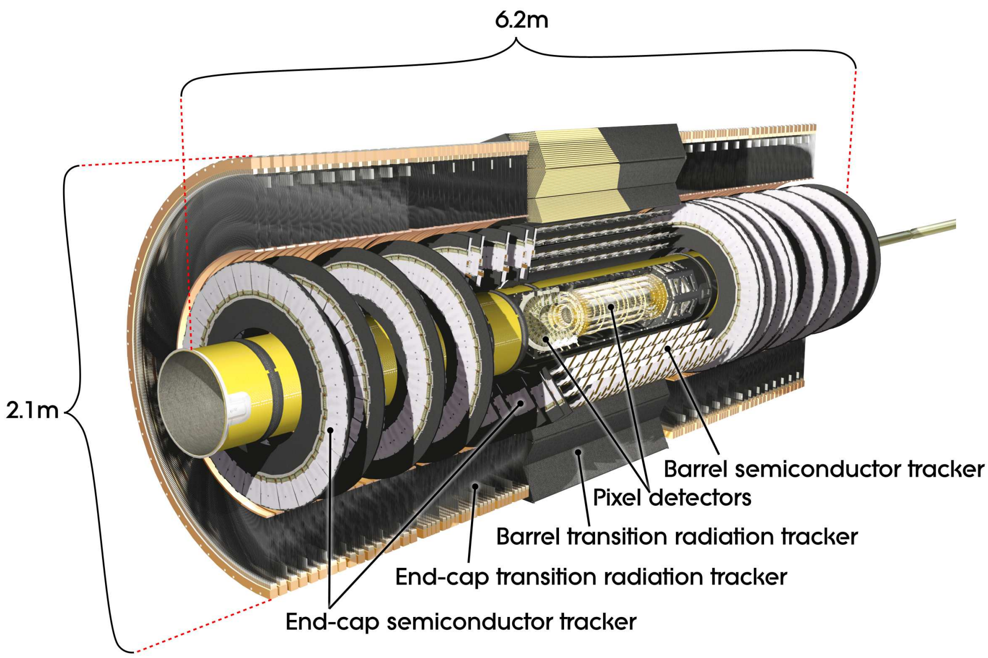

Figure 3.9: Schematic overview of the ATLAS Inner Detector

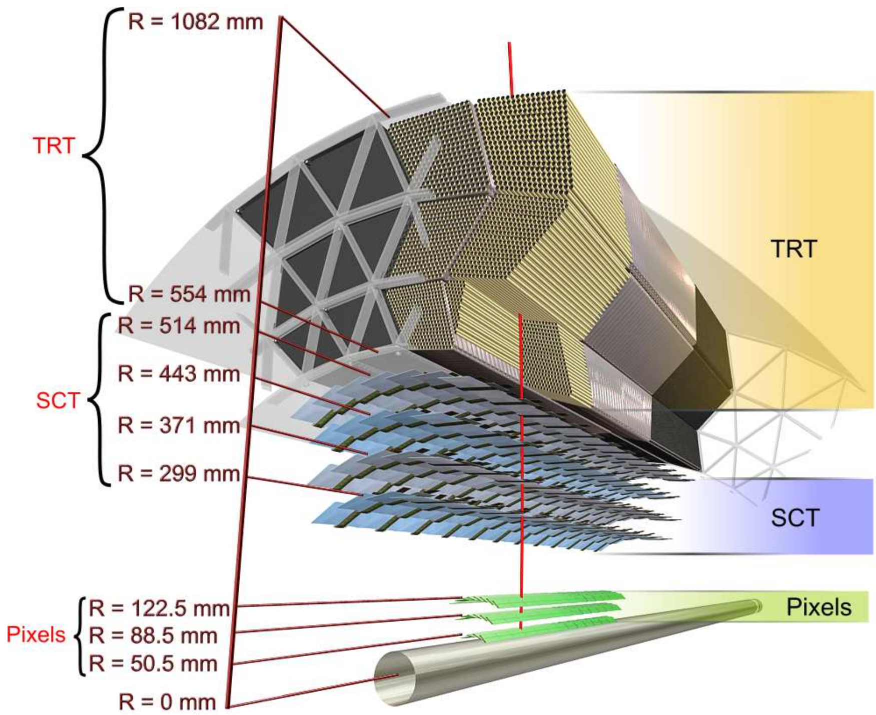

Figure 3.10: Schematic overview of the Inner Detector, including the radial distance of the various layers. [33]

The Inner Detector of the ATLAS experiment [26, 27, 33] meets those requirements with three main detector parts, as shown in Figure 3.9. The three parts are separated in a barrel and two end-cap regions. In the barrel region, the innermost part closest to the collision point is a silicon pixel detector (Pixel Detector, Chapter 3.5.1), with a total number of three layers of silicon pixel modules with radial distances between 50.5 mm and 122.5 mm. Following the same physical principle, a silicon microstrip detector (Semiconductor Tracker SCT, Chapter 3.5.2) provides four additional layers at radii between 299 mm and 514 mm. The Transition Radiation Tracker TRT (Chapter 3.5.3) is the outermost layer of the Inner Detector, starting at radius 554 mm up to 1082 mm. Its dimension defines the total diameter of the Inner Detector of approximately 2.1 m.

In order to provide a good coverage in pseudo-rapidity, end-cap disks of the Pixel detector and SCT are designed to cover particle tracks up to a pseudo-rapidity of $|\eta| = 2.5$. The TRT end-cap can cover particles up to approximately $|\eta| = 2.0$. Figure 3.11 shows the η coverage of the end-cap disks in more detail. Including all of the supporting structure, the cylindrical envelope holding the Inner Detector in total has a length of 7.0 m.

The inner solenoidal magnet system surrounding the Inner Detector is creating an

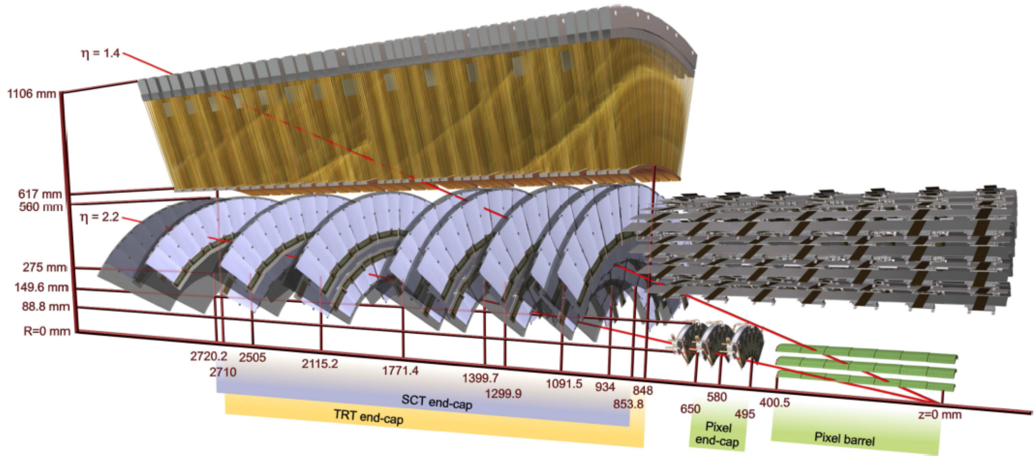

Figure 3.11: Schematic overview of the Inner Detector end caps and the dependence on the pseudo-rapidity η. [33]

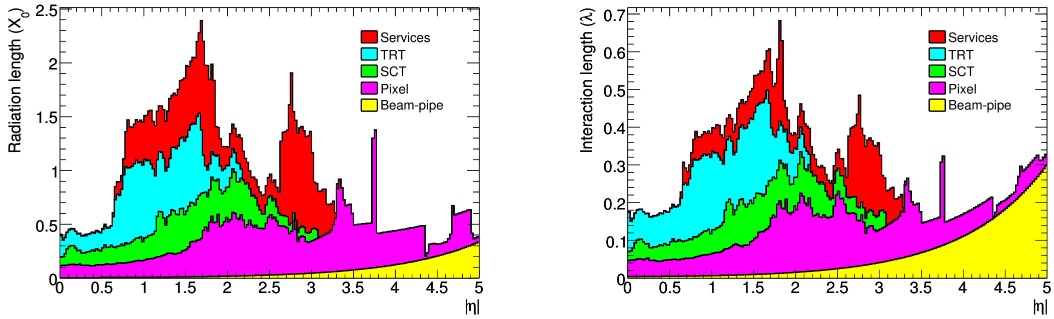

(a) (b)

Figure 3.12: Material distribution in units of radiation length X_0 (a) and nuclear ineteraciton length λ (b) at the exit of the Inner Detector envelope as a function of $|\eta|$ and averaged over φ. [33]

axial symmetric magnetic field of 2 T bending charged particles into the $R-\varphi$ plane due to the Lorentz force. This allows the measurement of the particles transverse momenta down to a minimum of $p_T = 0.5$ GeV. Particles with a p_T lower than 0.5 GeV are bended to very small radii, preventing the particles to leave the Inner Detector. Additional, at low momentum the efficiency is reduced due to large material effects.

In order to scope with energy loss of the particles with the detector material, both the Inner Detector and the solenoid magnet system are required to have a low radiation length X_0 and nuclear interaction length λ. In the barrel region ($|\eta| < 0.6$), both X_0 and λ are kept at a value below 0.5 averaged over φ. Particles traversing Inner Detector end-cap elements between ($0.6 < |\eta| < 0.6$) pass through matter corresponding to X_0 and λ in the order of $0.5 - 2.5$, strongly depending on the pseudo-rapidity as shown in Figure 3.12.

3.5.1 Pixel Detector

The innermost part of the Inner Detector consist of silicon pixel detectors [1, 150]. Three barrel layers are arranged on concentric cylinders around the beam axis at radii of 50.5 mm, 88.5 mm and 122.5 mm with a length of 800.1 mm. Three end-cap disks perpendicular to the beam axis are built at distances in z-direction of ± 495 mm, ± 580 mm and ± 650 mm, respectively. In Figure 3.13 the alignment of the layers and disks within the support structure are shown.

The Pixel Detector consists of 1744 Modules, each with 47232 pixels, where 286, 494 and 676 modules are in the three barrel layers respectively, and each of the six disks consists of 48 Modules. In total this gives a number of approximately 80.4 million read-out channels for the Pixel Detector. The active detection area of each module is 16.4×60.8 mm^2, giving a total detection area of approximately 1.8 m^2.

A pixel module is made of a n-type oxygenated silicon wafer with p^+ implanted on one side, and n^+ implanted regions (pixels) on the other side. Charged particles passing the detector create electron-hole pairs, the created charge then is collected in the pixels

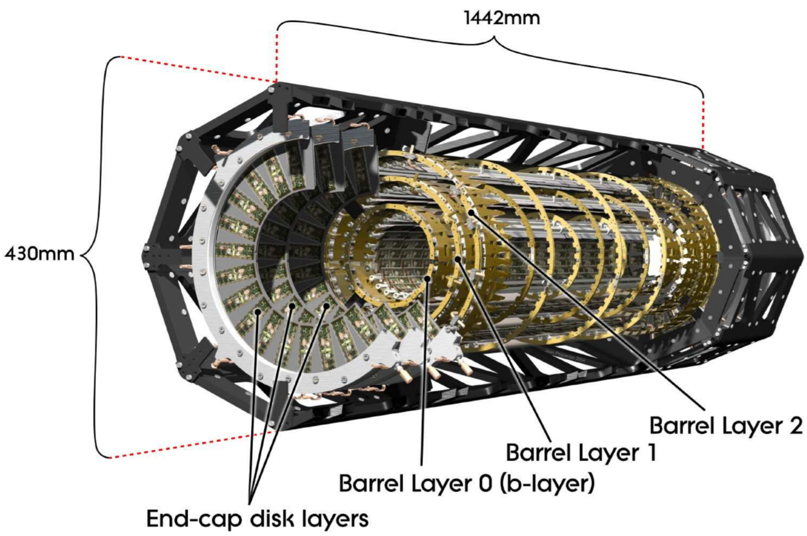

Figure 3.13: The alignment of the silicon pixel detectors into three barrel layers and three disks each side. [1]

due to the applied voltage. The initial operation voltage is about 150 V, but could reach up to 600 V to keep up the charge collection. A pixel supplies a signal, if the collected charge exceeds a certain threshold.

90% of the pixels have a size of 50×400 μm^2, the rest of the pixels, close to the front-end electronics, have a resolution of 50×600 μm^2. The pixels are arranged in $R - \varphi$ and z in the barrel regions and in $R - \varphi$ and R in the disks. The intrinsic measurement accuracy in the azimuth $R - \varphi$ is 10 μm, the axial accuracy in z is 115 μm. In the end-cap disks, the axial resolutions transforms into a radial resolution in R of 115 μm.

Due to the high irradiation close to the collision point, the material of the pixel sensors suffer from depletion. At the design luminosity of $\mathcal{L} = 10^{34}$ cm^{-2}s^{-1} the expected dose for the first layer, called "vertexing layer" or "b-layer", is expected to be around 500 kGy, the two other layers will reach this dose after the ten-year design lifetime of the experiment. Testbeam experiments have shown, that the detection efficiency of an unirradiated module is 99.9%, whereas irradiated modules have a reduced efficiency of 96.4% up to 98.4%. Therefore, the "b-layer" will have to be replaced after three years of running at design luminosity, the two other layers are expected to run for lifetime of the experiment.

3.5.2 Semiconductor Tracker

The barrel and end-caps of the Semiconductor Tracker SCT are described in detail in [5, 6]. In the SCT stereo pairs of microstrip layers are arranged in four co-axial layers in the barrel region and in nine end-cap modules on each side, as shown in the schematic overview of the Inner Detector in Figure 3.9. The radial distance of the barrel layers is 299 mm, 371 mm, 443 mm and 514 mm respectively, as shown in Figure 3.10. The SCT end-caps are placed on both sides with distances between and the coverage in pseudo-rapidity in Figure 3.11.

The detector principle is similar to the Pixel Detector: electron-hole pairs are created by charged particles and the charges are collected in one end of a strip. The operation voltage is of the order 250 V to 350 V. Instead of pixel elements, the position of a particle in the barrel region is measured with a double layer of microstrip sensors, one layer with strips parallel to the beam pipe for the precise measurement of φ and the other one with a stereo angle of 40 mrad. In the end-caps, perpendicular to the beam pipe, one layer is arranged radial, the other layer again with a stereo angle of 40 mrad. The microstrips have a pitch width of 80 μm and a length of 6 cm. The angle is chosen that small in order to avoid ambiguities when two particles are passing the same area in the SCT.

The SCT consists of 2112 modules in the barrel region and 1976 modules in the 18 end-caps. The total area covered by the SCT is 63 m^2, with a total of 6.3 million of read-out channels. In the barrel region, the intrinsic measurement accuracy is 17 μm in the φ-direction and 580 μm in z-direction. Rotated to a position perpendicular to the beam pipe, the measurement accuracy in the end-caps is translated into 17 μm in the φ-direction and 580 μm in R-direction.

3.5.3 Transition Radiation Tracker

The outermost sub-detector of the Inner Detector is the Transition Radiation Tracker TRT, described in detail in [2] and illustrated in Figure 3.9.

In the TRT particles are detected by taking advantage of the transition radiation effect. Relativistic charged particles emit transition radiation X-ray photons when crossing the interface of two materials with different dielectric constants. The energy loss of the particles per crossing is depending on the relativistic Lorentz factor $\gamma = E/mc^2$, hence the intensity of the radiation is proportional to the particles energy and mass. Therefore, the number of photons produced in one transition increases with decreasing mass, providing a good way to distinguish between electrons and pions. With special emphasis on the ATLAS TRT, this effect is described in detail in [12]. E.g. at a transverse momentum of $p_T = 25$ GeV the electron identification efficiency is about 90%, whereas the probability of misidentifying a pion as an electron is in the order of a few percent [34]. The radiation is emitted mainly in the direction of the particles trajectory, with a peak at an angle of $\Theta = 1/\gamma$.

The X-rays typically are measured by gaseous detectors embedded in transition radiation material. In the case of ATLAS, the transition radiation material in the barrel region is a matrix of polypropylene fibres [3]. In the two end-cap detectors the transition radiation material consists of thin polypropylene foils with a thickness of 15 μm and a polypropylene net between the foils [4].

The detectors in the ATLAS TRT are kapton (polyimide) straw tubes coated with a conductive material. The diameter of the tubes is 4 mm, the length is 144 cm for the tubes in the barrel, 37 cm in the end-cap. The straw tubes are filled with 70% of Xe, 27% of CO_2 and 3% O_2. The xenon ensures a good X-ray absorption, the CO_2 and O_2

are responsible for a short drift time and photon-quenching. While the straw tube works as a cathode, the anode in the centre of the tube is a 31 μm tungsten wire plated with a thin film of gold.

The $52,544$ tubes in the barrel are divided in the middle of each tube, hence the tungsten wire is electrically split in two parts read out on each side. The straw tubes are arranged parallel to the beam pipe. In the end-caps, the $245,670$ straw tubes arranged radial are read out at the outer radius. This gives a total number of read-out channels of approximately $350,000$.

As shown in Figure 3.11, the TRT end-caps can detect particles with a pseudo-rapidity of $|\eta| < 2.0$. The barrel TRT can detect particles with a pseudo-rapidity of $|\eta| < 1.0$, where charged tracks will traverse at least 36 straws. An electron with a transverse momentum of $p_T = 2$ GeV will typically leave seven high-threshold hits at $|\eta| = 0$. At high η particles will traverse up to 22 straw tubes in the end-caps. The intrinsic measurement accuracy for a single straw tube is 130 μm in the $R-\varphi$ plane. Due to the high number of space points, this uncertainty can be compensated, as shown for a TRT prototype in the testbeam [13].

3.6 Calorimeter

In general, the energy of all stable particles but muons and neutrinos can be measured in a calorimeter. A particle entering a calorimeter looses all its energy in a particle shower. The total particle energy is reconstructed by measuring ionisation, scintillation light or Cherenkov radiation.

In the ATLAS detector the calorimetry system [21–23] is divided into a number of sampling detectors dedicated to the measurement of the particles energies. In principle particles entering a calorimeter transfer their energy to the detector material, producing new particles by interactions with the detector material in the calorimeter. Typical interactions are e.g. the production of new photons due to bremsstrahlung or the creation of an electron positron pair due to the interaction of a photon with the coulomb field of an atom. These secondary new particles interact themselves with the calorimeter, creating new particles until the particles energy is too low to create new particles. Due to this cascade one particle entering the calorimeter leaves a shower of particles, each with low energy. By measuring the total energy of all particles created in this shower, the initial particles energy can be reconstructed.

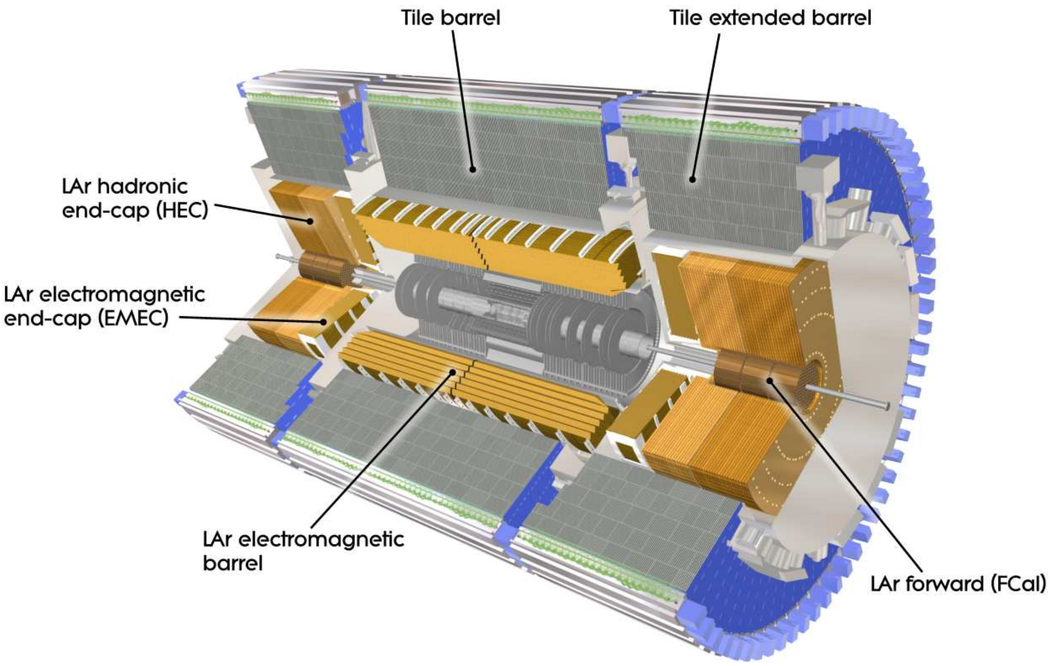

Figure 3.14: Schematic Overview of the ATLAS calorimeter

One of the main requirements of the calorimeter is the hermeticity in order to measure missing transverse energy $E_{T,miss}$ at a good resolution. The ATLAS calorimeter fulfils this requirement with a coverage over the whole range of φ and up to a pseudo-rapidity of $|\eta| = 4.9$. Surrounding the Inner Detector and solenoidal magnetic system, the calorimeter itself is split into several parts, depending on the type of interactions particles undergo in the detector material and the position within the detector.

The separation due to the interaction allows the differentiation into two groups of particles. In the electromagnetic calorimeters electrons (positrons) and photons are detected, in the hadronic calorimeters particles interacting mainly via the strong force are measured. The electromagnetic calorimeter is required to provide a fine segmentation for a precise measurement of electrons and photons. As the hadronic calorimeter mainly aims at the reconstruction of jets and the measurement of missing energy, the granularity is more coarse.

In the barrel region the innermost part of the calorimetry system is the LAr electromagnetic barrel surrounded by the hadronic Tile barrel. In the end-cap region, a LAr electromagnetic end-cap (EMEC) is followed by a LAr hadronic end-cap (HEC). In addition, covering the region close to the beam pipe, the forward calorimeter FCal detects electromagnetically interacting particles at large pseudo-rapidity. In Figure 3.14 these detector parts are shown schematically.

In order to reduce the punch-through probability of particles into the muon system and therefore keep the accuracy of the energy measurement high, the total material in the calorimeter provides a radiation length of > 22 in units of X_0 and a nuclear interaction length λ of > 10 as shown in Figure 3.15.

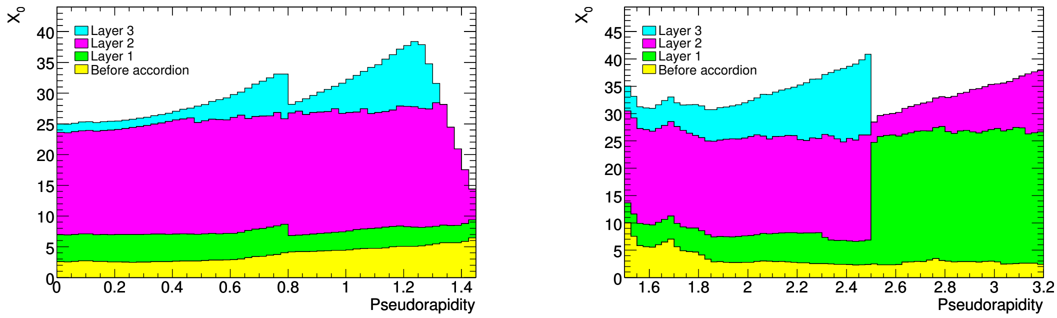

(a) (b)

Figure 3.15: Cumulative material distribution in units of radiation length X_0 and as a function of $|\eta|$ for the electromagnetic calorimeter and before. The plots are separated into a distribution for the barrel (a) and one for the end-cap (b). [33]

In the following, the calorimeter parts are described corresponding to their predominant interaction type, in Chapter 3.6.1 the electromagnetic calorimeter, in Chapter 3.6.2 the hadronic calorimeter and in Chapter 3.6.3 the combined electromagnetic and hadronic forward calorimeter FCal.

3.6.1 Electromagnetic Calorimeter

The LAr electromagnetic calorimeter in the barrel region and in the end-cap consists of detector elements built in accordion geometry, with alternating layers of absorber material and electrodes. In between, liquid-argon LAr acts as active material due to its good energy resolution and its high radiation hardness. The shower particles created in the calorimeter create ion-electron pairs in the LAr collected by the kapton electrodes. The electric signal is proportional to the number of ion-electron pairs and therefore to the energy deposited in the LAr due to ionisation. As absorber material lead plates with a stainless steel film are used.

In order to provide a fill coverage in φ, the accordion geometry is used in both, the barrel and end-cap region. The main disadvantage of this layout is the long simulation time of particles passing the calorimeter.

The LAr electromagnetic calorimeter is separated into a barrel region covering particles up to a pseudo-rapidity of $|\eta| < 1.475$ and two electromagnetic end-caps EMEC covering $1.375 < |\eta| < 3.2$.

The granularity of the LAr calorimeter depends on η and the radius from the proton-proton collision point. In the barrel region the granularity $\Delta\eta \times \Delta\varphi$ can be as fine as 0.025×0.025, in the end-caps the granularity increases from 0.05×0.1 ($\eta = 1.5$) up to 0.2×0.2 ($\eta = 3.2$). As shown in Figure 3.15, the material particles have to traverse before reaching the calorimeter accordion corresponds to a radiation length X_0 of 2.3 ($\eta = 0$) up to a maximum of about 7 ($\eta = 1.5$) at the transition between the barrel region and the end-caps. To overcome the energy loss due to dead material in front of the electromagnetic calorimeter, a separate thin layer of liquid-argon is installed as presampler. The granularity $\Delta\eta \times \Delta\varphi$ of the presampler is of the order 1.52×0.2.

According to measurements with the test beam, the energy resolution in the barrel region, depending from the incoming particles energy, is [10]:

$$\frac{\sigma(E)}{E} = \frac{10\ \%}{\sqrt{E}} \oplus 0.17\ \%. \tag{3.8}$$

For the LAr electromagnetic end-caps similar results in energy resolution have been obtained.

3.6.2 Hadronic Calorimeter

The hadronic calorimeter uses two different detector types: the tile calorimeter covers the region up to a pseudo-rapidity of $|\eta| = 1.7$, (central barrel and extended barrel), LAr hadronic end-caps HEC the region between $1.5 < |\eta| < 3.2$.

The tile calorimeter consists of steel absorbers and plastic scintillator tiles. In contradiction to the LAr electromagnetic calorimeter, the tile calorimeter is not designed in an accordion shape, but the steel scintillator sandwiches are oriented radial and perpendicular to the beam pipe. Surrounding the LAr electromagnetic barrel, in the central area three layers of the tile calorimeter cover a pseudo-rapidity range of up to $|\eta| < 1.0$, the three layers of the extended barrel increase this range up to $|\eta| < 1.7$. As shown in Figure 3.16, the integrated nuclear interaction length as a function of $|\eta|$ with the corresponding detector elements illustrate the gap between the central and the extended barrel. In beam tests with single pions the energy resolution has been found to be of the order [8]:

$$\frac{\sigma(E)}{E} = \frac{53\ \%}{\sqrt{E}} \oplus 5.7\ \%. \tag{3.9}$$

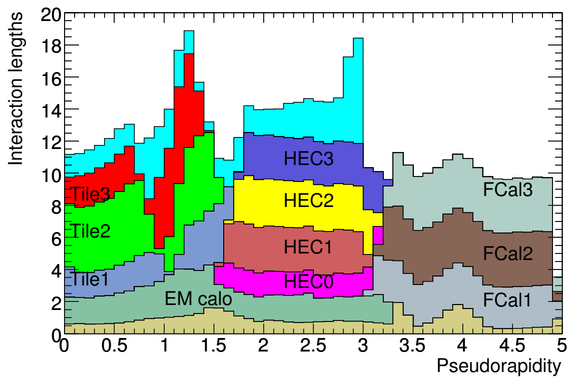

Figure 3.16: The cumulated distribution of the nuclear interaction length λ as a function of $|\eta|$ separated into the various calorimeter modules. [33]

The hadronic end-caps HEC consist of alternating flat layers of copper and liquid-argon covering a pseudo-rapidity range of $1.5 < |\eta| < 3.2$. The detection principle is analogous to the LAr electromagnetic calorimeter, but with a flat geometry and copper instead of lead as inactive material. Measurements with single pions in the testbeam result in a resolution of [76]:

$$\frac{\sigma(E)}{E} = \frac{70\ \%}{\sqrt{E}} \oplus 5.8\ \%. \tag{3.10}$$

In addition to the measurement of the hadronic particles energy, the iron in the tile calorimeter acts as a return yoke of the magnetic field lines of the Central Solenoid.

3.6.3 Forward Calorimeter

In addition to the barrel and end-cap modules, combined electromagnetic and hadronic forward calorimeters FCal are installed to cover particles at high pseudo-rapidity ($3.1 < |\eta| < 4.9$). The high η and the relatively short distance of 4.7 m to the interaction point leads to a high particle flux and therefore to a large radiation exposure.

The FCal splits into three layers, one electromagnetic layer and two hadronic layers. While in all layers thin films of liquid argon act as active material, the dead material in the case of the electromagnetic layer is made of copper and in the two hadronic layers of tungsten. Testbeam results with electrons and pions respectively have been fitted to the following energy resolution [18]:

$$\frac{\sigma(E_e)}{E_e} = \frac{29\ \%}{\sqrt{E_e}} \oplus 3.5\ \% \tag{3.11}$$

$$\frac{\sigma(E_\pi)}{E_\pi} = \frac{94\ \%}{\sqrt{E_\pi}} \oplus 7.5\ \%. \tag{3.12}$$

3.7 Muon System

The outermost part of the ATLAS experiment is the Muon System, described in more detail in [28]. It is designed to measure charged tracks and their momenta up to a pseudo-rapidity of $|\eta| < 2.7$. In addition the muon triggers are integrated into the muon system, designed to trigger on muons up to a pseudo-rapidity of $|\eta| < 2.4$. In Figure 3.17 the various detector types of the Muon System are illustrated together with the Magnetic System.

3.7.1 Muon Tracking Chambers

Over a large area of pseudo-rapidity up to $|\eta| < 2.7$, the muon track coordinates are measured by monitored drift tubes (MDT). In the barrel region, the MDT chambers are aligned in three layers: the innermost layer surrounding the tile calorimeter, one layer between the barrel toroid BT and the outermost layer enclosing the BT.

In principle, the measurement of the muons momenta is a measurement of the particles trajectory at three spacepoints. While in the barrel region one layer of muon chambers

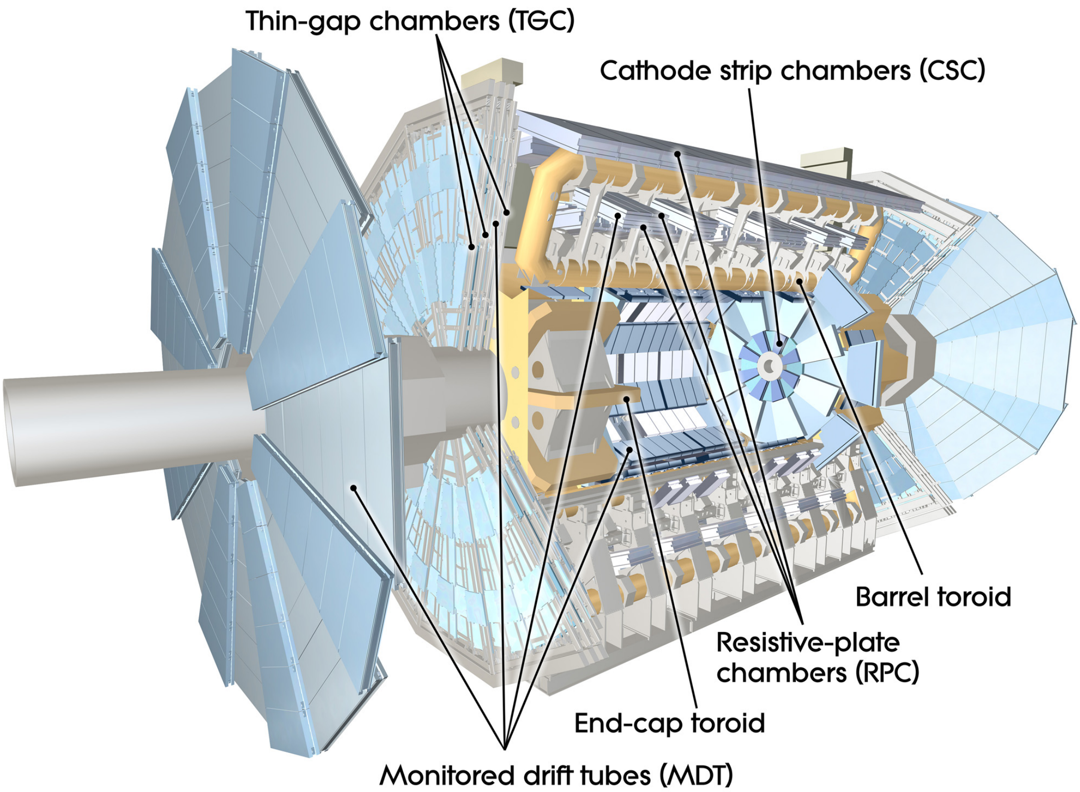

Figure 3.17: Schematic overview of the muon spectrometer and the toroid magnets. [33]

is placed within the toroidal magnet system, in the end-caps the toroid is placed between the first and the second layer. Hence, the measurement principle differs in these two regions. The measurement principles are illustrated in Figure 3.18. In the case of the barrel region, the muons momentum is reconstructed from the measurement of the trajectories deviation of a straight line, the so called sagitta s, and the direct distance L between the two measurement points in the first and third layer. Taking into account the magnetic field B, the transverse momentum is calculated as

$$p_T = \frac{L^2 B}{8s}. \tag{3.13}$$

In the case of the end-caps, the trajectory is bent between the first two layers of muon chambers, but a straight line between the second and the third layer. Hence, the reconstruction of the muons momentum depends on a point angle measurement.

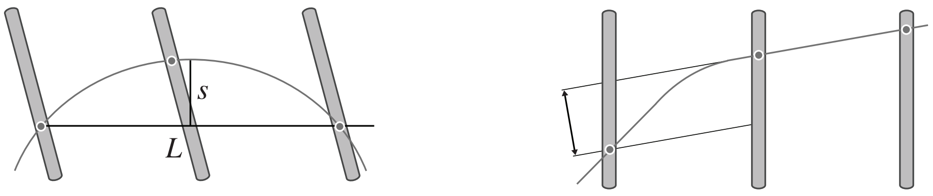

(a) (b)

Figure 3.18: The reconstruciton of the muons momentum depends on a measurement of the particles trajectories sagitta in the barrel region (a). In the end-caps the momentum is reconstructed by a point angle measurement (b).

The muon system is able to perform a stand-alone reconstruction of muons momentum at a resolution of 10 % for tracks with a momentum of 1 TeV. It is capable to measure muon tracks with a momentum of a few GeV, also stand-alone. The total muon momentum resolution as a function of the transverse momentum is shown in Figure 3.19 for the barrel region (a) and the end-cap region (b), separately.

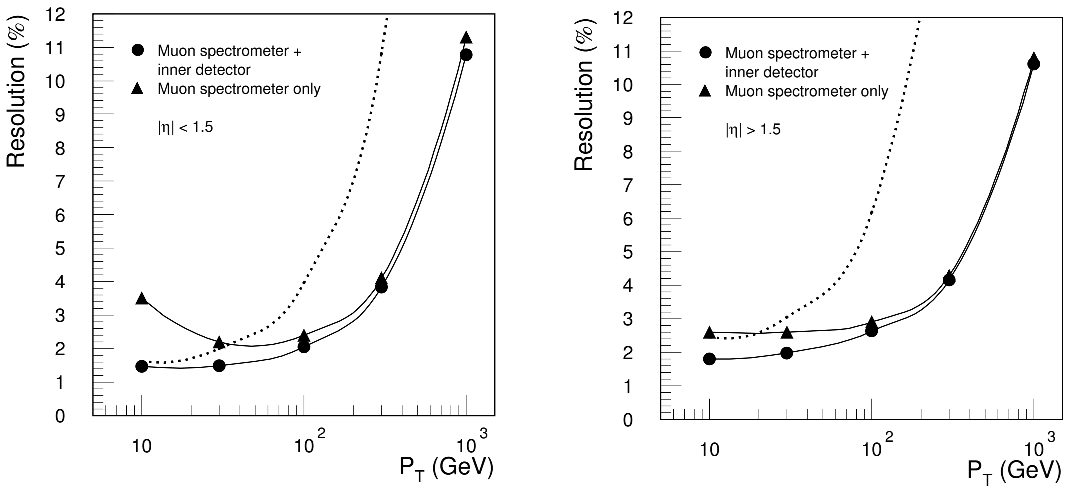

(a) (b)

Figure 3.19: The momentum resolution as a function of the muons transverse momentum p_T for the muon spectrometer, averaged over the azimuth. In (a) this function is shown for $|\eta| < 1.5$, in (b) for $|\eta| > 1.5$. The two solid lines show the resolution for the reconstruction using the muon spectrometer only or taking into account the information from the Inner Detecter. [28]

Monitored Drift Tubes

Within the muon spectrometer, precise muon tracking is performed by the Monitored Drift Tubes (MDT), except for the innermost end-cap region close to the beam pipe, where Cathode Strip Chambers (CSC) take over this role.

Monitored Drift Tubes are gaseous detectors with a diameter of approximately 30 mm and a wall thickness of 0.4 mm, filled with a mixture of Ar (93 %) and CO_2 (7 %) at a pressure of 3 bar. In the centre of each tube a gold-plated tungsten-rhenium wire with a thickness of 50 μm works as anode at a voltage of 3000 V. Charged particles passing such a drift tube ionise the gas, creating electrons. These electrons drift to the central wire, further ionising the gas and producing an avalanche of electrons, which all together are collected in the wire creating a signal.

The arrangement of the MDT chambers is illustrated in Figure 3.17. One MDT chamber consists of two multi-layers, which themselves consist of three or four layers of drift tubes each. A total of 1088 MDT chambers cover a total area of 5500 m^2. Depending on the distance to the interaction point, the size of a chamber increases with increasing radius or z-coordinate. In the barrel region, three layers of MDT chambers cover a pseudo-rapidity of up to $|\eta| < 1.3$. The layers are at radii of approximately 5 m, 8 m and 10 m, where the layer in the middle is surrounded by the large barrel toroid. In the end-caps the MDT cover the range up to $|\eta| < 2.7$, except in the innermost layer, where the Cathode Strip Chambers cover the range between $2.0 < |\eta| < 2.7$. The six muon end-caps are positioned on both sides at $|z| = 7.5 / 14.0 / 22.5$ m, respectively.

The drift tubes are arranged in a way, that only the position in η can be measured, corresponding to the bending of the muons trajectories in the toroidal magnetic field. The position along the wire corresponding to φ cannot be measured. The precision of the position measurement in η is about 80 μm.

Cathode Strip Chambers

In the inner muon end-cap, close to the beam pipe, Cathode Strip Chambers CSC replace the MDT chambers in the η region between $2.0 < |\eta| < 2.7$. Due to the high radiation due to thermalised neutrons from the calorimeter a different detector design has been chosen for this region. The CSC are multiwire proportional chambers, with anode wires oriented in a radial direction, while the cathode wires are oriented perpendicular to the anodes.

Muon tracks passing the CSC will give several position measurements in η and φ with a resolution in η of 60 μm. The CSCs are filled with a small gas volume, consisting of Ar (80 %) and CO_2 (20 %). The gas mixture provides a low neutron sensitivity, the small gas volume a short drift time of less then 40 ns. In total, the timing resolution of a CSC is about 7 ns.

3.7.2 Muon Trigger System

The ATLAS trigger chambers are designed to provide fast information on muons over the full range of φ and up to a pseudo-rapidity of $|\eta| < 2.4$. In a first approximation the muon momentum range has to be determined, the correct bunch-crossing has to be identified and trigger hits from neutrons and photons from the cavern have to be minimised.

In the barrel region ($|\eta| < 1.05$), the muon trigger consist of Resistive Plate Chambers (RPCs). As illustrated in the schematic in Figure 3.20, three concentric cylindrical layers of RPCs are installed: two layers surrounding the middle MDT layer, and one layer outside the outer MDTs. Due to the bending of the muons, the large distance between the inner and outer layer allow the triggering of high-p_T muons in the p_T range of $9 - 35$ GeV, the two inner layers trigger on low-p_T muons between $6 - 9$ GeV.

RPCs are gaseous parallel electrode-plate detectors with two resistive plates at a distance of 2 mm at a voltage of 9.8 kV. Metallic strips for the measurement of η (φ) with a pitch distance of 25 (30) mm are mounted on the outer faces of the plates. The strips are read out via capacitative coupling. Each layer of RPC consists of two independent detector layers. The RPCs provide a measurement of η and φ in all layers, giving a total number of six coordinates in η and φ. The detection efficiency per layer is measured to be 97 % with a time resolution of 1.5 ns.

In the end-caps, the trigger system consist of Thing Gap Chambers. As shown in Figure 3.20, TGCs are installed in four planes around the beam pipe. The inner TGC plane is a double layer detector, mounted around the support structure of the barrel toroid at $|z| \approx 7$ m. Three other TGC planes are mounted on wheels at a distance $|z| \approx 14$ m, surrounding the middle MDT layer. The three outer layers consist of one triplet detector and two doublet detectors, giving a total of seven planes a muon has to traverse.

TGCs are multi-wire proportional chambers filled with a gas mixture of CO_2 and $n - C_5H_{12}$ (55 : 45). At a potential of 2900 V, the distance between the wires and the graphite cathodes is 1.4 mm, while the distance between the wires is 1.8 mm.

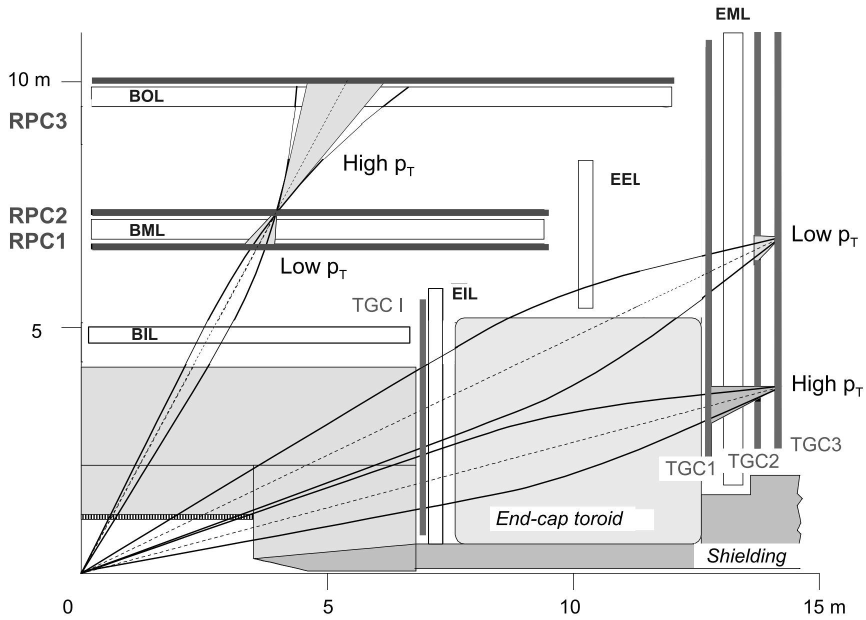

Figure 3.20: Schematics of the muon trigger system. [33]

The TGC chambers are aligned in a way, that the wires measure the radial distance to the beam pipe. In addition, copper layers segmented in radial direction (Cu Strips) allow the measurement of the azimuthal coordinate φ. While not as fast as the RPCs, the TGCs can identify muons within the bunch-crossing time of 25 ns with an efficiency greater than 99 %.

3.8 Additional Detector Systems

Beside the main ATLAS detector, three additional detector sets are installed on both sides along the beam pipe in the very forward direction. More information can be found in [106]. At this point these detectors will just be described very briefly.

At a distance of ±17 m, within the ATLAS detector, the Luminosity measurement using Cerenkov Integrating Detector (or short LUCID) is the main relative luminosity detector for ATLAS. By detecting inelastic $p - p$ scattering in the forward direction, the LUCIDs main purpose is the measurement of the the integrated luminosity. In addition it provides online monitoring for the instantaneous luminosity and the beam condition.

Placed well outside the ATLAS detector at ± 140 m, where the LHC proton beams are separated into two beam pipes, the Zero-Degree Calorimeter ZDC measures very forward neutrons in heavy-ion collisions.

In the ATLAS experiment, the measurement of the absolute luminosity is performed by measuring the elastic-scattering amplitude at zero angle, which directly relates through the optical theorem to the total cross-section. This measurement is done with the the Absolute Luminosity for ATLAS (ALFA) detector, located ± 240 m away from the interaction point. The ALFA detector consists of Roman-pot detectors, which could be moved as close as 1 mm to the proton beam from up or down.

3.9 Trigger System

With a total number of 10^8 read-out channels, the expected size of stored data per event is of the order 1.5 MByte. At the LHC design luminosity of 10^{34} cm^{-2}s^{-1} the bunch crossing rate goes up to 40 MHz. With an average number of 22 pp interactions per bunch crossing, the total interaction rate will be of the order 10^9 Hz. It is impossible to store this huge amount of data, therefore it is crucial to reduce the number of events to a small fraction in the order of 200 Hz or a data rate of about 300 MByte/ s. This corresponds to a reduction factor of about 10^7.

The main target of the ATLAS trigger system is the proper selection of events with interesting physics. Pythia predictions [34] of the total pp cross-section at a centre-of-mass energy of 14 TeV are of the order 102 mb, where the fraction of inelastic scattering pp cross-section is of the order 79 mb and the fraction of minimum bias events is predicted to be about 65 mb. Consequently, corresponding to the reduction factor of 10^7, the processes of primary physics interest at the ATLAS experiment have cross-sections of the order $\mathcal{O}$(nb) or smaller. To achieve this reduction, the ATLAS trigger system has to perform an efficient rejection of background events, while the selection efficiency of interesting events has to be excellent. At ATLAS the trigger consist of following three subsequent levels of event selection:

- First Level Trigger LVL1
- Second Level Trigger LVL2
- Event Filter EF

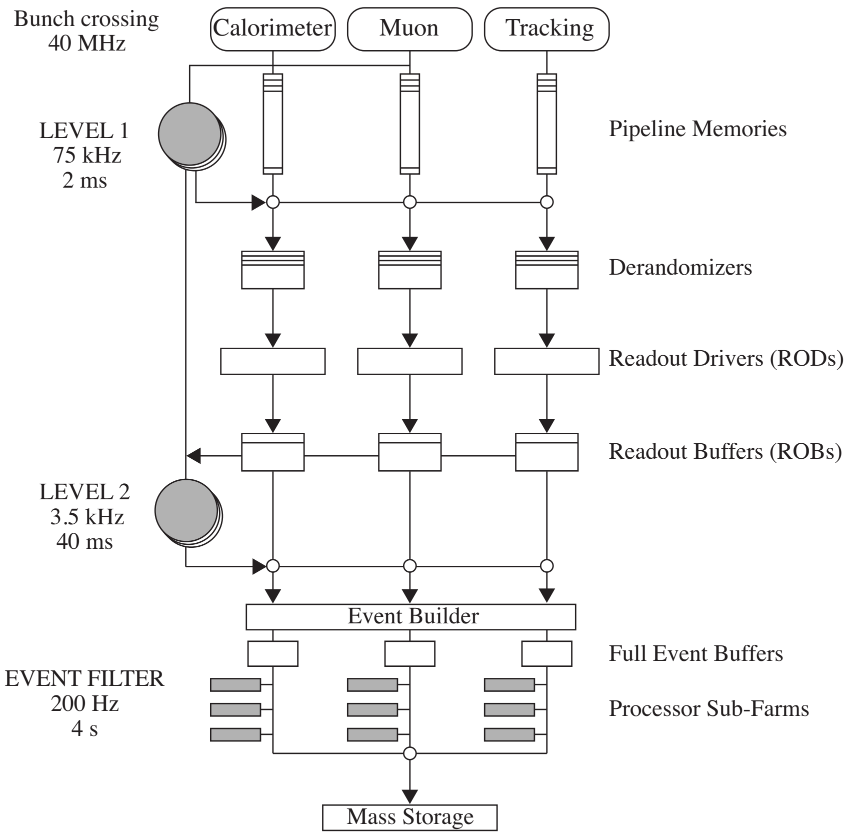

Figure 3.21: Schematic view of the ATLAS three-level trigger system.

Sometimes the two levels LVL2 and EF in combination are referred to as High Level Trigger HLT.

Each of the three trigger level reduces the amount of data subsequently by some orders of magnitude, while each trigger level has more time available to refine the selections of the previous trigger in order to perform more complex selection algorithms of the detector signals. Each trigger level passes the gathered trigger information to the subsequent trigger level. In addition, with increasing level, a trigger can access more detailed detector information. In Figure 3.21 the workflow of the three trigger levels is schematically illustrated. In the following sections, the trigger levels are discussed in more details. An overview on the whole trigger system is given in [30, 31, 33], the First Level Trigger LVL1 is described in all details in [29], the HLT in [105].

3.9.1 First Level Trigger

The LVL1 is a pure hardware based trigger, designed to analyse all bunch crossings and reduce the input data at a rate of 40 MHz down to 75 kHz. The output rate of the LVL1 could be increased the output rate up to about 100 kHz.

The LVL1 trigger selects events using a subset of detectors, i.e. the calorimeter and the muon trigger chambers. Due to the time usage for track reconstruction, information from the Inner Detector is not used at this stage. The muon trigger searches for events containing one or more muons, based on the measurements of the muon trigger chambers in the barrel and end-cap region. The calorimeter trigger system searches for high energy depositions E_T due to photons and electrons, jets, τ leptons decaying into hadrons or missing transverse energy $E_{T,miss}$. Both, electromagnetic and hadronic calorimetric information from the barrel region and end-caps are use with a coarse granularity.

One of the main requirements of the LVL1 trigger is the time consumption for one single trigger decision. For a fast decision, coarse trigger informations on detected signals and flags on passed thresholds are sent to the Central Trigger Processor CTP. In the CTP the input data is compared to look-up tables from a maximum 256 trigger conditions, which could be e.g. "one muon with a certain p_T threshold" or "missing energy $E_{T,miss}$ with a certain threshold". In addition, each trigger condition can be modified by applying a priority, which is responsible for the dead-time between to events with the same trigger decision, and by a pre-scale factor, reducing the trigger rate to a decision every n^{th} event.

In order to reduce the time consumption of the subsequent HLT trigger, in the CTP so called Regions of Interest (RoI) are defined around each triggered item. All the trigger information of accepted events are pipelined to the Read Out Buffers ROBs, from where the information then subsequently is forwarded to the HLT. In the LVL2trigger further algorithms search for additional features and signatures within these regions instead of analysing all detector information using the Full Scan (FS) method. This method decreases the processing time at the expense of trigger efficiency.

Calorimeter Trigger

In the Calorimeter Trigger all hadronic and electromagnetic calorimeter detectors are read out at a coarse granularity $\Delta\eta \times \Delta\varphi$ of 0.1×0.1, corresponding to a total number of approximately 7000 analogue trigger towers. In all calorimeter detectors, a trigger is set off if the energy deposit in one trigger tower exceeds a certain threshold. Within a time period of 1.5 μs the Calorimeter Trigger sends the results to the CTP, resulting in a total latency of 2.1 μs for a final LVL1 calorimeter decision.

The Calorimeter Trigger identifies electrons and photons as electromagnetic clusters as well as τ-leptons decaying into hadrons by searching for transverse energy deposits above a tuneable threshold and, if required, a certain isolation from other energy deposits. Furthermore, hadronic jets are triggered with a coarser granularity using four trigger towers resulting in a resolution of 0.2×0.2 in $\Delta\eta \times \Delta\varphi$. In addition, the missing transverse energy $E_{T,miss}$ and the total transverse energy are calculated and can be triggered.

The electron/photon and τ-lepton trigger cover a pseudo-rapidity range of up to $|\eta| < 2.5$, jets are triggered up to $|\eta| < 3.2$ and the total transverse energy and $E_{T,miss}$ up to $|\eta| < 4.9$ by taking advantage of the FCal. The type of the energy deposit (electromagnetic cluster, τ-lepton or jet) together with its position is submitted to the RoI builder. These information is forwarded to the LVL2 trigger for further analysis of this region.

Muon Trigger

As already described in 3.7.2, the Muon Trigger consists of separate trigger chambers, integrated into the Muon System. The Muon Trigger consists of three layers of finely segmented trigger chambers in both, barrel region (RPCs) and the two end-caps (TGCs).

Muons penetrating the Muon System leave hits in each trigger layer, leaving a path through the Muon System. The Muon Trigger requires a coincidence of the hits in the different muon trigger layers following a road around the muon track. As illustrated in Figure 3.20, the curvature of a muon track increases with a decreasing transverse momentum, the width of the road corresponds to the muons p_T threshold. While a muon with a very high p_T leaves a straight line in the muon system due to the toroidal magnetic field, a low-p_T muon leaves a track with a strong curvature. Therefore, trigger hits within a road with a smaller width can be associated to muons with a higher p_T.

In both, barrel region and end-caps, a total of six programmable thresholds of muons p_T are implemented, allowing to trigger on three low-p_T ($6 - 9$ GeV) and three high-p_T ($9 - 35$ GeV) muons, respectively. All muon signals are combined into one set of multiplicities for each threshold per bunch-crossing.

In the barrel region up to a pseudo-rapidity of $|\eta| < 1.05$ three RPC doublets trigger the muons. If a muon hits the second RPC doublet or the so called pivot plane (see Figure 3.20), a straight road is constructed between the interaction point and the hit in the pivot plane, corresponding to a muon coming from the collision point, i.e. a muon track with infinite momentum. As described before, the width of the road can be translated into a threshold on the muons p_T. Out of four possible hits in the first two RPC1 and RPC2 doublet layers a total of three hits within the road are required to give a positive muon trigger signal. This way background tracks (e.g. neutrons or gammas from outside the detector) are prevented to be misinterpreted as muons.

Making use of the low-p_T trigger hits, the high-p_T trigger works in a similar way. Again, a straight road is extrapolated from the interaction point through the hit in the pivot plane to the outermost layer. In addition to the hits in the first two layers, one out of two possible hits in the outermost layer is required. Combing the results from the low-p_T trigger and the hight-p_T trigger, the coordinates η and φ and the associated RoI information are forwarded with a total number of six threshold numbers to the CTP.

In order to obtain a trigger result in the barrel region, the aligned trigger signals from the layers are compared with a lookup table on a coincidence matrix chip. Starting from the hit in the pivot plane, the allowed hits for low-p_T and hight-p_T muons in the RPC1 and RPC3 layers, respectively, are compared with the measured hits.

Using the TGC trigger chamber in the end-cap regions, the trigger algorithm works in a similar way like in the barrel region. In the end-caps, the outer most doublet trigger plane TGC3 works as pivot plane (see Figure 3.20). Again, following the infinite momentum assumption for muons originating from the collision, a straight line from the hit in the pivot plane to the interaction point is created. Three possible low-p_T thresholds can be evaluated by using three out of four hits in the two doublet layers TGC2 and TGC3. The high-p_T triggers uses the hits in the two outer layers and evaluates the trigger threshold by using the TGC1 triplet layer.

The muon trigger efficiency is defined as $N_{\mu,trig}/N_{\mu}$, where $N_{\mu,trig}$ is the number of events with a triggered muon, and N_{μ} is the number of events with an actual muon. While the efficiency of the muon triggers in both, barrel and end-caps, is above 99 %, magnetic ribs, support material and the muon spectrometer crack at $\eta \approx 0$ reduce the acceptance of the LVL1 trigger to a value of approximately 82 % (78%) for low-p_T (high-p_T) muons. The geometrical distribution of the inefficient regions in the $\eta - \varphi$-plane due to the crack region and the magnet support structure is shown in Figure 3.22.

In Figure 3.23, the trigger efficiency as a function of muons p_T is shown for the barrel and end-cap with various p_T thresholds. The efficiency shows up as a turn-on function with a plateau in the barrel region of 82 % (78 %) for low-p_T (high-p_T) thresholds and in the

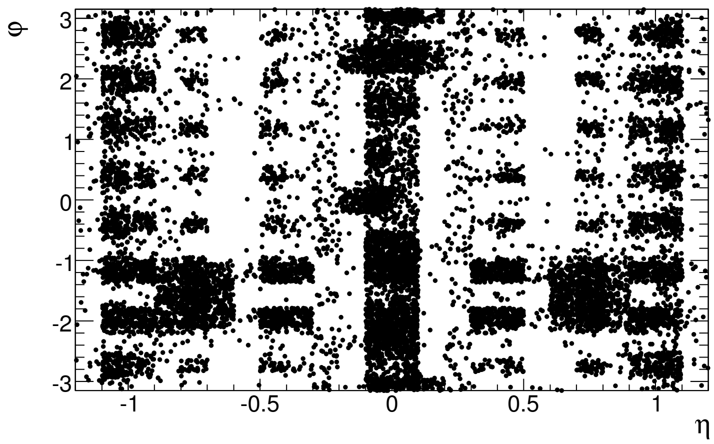

Figure 3.22: LVLI muon trigger geometrical acceptance in the $\eta - \varphi$-plane for the barrel region. [34]

end-caps between 93 % and 95 %. The effective trigger thresholds are defined as the value, where the efficiency is 90 % of the corresponding nominal trigger value. Consequently, the effective trigger thresholds are slightly below the nominal trigger thresholds (e.g. the effective MU6 threshold is at 5.3 GeV).

In a last step, the muon trigger signals are combined and the total muon multiplicity for each of the six p_T thresholds is forwarded to the CTP. The maximum multiplicity taken into account is seven candidates. In the CTP the muon trigger signals are evaluated. Beside the single-muon trigger, di-muon triggers with different p_T thresholds for the muons are possible. Therefore, special care has to be taken in order to avoid double-counting of muons. Especially the overlapping areas between neighboured trigger sectors in the barrel region and overlaps between barrel and end-cap triggers have to be treated properly.

3.9.2 Second Level Trigger

In difference to the LVL1 trigger, in the Second Level Trigger LVL2 a processing farm performs the event selection. The aim of the LVL2 trigger is to reduce the LVL1 event rate by a rejection factor of approximately 30 down to a LVL2 event rate of 3.5 kHz. Each decision should use a processing time less than 40 ms.

At design luminosity, the LVL2 event processing is seeded by the RoI information from the LVL1. In a first step, the more detailed detector information within the RoI is merged with the LVL1 trigger information. In an alternative way, using the Full Scan

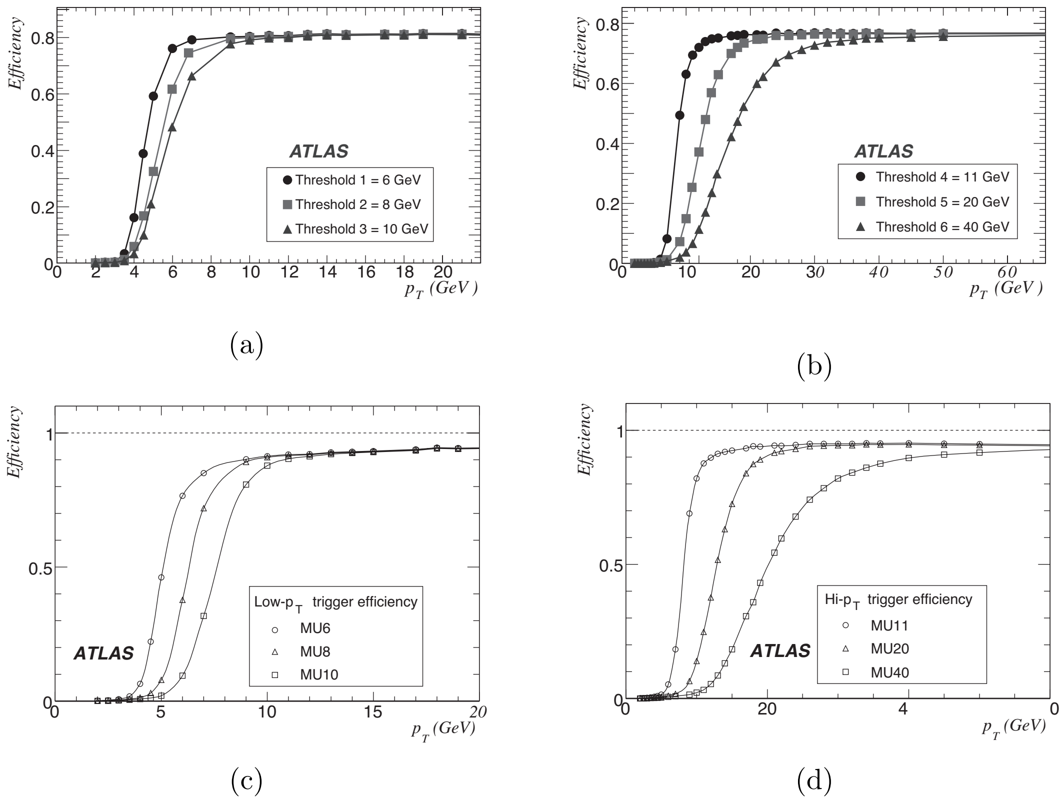

Figure 3.23: The LVLI muon trigger efficiency for low p_T muons (6, 8 and 10 GeV) in the barrel region (a) and in the end-caps (c), respectively for high p_T muons (11, 20 and 40 GeV) in the barrel (b) and end-caps (d). [34]

FS method, the detector information from all sub-detectors (Inner Detector, calorimeter, muon spectrometer) can be transferred to the LVL2 resulting in an increased processing time. While at design luminosity only the RoI method will be used for event selection, at lower luminosities the FS method can be chosen alternatively.

The LVL2 trigger has access to the detector information in full resolution. The calorimeter signals have the full granularity, the muon tracking precision chambers are fully accessible, and the signals coming from the Inner Detector can be already used for tracking and vertexing.

In the LVL2 trigger subsequently trigger decisions are applied, each step refining the information by adding additional detector information from all sub-detectors. Physics trigger signatures are identified by trigger chains. In a first step, within the RoI features like tracks or energy deposits are identified, in a second step a hypothesis algorithms checks, whether the features fulfil the requested criteria or not. Subsequently features are added, until the complete physics signature is confirmed.

As one example from the B Physics, for searching the physics signature $J/\psi \to \mu^+\mu^-$ in a first step the two muons identified in the LVL1 trigger will be identified within the RoI. After combining the track information from the Inner Detector with the signals from the muon chambers, the two muons are combined and a mass cut on the resulting invariant mass triggers is applied.

3.9.3 Event Filter

The second part of the HLT and the third level of the ATLAS trigger, the so call Event Filter (EF), reduces the event rate from 3.5 kHz down to 200 Hz. The trigger decision takes up to 4 s, computed parallel in a processing farm.

While the steering for the EF is the same as for the LVL2 trigger, the EF uses the standard ATLAS event reconstruction and analysis application [32]. This allows e.g. a more precise muon and track reconstruction and consequently a more precise vertex reconstruction.

The precise analysis of the event topology allows a first estimation of the physics criteria fulfilled. For a detailed offline analysis, based on certain criteria, TAGs are added as metadata.

3.10 Data Storage

With an average event size of 1.6 MByte and a maximum Event Filter EF output rate of 200 Hz, the estimated amount of data produced by the ATLAS experiment is of the order 320 MByte/ s. With an estimated data taking time of 10^7 seconds per year, the amount of data collected annually will be of the order 3.2 PByte. All LHC experiments together will produce a roughly estimated number of 15 PByte of raw data per year.

The need for Storage and computing power for reconstruction and data analysis by far pushes the boundary of a single computing centre at CERN. For this reason, the Worldwide LHC Computing Grid (WLCG) [110] has been established in order to build and maintain a distributed computing infrastructure meeting the needs of the LHC experiments.

The WLCG combines more than 130 computing centres distributed worldwide. The computing centres are connected in order to distribute the workload of storing, processing and analysing. The centres are structured in three (or more) layers, so called “tiers“: one Tier-0, the computing centre at CERN, eleven large Tier-1 centres and many Tier-2 centres. It is foreseen to add a Tier-3 layer, meeting the needs for small, local analysis facilities.

The raw data selected by the EF is transferred to the first-pass processing facility, the Tier-0 computing centre at CERN. The raw data is archived on the CASTOR storage system at CERN, and in addition one copy is transferred to one of the Tier-1 centres in parallel, also for permanent archiving. The raw data is processed in a first step at the Tier-0 centre, resulting in the derived Event Summary Data ESD, stored on the CASTOR system and distributed to two external Tier-1 centres.

Beside reprocessing the raw data to new ESD datasets, the Tier-1 centres main responsibility is the further processing of the ESD to the so-called Analysis Object Data (AOD) and the derived TAG event metadata. The TAG information is archived on the CASTOR system and in one Tier-1 centre. The AOD datasets are further shared between the Tier-2 centres. About one hundred Tier-2 centres provide the bulk computing and storage capacity for the physics simulation and data analysis.

3.11 Detector Control System

For a coherent and safe operation of the ATLAS detector, a Detector Control System (DCS) [135] is used to control various tasks. The DCS gives the possibility to steer the operational state of the ATLAS detector, both by a human interface and by taking automated actions. The DCS provides interfaces to all sub-detectors of ATLAS to the data acquisition system and to independently operated systems like the LHC accelerator.

The DCS monitors and stores the ATLAS run parameters, shares this information with the data acquisition system and, if needed, take automated or manual corrective actions to the detector sub-systems.

The bi-directional communication between the DCS and the LHC machine gives ATLAS information about the quality of the beam and collisions. In addition, the primary 40 MHz bunch clock is transmitted from the LHC to the DCS and after refinement and calibration distributed to the LVL1 trigger system. ATLAS sends information about local conditions to the LHC, allowing the accelerator to optimise the beam conditions.

CHAPTER

FOUR

Event Production and Reconstruction

While the ATLAS detector takes data, the comparison of data with simulated events are indispensable for understanding the detector, material effects, the background and interesting physics events. Simulated data is the primary tool for the development of analysis strategies and, more general, the preparation of the reconstruction software for data analysis of real data events. But not only for the preparation simulated data is crucial, also while data is taken the production of simulated data continues. The refinement of data analysis methods strongly depends on the comparison of simulated with real data. For a proper identification and analysis of interesting physics events, all possible polluting background events have to be understood in detail and all sources of background have to be identified.

In this thesis only simulated events are used for the preparation of flavour tagging methods. Therefore, in this chapter all essential steps for the generation of simulated events are discussed. First, in Chapter 4.1 an overview of the ATLAS computing model is given. In Chapter 4.1.1 the various steps of the generation of Monte Carlo events are outlined. In Chapter 4.1.2 and 4.1.3 the simulation of the ATLAS detector, the propagation of the Monte Carlo particles through the detector material as well as the detector response and data processing will be detailed. The next step, common to real and simulated data, is the reconstruction of the detector signals in Chapter 4.1.4. The data types used in all those steps are introduced in 4.1.5.

The computing infrastructure used for the generation, simulation, reconstruction and data analysis as well as the Worldwide LHC Computing Grid (WLCG) are shortly introduced in Chapter 4.2.

4.1 The ATLAS Computing Model

The production of simulated data, the reconstruction of both, simulated and real data, and the physics analysis are performed within the C++ based object-oriented modular ATLAS computing framework Athena, described in detail in [32]. Athena is an enhanced version of Gaudi [46], developed by the LHCb collaboration. Within Athena all steps can be taken, starting with the Monte Carlo generation of events, processing their propagation and interaction through the detector, the reconstruction of events and the analysis of the data.

The details of a typical production of simulated data is illustrated in Figure 4.1. After the generation of four-vectors of particles, including hadronisation and the decay of unstable particles, a particle filter can be used to select events according to different criteria, e.g. events containing certain particles or a particular decay pattern.

The propagation of the stable particles through the detector and the magnetic field as well as their interaction with the the detector material are calculated in the simulation step. These informations are used in the next step of digitisation to create detector signals, looking identical to data obtained from the ATLAS detector. In the reconstruction step physical objects are identified in both, real and simulated data, and interpreted as charged tracks, photons, muons or any other final state product with a certain four-momentum. The huge amount of information is condensed, and depending on the physics requests the interesting information is extracted. The main task of this step is the reduction of the data in order to reduce the needed storage. From this step on the users analysis takes place.

Within Athena there are two fast methods to create simulated data, both illustrated in Figure 4.2. AtlFast [89] is a very fast one, which takes the four-vectors of the generated HepMC particles and produces AODs by smearing. FatRas [80] is a more complex but nevertheless very fast alternative to the full simulation. In a first step FatRas generates

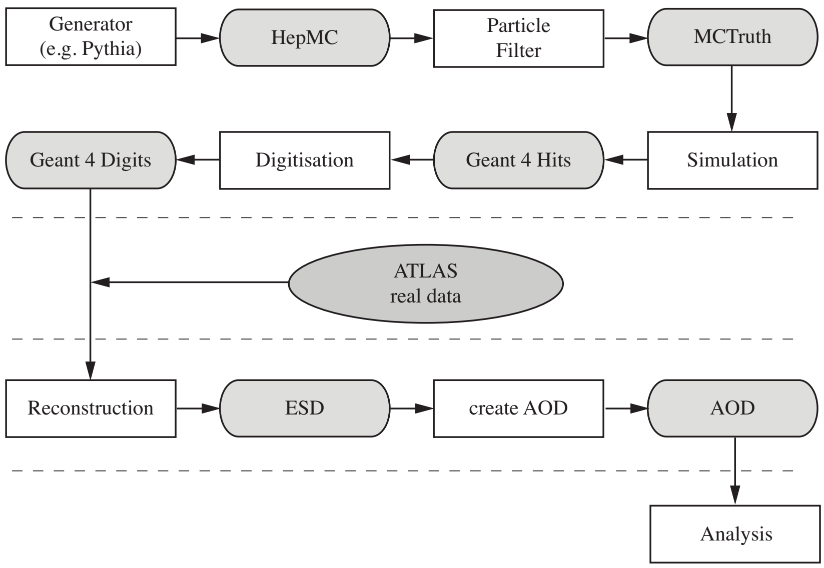

Figure 4.1: The simulation data flow in the ATLAS experiment. White rectangles represent processing stages, grey, rounded rectangles represent the data objects in the event data model. The event data model is separated by dashed lines in the upper most part, which corresponds to the event generation using Monte Carlo methods, the second part introduces real data from the ATLAS detector, the next part corresponds to the event generation and the very bottom part is the data analysis by the physicist. Figure adapted from [32].

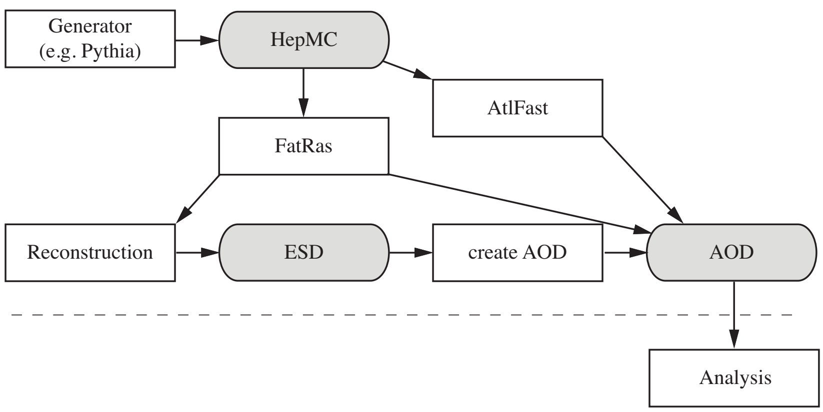

Figure 4.2: The fast simulation data flow in the ATLAS experiment. While the FatRas program can produce both, ESDs and AODs, the AtlFast directly produces AODs.

tracks out from the Monte Carlo data and applies material effects, particle decays, photon conversions and the digitisation in a fast, statistical approach. However, as the simulated data in this thesis is produced by the full simulation and reconstruction chain, the fast simulation methods AtlFast and FatRas will not be explained in detail.

4.1.1 Event Generation

The first step in the queue of data simulation is the Monte Carlo event generation. Its aim is the production of data samples by calculating physics processes from hadron hadron collisions as already described in Chapter 2.2.1. In this process the collision of two protons is simulated, the particles created in the hard process and in the underlying event are generated and the complicated mechanisms of hadronisation and decay take place. In order to precisely describe such a collision, perturbative and non-perturbative effects have to be taken into account. All those elements can be performed by complex Monte Carlo programs[3], simulating all physical processes so far known, based on the knowledge of previous experiments. A more detailed review on Monte Carlo programs can be found in [138].

The structure of a typical proton-proton collision is shown in Figure 4.3. The production process can be divided into several stages, shortly described in the following.

The interaction in proton-proton collisions is governed by the interaction of its constituents, the so called partons (gluons and quarks). It can be assumed, that one parton of type i interacts with another parton of type j from the other proton in a hard process with a high four-momentum transfer Q^2. Then based on the underlying theory the partonic cross section $\hat{\sigma}_{ij}$ for the scattering of two partons is calculated by the matrix elements for each specific partonic process. However, as the result strongly depends on the initial conditions of the partons, the partonic cross section has to be convoluted with the probability to find a parton with a momentum fraction x of the total proton momentum, the so called parton distribution functions (PDFs) $f(x, Q^2)$. The cross section of a process $p + p \to a + X$, where the particle a is produced in the partonic hard interaction and X denotes the debris of the collision, has to be associated to a partonic cross section $\hat{\sigma}_{ij\to a}$. The cross section then can be written as

$$\sigma_{pp\to aX} = \sum_{ij} \int_0^1 dx_1 \int_0^1 dx_2 f_i(x_1, Q^2) f_j(x_2, Q^2) \hat{\sigma}_{ij\to a}, \tag{4.1}$$

[3]These programs often are referred to as Monte Carlo generators.

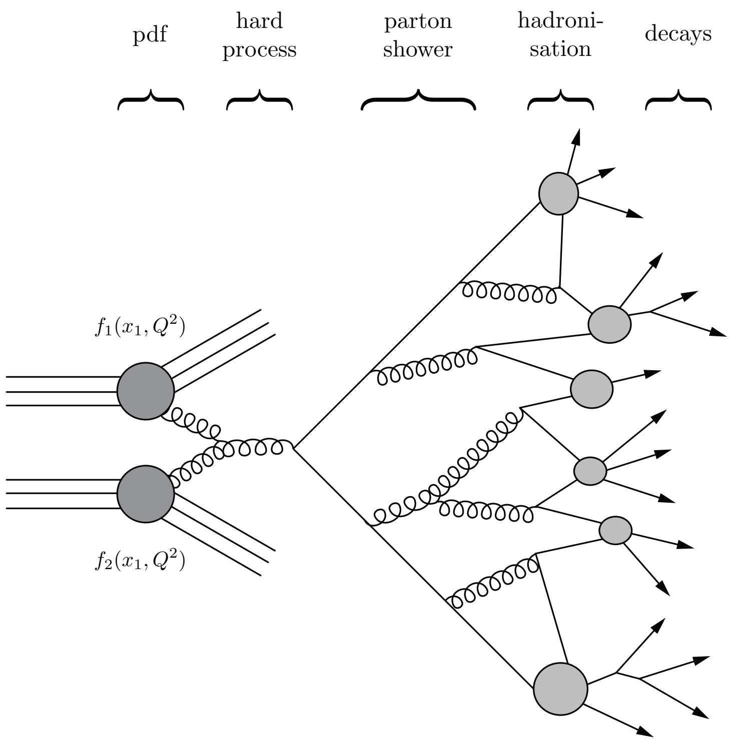

Figure 4.3: Proton-proton collision generated by Monte Carlo program like PYTHIA. Starting from left, the generator calculates the proton proton collision using the PDFs, does the hard process and the underlying event. In the middle the parton shower evolves, the partons hadronise and finally the particles decay into stable particles.

where the sum denotes all possible initial partons i and j, whose interaction could produce the final state particle a. In the case of Figure 4.3 one specific process $gg \to g$ illustrates the partonic process.

The collision of partons leads to an acceleration of colour charges, hence, like in Electrodynamics, radiation of gluons through QCD bremsstrahlung has to occur. Incoming partons produce initial state radiation ISR, outgoing partons final state radiation FSR, both resulting in a cascade of partons or a parton shower. The correct approach of calculating matrix-elements order by order in α_s could be used, however under LHC conditions the calculations become arbitrary difficult. For proton proton collisions the common method is to separate the whole process into the hard process, calculated by matrix elements, and describing the parton shower as a series of bremsstrahlung emissions or branchings of the type $q \to qg$, $g \to gg$ or $g \to q\bar{q}$.

As the partons move apart, the strong force between them rises, leading to further emissions, until they reach the regime of confinement, where they cannot be seen as free particles anymore. The partons assemble together to build hadrons. This process is either called hadronisation or fragmentation. This step is not fully understood from first principle due to the highly non-perturbative strong interaction at long distances. However, various phenomenological models, as e.g. the Lund string model [17], describe the fragmentation. These models are tuned by using experimental measurements.

In a proton proton collision the hard process is accompanied by additional parton remnants, possibly undergoing additional hard interactions leading to multiple interactions (MI) as described in [140]. They in turn undergo further ISR and FSR. The remnants not undergoing MIs are linked by their colour charges, leading to further parton showers and hadrons. All those particles together build the so called underlying event. Since the transverse momenta of these particles are very low, the underlying event is produced by a non-perturbative process. Currently the underlying event can only be simulated by phenomenological models tuned to experimental input.

At this stage no more partons are present. In a last step the unstable particles produced in the hadronisation subsequently decay into stable (or pseudo-stable) particles. Particles are viewed as stable, provided that their lifetime lasts long enough to reach the first detector layers. Further decays within the detector (e.g. muons, kaons or pions) are handled by the process of detector simulation.

The large proton density in the LHC bunches leads to a non-negligible probability of multiple inelastic proton-proton interactions. The superposition of several proton collisions within one bunch crossing is called pile-up. However, the cross section for low p_T inelastic collisions, referred to as minimum bias events, is much larger than the cross section for hard scattering. Therefore the vast majority of proton collisions result in minimum bias events. In the first years of LHC running, at a low luminosity $\mathcal{L} = 10^{33}$ cm^{-2}s^{-1}, the average number of minimum bias events accompanying a hard process is expected to be about 2.3. At design luminosity of $\mathcal{L} = 10^{34}$ cm^{-2}s^{-1} this number increases to 23.

The full Monte Carlo information, starting from the initial protons, the hard process as well as the underlying event, the hadronisation and the decays are stored for further processing. For each particle in any process the type as well as the kinematic quantities are stored. For further processing the ancestry relation and position of their decays is stored too. This all together is called Monte Carlo truth information, providing a reliable tool for further studies of e.g. efficiencies or background.

A very convenient method to refine the selection of events is the method of particle filtering, thus reducing the number of events for the time-consuming detector simulation. As shown in Figure 4.1, this step takes place after the event generation. The Particle Filter searches through the Monte Carlo truth information for e.g. kinematic observables or particle types and filters events, that would not be selected in the final analysis in any way. As an example a Particle Filter could search for a decay including at least one muon with a certain minimum transverse momentum p_T.

In this thesis all simulated events are generated with the PYTHIA program [137, 139], one of the most common Monte Carlo generators used in High Energy physics. Dedicated heavy flavour B events can be produced within the ATHENA framework with the PYTHIAB interface [141], dedicated to the production of events containing B hadrons. Triggered by the absence of a $b\bar{b}$ pair in the hard scattering process the PYTHIAB interface can skip the event to reduce the long processing time of the parton shower, hadronisation and decay. Furthermore, by defining certain decay topologies the PYTHIAB interface also acts as a particle filter.

4.1.2 Detector Simulation

The output of the Monte Carlo generators cannot be used directly for performing a physics analysis, as detector effects, misalignment, acceptance or resolution are not included yet. The (pseudo-)stable particles have to undergo a detector simulation. The aim of the detector simulation is the production of events including all experimental effects, in order to get events comparable to real data events from the ATLAS detector.

In the detector simulation the particles trajectory through the detector and the interactions with the detector material are simulated. A detailed and accurate description of all active detector components, support structure and read-out electronics is crucial for this task as well as a realistic magnetic field map. In ATLAS the ATHENA package GEOMODEL passes any detailed information about the detector geometry to the detector simulation. Additional particles created through a particle decay or an interaction with the detector material knocking out further particles are added to the Monte Carlo truth information. The output of the detector simulation is written into so called *hit*-files, in which the energy deposited in the detector elements is stored.

In the case of ATLAS the detector simulation is performed by the GEANT4 toolkit [9, 91]. In GEANT4 a broad variety of interactions as e.g. decays, scattering, energy loss, bremsstrahlung etc. with the detector material are calculated by Monte Carlo methods.

The particle propagation within the detector is calculated by the use of transportation models based on macroscopic parametrisation.

4.1.3 Hit Digitisation

The energy deposits in all sub-detectors, created in the detector simulation, have to be translated into detailed detector signals. During the hit digitisation dead cells in the detector are considered, noise is injected and the front-end electronic behaviour is simulated. After this process the simulated data in principle looks identical to the real data produced in the detector. As the the simulated and real data have the same data format, further processing is identical. However, for detailed studies the Monte Carlo truth information still is available in the simulated data.

4.1.4 Event Reconstruction

The information, coming either from the detector as real data or as simulated events from the production chain described so far, has to be interpreted in order to identify physical objects. The ATLAS detector can identify a broad variety of different physical objects, such as charged tracks, electrons, photons, muons, jets or missing energy. Each of those objects has to be related to a four-momentum. One object without any detector signal is the so called missing transverse energy, which can be interpreted as to the appearance of neutrinos or supersymmetric particles.

In Chapter 3.3 an overview of the ATLAS detector has been presented. As shown in Figure 3.7, depending on the signals from the detector various types of particles can be identified. Charged particles, as muons, electrons and charged hadrons, leave tracks in the Inner Detector. The appearance of a track in the muon system associated with a track in the Inner Detector identifies the track as a muon candidate, whereas an energy deposit in the electromagnetic calorimeter with an associated track is an electron candidate.

The lack of hadron identification is one disadvantage of the ATLAS detector, especially for the B physics. As shown in Figure 4.4 the separation of kaons and pions is below 1σ. This has to be taken into account when reconstructing complicated decay topologies as e.g. $B_s^0 \to D_s^-(\phi\pi^-)\pi^+$ with $\phi \to K^+K^-$.

In this thesis the objects of major interest are muons and charged tracks, i.e. pions and kaons. Therefore in Chapter 4.1.4.1 the reconstruction of charged tracks, using the Inner Detector, is described. Chapter 4.1.4.2 is dedicated to the reconstruction of muons.

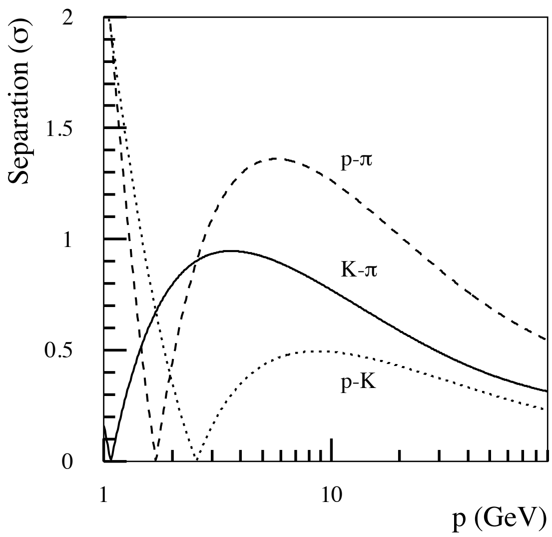

Figure 4.4: Study of the separation of $K - \pi$, $p - \pi$ and $p - K$ based on the energy loss dE/dx in the TRT as a function of the particle momentum. Figure taken from [30].

4.1.4.1 Track Reconstruction

The layout of the Inner Detector and its technical specifications have been described in detail in Chapter 3.5. The reconstruction of tracks is performed within the Athena framework by a modular package described in more details in [72]. In this section the main steps of the reconstruction are outlined. There exist two strategies for track finding: the main inside-out track reconstruction and the complementary outside-in tracking.

In the inside-out sequence, track seeds are found in all three Pixel layers and the innermost SCT layer. Within a window of search, defined through the initial track seed, additional hits in all Pixel and SCT layers are added or rejected, based on a simplified Kalman filtering method [90]. After resolving ambiguities, removing outlining measurements and rejecting fake track candidates, the remaining candidates are extended into the TRT, followed by a final refitting using the full track information.

The outside-in sequence starts with a global pattern recognition in the TRT. Tracks are built by extending these track segments into the SCT and Pixel detector. With this second approach tracks produced by particles coming from secondary vertices inside the Inner Detector Volume can be reconstructed.

The charged tracks are parametrised by its trajectory, defined at its closest point to the interaction point in the transverse plane as illustrated in Figure 4.5. The trajectory is parametrised by its impact parameters d_0 and z_0, the distance to the interaction point in the transverse $x-y$ plane and longitudinal in z direction, respectively. Furthermore the trajectory is parametrised by the tracks momentum, typically p (or $1/p$), the azimuthal angle ϕ and the polar angle θ. To distinguish between positively and negatively charged track candidates, the inverse momentum is usually multiplied by the track charge, leading to the momentum representation q/p.

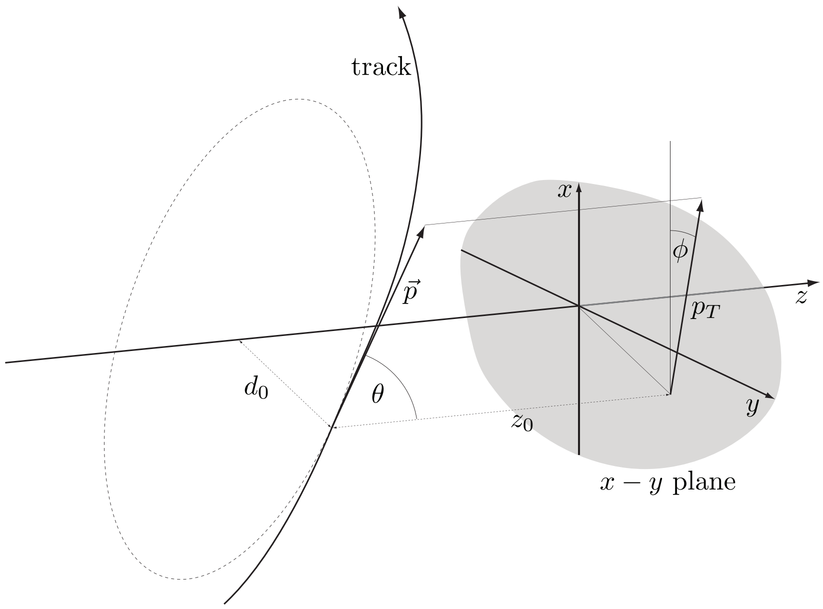

Figure 4.5: Parametrisation of a Track, where the z-axis is defined by the beam axis. The momentum vector at the point of closest approach is projected into the $x-y$ plane in order to visualise the transverse momentum p_T and the angle ϕ. Figure adapted from [72].

In Figure 4.6 the track reconstruction efficiency of pions, muons and electrons is shown as a function of the pseudo-rapidity $|\eta|$. As pions undergo hadronic interactions with the detector material and electrons suffer from Bremsstrahlung, the reconstruction efficiency decreases with $|\eta|$. Muons can be reconstructed with a very high efficiency over the range of pseudo-rapidity up to $|\eta < 2.5|$.

4.1.4.2 Muon Reconstruction

The muon reconstruction can be separated into two families, corresponding to their algorithms, Staco [97] and Muid [114]. In this thesis the default reconstruction algorithm used is Staco.

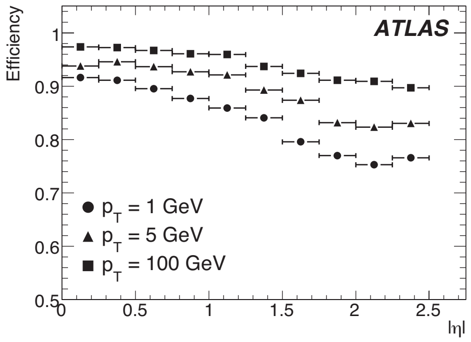

(a)

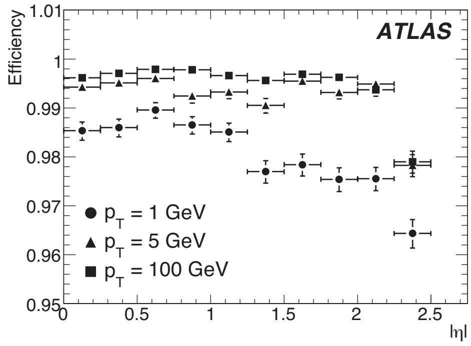

(b)

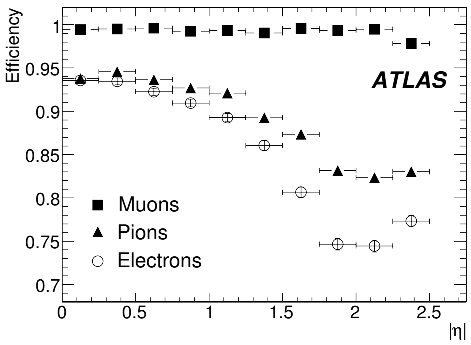

(c)

Figure 4.6: Track reconstruction efficiencies as a function of $|\eta|$ for isolated pions (a) and muons (b) with transverse momenta $p_T = 1$, 5 and 100 GeV, and for muons, pions and electrons at $p_T = 5$ GeV in (c). Notice the different scales on the y-axis. Figures taken from [34].

Beside the algorithm, the reconstruction of muons can be done by a variety of strategies. Making use of the huge Muon System, *standalone* muons can be reconstructed by building tracks from the hits in the muon chambers and extrapolating those tracks to the beam pipe. The matching of standalone muon tracks with nearby tracks in the Inner Detector leads to *combined* muons. *Tagged* muons are found by extrapolating tracks from the Inner Detector to the Muon System, searching for hits not used by standalone reconstruction. This strategy primarily aims at muons with a low transverse momentum, not reaching the very outer layers of the Muon System.

The reconstruction of *standalone* muons in principle is illustrated in Figure 3.18. In each of the three muon stations a track segment is built. They are linked together and the muon track candidate is extrapolated to the beam pipe. In ATLAS two different standalone muon reconstruction algorithms are used: MOORE [7] used by MUID and MUONBOY [87] used by STACO. Multiple scattering and energy loss in the calorimeter have to be taken into account when extrapolating the muon tracks to the beam line. This has been e.g. implemented in the MUID reconstruction [127].

Both algorithms, STACO and MUID, can match standalone muons with tracks from the Inner Detector, in order to find *combined* muons. The combination of the two tracks is done by minimising χ^2 defined as [34]

$$\chi^2 = (\mathbf{T}_{MS} - \mathbf{T}_{ID})^T \cdot (\mathbf{C}_{MS} + \mathbf{C}_{ID})^{-1} \cdot (\mathbf{T}_{MS} - \mathbf{T}_{ID}), \tag{4.2}$$

where $\mathbf{T}$ denotes the vector of the five track parameters and $\mathbf{C}$ is the covariance matrix of the tracks from the Muon System MS or from the Inner Detector ID, respectively. This fit tests, if the two tracks are compatible with each other. Subsequently the two tracks are combined by a statistical re-weighting. Combined muon tracks have a significantly smaller rate of fake muons from punch-through particles, produced by kaons and pions in the calorimeter [133].

The propagation of Inner Detector tracks to the Muon System and the subsequent search for unused hits leads to *tagged* muons. Two possible algorithms use either a χ^2 based method [97], using the distance between the hit and the extrapolated track, or a method based on an artificial neural network, defining a discriminant [143]. If an Inner Detector track has found an associated hit in the Muon System, the track consequently is tagged as a muon.

4.1.5 Further Data Processing

In the previous steps the Monte Carlo events have been processed from RAW files corresponding to the detector output to Event Summary Data ESD. While in the RAW format the average file size is approximately 1.6 MByte per event the reconstructed event has a size of 0.5 MByte per event in the ESD format. ESDs are stored in an object oriented POOL ROOT file, accessible via the ROOT software [58].

However, as barely any physics analysis takes into account all event information, the size can be reduced by omitting objects uninteresting for the specific physics analysis. In this post-processing step the file size can be reduced to a size of $\mathcal{O}(100$ kByte$)$ per event in the Analysis Object Data format AOD in the POOL ROOT format. In order to provide a fast method for identifying real data events, event-level metadata TAG contains thumbnail information stored in a relational database at a tiny size of approximately 1 kByte per event.

For a fast physics analysis on very dedicated physics object the AOD data can be further reduced by creating Derived Physics Data DPD. Undergoing three steps, in the first a filter selects only the events of interest (skimming), in the second only the objects of interest are written out (thinning) and in the last step unneeded properties of the saved objects are removed (slimming). The DPDs are saved in n-tuples for analysis and histogramming using ROOT.

4.2 ATLAS Computing

4.2.1 The Worldwide LHC Computing Grid

As already described in Chapter 3.10, the output of the Event Filter EF has a rate of approximately 320 MByte per second, delivering an estimated annual amount of 3.2 PByte. The data processing, corresponding to the ATLAS Computing Model described in Chapter 4.1, is carried out by the hierarchical structured Worldwide LHC Computing Grid WLCG. The data flow and the tasks of the first three layers of computing centres are illustrated in Figure 4.7.

The RAW data is stored in the CASTOR system in the Tier-0 at CERN. One additional backup is stored in one Tier-1. The reconstruction process described in 4.1.4 is performed in a first instance in the Tier-0. The ESD data is stored in the Tier-0 centre, and two more copies are transferred to Tier-1 centres. In a second instance, the RAW data is re-processed in the Tier-1 centres.

The data produced in further processing corresponding to Chapter 4.1.5 results in AODs archived in the Tier-0 and copied to all Tier-1 centres. The AODs are shared between the Tier-2 centres for the users physics analysis. Likewise the metadata TAG is stored in the Tier-0 and in all Tier-1 centres, but no copy is sent to any Tier-2.

The production of Monte Carlo simulated events as well as the users physics analysis mainly is carried out by the Tier-2 centres. The data produced will be copied to the Tier-1 centres for permanent storage.

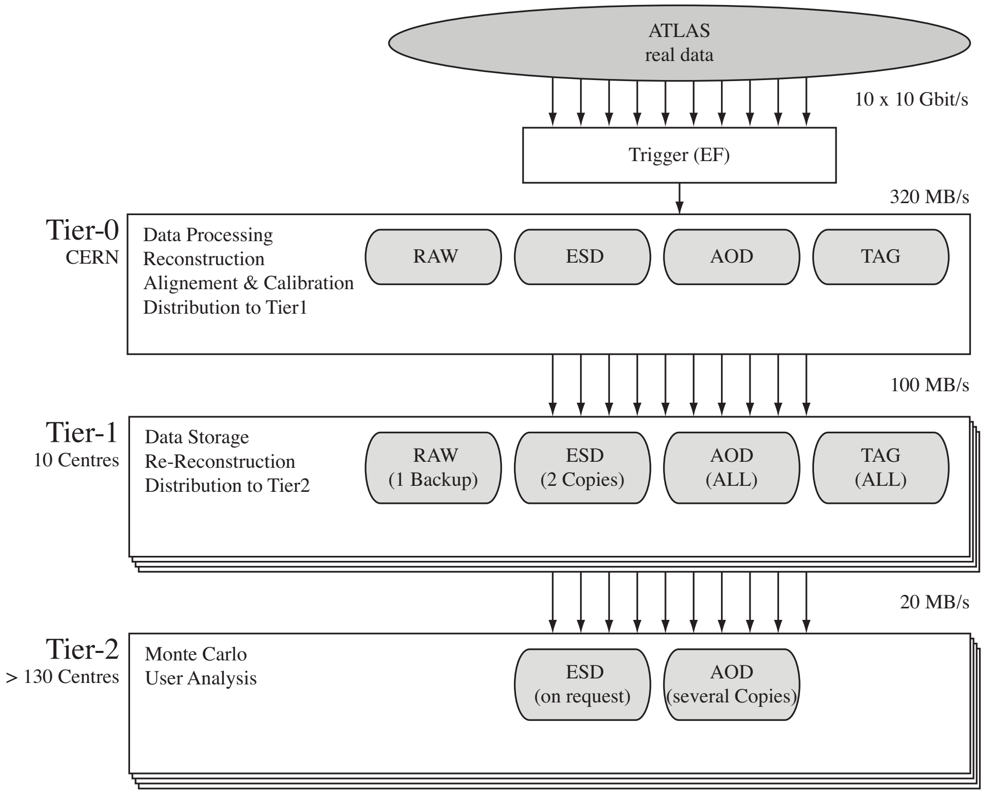

Figure 4.7: Hierarchical Tier structure of the WLCG, illustrating the tasks of the individual layers, the stored data objects and the data flow.

4.2.2 Software Tools

The primary software for any ATLAS related task is the modular Athena framework, handling both real and simulated data. Within the Athena framework Monte Carlo production (Pythia), reconstruction of events (e.g. tracking, vertexing, B tagging of jet finding) as well as the users analysis take place. Integrated into Athena n-tuples containing condensed event information can be analysed with Root [58], a C++ based modular data analysis software.

For the well structured event simulation as well as for the data analysis Grid resources can be used by using distributed analysis tools. The main tools are Ganga [123] and pAthena [74]. Any dataset stored within the Grid and registered to the database can be searched by using the AMI [37] database, the data is managed by DQ2 [56] and therefore can be retrieved by using DQ2 tools.

CHAPTER

FIVE

Flavour Tagging Methods

In this chapter, first the observables relevant for flavour tagging like wrong tag fraction, tagging efficiency or dilution will be discussed in Section 5.1. In Section 5.2 the various methods of tagging the initial flavour of a B meson will be explained.

5.1 Flavour Tagging Observables

5.1.1 Efficiency, Dilution, Wrong Tag Fraction

Given is a sample of N decays, in which a neutral B_q^0 meson decays into some decay channel. As these particles are subject to oscillations, the initial state at production time and the final state at decay time may differ. The final state of the B meson is reconstructed by analysing the decay products, the initial flavour is determined by flavour tagging methods. If the initial state is identical to the final state, the events are denoted as A, if the two states differ the events are denoted as B. The relation of the true number of events of both kinds can be described by the asymmetry

$$A_{true} = \frac{N_A - N_B}{N_A + N_B}, \tag{5.1}$$

where N_A and N_B are the number of events of type A or B, with $N = N_A + N_B$. The measurement of the two states can be performed with a finite efficiency, leading to a measured asymmetry of

$$A_{meas} = \frac{n_a - n_b}{n_a + n_b}, \tag{5.2}$$

where n_a and n_b are the numbers of events flavour tagged as type a and b, resepectively.

Depending on the flavour tagging method, the probability of tagging an event is described by the *tagging efficiency.* Applying the flavour tagging method to the sample, the tagging efficiency has to be measured and is written as

$$\varepsilon = \frac{n_a + n_b}{N_A + N_B}. \tag{5.3}$$

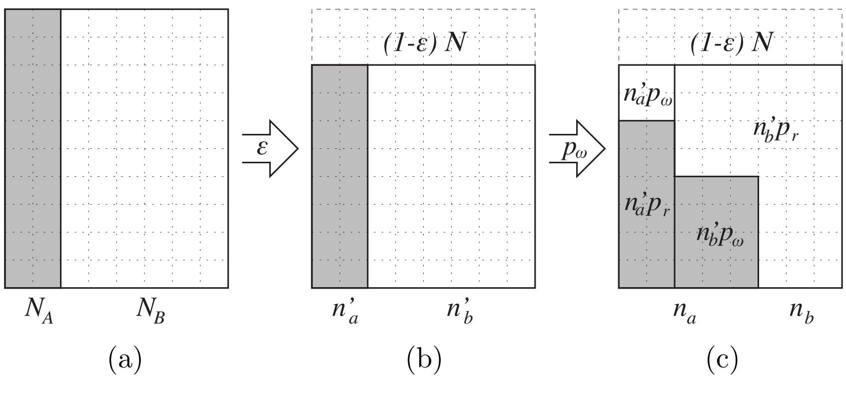

Figure 5.1: Illustration of the flavour tagging process: the true number of events of type a and b N_A and N_B illustrated in (a), with $N_A + N_B = N$ the total number of events are tagged with a tagging efficiency ε, leading to a measured sample of $n'_a + n'_b$ events (b). The measurement leads to a diluted number of events n_a and n_b, where the real and measured numbers of events are related via the wrong tag and right tag fraction P_w and P_r (c).

However, in a flavour tagging measurement there is a non-negligible probability of assigning the wrong flavour to a given event. Therefore, the number of measured events n_a and n_b does not directly reflect the initial true number of events N_A and N_B. As shown in Figure 5.1 (a) and (b), the true number of events of type n'_a and n'_b can be measured with the efficiency ε. Due to symmetry reasons it can be assumend, that the tagging efficiency is the same for both types of events. Therefore, we can write the real number of measured events as

$$n'_a = \varepsilon N_A \text{ and} \tag{5.4}$$

$$n'_b = \varepsilon N_B. \tag{5.5}$$

Events of type a can be either tagged correctly with a probabily of P_r (right sign tag) or incorrect with a probability of $P_w = 1 - P_r$ (mistag, *wrong tag fraction*). Consequently, the measured number of events n_a and n_b can be written as a combination the real number of events of type a and b:

$$n_a = P_r n'_a + P_w n'_b \tag{5.6}$$

$$n_b = P_r n'_b + P_w n'_a \tag{5.7}$$

By substituting the Equations (5.6) and (5.7) into the measured asymmetry (5.2), one obtains

$$A_{meas} = \frac{(P_r n'_a + P_w n'_b) - (P_r n'_b + P_w n'_a)}{n_a + n_b}. \tag{5.8}$$

Using the definitions of ε (5.3) and above assumptions on the real number of measured events (5.4) and (5.5), this equation becomes

$$A_{meas} = \frac{\varepsilon N_A (P_r - P_w) - \varepsilon N_B (P_r - P_w)}{\varepsilon (N_A + N_B)}. \tag{5.9}$$

The efficiency ε cancels out and finally leads to a relation between the true and the measured asymmetry:

$$A_{meas} = (P_r - P_w) \cdot \frac{N_A - N_B}{N_A + N_B} = D \cdot A_{true} \tag{5.10}$$

with

$$D = P_r - P_w = 1 - 2P_w, \tag{5.11}$$

the so called *dilution*. Apparently, as shown in Equation (5.10), a good flavour tagging method has a dilution close to one, poor flavour tagging methods close to zero. Consequently, as illustrated in the relation between dilution D and wrong tag fraction P_w in Equation (5.11), a good tagger has a low wrong tag fraction close to zero, a poor flavour tagger has $P_w \approx 0.5$.

5.1.2 Statistical Uncertainty and Tagging Power

Calculating the variance of A_{true} (in these calculations written shortly as A), the dilution D, the tagging efficiency ε, the total number of tagged events, $n := n_a + n_b = \varepsilon N$ and consequently the number of events before the tagging N can be seen as constant. Therefore the probability of tagging n_a events as type a out of n follows a binomial distribution. The probability of measuring an event of type a is given by

$$P_a = \frac{n_a}{n} = \frac{1 + AD}{2}. \tag{5.12}$$

The binomial distribution [45, 73] of measuring n_a events out of a sample of n events with a given probability of P_a is given by the probability function

$$\mathrm{P}(n_a; P_a, n) = \mathrm{P}\left(n_a; \frac{1 + AD}{2}, \varepsilon N\right). \tag{5.13}$$

Therefore the expectation value to measure n_a events can be written as

$$\mathrm{E}(n_a) = \varepsilon N \cdot \frac{1 + AD}{2} \tag{5.14}$$

and the variance as

$$\begin{aligned} \mathrm{Var}(n_a) &= \varepsilon N \cdot \frac{1 + AD}{2} \cdot \frac{1 - AD}{2} = \\ &= \varepsilon N \cdot \frac{1 - A^2 D^2}{4}. \end{aligned} \tag{5.15}$$

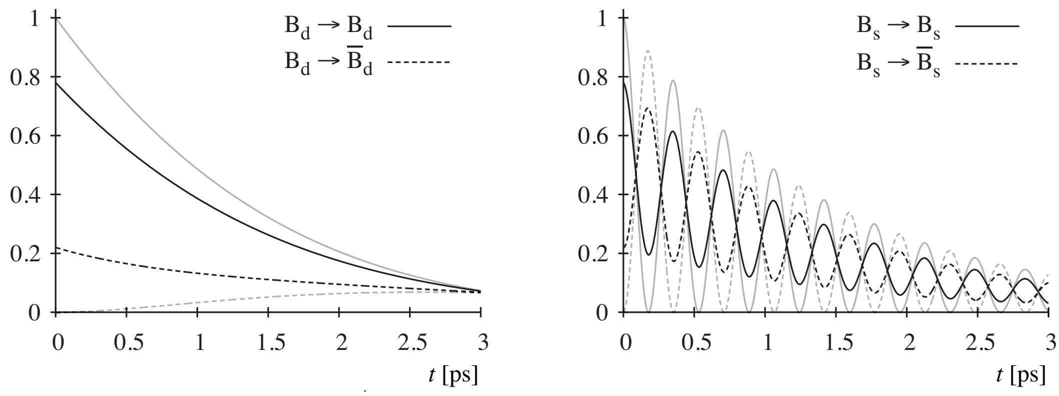

(a) (b)

Figure 5.2: In light grey the time dependent probability is shown, that an initial flavour eigenstate B_q^0 meson decays as B_q^0 (solid lines) or its anti-particle, $\bar{B}_q^0$ (dashed lines). Assuming a flavour tagging method with a dilution of $D = 0.56$, the measured time dependent probability is displayed in black. In (a) the oscillation of B_d^0 mesons is shown, in (b) of B_s^0 mesons.

In addition, the maximum likelihood method shows, that the arithmetical mean $\mathrm{E}(n_a) = P_a \cdot n$ is a minimum variance estimator with the variance $\mathrm{Var}(n_a) = n \cdot P_a \cdot (1 - P_a)$, leading to the same result as in the Equations 5.14 and 5.15 [57].

Rewriting the true asymmetry A_{true} from Equation (5.10), and using $\mathrm{Var}(n_a)$ from Equation (5.14) one can calculate the variance of A_{true}:

$$\begin{aligned} \mathrm{Var}(A_{true}) &= \mathrm{Var}\left(\frac{n_a - n_b}{n_a + n_b} \cdot \frac{1}{D}\right) \\ &= \frac{4}{\varepsilon^2 D^2 N^2} \mathrm{Var}(n_a) \\ &= \frac{1 - A^2 D^2}{\varepsilon D^2 N}, \end{aligned} \tag{5.16}$$

giving the final statistical uncertainty of A_{true}

$$\sigma_A = \sqrt{\frac{1 - A^2 D^2}{\varepsilon D^2 N}}. \tag{5.17}$$

As σ_A is proportional to $1/\sqrt{\varepsilon D^2}$, εD^2 determines the statistical power of a flavour tagging method and therefore is called *tagging power*. The primary goal of a good flavour tagging method is the optimisation of εD^2.

The effect of dilution in flavour tagging becomes obvious in Figure 5.2, where the number of tagged B_q^0 and $\bar{B}_q^0$ mesons is shown for the two neutral B mesons, B_d^0 and B_s^0. In this figure the initially pure B_q^0 sample is wrong tagged with a probability of $P_w = 0.22$, corresponding to a dilution of $D = 0.56$. Starting only with B_q^0 mesons, the number of events tagged as B_q^0 or $\bar{B}_q^0$ is proportional to:

$$N_{B_q^0} \sim e^{-\Gamma t}(1 + D \cdot \cos(\Delta m_q t)) \text{ and} \tag{5.18}$$

$$N_{\bar{B}_q^0} \sim e^{-\Gamma t}(1 - D \cdot \cos(\Delta m_q t)). \tag{5.19}$$

Beside dilution due to the flavour tagging, additional smearing happens due to the proper time resolution in the reconstruction of the full B_q^0 decay.

For the measurement of oscillation the good knowledge of the dilution of a flavour tagger is crucial, in order to calculate the systematic uncertainties. The dependence of the dilution on kinematic variables in an event or the event shape has to be studied in detail.

In summary, flavour tagging can be described by the following variables:

Tagging Efficiency	...	probability of a successful flavour tag.
Wrong Tag Fraction	...	probability of a wrong flavour tag.
Dilution	...	asymmetry between correct and wrong tags, factor in the oscillating part of the time dependent probability distribution.
Tagging Power	...	statistical power of a flavour tagger.

5.2 Flavour Tagging Methods

At production time $t = t_0$ the initial flavour of a neutral B meson is given by the quark flavour of its b quark, mainly produced in a $b\bar{b}$ pair production process. Accordingly, the second b quark contains the opposite quark flavour. At first order this particle traverses into the opposite hemisphere of the detector with respect to the neutral B meson. Therefore these particles are referred to as *signal side* and *opposite side* B hadrons.

For measurements of neutral B mesons the flavour at production and at decay time are of interest. In the hadronic decay channels used to measure the oscillation frequency Δm_s, which are $B_s^0 \to D_s^-(\phi\pi^-)\pi^+$ and $B_s^0 \to D_s^-(\phi\pi^-)a_1^+$, the flavour at decay time easily can be reconstructed by the charges of the final state particles. As the neutral B meson is subject to B oscillation, its initial flavour cannot be identified directly by measuring the decay products. Instead of that the initial b quark content (b or $\bar{b}$) can be determined by analysing the opposite side B hadron produced together with the neutral B meson. Methods tagging the initial flavour by utilising the opposite side hadron are called *Opposite Side Flavour Tagging*, detailed in Section 5.2.1. These methods correspond to the measurement of a signature in the lower half of Figure 5.3. Alternatively, it is possible to draw conclusion about the initial b content by analysing particles produced adjacent to the neutral B meson, leading to some methods of *Signal Side Flavour Tagging*, highlighted in Section 5.2.3. Some examples are illustrated in the upper half of Figure 5.3. Despite in this thesis the main emphasis is on opposite side soft lepton flavour tagging, all possible

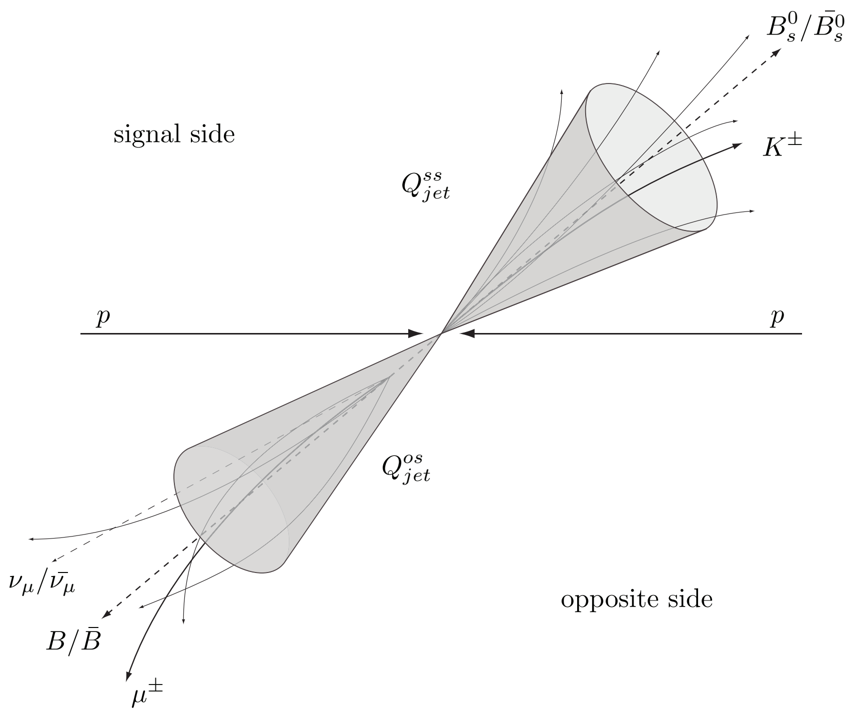

Figure 5.3: Topology of a B_s^0 event. The dashed B_s^0 meson on the signal side builds a jet, vice versa on the opposite side the associated B hadron from the initial $b\bar{b}$ pair. Possible flavour tagging methods illustrated are the measurement of the jet charge Q_{jet} on both sides, same side Kaon tagging ($K^\pm$) and opposite side soft lepton tagging ($\mu^\pm$).

flavour tagging methods are described in the following sections.

5.2.1 Opposite Side Flavour Tagging

The perfect way of analysing the opposite side B hadron of course would be the full reconstruction of the exclusive decay channel, giving a stringent indicator on its B flavour content. However, as the ATLAS detector has a limited kaon/pion separation, in most cases the exclusive decay cannot be fully reconstructed. Therefore the determination of a tag depends on inclusive methods.

The most relevant inclusive method in hadronic B decays at ATLAS is the *opposite side soft lepton tagging*, using the charge of a soft muon as flavour tag as illustrated in Figure 5.4. As described in more detail in Chapter 6, hadronic B events are triggered by a muon trigger, where the opposite side B hadron is supposed to decay semi-leptonically, producing a muon. The charge of the muon is defined by the flavour of the b quark. Assuming a composition of hadrons, as shown in Table 2.3, the inclusive branching fraction for $B \to \mu^- \bar{\nu}_\mu X$ has been measured to be $(10.95^{+0.29}_{-0.25})\%$. Alternatively to muons electrons can be used to determine the B flavour.

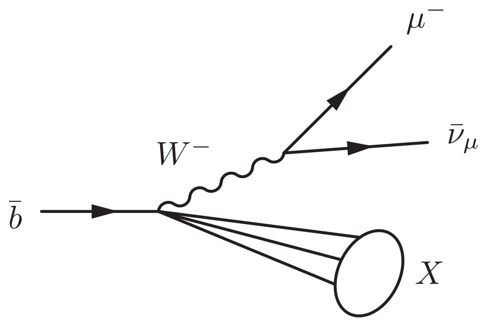

Figure 5.4: Illustration of a semi-leptonic decay of a $\bar{b}$ quark, resulting in a μ^-, $\bar{\nu}_\mu$ and some hadrons X.

The cascade decay of the opposite side B hadron can be further exploited in opposite side kaon tagging. A B hadron containing a $\bar{b}$ quark is favoured to decay into a particle containing a $\bar{c}$ quark, which in succession decays into a strange particle. Correspondingly, a $\bar{b}$ hadron leads more likely to a final state K^+/K^0, whereas a b hadron leads to a final state $K^-/\bar{K}^0$. However, as the ATLAS detector is lacking a sufficient kaon/pion separation, the only possible approach is the tagging via the resonance $K^*(892) \to K\pi$ and assuming kaon and pion mass on the final state particles.

Instead of looking at the cascade decay of a B hadron, analysing the particles produced together with the opposite side B also leads to a possible flavour tag. As illustrated in Figure 5.5, in the fragmentation process the additional quarks come in pairs with corresponding anti-quarks, from which various final state particles can emerge in the hadronisation process. In the case of neutral B mesons positively charged pions or kaons are likely to be produced. In the case of charged B mesons the adjacent particles more likely have a negative charge. By calculating the weighted sum of all track charges within a B jet, the correlation of the initial B flavour and the jet charge can be utilised to perform an *opposite side jet charge tag*.

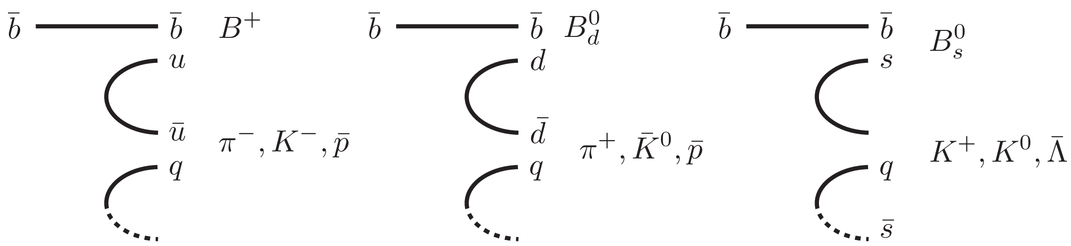

Figure 5.5: Some possible particles produced adjacent to various B mesons in the fragmentation process.

If the opposite side B hadron is a charged meson, instead of a full reconstruction a possible simplified method is the measurement of the opposite side vertex charge. A positive B charge corresponds to a $\bar{b}$ quark and a negative to a b quark, providing a *vertex charge tag*.

5.2.2 Opposite Side Meson Mixing

Obviously, as the opposite side B hadron could be neutral and consequently oscillate itself, the B flavour cannot be identified definitely. In Table 2.3 the fractions of B hadrons produced in $p\bar{p}$ collisions are shown, i.e. B_s^0 in $f_s = (11.0 \pm 1.2)$ % and B^0 in $f_d = (39.9 \pm 1.1)$ % of all cases. Altogether approximately 50% of the B hadrons are subject to flavour oscillation. The time integrated probability of an initial B hadron to be measured in a mixed state is defined as

$$\bar{\chi} = f_d \chi_d + f_s \chi_s, \tag{5.20}$$

where χ_d and χ_s are the time integrated mixing probabilities for B_d^0 and B_s^0, respectively. The combination $\bar{\chi}$ has been measured at LEP in $Z^0 \to b\bar{b}$ events ($\bar{\chi} = 0.1259 \pm 0.0042$ [14]) and at Tevatron in $p\bar{p}$ collisions ($\bar{\chi} = 0.147 \pm 0.011$ [64, 75]), separately. The 1.8 σ difference between these results can be considered as a hint, that the fractions might vary between Z decays and $p\bar{p}$. In simulations estimating the wrong tag fraction using the opposite side, the time integrated mixing probability has to be considered.

5.2.3 Same Side Flavour Tagging

In the case of same side flavour tagging the initial B flavour cannot be determined by analysing the decay fragments. One fully relies on two methods already described for the opposite side case.

First, in the case of a *same side jet charge tagger*, a jet is built around the signal B meson and the weighted jet charge is built. This flavour tagger has been intensively studied in [34] for the decay channels $B_s^0 \to J/\psi\phi$ and $B_d^0 J/\psi K^{0*}$.

Second, measuring the decay of the resonance $K^*(892) \to K\pi$ could be used to determine the initial flavour of a neutral B_s^0 meson. Due to the resonance character of the $K^*(892)$ meson this flavour tagging method can be used in the ATLAS experiment despite its limited kaon/pion separation.

CHAPTER

SIX

Trigger

The large rate of proton proton collisions at the LHC and the huge number of signal channels in the ATLAS detector makes it inevitable to select the events of physics interest out of the massive QCD background properly. The ATLAS trigger system dedicated to this selection has been described briefly in Section 3.9. In this chapter the trigger strategies relevant for the measurement of B events, especially hadronic decay channels, will be discussed.

In Section 6.1 the general strategy for the B physics trigger, with special emphasis on the hadronic decay channels $B_s^0 \to D_s^-(\phi\pi^-)\pi^+$ and $B_s^0 \to D_s^-(\phi\pi^-)a_1^+$ is given. In Section 6.2 various trigger scenarios are evaluated by using Monte Carlo information, as published in [107].

6.1 Triggering B events

Regarding the maximum trigger bandwidth, a flexible trigger strategy is crucial for the successful measurement of interesting events. As ATLAS is a multi-purpose experiment,

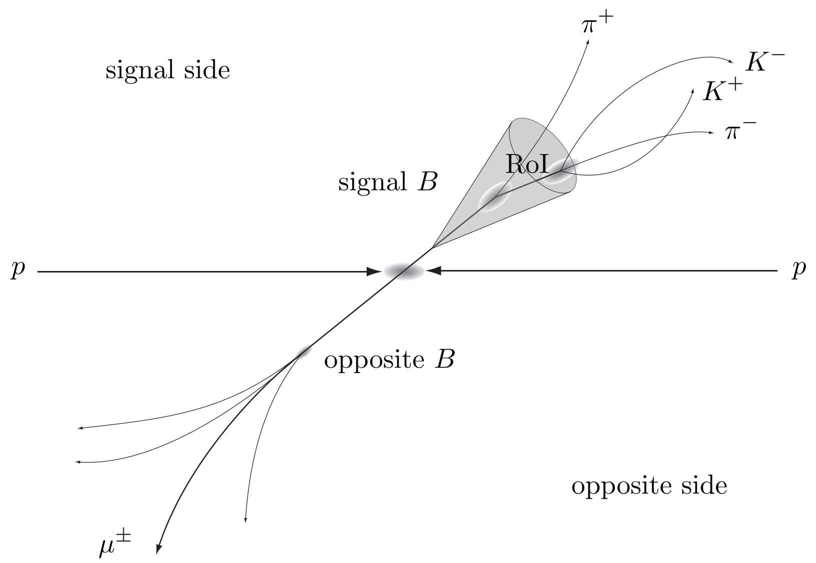

Figure 6.1: Illustration of the strategy to measure events of the type $B_s^0 \to D_s^- \pi^+$. At LVL1 the trigger is based on the semi-leptonic decay of the second B hadron, in particular the resulting muon. At LVL2 and EF the muon trigger will be confirmed and the decay topology $D_s \to \phi(K^+K^-)\pi$ is searched either by using the full information of the Inner Detector (Full Scan method) or alternatively within a Region of Interest (RoI) seeded by a jet trigger.

the various trigger strategies for all different kinds of searches is limited. In particular, with increasing luminosity the large production cross section of background events would lead to a large rate of uninteresting events, by far exceeding the capacity of the trigger system. With a good trigger strategy signal events are selected with a high efficiency, while background events are strongly suppressed. Out of the given list of all possible triggers an appropriate selection has to be made at LVL1 in order to preselect interesting events with high efficiency and a reasonable purity. Considering the LVL2 trigger and the EF one additional constraint is the minimisation of computing time per event.

In the following the trigger strategy for the measurement of hadronic decay channels (i.e. $B_s^0 \to D_s^-(\phi\pi^-)\pi^+$ and $B_s^0 \to D_s^-(\phi\pi^-)a_1^+$) will be discussed.

6.1.1 First Level Trigger

The LVL1 trigger uses the fact that at the LHC heavy flavour B hadrons originate primarily from $b\bar{b}$ pair production, as discussed in 2.2.2. The two resulting B hadrons are classified as the *signal side B hadron*, decaying into the signal decay channel of interest, whereas the second B hadron is called the *opposite side B hadron*. At LVL1 a muon from a semi-leptonic b decay on the opposite side is required, as illustrated in Figure 6.1. As discussed in Chapter 3.9.1, the LVL1 muon trigger can be classified in three low-p_T and three high-p_T muon triggers. Depending on the cut on p_T the corresponding LVL1 muon triggers are named e.g. `MU06` for muons with $p_T > 6$ GeV. For a maximum efficiency the p_T cut should be as low as possible.

In addition the hadronic signal decay channel is triggered by the hadronic LVL1 trigger defining Regions of Interest (RoIs) for further processing in the subsequent trigger stages. The electromagnetic and hadronic trigger towers have a granularity $\Delta\phi \times \Delta\eta$ of approximately 0.1×0.1 (see 3.9.1). The jet trigger algorithm builds clusters of 4×4 towers, corresponding to a size of $\Delta\phi \times \Delta\eta = 0.4 \times 0.4$, and searches for RoIs in which the transverse energy E_T is a local maximum and the transverse energy deposited in the cluster passes some required threshold cuts.

6.1.2 High Level Trigger

At the LVL2 stage the trigger muons found at LVL1 are confirmed by a more precise muon momentum measurement. Taking into account the information from the precision muon chambers, the fast LVL2 muon algorithm MuFast [105] reconstructs the muon tracks. By comparing η, ϕ and the sagitta of the muons with a lookup table a quick estimation of p_T can be performed.

By this time all the signals from the Inner Detector are available. The tracks from the Inner Detector are combined with the signals from the Muon System by the MuComb algorithm [105]. This step helps to improve the measurement of the momentum and increases the rejection of decaying kaons and pions as well as fake muon tracks created e.g. by cavern background or by punch through particles.

At the Event Filter stage the p_T of the muons seeded by the LVL2 muon trigger is determined using the TrigMOORE algorithm. This algorithm is based on the MOORE algorithm [7], also used in the Muid muon reconstruction as described in 4.1.4.2.

The triggering of the hadronic decay channels used in this thesis is implemented by reconstructing the decays $D_s^\pm \to \phi(K^+K^-)\pi^\pm$. As this decay channel is common for both decays $B_s^0 \to D_s^-(\phi\pi^-)\pi^+$ and $B_s^0 \to D_s^-(\phi\pi^-)a_1^+$, this `DsPhiPi` trigger can be used for both channels.

The `DsPhiPi` trigger first searches for ϕ candidates by combining to tracks reconstructed with the fast IDSCAN algorithm [43]. The two tracks are required to have opposite sign tracks and a $p_T > 1.4$ GeV each. The track pairs are considered as ϕ candidates if they fulfil kinematic cuts as $|\Delta z| < 3$ mm, $|\Delta\phi| < 0.2$, $|\Delta\eta| < 0.2$ and the pair mass is close to the ϕ mass, $1005 \text{ MeV} < M_{KK} < 1035$ MeV. $\Delta\phi$ and $\Delta\eta$ are the difference in ϕ and η, Δz the difference of the longitudinal impact parameter of the two tracks. The ϕ mass is calculated using the K mass hypothesis for both tracks.

In the next step these ϕ candidates are combined with a third track to build a $D_s^\pm$ candidate. A cut of $1908 < M_{KK\pi} < 2028$ MeV is used on the mass of the $D_s^\pm$ candidates. The three tracks are combined using a fast vertexing algorithm. If at least one $D_s^\pm$ vertex in an event can be found, the event passes the LVL2 `DsPhiPi` trigger, the resulting trigger object is passed to the EF. For further reduction a χ^2 cut on the vertex may be applied for a reduction of the LVL2 output rate.

With increasing LHC luminosity the output rate of the `DsPhiPi` trigger has to be reduced. Therefore two different LVL2 trigger strategies can be used: the Full Scan (FS) method or the RoI-based method. In the Full Scan approach, favoured at low luminosities, the information of all the Inner Detector is used to reconstruct $D_s^\pm$ candidates. With increasing luminosity the computing time to perform a Full Scan is likely to exceed the maximum allowed processing time. Therefore the RoIs found in the LVL1 jet trigger are used as seeds to search for $D_s^\pm$ candidates in regions of $\Delta\phi \times \Delta\eta = 1.5 \times 1.5$ around the centre of the RoIs. As found in [34], the trigger strategy has to be changed at a luminosity of approximately $\mathcal{L} = (10^{32} - 10^{33})$ cm^{-2}s^{-1}. In order to further reduce the output rate a cut on the χ^2 of the $D_s^\pm$ vertex may be applied.

In the EF stage a similar $D_s^\pm$ strategy as at LVL2 is performed. Both, FS and RoI-guided modes, can be used in the EF. The same trigger signature as at LVL2 is used. However, due to the better track resolution the mass resolution is expected to improve.

6.1.3 Trigger Strategies

With increasing luminosity the output rate of the hadronic B triggers are likely to exceed the maximum bandwidth. Furthermore, the $b\bar{b}$ production cross section has not been measured for protons at the LHC collision energy. In order to trigger an adequately high number of interesting events, the trigger has to be very flexible to adapt to all possible scenarios. Several actions can be taken in order to keep the trigger rate sufficiently low:

- Increase the p_T cut of the single muon trigger.
- Implementation of a two muon trigger.
- Increase the E_T cut of the LVL1 jet trigger.
- Use the RoI-seeded `DsPhiPi` trigger instead of the Full Scan.
- Introduce tighter and additional cuts to the `DsPhiPi` trigger [4].
- Introduce a χ^2 cut in the vertexing at LVL2 and EF.
- Introduce a `BsDsPi` trigger.

One further possibility to decrease the trigger rate could be achieved by pre-scaling the `DsPhiPi` trigger. Instead of every triggered event just a fractional amount of events are chosen, therefore reducing the the number of signal and background events by the same factor.

6.2 Trigger Scenarios

6.2.1 Muon Trigger Scenarios

In this section various muon trigger scenarios are discussed, as published by the author in [107] and further detailed. All these scenarios could be directly implemented in the LVL1 trigger, reducing the trigger rate already at the first stage.

For this analysis 50 000 events of the hadronic decay channel $B_s^0 \to D_s^-(\phi\pi^-)\pi^+$ with $\phi \to K^+K^-$ are generated with Pythia. B^0 meson mixing is not implemented in the production process. In pp collisions at a centre-of-mass energy of $\sqrt{s} = 14$ TeV the $\bar{b}$ quark is forced to produce the corresponding decay channel. All final state particles from the decay channel are required to have a transverse momentum $p_T > 0.5$ GeV and a pseudo-rapidity $|\eta| < 2.5$. In addition for each event a muon with $p_T > 6$ GeV and $|\eta| < 2.5$ is required, which will be interpreted as the trigger muon. All further muons have no conditions on p_T and η. For the comparison with the second hadronic B_s^0 decay channel 50 000 events of the type $B_s^0 \to D_s^-(\phi\pi^-)a_1^+$ with $a_1 \to \rho^0(\pi^+\pi^-)\pi$ are generated, as published in [107].

[4]Possible selection cuts have been published in [35]

The observables discussed in this section are introduced in detail in Section 5.1. Of primary concern are the wrong tag fraction P_w and its related dilution D, the efficiency ε, defined as the ratio of events passing the cuts out of all events, and the tagging power εD^2. Note, that in the calculation of the tagging power the trigger efficiency is used instead of the tagging efficiency. When calculating the statistical error of those observables with a small number of selected events or at a large asymmetry, the usual Binomial approach is not correct anymore. Therefore an asymmetric error calculation based on a bayesian approach is used. These calculations are detailed in Appendix B. Using this kind of error calculation, the asymmetric errors become symmetric in the special case of $P_w = 50\%$ or $\varepsilon = 50\%$.

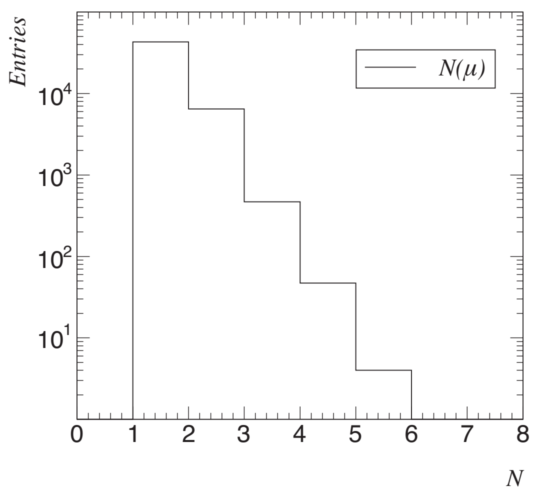

Figure 6.2: Number N of muons per event in Monte Carlo truth information of 50000 events of the type $B_s^0 \to D_s^- \pi^+$ generated with PYTHIA.

In Figure 6.2 the number of muons per event is shown for $B_s^0 \to D_s^- \pi^+$. While most of the events contain only one single muon, $13.93^{+0.16}_{-0.15}\%$ of the events contain two or more muons. The vast majority of these additional muons arise from semi-leptonic decays of D mesons and charmed baryons, which themselves either origin from semi-leptonic B hadron decays or from additional c-quarks pairs. Furthermore muons are produced by additional b-quark pairs or by sources like J/ψ mesons. The various sources are listed in more detail in Table 6.1.

It becomes obvious, that with the implementation of a two muon trigger a possible wrong tag due to J/ψ mesons decaying into two muons increases. However, by excluding muon pairs around the invariant mass of a J/ψ meson this contribution easily can be suppressed. Table 6.1 clearly shows, that multiple-muon events, in which the highest

	single μ	multiple μ_1	multiple μ_2
B mesons	79.4 ± 0.2	72.9 ± 0.5	10.0 ± 0.4
B baryons	8.9 ± 0.14	$4.4^{+0.3}_{-0.2}$	0.7 ± 0.1
D mesons	9.8 ± 0.1	11.9 ± 0.4	74.1 ± 0.5
charmed baryons	0.40 ± 0.03	$0.65^{+0.11}_{-0.10}$	$3.50^{+0.23}_{-0.22}$
J/ψ meson	–	8.5 ± 0.3	8.4 ± 0.3
other sources	1.45 ± 0.06	$1.69^{+0.17}_{-0.15}$	$3.20^{+0.23}_{-0.21}$

Table 6.1: Parent particles of the muons with the highest transverse momentum p_T in percent. In the first column events with one single muon are listed, in the second and third column events with two or more muons, where μ_1 and μ_2 denote the muons with the highest and second highest p_T, resepectively.

p_T muon comes from a semi-leptonic B decay, form the larges fraction. Kaon and pion in-flight decays producing additional muons are not included in this sample.

As $\bar{b}$ is forced to build the B_s^0 decay channel, the opposite side B hadron in the optimal case is supposed to decay semi-leptonically, producing a negatively charged muon. Shown in Figure 6.3 (a), as expected the number of negatively charged muons is one order of magnitude larger than positvely charged muons in the entire area of $p_T > 6$ GeV. In the range of lower transverse momentum $p_T < 6$ GeV this effect turns over, leading to a majority of positively charged muons in this range.

In Figure 6.3 (b) the distribution of the muon pseudo-rapidity η is shown. The solid line shows the dominant negatively charged, the dashed line the positively charged muons. The two vertical lines display the cut on $|\eta| = 2.5$ as required in the Pythia production for the trigger muon. A small fraction of additional muons have $|\eta| > 2.5$, however no charge is preferred in this regime.

The trigger efficiency is defined to be $\varepsilon = 1$ for selecting all 50 000 events. An event is counted as not tagged if it fails the cut on the muon transverse momentum p_T. If an event is regarded as tagged, the charge of the muon with the highest p_T defines the flavour tag: a μ^- is counted as a correct tag, a μ^+ as a wrong tag. Accordingly, the muon with the highest p_T is denoted by the term *tagging muon*, μ_{tag}. In Figure 6.4 (a) and (c) the wrong tag fraction P_w and the efficiency ε are shown as a function of the cut on the tagging

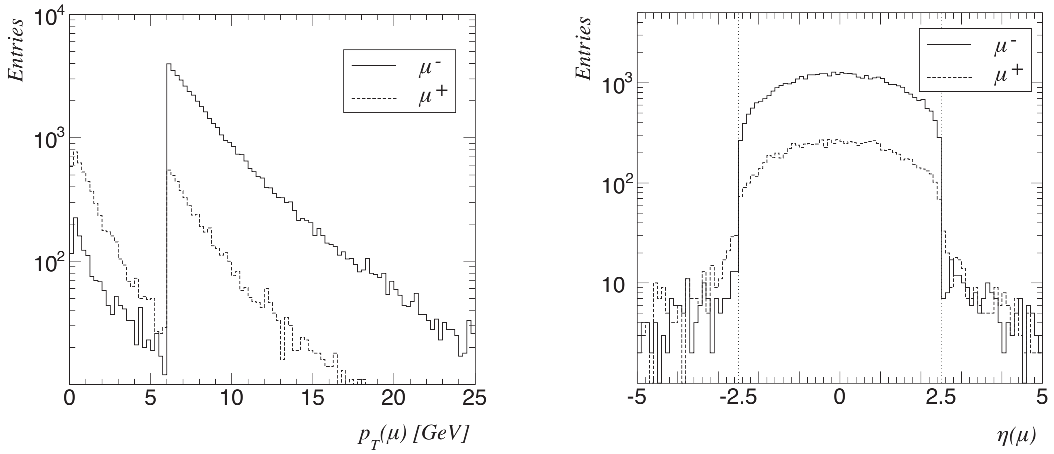

(a) (b)

Figure 6.3: Distributions of Monte Carlo truth information of 50 000 $B_s^0 \to D_s^- \pi^+$ events. In (a) the p_T distribution of the muon with the highest p_T, if available the second highest p_T is shown for negatively (solid line) and positively (dashed line) charged muons, in (b) in the same way the pseudorapidity η distribution is shown. The dotted, vertical lines denote the cuts on $|\eta| < 2.5$.

muon p_T, respectively. The dashed line corresponds to all events, whereas the solid line corresponds to the events with two or more muons. In terms of trigger scenarios, the dashed line describes a single-muon trigger with a cut on the trigger muon p_T, whereas the solid line corresponds to a di-muon trigger with no cut on p_T of the second muon . The grey shaded area displays the asymmetric statistical error. While all events reduce their wrong tag fraction with increasing $p_T(\mu_{tag})$, events with multiple muons have no significant dependence on the tagging muons p_T. However, the wrong tag fraction for events with more muons is significantly higher over the entire range of $p_T(\mu_{tag})$ while the efficiency is reduced by approximately one order of magnitude.

Note, that these values of P_w and ε are based on a very unrealistic scenario, assuming a trigger and tracking efficiency of 100% and disregarding neutral meson oscillation. The latter will be discussed in detail in Chapter 7. Regarding low-momentum muons ($p_T < 0.5$ GeV), the reconstruction is difficult due to the high curvature of the track and consequently the increased multiple scattering. To illustrate the dependence of tagging observables on the second muon, in Figure 6.4 (b) and (d) P_w and ε are shown as a function of the transverse momentum of the muon with the second highest $p_T(\mu_2)$, assuming an additional cut of $p_T(\mu_{tag} > 6$ GeV). The cut on $p_T(\mu_2)$ corresponds to a di-muon trigger cut on the second muons p_T. Again, the grey shaded area illustrates the statistical error, only. With an increasing cut on $p_T(\mu_2)$ the wrong tag fraction strongly raises,

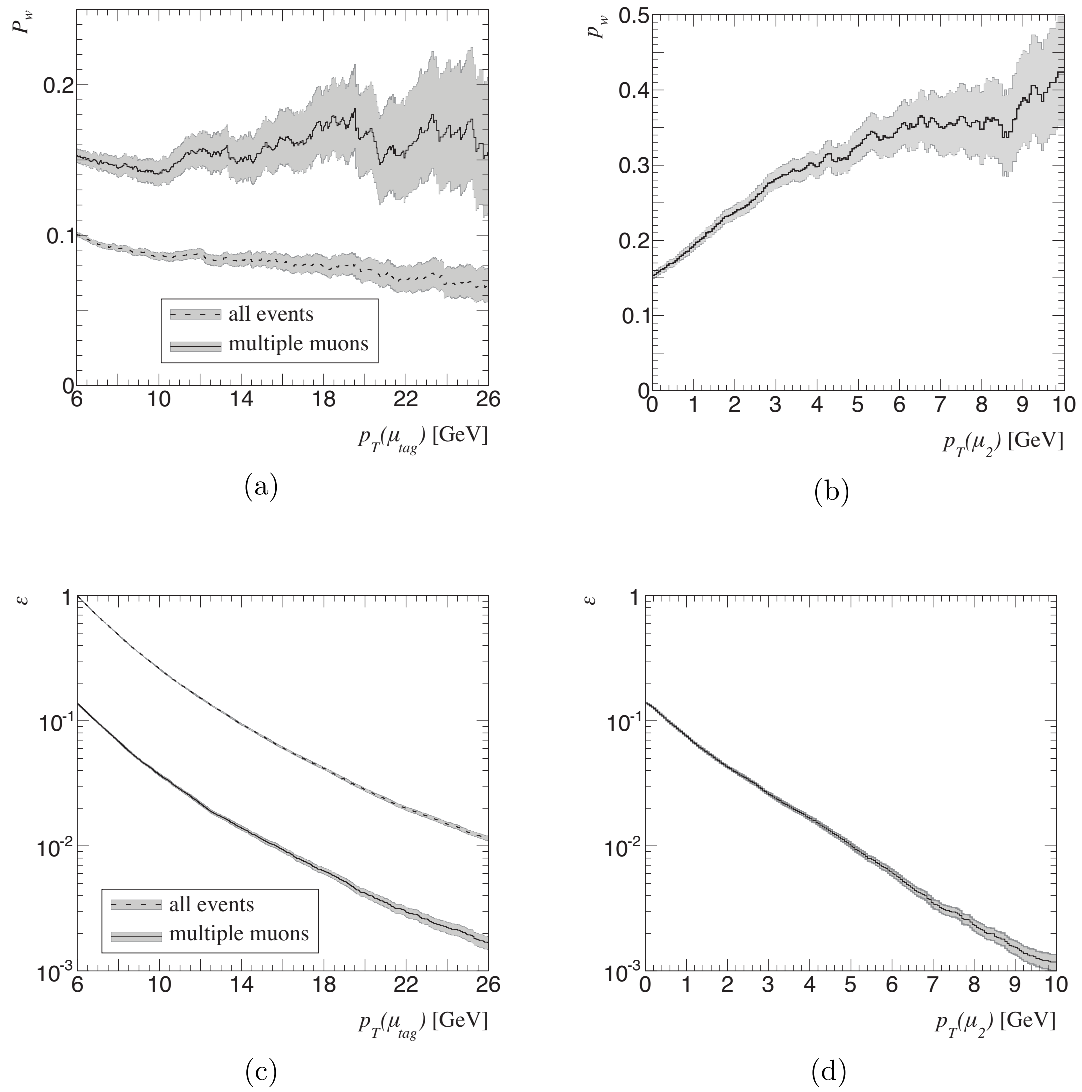

Figure 6.4: Wrong Tag Fraction P_w as a function of the cut on the transverse momentum p_T of the tagging muon μ_{tag} (a) and the muon μ_2 with the second highest p_T. In (a) the dashed line shows the wrong tag fraction taking into account all 50 000 events of the Pythia sample. The solid line in both, (a) and (b), illustrates the wrong tag fraction for 6 963 events containing more than one Monte Carlo muon. The grey shaded area displays the asymmetric statistical error of this sample. Figure (c) and (d) show the trigger efficiency as a function of the muons p_T as in (a) and (b). No muon reconstruction efficiency is applied in these plots.

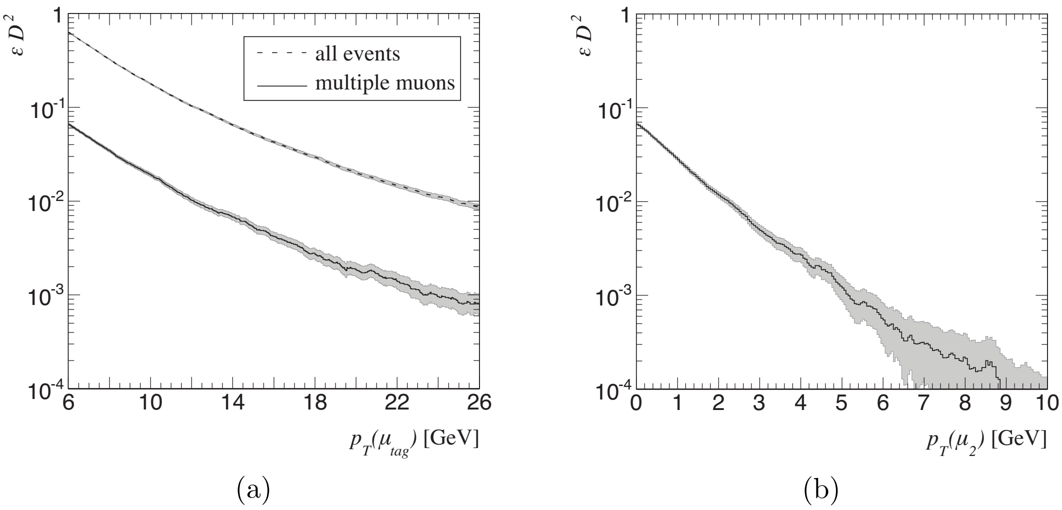

Figure 6.5: The tagging power as a function of the cut on the transverse momentum p_T of the muon with the highest p_T (a) and second highest p_T (b). The grey shaded area corresponds to the statistical error. In (a) both, all events and the events containing more than one muon are shown, in (b) consequently only the events with at least two muons. No muon reconstruction efficiency is applied in these plots.

whereas the efficiency decreases exponentially. In numbers, assuming a minimum $p_T(\mu_2)$ compared to the case without any cut, the wrong tag fraction increases from $(15.3 \pm 0.4)\%$ to $(16.9 \pm 0.4)\%$, while the efficiency decreases from $(13.4 \pm 0.4)\%$ to $(10.5 \pm 0.5)\%$.

In Figure 6.5 the wrong tag fraction and efficiency are combined to the tagging power εD^2 as introduced in Section 5.1.2. In subfigure (a) the tagging power is shown as a function of a cut on $p_T(\mu_{tag})$ for all events (dashed line) and for events containing two or more muons (solid line). In (b) the tagging power is plotted as a function of the cut on $p_T(\mu_2)$, assuming $p_T(\mu_{tag}) > 6$ GeV.

In order to get an estimate on efficiency, wrong tag fraction and tagging power of various combinations of cuts on muons p_T, in Table 6.2 the results for different scenarios are shown. The first six lines show the numbers for a single-muon scenario, no additional muons are required, whereas the further lines assume a di-muon scenario. While no reconstruction efficiency has been taken into account in the single-muon scenario, a reconstruction factor of 0.82 has been applied for the efficiency and the tagging power. This factor takes into account the muon detection efficiency for the second muon. When increasing the single-muon cut from $p_T(\mu) > 6$ GeV to $p_T(\mu) > 8$ GeV approximately 50% of the events get lost. The wrong tag fraction decreases as well, nonetheless this cannot compensate for the decreased efficiency. When comparing a single- and a di-muon scenario

Cut [GeV] $p_T(\mu)$		Efficiency ε [%]	Wrong Tag Fraction P_w [%]	Tagging Power εD^2
> 6		100	10.09 ± 0.14	0.637 ± 0.001
> 8		48.86 ± 0.22	9.10 ± 0.19	0.327 ± 0.002
> 10		26.13 ± 0.20	8.57 ± 0.25	0.179 ± 0.003
> 12		15.24 ± 0.16	$8.78^{+0.34}_{-0.33}$	0.104 ± 0.003
> 16		6.12 ± 0.11	$8.21^{+0.53}_{-0.50}$	0.043 ± 0.005
> 20		$2.82^{+0.08}_{-0.07}$	$7.59^{+0.77}_{-0.71}$	0.020 ± 0.008
> 6	> 0	11.42 ± 0.13	$15.29^{+0.44}_{-0.43}$	$(5.50 \pm 0.14) \times 10^{-2}$
> 6	> 2	3.56 ± 0.09	$23.66^{+0.95}_{-0.92}$	$(0.99 \pm 0.07) \times 10^{-2}$
> 6	> 4	1.39 ± 0.05	$29.78^{+1.66}_{-1.61}$	$(0.23 \pm 0.04) \times 10^{-2}$
> 6	> 6	0.51 ± 0.03	$34.83^{+2.92}_{-2.81}$	$(0.04 \pm 0.02) \times 10^{-2}$
> 8	> 2	2.08 ± 0.07	$21.01^{+1.21}_{-1.16}$	$(6.98 \pm 0.56) \times 10^{-3}$
> 8	> 4	0.94 ± 0.04	$26.73^{+1.97}_{-1.89}$	$(2.05 \pm 0.35) \times 10^{-3}$
> 8	> 6	0.43 ± 0.03	$33.58^{+3.17}_{-3.04}$	$(0.46 \pm 0.02) \times 10^{-3}$
> 10	> 2	1.27 ± 0.05	$19.43^{+1.53}_{-1.45}$	$(4.73^{+0.46}_{-0.44}) \times 10^{-3}$
> 10	> 4	0.61 ± 0.03	$24.66^{+2.45}_{-2.31}$	$(1.55^{+0.30}_{-0.28}) \times 10^{-3}$
> 10	> 6	0.29 ± 0.02	$33.33^{+3.92}_{-3.72}$	$(0.32^{+0.18}_{-0.17}) \times 10^{-3}$

Table 6.2: Results of various scenarios with various cuts on one $p_T(\mu)$ in the case of single-muon scenarios and two cuts on $p_T(\mu_1)$ and $p_T(\mu_2)$ in the case of di-muon scenarios for 50 000 events of the type $B_s^0 \to D_s^-(\phi\pi^-)\pi^+$ using Monte Carlo information. The errors are the statistical errors based on the Monte Carlo sample. Shown are the cut efficiency, the wrong tag fraction and the tagging power εD^2.

with similar efficiency (e.g. $p_T(\mu) > 20$ GeV versus $p_T(\mu_1) > 8$ GeV and $p_T(\mu_2) > 2$ GeV) it becomes obvious, that the wrong tag fraction of the di-muon scenario always exceeds the corresponding value of the single-muon scenario.

The results for the decay channel $B_s^0 \to D_s^-(\phi\pi^-)\pi^+$ are compared with the second hadronic decay channel which is foreseen to be triggered at ATLAS, $B_s^0 \to D_s^-(\phi\pi^-)a_1^+$, as published in [142]. In Table 6.3 these two channels are compared in some trigger scenarios, showing the efficiency and the wrong tag fraction of each channel. Note, that the statistical errors for the results of the $B_s^0 \to D_s a_1$ channel are smaller due to the larger sample used for this analysis, 50 000 events of type $B_s \to D_s \pi$ versus 151 706 events of type $B_s \to D_s a_1$. Within the statistical error, for the decay channel $B_s \to D_s a_1$ the wrong tag fraction is significantly higher in single-muon scenarios and compatible for di-muon scenarios.

6.2.2 Muon-Electron Trigger Scenarios

In addition to a pure di-muon trigger scenario, additional scenarios involving electrons are studied in [107, 142], using Monte Carlo truth information without any detector simulation. In Table 6.4 and 6.5 the results of two additional scenarios are shown: a muon-electron scenario, with variable cuts on the highest p_T muon and the highest p_T electron, and a muon-lepton scenario, in which the lepton either is a muon or an electron. As before, taking into account a limited reconstruction efficiency, a correction factor of 0.82 is applied on all efficiency results.

Comparing the results of the di-muon and the muon-electron scenario, the trigger efficiency is higher in the latter case. However, with increasing p_T this difference vanishes. Regarding the overlap of the muon-electron and di-muon scenarios, with an increasing cut on the leptons p_T the overlap is decreasing leading to an improvement of efficiency compared to the pure di-muon or muon-electron triggers.

Cut [GeV]		Efficiency ε [%]		Wrong Tag Fraction P_w [%]	
$p_T(\mu)$		$B_s^0 \to D_s\pi$	$B_s^0 \to D_s a_1$	$B_s^0 \to D_s\pi$	$B_s^0 \to D_s a_1$
> 6		100	100	10.09 ± 0.14	11.32 ± 0.08
> 8		48.86 ± 0.22	50.20 ± 0.13	9.10 ± 0.19	10.02 ± 0.11
> 10		26.13 ± 0.20	27.53 ± 0.14	8.57 ± 0.25	9.16 ± 0.14
> 6	> 0	11.42 ± 0.13	12.61 ± 0.14	$15.29^{+0.44}_{-0.43}$	15.6 ± 0.2
> 6	> 4	1.39 ± 0.05	1.40 ± 0.03	$29.78^{+1.66}_{-1.61}$	30.4 ± 0.9
> 8	> 4	0.94 ± 0.04	$0.96^{+0.03}_{-0.02}$	$26.73^{+1.97}_{-1.89}$	$26.9^{+1.1}_{-1.0}$

Table 6.3: Results for some trigger scenarios, comparing efficiencies and wrong tag fraction of the two decay channels $B_s^0 \to D_s^-(\phi\pi^-)\pi^+$ (50 000 events) and $B_s^0 \to D_s^-(\phi\pi^-)a_1^+$ (151706 events) on Monte Carlo level. For the di-muon scenarios a reconstruction factor of 0.82 has been applied on the effieciency.

Cut [GeV]		Efficiency ε [%]		Wrong Tag Fraction P_w [%]	
$p_T(\mu)$	$p_T(e)$	$B_s^0 \to D_s\pi$	$B_s^0 \to D_s a_1$	$B_s^0 \to D_s\pi$	$B_s^0 \to D_s a_1$
> 6	> 0.1	40.14 ± 0.18	42.32 ± 0.13	11.0 ± 0.2	12.2 ± 0.1
> 6	> 4	1.52 ± 0.05	1.68 ± 0.03	34.4 ± 1.6	34.7 ± 0.9
> 8	> 4	0.95 ± 0.04	1.01 ± 0.03	$28.9^{+2.0}_{-1.9}$	29.5 ± 1.1

Table 6.4: As in Table 6.3, results for muon-electron scenarios comparing $B_s^0 \to D_s^-(\phi\pi^-)\pi^+$ (50 000 events) and $B_s^0 \to D_s^-(\phi\pi^-)a_1^+$ (151 706 events) on Monte Carlo level. As for muons, a reconstruction factor of 0.82 has been applied on the efficiency.

Cut [GeV]		Efficiency ε [%]		Wrong Tag Fraction P_w [%]	
$p_T(\mu)$	$p_T(l)$	$B_s^0 \to D_s\pi$	$B_s^0 \to D_s a_1$	$B_s^0 \to D_s\pi$	$B_s^0 \to D_s a_1$
> 6	> 0	46.02 ± 0.18	48.29 ± 0.13	11.5 ± 0.2	12.6 ± 0.1
> 6	> 4	2.87 ± 0.07	3.05 ± 0.03	$31.8^{+1.2}_{-1.1}$	32.7 ± 0.6
> 8	> 4	$1.86^{+0.06}_{-0.05}$	1.95 ± 0.04	$27.4^{+1.4}_{-1.3}$	$28.3^{+0.8}_{-0.7}$

Table 6.5: As in Table 6.3, results for muon-lepton scenarios comparing $B_s^0 \to D_s^- \pi^+$ (50000 events) and $B_s^0 \to D_s^- a_1^+$ (151 706 events) on Monte Carlo level. The lepton l can be either a muon or an electron. As before, a reconstruction factor of 0.82 has been applied on the efficiency.

CHAPTER

SEVEN

Soft Lepton Flavour Tagging

In this chapter the application of opposite side soft lepton flavour tagging on hadronic decay channels is presented. The reconstruction of the hadronic B_s decay channels $B_s^0 \to D_s^- \pi^+$ and $B_s^0 \to D_s^- a_1^+$ as well as the flavour tagging algorithm are detailed in Chapter 7.1. In Chapter 7.2 the results of the flavour tagging analysis as initially published in [34] are shown. In the last part, Chapter 7.3, the combination of various kinematic observables are combined by multivariate methods in order to assign a wrong tag fraction on an event-by-event basis.

7.1 Data Samples and Offline Analysis

As already introduced in Chapter 5.2.1, opposite side soft muon flavour tagging is the main method for the determination of the initial b quark content in the case of purely hadronic B_s decays. In the ATLAS experiments hadronic B_s decay channels will be used e.g. for the determination of the oscillation frequency Δm_s.

Channel	Events	Cross section [pb]
$B_s^0 \to D_s^-(\phi\pi^-)\pi^+$	88 450	10.4 ± 3.5
$B_s^0 \to D_s^-(\phi\pi^-)a_1^+$	98 450	5.8 ± 3.2
$B_d^0 \to D_s^+\pi^-$	43 000	0.2 ± 0.1
$B_d^0 \to D_s^+a_1^-$	50 000	limit: < 8.9
$B_d^0 \to D^-\pi^+$	41 000	6.2 ± 1.1
$B_d^0 \to D^-a_1^+$	50 000	3.7 ± 2.1
$B_s^0 \to D_s^{*-}\pi^+$	40 500	9.1 ± 2.8
$B_s^0 \to D_s^{*-}a_1^+$	100 000	12.1 ± 2.7

Table 7.1: Number of generated events of the two hadronic B_s^0 decay channels and different exclusive background samples, and the cross section calculated by using the Pythia output and the branching ratios given in [125]. Table from [34].

7.1.1 Simulated Data Samples

For the analysis in this chapter 88450 events of the type $B_s^0 \to D_s^-\pi^+$ and 98450 events of the type $B_s^0 \to D_s^-a_1^+$ have been generated using Pythia 6.4 [139]. These data samples correspond to the data used in [34]. The $\bar{b}$ quarks are required to decay into one of the two decay channels. Similar to the evaluation of muon trigger scenarios in Chapter 6.2, only events with a muon with a transverse momentum of $p_T > 6$ GeV and a pseudo-rapidity of $|\eta| < 2.5$ are selected. All final state particles from the decay channel are required to have $p_T > 0.5$ GeV on generator level. Based on the cross section values given by Pythia and the branching ratios given in [125] the cross sections have been calculated in Table 7.1.

In addition to the signal channels, also displayed in Table 7.1, certain exclusive background channels have been generated in order to perform a full background study, as published in [34]. However, for the flavour tagging itself the background samples are not crucial.

The details of the generation, simulation, digitisation and reconstruction of the data samples are given in Chapter 4.1.

7.1.2 Trigger Selection

In Chapter 6.1.2 an introduction into the high level triggering of hadronic B decays is given. As published in [34], many trigger settings have been analysed and studied referring to the output rate of the LVL2 and EF trigger.

Considering the full reconstruction of the hadronic decay channels, the trigger approach used in this thesis is the L2mu6RoI trigger set. The typical trigger chain starts at LVL1 with the requirements for a muon with a threshold of 6 GeV and energy deposited in the calorimeter, defining a region of interest (RoI). The transverse energy deposited in the RoI is required to be above a threshold of 4 GeV. At LVL2 the confirmation of the muon and the reconstruction of the $D_s^\pm$ around the RoI takes place, and finally at EF the muon track is reconstructed and the $D_s^\pm$ is reconstructed with the same mass cuts as at LVL2. For the $\phi \to K^+K^-$ reconstruction a mass window of 1005 MeV $< m_{KK} <$ 1035 MeV is used, for the $D_s^\pm \to \phi(KK)\pi^\pm$ selection the mass window is $1908 < m_{KK\pi} < 2028$ MeV. Within the RoI a cut on all tracks transverse momentum of $p_T > 1.4$ GeV is applied. The full hadronic trigger chain is described in more details in Chapter 6.1.2.

7.1.3 Reconstruction of the decays $B_s^0 \to D_s^-\pi^+$ and $B_s^0 \to D_s^-a_1^+$

The reconstruction of $B_s^0 \to D_s^-\pi^+$ has been intensively studied, as published in [82–84], the decay channel $B_s^0 \to D_s^-a_1^+$ is discussed in all details in [142]. The prospects for measuring the oscillation frequency Δm_s combining both decay channels has been analysed in [34]. In the following the reconstruction of the two hadronic B_s decay channels $B_s^0 \to D_s^-(\phi\pi^-)\pi^+$ and $B_s^0 \to D_s^-(\phi\pi^-)a_1^+$ with $D_s^- \to \phi(K^+K^-)\pi^-$ and $a_1^+ \to \rho^0(\pi^+\pi^-)\pi^+$ is outlined.

In principle the reconstruction of the B_s^0 follows the same strategy as the High Level Trigger (see Chapter 6.1.2). Only tracks with a pseudo-rapidity $|\eta| < 2.5$ are selected. In a first step, two oppositely charged tracks with $p_T > 1.5$ GeV are combined to build a ϕ vertex, where kinematic cuts on the azimuthal and polar angles between the kaons of $\Delta\varphi < 10°$ and $\Delta\theta < 10°$ are imposed. Assigning the kaon mass to both tracks a common vertex is fitted. Only track combinations are selected where the vertex has a fit probability greater than 1 % and the invariant mass is within a window of three standard deviations around the ϕ mass. In the case of $B_s^0 \to D_s^-\pi^+$ the mass resolution has been found to be $\sigma_\phi = (4.30 \pm 0.03)$ MeV, for $B_s^0 \to D_s^-a_1^+$ the mass resolution is $\sigma_\phi = (4.28 \pm 0.03)$ MeV

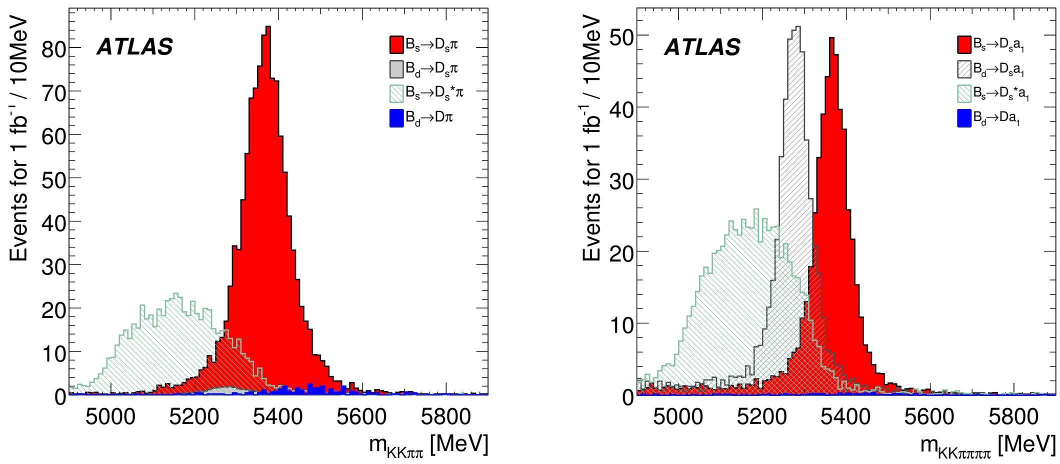

(a) (b)

Figure 7.1: The reconstructed invariant mass $m_{KK\pi\pi}$ (a) and $m_{KK\pi\pi\pi\pi}$ (b) for the signal and background channels. Figures taken from [34].

[34]. The full width of the $\phi(1020)$ resonance is $\Gamma = (4.26 \pm 0.04)$ MeV [125], contributing to the mass resolution by approximately one half.

For the reconstruction of a D_s meson a third track is combined with all ϕ vertex candidates, assigning the pion mass to this track and fitting a common vertex. As before, D_s vertex candidates have to pass a cut on the fit probability of 1 % and the invariant mass has to be within three standard deviations. The mass resolution of the D_s is $\sigma_{D_s} = (17.81 \pm 0.13)$ MeV for the $B_s^0 \to D_s^- \pi^+$ channel and $\sigma_{D_s} = (17.92 \pm 0.13)$ MeV for the $B_s^0 \to D_s^- a_1^+$.

For the reconstruction of a $B_s^0 \to D_s^- \pi^+$ decay from the remaining tracks a fourth track is added, where it is required to have $p_T > 1$ GeV and the opposite charge of the pion from the D_s vertex. The four tracks are fitted to a common vertex, including the preconditions on the mass windows of the ϕ and D_s candidates.

In the case of the decay channel $B_s^0 \to D_s^- a_1^+$, first a ρ^0 vertex is constructed by assigning the pion mass to two oppositely charged tracks. Track pairs with an invariant mass within 400 MeV around the nominal ρ^0 mass are combined with a third pion track. The final $a_1^\pm$ candidate vertex is required to have an invariant mass within 325 MeV of the a_1 mass. All three tracks from the $a_1^\pm$ vertex have to fulfil a cut of $p_T > 0.5$ GeV. The three tracks from the a_1 candidate are fitted together with each reconstructed D_s candidate to a common vertex, including the constraints on the a_1, ρ^0, ϕ and D_s mass windows.

In both decay channels, the resulting B_s^0 candidate is required to have a total momentum vector pointing to the primary vertex. Again, the fit probability has to be greater than 1 %. In Figure 7.1 the distribution of the invariant mass $m_{KK\pi\pi}$ (for $B_s^0 \to D_s^- \pi^+$) and $m_{KK\pi\pi\pi\pi}$ (for $B_s^0 \to D_s^- a_1^+$) are shown for the two signal channels and the exclusive background channels listed in Table 7.1. In these two figures published in [34] for the sake of reducing the number of background events further cuts have been imposed: the proper decay length d_{xy} has to be positive, the proper time has to be greater than $\tau_0 > 0.4$ ps, and the transverse momentum of the track quadruplet (or sextuplet) is required to have a transverse momentum greater than $p_T > 10$ GeV.

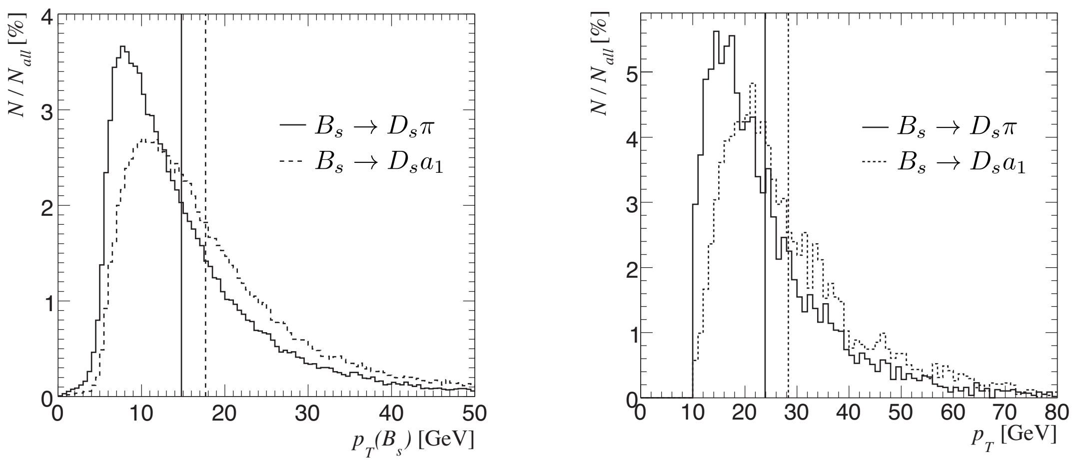

(a) (b)

Figure 7.2: Normalised distributions of true signal B_s^0 transverse momentum p_T of the two channels $B_s^0 \to D_s^-(\phi\pi^-)\pi^+$ (solid lines) and $B_s^0 \to D_s^-(\phi\pi^-)a_1^+$ (dashed lines) for all generated events (a) and correspondingly for reconstructed B_s^0 meson (b). The vertical lines represent the mean values of the distributions, in the case of $B_s^0 \to D_s^-\pi^+$ the mean is 14.80 ± 0.03 GeV (23.90 ± 0.16 GeV), in the case of the decay $B_s^0 \to D_s^- a_1^+$ 17.68 ± 0.03 GeV (28.33 ± 0.17 GeV) on generator level (reconstructed-track level). The observed difference is due to the track selection cuts. Left plot taken from [34].

In connection with opposite side flavour tagging, the main difference between the two decay channels is illustrated in Figure 7.2. In the following sections it will be explained, that the probability of a wrong tag depends on the transverse momentum of the signal B_s^0. On both, Monte Carlo generated events and reconstructed B_s^0 mesons, cuts on p_T of the final state particles have been applied. Therefore one expects different $p_T(B_s)$ distributions for final states with different kinematical configurations, i.e. a harder spectrum for events with more final state particles. In the case of $B_s^0 \to D_s^- \pi^+$ (solid lines) there are four final state particles, in the case of $B_s^0 \to D_s^- a_1^+$ (dashed lines) there are six particles.

On Monte Carlo level a generation cut of $p_T > 0.5$ GeV on all tracks has been imposed, leading to a difference of the mean $p_T(B_s^0)$ of 14.80 ± 0.03 GeV in the case of $B_s^0 \to D_s^- \pi^+$ and 17.68 ± 0.03 GeV in the case of $B_s^0 \to D_s^- a_1^+$. The $p_T(B_s^0)$ distributions are shown in Figure 7.2 (a) on generator level. For the reconstruction, the tracks from the D_s decay have $p_T > 1$ GeV, the pion track in $B_s^0 \to D_s^- \pi^+$ has $p_T > 1$ GeV and the pions from the a_1 decay each has $p_T > 0.5$ GeV. Therefore, also in the true p_T spectrum for reconstructed B_s^0 a difference can be expected, which is shown in Figure 7.2 (b). Due to the reconstruction cut on $p_T(B_s^0) > 10$ GeV, the mean values are higher compared to the Monte Carlo distribution: 23.90 ± 0.16 GeV ($B_s^0 \to D_s^- \pi^+$) and 28.33 ± 0.17 GeV ($B_s^0 \to D_s^- a_1^+$). Figure 7.3 shows the reconstruction efficiency for the channel $B_s^0 \to D_s^- \pi^+$ as a function of the signal B_s^0 true p_T.

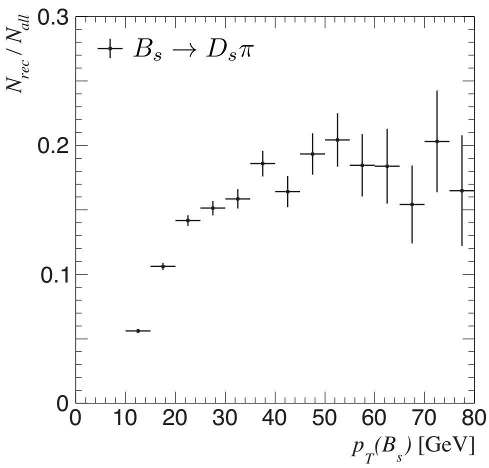

Figure 7.3: Reconstruction efficiency of the channel $B_s^0 \to D_s^-(\phi\pi^-)\pi^+$ as a function of the true signal B_s^0 transverse momentum, where N_{rec} correspond to the number of reconstructed events and N_{all} to all generated 88 450 B_s^0 mesons.

7.1.4 The Soft Muon Flavour Tagger

The opposite side soft muon flavour tagging software is based on the BFlavourCombinedTagger in the Athena package AtlasPhysics/BPhys/BPhysAnalysisTools. In the BFlavourCombinedTagger currently two different methods of flavour tagging are implemented: the same side jet charge tagging as studied in detail for the analysis of the decay channel $B_s^0 \to J/\psi(\mu^+\mu^-)\phi(K^+K^-)$ in [34], and the opposite side soft lepton flavour tagger.

The main object of interest in the soft lepton tagging is the muon with the highest transverse momentum. The software can handle all different types of muon objects, e.g. Staco or Muid objects. The different methods for the muon reconstruction have been described in Chapter 4.1.4.2. Further on, instead of muons the software is able to determine a flavour tag using electrons, or a combination of those two. Due to the main trigger strategy, which depends on low p_T muons, within this thesis only muons are considered. In addition to the leptons, correlations between the muons and the closest particle jet have been studied. Therefore, beside the muons the BFlavourCombinedTagger also checks for a collection of jets in an event. A description of the jet reconstruction methods have been omitted within this thesis. However, the principles of building a jet object are outlined in Chapter 3.6, more details can be found in [34].

While the overall result of the flavour tagging slightly depends on the choice of the data collection, within this thesis the choice is arbitrary. The muon collection used is the StacoMuonCollection, the jet collection is the Cone4H1TowerJets. This collection corresponds to jets with a cone of radius $R = 0.4$ around the jet vector $\vec{p}_{jet}$.

In a first step, the BFlavourCombinedTagger identifies all muons and performs a simple flavour tag by identifying the charge of the muon. All muons are sorted for their transverse momentum p_T. Assuming, that the muon with the highest p_T is originating from a semi-leptonic decay of the opposite side B meson, the charge of this muons determines the outcome of the flavour tag. If the charge of the muon is negative, the signal sides initial flavour is identified as a B_s^0 meson, if it is positive the flavour is identified as $\bar{B}_s^0$. In order to avoid a flavour tag by muons coming from background sources already identified by some algorithm (e.g. muon pairs from a J/ψ decay), these muons can be excluded in the flavour tagger. However, for a detailed analysis of all possible sources of a wrong tag within this thesis, this optional possibility has not been used in this analysis.

If the data sample is based on Monte Carlo samples without the oscillation of B_d^0 or B_s^0 mesons, mixing can be introduced artificially by swapping the flavour of the neutral opposite side B_q^0 mesons. This method allows the evaluation of wrong tags due to meson mixing. In the software the full decay chain of a Monte Carlo muon is checked for the occurrence of a neutral B_q^0 meson. If one of those mesons is found in the muons history, the muons charge is swapped with a probability equal to the time integrated mixing probabilities introduced in Chapter 2.3.2 (i.e. $\chi_d \approx 19$ % and $\chi_s \approx 50$ %).

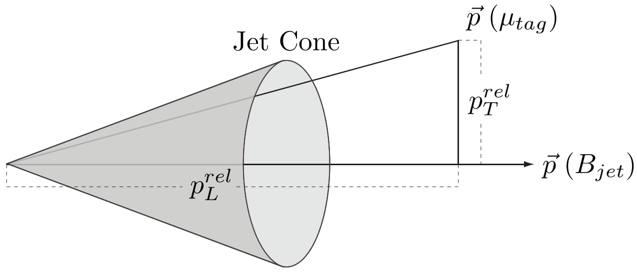

Figure 7.4: Considering the jet closest to the tagging muon as the opposite side B jet, the component of the muon momentum perpendicular to the jet axis is denoted as p_T^{rel}, consequently the parallel component is denoted as p_L^{rel}.

The outcome of the BFlavourCombinedTagger is a vector of tagging objects BFlavourParticle (in this thesis muons), the corresponding flavour tag for each lepton and certain kinematic properties. The vector is ordered by the muons transverse momentum.

One crucial property of each muon is its distance to the closest jet as illustrated in Figure 7.4. Within the BFlavourCombinedTagger for each muon the transverse momentum p_T^{rel} relative to the closest jet is calculated. The jet vector $\vec{p}_{jet}$ is required to point into the same hemisphere as the muon trajectory. The distance between these two objects is calculated as $\Delta R = \sqrt{\Delta\eta^2 + \Delta\phi^2}$. In Figure 7.5 the distribution of p_T^{rel} is shown for the two decay channels $B_s^0 \to D_s^- \pi^+$ and $B_s^0 \to D_s^- a_1^+$. The physical motivation for this observable will be given in the next section.

The BFlavourCombinedTagger can be implemented within any analysis algorithm in Athena, giving a soft lepton flavour tag. For the following analysis the dedicated algorithm has been used.

7.2 Opposite Side Soft Muon Flavour Tagging Analysis of Hadronic B_s^0 decays

The Athena analysis algorithm BsMuonTagging[5] is dedicated for a detailed study of opposite side soft muon tagging on hadronic decay channels. The application of this algorithm on the two signal channels $B_s^0 \to D_s^-(\phi\pi^-)\pi^+$ and $B_s^0 \to D_s^-(\phi\pi^-)a_1^+$ will be discussed in this chapter.

[5]In the Athena package PhysicsAnalysis/BPhys/HadronicDecayAlgs

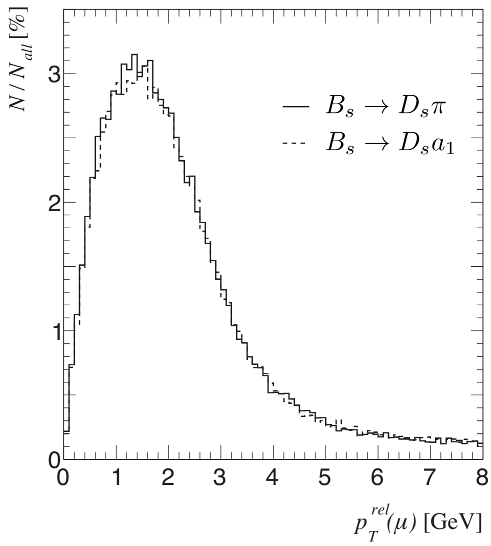

Figure 7.5: Normalised distributions of the tagging muons p_T^{rel} of the two channels $B_s^0 \to D_s^-(\phi\pi^-)\pi^+$ and $B_s^0 \to D_s^-(\phi\pi^-)a_1^+$.

7.2.1 Inclusive results for generated, triggered and reconstructed events

Table 7.2 shows the number of events for each stage, the tagging efficiency ε and the wrong tag fraction P_w for both signal channels $B_s^0 \to D_s^-\pi^+$ and $B_s^0 \to D_s^-a_1^+$. These observables are explained in detail in Chapter 5.1. As already introduced in Chapter 6.2.1, instead of the usual Binomial errors the errors in this chapter are calculated based on a bayesian approach as detailed in Appendix B. In some cases this error calculation leads to slight asymmetries.

The three stages of reconstruction in Table 7.2 are *all events*, which correspond to all events generated and reconstructed as shown in Table 7.1, *triggered* are all events selected by the L2MU6ROI, and *reconstructed* corresponds to all triggered events which have been successfully reconstructed as described in Chapter 7.1.3.

Regarding all event, for both channels the tagging efficiency is of the same order, around 96 %. Applying the L2MU6ROI trigger increases the tagging efficiency for both channels up to approximately 98.5 %, the further reconstruction of the B_s^0 decay channels has no influence on the tagging efficiency.

In the case of the wrong tag fraction, there is a difference between the two decay channels of approximately 1 %, regardless of the stage. In total, for $B_s^0 \to D_s^-\pi^+$ the wrong tag fraction is 20.29 ± 0.14, for $B_s^0 \to D_s^-a_1^+$ $P_w = 21.05 \pm 0.13$. While the trigger

Type of Events	Number of Events	Tagging Efficiency [%]	Wrong Tag Fraction [%]	Tagging Power
$B_s^0 \to D_s^- \pi^+$:				
all events	88 450	96.08 ± 0.07	20.29 ± 0.14	0.339 ± 0.001
triggered	21 613	98.77 ± 0.07	22.96 ± 0.29	0.289 ± 0.003
reconstructed	5 687	$98.79^{+0.14}_{-0.15}$	$22.30^{+0.56}_{-0.55}$	0.303 ± 0.005
$B_s^0 \to D_s^- a_1^+$:				
all events	98 450	95.93 ± 0.06	21.05 ± 0.13	0.322 ± 0.001
triggered	27 118	98.55 ± 0.07	23.91 ± 0.26	0.268 ± 0.002
reconstructed	5 757	$98.47^{+0.16}_{-0.17}$	$23.31^{+0.56}_{-0.55}$	0.281 ± 0.005

Table 7.2: Tagging efficiency wrong tag fraction and tagging power for the signal channels $B_s^0 \to D_s^- \pi^+$ and $B_s^0 \to D_s^- a_1^+$ are shown for three different stages: all simulated events, all triggered events passing the LVL1 muon trigger and the LVL2 RoI trigger, and finally the numbers for the reconstructed events. The errors are statistical only. [34]

selection improves the tagging efficiency, a significant increase of the wrong tag fraction of more than 2.5 % counteracts this improvement. In terms of tagging power εD^2 the trigger reduces this value from 0.339 to 0.289 for the $B_s^0 \to D_s^- \pi^+$ channel, from 0.322 to 0.268 for $B_s^0 \to D_s^- a_1^+$. The reconstruction of the B_s^0 decay channels slightly decreases P_w for both channels, however the values for *triggered* and *reconstructed* events are compatible within the statistical errors. The tagging power for the reconstructed events has been found to be 0.303 ± 0.005 for $B_s^0 \to D_s^- \pi^+$ and 0.281 ± 0.005 for $B_s^0 \to D_s^- a_1^+$.

Compared to the wrong tag fraction of all events, the wrong tag fraction in triggered and reconstructed events is significantly larger. This can be explained by taking a look at the initial $b\bar{b}$ pair production. At first order the quark pair has a transverse momentum equal to zero. Therefore, the two quarks receive the same share of kinetic energy. Their $|p_T|$ can be assumed to be equal, while the quarks traverse in opposite directions. Despite the quarks undergo fragmentation and hadronisation, the transverse momenta of the two resulting B hadrons still are correlated. With an increasing transverse momentum of the opposite side B hadron, a muon produced in a cascade $b \to c \to \mu$ also has an increased p_T, increasing the probability for the cascade muon to be triggered. As a muon from a cascade decay has the opposite decay as one from a direct B decay this leads to an increased wrong tag fraction.

Sources of Wrong Tag Fraction	P_w [%] $B_s^0 \to D_s^- \pi^+$	P_w [%] $B_s^0 \to D_s^- a_1^+$
mixed $b \to \mu$	9.53 ± 0.10	9.37 ± 0.09
chain $b \to c \to \mu$	8.22 ± 0.09	9.73 ± 0.09
additional c pairs	1.51 ± 0.04	1.47 ± 0.03
additional b pairs	0.18 ± 0.01	0.18 ± 0.01
other sources	0.81 ± 0.03	0.79 ± 0.02

Table 7.3: Sources of wrong tag fraction and their absolute contribution to the total wrong tag fraction as shown in Table 7.2 for *all events*. The errors are statistical only.

Using the Monte Carlo truth information stored in all events, the various sources can be identified in detail. All possible sources and their absolute contribution to the wrong tag fraction of *all* events are listed in Table 7.3 for both hadronic decay channels. In principle, the various sources can be classified in two different categories: wrong tags which are influenced by the opposite side B flavour and wrong tags which are independent of these very hadrons. In the second category the main contribution arises from additional $c\bar{c}$ pairs, in which one of the c hadrons decays semi-leptonically, leading to a wrong tag. Correspondingly, with a smaller fraction, additional $b\bar{b}$ pairs could lead to a wrong tag.

In Table 7.3 *"other sources"* represents the wrong tag fraction due to particles decaying into a $\mu^+\mu^-$ pair, e.g. $J/\psi \to \mu^+\mu^-$. The occurrence of events with a wrong tag due to muons from $b\bar{b}-$ and $c\bar{c}$ pairs or from di-leptonic $\mu^+\mu^-$ decays can be expected to lead to a wrong tag or to a correct tag with the same probability. Consequently, the approximately 2.5 % of wrong tags in those events have a counterpart of an estimated 2.5 % with a correct tag.

However, the remaining 95 % of events are subject to oscillations of the opposite side B hadron (see Chapter 5.2.2 for details). B hadrons decaying semi-leptonically could lead to a wrong tag due to mixing, which is reflected in the large fraction of wrong tags, (9.53 ± 0.10) % in the case of $B_s^0 \to D_s^- \pi^+$ and (9.37 ± 0.09) % in the case of $B_s^0 \to D_s^- a_1^+$. Of the same order, wrong tags due to the chain decay $b \to c \to \mu$ are subject to mixing, too. Consequently, a certain percentage of chain decays lead to a wrong tag due to mixing.

In Table 7.3 the different wrong tag fraction between the two hadronic channels becomes obvious. The main difference arises from chain decays $b \to c \to \mu$, which can

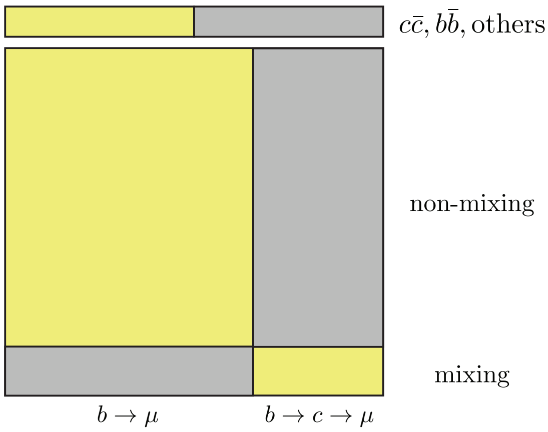

Figure 7.6: Illustration for the interplay between wrong tags due to chain decays $b \to c \to \mu$ and wrong tags due to oscillations. The whole area represents all events, the coloured boxes the correctly tagged and the grey ones the wrong tagged. Mistags due to additional $b\bar{b}$- and $c\bar{c}$-pairs or due to other sources can be assumed to have a corresponding counterpart of good tags. By reducing the wrong tags due to chain decays (illustrated with the arrows), the wrong tags due to mixing increase.

be explained by the different kinematic situation of the two channels. While the decay $B_s^0 \to D_s^- \pi^+$ leads to a total number of four final state particles, $B_s^0 \to D_s^- a_1^+$ has six of those particles, leading to a different distribution of $p_T(B_s^0)$ (see Figure 7.2). As in the argumentation before, a higher p_T of the signal B_s^0 leads to a higher p_T of the opposite side B hadron in first order. Consequently, a muon from a decay $b \to c \to \mu$ has a higher p_T and therefore a higher probability to be triggered. In short, with increasing number of final state particles of the signal decay the occurrence of higher p_T chain decay muons increases, leading to a higher wrong tag fraction.

A further, but significantly smaller difference is expected in the fraction of wrong tags due to mixing in events, where the muon directly originates from a semi-leptonic B decays. A higher probability of occurrence of chain decays are at the expense of muons from $b \to \mu$ decays. Therefore, with increasing number of final state particles the wrong tag fraction due to mixing is expected to be smaller. However, within the statistical error the values for the two hadronic decay channels are compatible, as shown in Table 7.3.

The interplay between wrong tags due to mixing with wrong tags due to chain decays is illustrated in Figure 7.6. Wrong tags due to additional $b\bar{b}$- and $c\bar{c}$-pairs or due to other sources can be assumed to have an equal counterpart of good tags. Mixing in these events does not change the total wrong tag fraction. The remaining events are subject to mixing. If the percentage of mixed events is below 50 %, a reduction of wrong tags due to chain decays $b \to c \to \mu$ leads to an improvement of the total wrong tag fraction. Corresponding to the fractions of B hadrons produced in pp collisions as shown in Table 2.3 and the integrated mixing probabilities shown in Table 2.6, this percentage can be calculated to be approximately 13 %.

7.2.2 Differential analysis of all events

In this section, the wrong tag fraction and its sources are discussed as a function of the tagging muons transverse momentum $p_T(\mu)$, the signal side mesons transverse momentum $p_T(B_s^0)$ and the tagging muons transverse momentum relative to its closest jet $p_T^{rel}(\mu)$. In all figures the bars in x-direction show the width of the bin, the error of the wrong tag fraction P_w is statistical, only. All 88 450 $B_s^0 \to D_s^- \pi^+$ events and all 98 450 $B_s^0 \to D_s^- a_1^+$ events are used for this analysis. However, one has to keep in mind that the reconstruction efficiency has a strong dependence on $p_T(B_s^0)$ as shown in Chapter 7.1.3.

In Figure 7.7 the wrong tag fraction of the two decay channels is shown as a function of $p_T(\mu)$. Disregarding mixing of the opposite side B hadron, the main contribution to P_w arises from chain decays $b \to c \to \mu$. With increasing $p_T(\mu)$ this fraction becomes smaller. This can be explained by the fact, that a muon from a chain decay is more likely to have a lower transverse momentum, therefore the percentage of muons originating from those decays decreases with $p_T(\mu)$. Consequently more muons from $b \to \mu$ decays are available, which leads to an increasing wrong tag fraction due to mixing, as discussed in the previous section. Comparing the decays $B_s^0 \to D_s^- \pi^+$ and $B_s^0 \to D_s^- a_1^+$, this behaviour is observable in both decay channels.

Regarding the minor sources of wrong tag fraction, which are independent of mixing, the contributions from additional $b\bar{b}$ pairs and other sources are slightly increasing with $p_T(\mu)$. The only exception are muons from additional $c\bar{c}$ pairs, whose contribution remains about at the same level for all values of $p_T(\mu)$.

In Figure 7.8 the wrong tag fraction and its individual sources are shown as a function of the signal side B_s^0 transverse momentum $p_T(B_s^0)$. In order to analyse the various sources of wrong tags with a high statistics, $p_T(B_s^0)$ is taken from the Monte Carlo and not from the small amounts of reconstructed values. Consequently, one has to keep in mind that the very low values of $p_T(B_s^0)$ cannot be reconstructed due to cuts on the individual final state particles p_T. This limitation of the reconstruction already has been discussed in Chapter 7.1.3 and can be seen clearly in Figure 7.2.

The dependency on $p_T(B_s^0)$ mainly is dominated by wrong tags due to muons from chain decays $b \to c \to \mu$. This behaviour arises again from the fact, that at first order a $b\bar{b}$ pair has a transverse momentum equal to zero. Therefore a higher p_T signal B meson is accompanied by a higher p_T opposite side B hadron. As the muon is boosted by the initial B momentum, a muon produced in the chain decay $b \to c \to \mu$ has an increased probability to be triggered and therefore be used as tagging muon, leading to a wrong tag. With the same reasons as before, with increasing occurrence of chain decays in a sample, wrong tags due to mixing decrease. In Figure 7.8 one can clearly see, that the wrong tag fraction dependence is dominated by chain decays, whereas the decrease due to mixing shows just a small effect.

Regarding the minor contributions, while wrong tags due to additional $c\bar{c}$ pairs show a slight decrease with growing $p_T(B_s^0)$, wrong tags due to additional $b\bar{b}$ pairs increase. Over the full range the fraction due to additional sources remain at the same level. Overall, the fraction due to all those minor sources together is reduced with $p_T(B_s^0)$.

It has been shown, that the wrong tag fraction strongly depends on the signal sides B hadron p_T. This dependence mainly originates from chain decays $b \to c \to \mu$. In order to discriminate between muons from semi-leptonic B decays and muons from semi-leptonic D decays the relative transverse momentum of a muon to its closest jet $p_T^{rel}(\mu)$ can be used. This observable has been introduced in Chapter 7.1.4, see Figure 7.4 for an illustration.

Comparing the two semi-leptonic decays $B^0 \to D^-\mu^+\nu_\mu$ and $D^0 \to K^-\mu^+\nu_\mu$, the mass difference between the initial meson and the particles in the final state is of the order 3.3 GeV for the B decay, for the D decay of the order 1.3 GeV. In the rest-frame of the decaying particles, the muon momentum has a maximum when the neutrino receives no momentum and the heavier particle goes in the opposite direction as the muon. Hence the maximum possible momentum of a muon in such a three body decay can be estimated by disregarding the neutrino. Calculating the maximum possible momenta of the muon this way, one gets in the case of the B decay approximately 2.3 GeV, in the case of the D decay less than 0.9 GeV. A boost in the direction of the B or D meson has no influence on the transversal momentum relative to the jet direction. Due to the mass of the D meson its p_T^{rel} is small compared to the muons p_T^{rel}. Therefore it can be expected that muons with a small value of p_T^{rel} are more likely to originate from a D decay, whereas high values of p_T^{rel} more likely can be assigned to B decays.

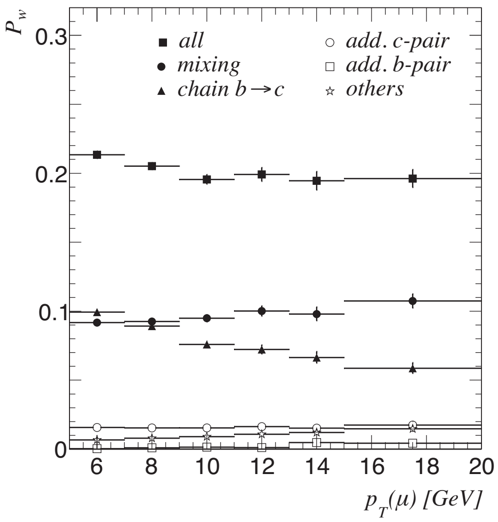

(a) $B_s^0 \to D_s^- \pi^+$

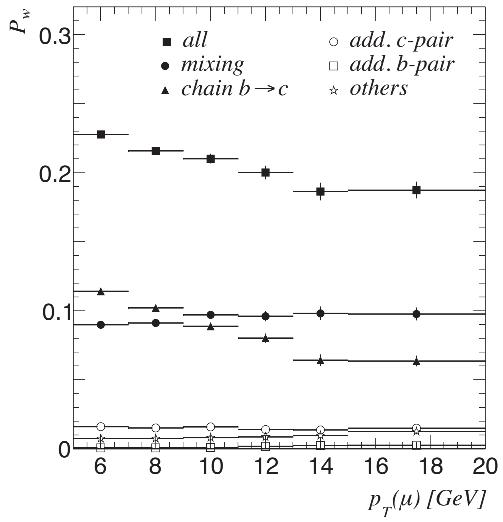

(b) $B_s^0 \to D_s^- a_1^+$

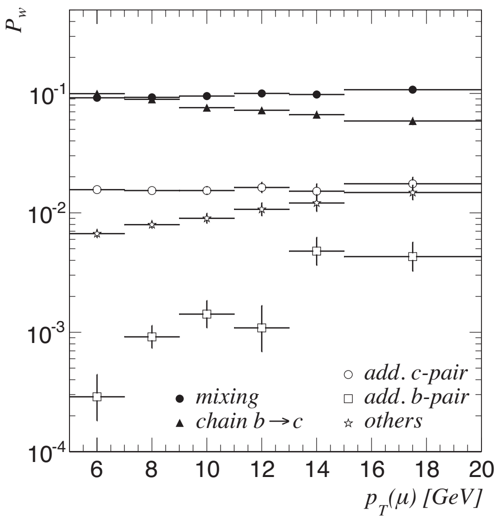

(c) $B_s^0 \to D_s^- \pi^+$

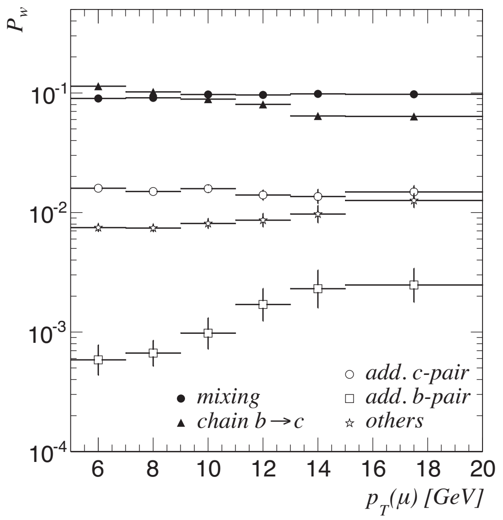

(d) $B_s^0 \to D_s^- a_1^+$

Figure 7.7: The wrong tag fraction P_w and its sources as a function of $p_T(\mu)$, left for $B_s^0 \to D_s^- \pi^+$, right for $B_s^0 \to D_s^- a_1^+$. The individual sources are muons chain decays $b \to c \to \mu$, muons from additional $b\bar{b}$ or $c\bar{c}$ pairs, muons from particles decaying into a $\mu^+\mu^- X$ final state, or wrong tags due to meson mixing of the tagging side B hadron. In the two top figures all distributions are compared on a linear scale, the filled squares correspond to the sum of all individual sources. The bottom figures detail the various sources of wrong tags on a logarithmic scale.

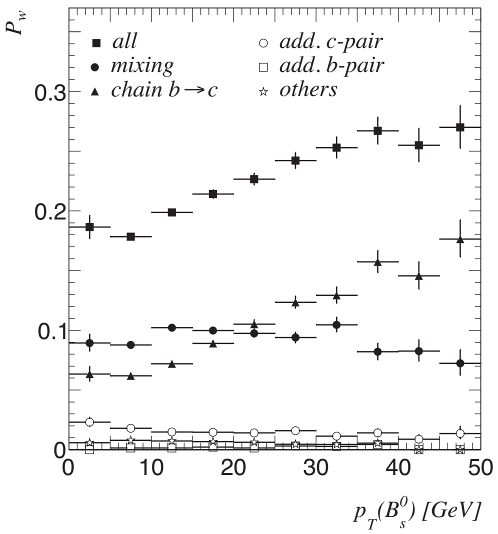

(a) $B_s^0 \to D_s^- \pi^+$

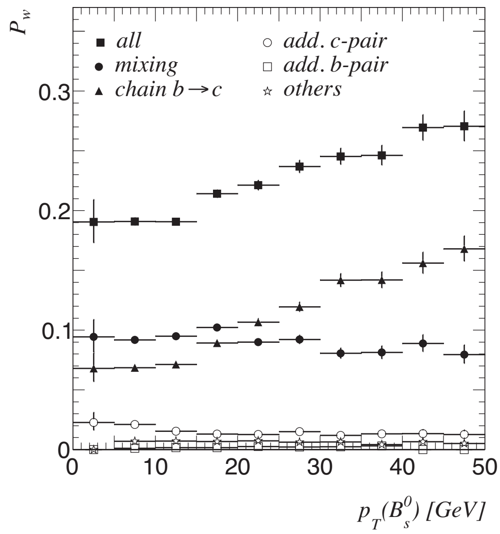

(b) $B_s^0 \to D_s^- a_1^+$

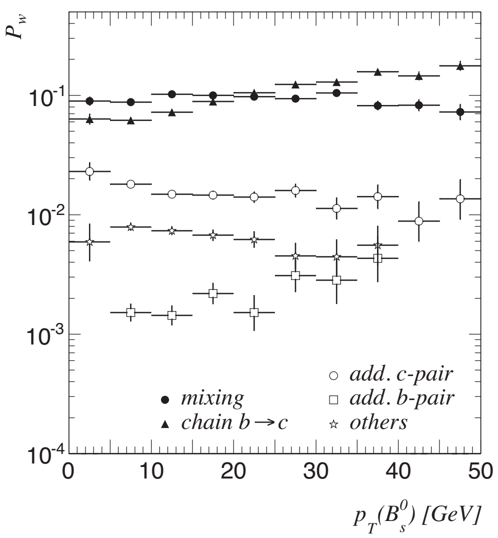

(c) $B_s^0 \to D_s^- \pi^+$

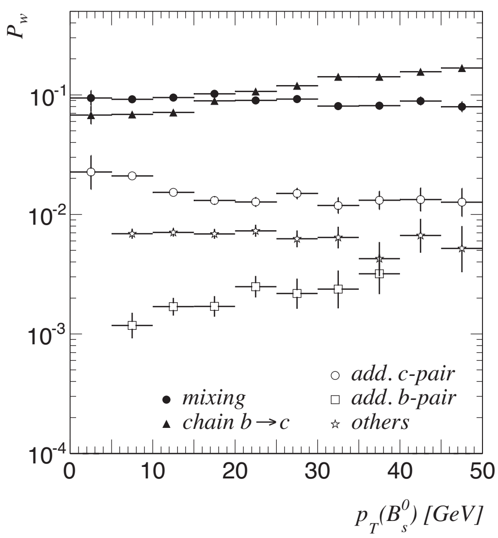

(d) $B_s^0 \to D_s^- a_1^+$

Figure 7.8: The wrong tag fraction P_w and its sources as a function of $p_T(B_s^0)$, left for $B_s^0 \to D_s^- \pi^+$, right for $B_s^0 \to D_s^- a_1^+$. The signal B_s^0 transverse momentum is taken from the Monte Carlo truth information. As in Figure 7.7, the total wrong tag fraction is split into its various sources. In the two top figures all distributions are compared on a linear scale, the filled squares correspond to the sum of all individual sources. The bottom figures detail the various sources of wrong tags on a logarithmic scale. The missing points in the logarithmic plots are due to zero entries in these bins.

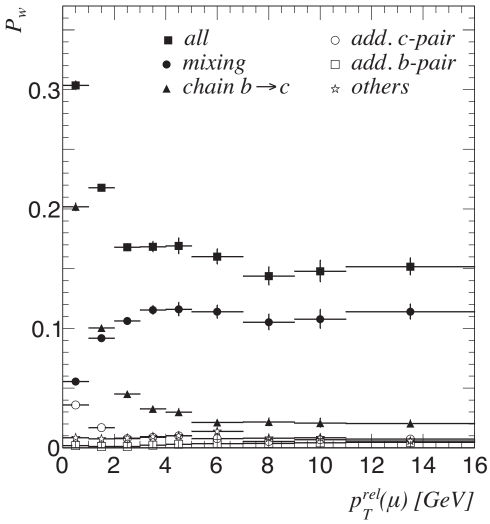

(a) $B_s^0 \to D_s^- \pi^+$

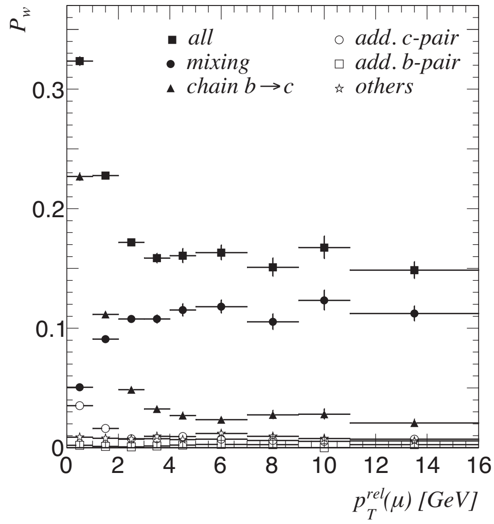

(b) $B_s^0 \to D_s^- a_1^+$

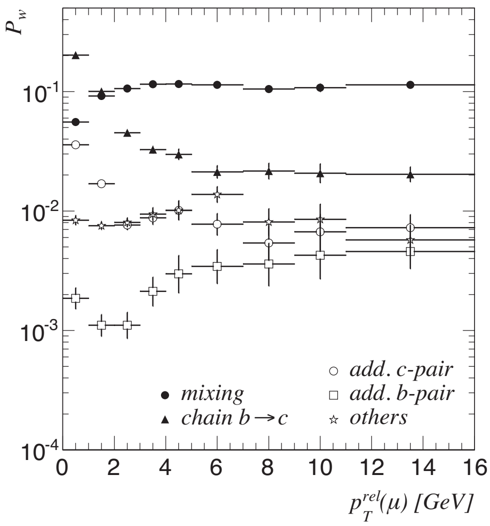

(c) $B_s^0 \to D_s^- \pi^+$

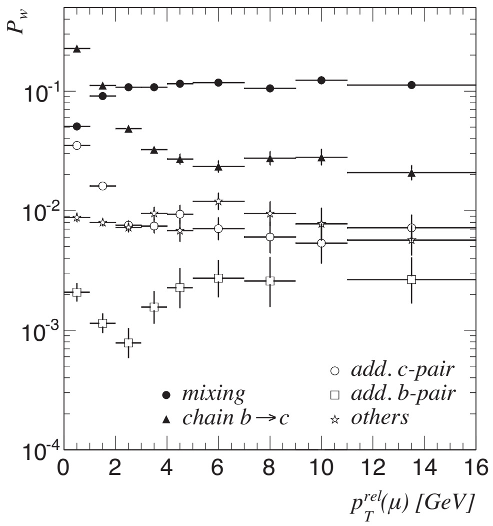

(d) $B_s^0 \to D_s^- a_1^+$

Figure 7.9: The wrong tag fraction P_w and its sources as a function of $p_T^{rel}(\mu)$, left for $B_s^0 \to D_s^- \pi^+$, right for $B_s^0 \to D_s^- a_1^+$. As in Figure 7.7, the total wrong tag fraction is split into its various sources. In the two top figures all distributions are compared on a linear scale, the filled squares correspond to the sum of all individual sources. The bottom figures detail the various sources of wrong tags on a logarithmic scale. The missing points in the logarithmic plots are due to zero entries in these bins.

In Figure 7.9 the wrong tag fraction and its various sources are shown as a function of $p_T^{rel}(\mu)$. As expected, for low values of $p_T^{rel}(\mu) < 1$ GeV the main contribution to the wrong tag fraction comes from chain decays $b \to c \to \mu$ in both hadronic decay channels. As an additional feature, the wrong tag fraction due to additional $c\bar{c}$ pairs is strongly increased in the low p_T^{rel} regime. Due to the large occurrence of muons from c-quarks fewer muons originate from semi-leptonic B decays. Consequently the wrong tag fraction due to mixing is strongly reduced in this regime. The total wrong tag fraction of events with $p_T^{rel}(\mu) < 1$ GeV is approximately 43.5 % for $B_s^0 \to D_s^- \pi^+$, and with approximately 48 % even larger for $B_s^0 \to D_s^- a_1^+$. In both cases, more than 70 % of those wrong tags arise from c-quarks decaying semi-leptonically.

It has been shown in Table 7.2, that between the two decay channels the total wrong tag fraction is larger for $B_s^0 \to D_s^- a_1^+$. Furthermore, in Table 7.3 it has been shown, that the main difference arises from wrong tags due to chain decays $b \to c \to \mu$. Without any kinematic cut, one does not expect such a difference. However, due to a different number of final state particles, cuts are introduced in the Monte Carlo generation as well as in the reconstruction. In Figure 7.9 it is shown, that with increasing $p_T^{rel}(\mu)$ the wrong tag fraction due to muons from chain decays and additional $c\bar{c}$ pairs is dropping, whereas the fraction due to mixing increases. In addition, in the low p_T^{rel} regime the wrong tag fraction due to chain decays differs between the two decay channels. As shown in the figures (a) and (b), at $p_T^{rel}(\mu) > 2$ GeV the wrong tag fraction is dominated by wrong tags from mixed B mesons. Further more, the total wrong tag fraction for the two decay channels is compatible in this regime:

$$B_s^0 \to D_s^- \pi^+ : \; P_w(p_T^{rel}(\mu) > 2 \text{ GeV}) = 0.164 \pm 0.002 \tag{7.1}$$

$$B_s^0 \to D_s^- a_1^+ : \; P_w(p_T^{rel}(\mu) > 2 \text{ GeV}) = 0.165 \pm 0.002. \tag{7.2}$$

This shows, that the difference in terms of wrong tag fraction between the two decay channels could be eliminated by properly selecting a cut on $p_T^{rel}(\mu)$. However, a cut of $p_T^{rel}(\mu) > 2$ GeV would lead to a loss in terms of tagging efficiency, resulting in $\varepsilon = 43$ % for both channels.

7.3 Multivariate Analysis for the Measurement of a Per-Event Wrong Tag Fraction

Flavour tagging is a crucial ingredient for the measurement of the B_s^0 oscillation frequency Δm_s, described in Chapter 2.3.2. This mixing parameter can be fitted by minimising a likelihood function. One crucial parameter in this method is the wrong tag fraction. One possible approach is the usage of a global wrong tag fraction for each decay channel. However, as we have seen before, the global wrong tag fraction strongly depends on the trigger menu or on kinematic cuts as e.g. on $p_T(B_s^0)$. Therefore for any modification of the experimental setup the wrong tag fraction for each sub-sample has again to be determined by Monte Carlo events.

Instead of using a global wrong tag fraction, an alternative method is based on the combination of the various known kinematic dependencies to one, single variable. Building the wrong tag fraction as an arbitrary function of such a variable allows the implementation of an event-by-event wrong tag fraction $P_{w,i}$ in the likelihood function. This way, for example increasing the trigger cut on the muon p_T has an influence on the global wrong tag fraction, but not on the individual event-by-event wrong tag fractions. Furthermore, compared to a global wrong tag fraction, the introduction of a per-event wrong tag fraction reduces the total error of the fit, as shown in more detail in [147]. Now the wrong tag fraction taking the role of per-event-errors, with increasing width of the distribution of the wrong tag probability, the errors of the parameters in the likelihood fit improve [108].

In Chapter 7.3.1 the determination of the fit parameters using a likelihood function is explained. The full work on this topic is published in all details for the decay channel $B_s^0 \to D_s^- a_1^+$ in [142]. In Chapter 7.3.2 various multivariate methods combining the known kinematic dependencies are compared and validated.

7.3.1 Likelihood Function

In this chapter, the construction of the likelihood function is outlined, more detail (e.g. on normalisation, resolution function or combinatorial background) can be found in [142]. The likelihood function for the determination of Δm_s starts with the time dependent probability functions $\mathcal{P}(t)(B^0 \to B^0)$ and $\mathcal{P}(t)(B^0 \to \bar{B}^0)$ given in the Equations (2.81) and (2.82). These two functions describe the probability, that an initial B_q^0 meson decays a B_q^0 or as its anti-particle, $\bar{B}_q^0$, where $q \in \{d, s\}$. These two probability functions can be combined to one common function

$$\mathcal{P}_q(t_0, \mu_0) = \frac{\Gamma_q^2 - \left(\frac{\Delta\Gamma_q}{2}\right)^2}{2\Gamma_q} \cdot e^{-\Gamma_q t_0} \cdot \left(\cosh\frac{\Delta\Gamma_q t}{2} + \mu_0 \cos(\Delta m_q t_0)\right), \tag{7.3}$$

where $\mathcal{P}$ depends on the proper time t_0 and the newly introduced parameter describing the mixing state, μ_0, where $\mu_0 = -1$ corresponds to the the oscillating case $\mathcal{P}(t)(B^0 \to \bar{B}^0)$ and $\mu_0 = +1$ to the non-mixing case $\mathcal{P}(t)(B^0 \to B^0)$.

The measurement of the proper decay time is based on the measurement of the decay length. Taking into account the dilution due to experimental effects, the probability function has to be convoluted with a detector resolution function $\text{Res}_q(t_{rec}|t_0)$ [142]:

$$q_q(t_{rec}, \mu_0) = \frac{1}{N_q}\int_0^\infty \mathcal{P}_q(t_0, \mu_0) \cdot \text{Res}_q(t_{rec}|t_0)dt_0. \tag{7.4}$$

The flavour tagging introduces an additional dilution, which alters the observed probability density function:

$$\tilde{q}_q(t_{rec}, P_w, \mu) = (1 - \mathcal{P}_w) \cdot q_q(t_{rec}, \mu) + \mathcal{P}_w \cdot q_q(t_{rec}, -\mu). \tag{7.5}$$

In this equation the parameter μ_0 has been replaced by the parameter μ, indicating, that the flavour of the signal B_q^0 meson has been determined by a flavour tagger. In contrast to [142], in (7.5) the wrong tag fraction P_w is not a global value for all events of one decay channel, but equivalent to a measurement variable.

For the full likelihood function, in addition to the signal channels an additional probability function describing the non-oscillating combinatorial background has to be considered. As the contribution of this background is decreasing with time an exponential decay with the decay width Γ_{cb} can be assumed. Following the same calculations as before, by setting Δm_q and $\Delta\Gamma_q$ to zero one gets the probability function independent of the actually measured wrong tag fraction and flavour tag:

$$\tilde{q}_{cb}(t, P_w, \mu) = \frac{\Gamma_{cb}}{2} \cdot e^{-\Gamma t}. \tag{7.6}$$

Considering the signal and background distributions $q' \in d, s, cb$ with its corresponding fraction $f_{q'}$, the complete probability density function becomes

$$\mathrm{pdf}(t_{rec}, P_w, \mu) = \sum_{q'=s,d,cb} f_{q'} \cdot \tilde{q}_{q'}(t_{rec}, P_w, \mu) \tag{7.7}$$

The total likelihood function for the N_{ch} decay channels is obtained by multiplying the individual probability density functions $\mathrm{pdf}^k(t_{rec,i}, P_{w,i}, \mu_i)$ of each decay channel k and for each event i:

$$\mathcal{L}(\Delta m_s, \Delta\Gamma_s) = \prod_{k=1}^{N_{ch}} \prod_{i=1}^{N_{ev}^k} \mathrm{pdf}^k(t_{rec,i}, P_{w,i}, \mu_i), \tag{7.8}$$

In this likelihood function the measured parameters for each event are the lifetime, the flavour tag and the wrong tag fraction. The parameters Δm_d and Γ_q are taken from reference tables [125], the only remaining parameters are Δm_s and $\Delta\Gamma_s$. Maximising the likelihood function (7.8) is used to measure these parameters.

7.3.2 Multivariate Analysis of Hadronic B_s^0 decays

In Chapter 7.2.2 we have seen, that the wrong tag fraction is a function of various kinematic observables. Consequently, regarding one single event, the determination of a tag probability has to merge all possible information gathered so far. The aim of this chapter is to merge several kinematic measurement variables discussed in the previous section into one single variable v_{mva}. The wrong tag fraction will be an arbitrary function of this variable. In order to improve the error of the Δm_s likelihood fit, the distribution of the per-event wrong tag fractions should have a large RMS [108]. This means, that the single variable v_{mva} is supposed to discriminate between events with a small and a large wrong tag fraction. Furthermore, as we have seen in Chapter 6.2, various trigger scenarios have different tagging efficiencies and wrong tag fractions. By creating the single variable v_{mva} with an unbiased sample, the wrong tag fraction becomes independent of the trigger scenario used, only depending on the kinematic input variables. In this chapter the input variables used are the tagging muon transverse momentum $p_T(\mu)$, the tagging muon relative transverse momentum to the closest jet $p_T^{rel}(\mu)$ as well as the signal B_s^0 transverse momentum $p_T(B_s^0)$.

In this chapter three different multivariate methods are used in order to obtain wrong tag fractions depending on a single discriminating variable v_{mva}: a *Fisher discriminator*, a *boosted decision tree* and a *artificial neural network*.

7.3.2.1 The Multivariate Analysis Software

The program TmvaAnalysis[6] used to train, test and validate the discriminating variable is based on the Toolkit for Multivariate Data Analysis with Root (Tmva). This toolkit is described in detail in [101], the various multivariate techniques used in the section all are explained in detail in [77]. In the following the common steps for all multivariate methods are described. Each method is applied separately to both hadronic decay channels $B_s^0 \to D_s^- \pi^+$ and $B_s^0 \to D_s^- a_1^+$.

The true signal B_s^0 flavour is given by the Monte Carlo truth information and compared with the tagging information retrieved from the BFlavourCombinedTagger. The events successfully tagged can be classified into two categories: correctly tagged or wrong tagged. The events not successfully tagged are not of concern here. For all event the kinematic observables $p_T(\mu)$, $p_T^{rel}(\mu)$ and $p_T(B_s^0)$ are calculated and set as input discriminating observables in the software. The data samples are split into two even parts: 50 % of the events are used as training samples, the remaining events are used as validation samples. The training samples are used to train the multivariate method to find a variable v_{mva} which discriminates the two event categories wrong and correct tagged.

In the next step, the trained multivariate analysis is tested with the training sample and furthermore validated with the validation sample. In this phase the program calculates correlations between the input observables and the resulting v_{mva}, the signal efficiency and the signal purity. Furthermore the training method is checked for overtraining, in which too many input observables have been chosen and adjusted to too few data points.

In a last step the multivariate analysis is applied to the events of the data training and validation sample separately. For each distribution with the knowledge of the true signal B_s^0 flavour the wrong tag fraction is created as a function of the variable v_{mva}. For the training sample, the wrong tag fraction is fitted as an polynomial function of v_{mva} (i.e. a polynomial). In order to check the statistical consistency between the training sample and the validation sample the corresponding χ^2/ndf is calculated.

[6]The source code can be downloaded here: `http://physik.uibk.ac.at/~jussel/tmvaTagging/`

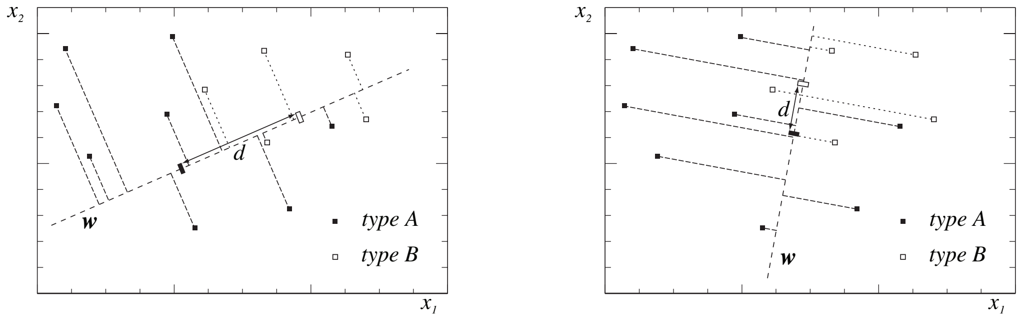

Figure 7.10: The same sample consisting of events of type A and type B projected on two different axis, denoted by w. The mean values of the two samples have a distance d. In the left Figure the axis better pushes the mean values of the two data samples apart.

The main criteria for a good multivariate method in this case is not a fast training cycle or an excellent discrimination, but that the distributions of both, training and validation sample, lie within their statistical error.

7.3.2.2 Multivariate Analysis Methods and Datasets

The first analysis method is the so-called *Fisher discrimination* [86]. In this method the n-dimensional data points are projected onto an axis in a lower dimensional hyperplane. The mean values of the two different event types (i.e. wrong and correct tags) are calculated. The axis is chosen such that the two mean values are pushed as far as possible from each other to get the best separation. The principle of this method is illustrated in Figure 7.10. In this figure the 2-dimensional data points of type A and B are projected onto a 1-dimensional axis $\mathbf{w}$. The distance between the mean values is denoted by d. The linear Fisher discrimination method is described in more detail in [77].

The second multivariate analysis method is a *boosted decision tree* (BTD). This method classifies the events by repeatedly asking questions about one single variable with answers of the type *yes/no*. As soon as some criterion on the first variable is fulfilled, another set of questions is posed on the next variable and so on. Following one leaf of questions, the events are classified as correct or wrong tagged, depending on the ratio of these event types in the training phase.

In a further step, if events have been misclassified in the first decision tree, the variables are boosted by giving these events a higher weight in the following decision tree. In this chapter the boosting is performed by the so-called AdaBoost method [47]. This

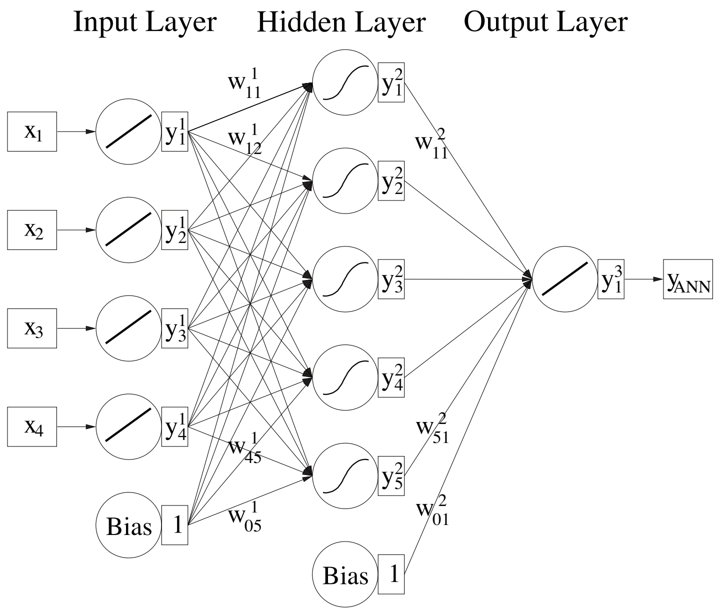

Figure 7.11: A multilayer perceptron with four input variables and one hidden layer. Image taken from [101].

way more decision trees are combined, building a decision forest. In the end the events can be discriminated by one single classifier.

The last multivariate analysis is done with *artificial neural networks* (ANN). Within this chapter two different feed-forward multilayer perceptrons are used: the Clermont-Ferrand neural network and the MultiLayerPerceptron MLP, both part of the TMVA package [101]. More on neural networks can be found in [77], here I will just give a very brief comment on the ANNs used.

The first ANN is named after the city in which is was developed. It has been used for the Higgs Analysis in the ALEPH collaboration as well as for a detailed background study in the BaBar collaboration. Originally it was written in Fortran, however it has been translated into C++ in the TMVA package. In principle the Clermont-Ferrand ANN is a feed-forward multilayer neural network. The second ANN is the ROOT neural network class TMULTILAYERPERCEPTRON. An example of a multilayer perceptron with one hidden layer is illustrated in Figure 7.11.

	correct tag			wrong tag		
	$p_T(\mu)$	$p_T(B_s^0)$	$p_T^{rel}(\mu)$	$p_T(\mu)$	$p_T(B_s^0)$	$p_T^{rel}(\mu)$
$B_s^0 \to D_s^- \pi^+$	$\begin{pmatrix} 1.000 & 0.151 & 0.167 \\ 0.151 & 1.000 & -0.046 \\ 0.167 & -0.046 & 1.000 \end{pmatrix}$			$\begin{pmatrix} 1.000 & 0.062 & 0.461 \\ 0.062 & 1.000 & -0.074 \\ 0.461 & -0.074 & 1.000 \end{pmatrix}$		
$B_s^0 \to D_s^- a_1^+$	$\begin{pmatrix} 1.000 & 0.157 & 0.134 \\ 0.157 & 1.000 & -0.048 \\ 0.134 & -0.048 & 1.000 \end{pmatrix}$			$\begin{pmatrix} 1.000 & 0.146 & 0.271 \\ 0.146 & 1.000 & -0.086 \\ 0.271 & -0.086 & 1.000 \end{pmatrix}$		

Table 7.4: Correlation matrix for the three observables $p_T(\mu)$, $p_T(B_s^0)$ and $p_T^{rel}(\mu)$ for the two decay channels $B_s^0 \to D_s^- \pi^+$ and $B_s^0 \to D_s^- a_1^+$ and separated for events with a correct tag (left) and a wrong tag (right).

7.3.2.3 Analysis and Results

In this analysis the two data samples of the decay type $B_s^0 \to D_s^- \pi^+$ and $B_s^0 \to D_s^- a_1^+$ from Table 7.1 are analysed. All events are required to have a successful flavour tag, either correct or wrong. Furthermore, the following three observables have to be reconstructed successfully: $p_T(\mu)$, $p_T(B_s^0)$ and $p_T^{rel}(\mu)$. However, in order to have enough events available, $p_T(B_s^0)$ is taken from the Monte Carlo truth information. These three observables are considered as input variables for the multivariate analysis, the events attribute *correct tag* or *wrong tag* is used for the classification of the events.

In a first step, the input variables of the multivariate analysis of both decay channels are checked for correlations. In the previous chapter the various correlations have been already discussed qualitatively. In Table 7.4 the correlation matrices for the two decay channels are shown, divided into the events with a correct tag and with a wrong tag. The correlation of two variables X and Y is defined as

$$\rho(X, Y) = \frac{\mathrm{cov}(X, Y)}{\sigma_X \sigma_Y}, \tag{7.9}$$

where $\mathrm{cov}(X, Y)$ is the covariance between the two variable. A correlation factor lies within $[-1, 1]$, where independent variables are described by correlation of *zero*.

One can see, that the correlations have a small dependence of the decay channel due to the different kinematic situation in the two channels. However, the correlation between the two muonic variables $p_T(\mu)$ and $p_T^{rel}(\mu)$ is larger for wrong tagged events. This correlation mainly origins from the different wrong tag fraction P_w in the regions of $p_T^{rel}(\mu) < 2$ GeV, where P_w is large and strongly varying, and $p_T^{rel}(\mu) > 2$ GeV, where P_w has reached a smaller, constant value. However, no input variable is fully correlated with another one.

In the first analysis shown in Figure 7.12 and Figure 7.13 the data is trained by a linear Fisher discriminator. In the first case, no re-weighting of the input variables is performed, in the latter the events have been re-weighted using the AdaBoost boosting method [47]. In the left figures the distribution of v_{mva} is shown for the first 50 % of the events, corresponding to the training sample (solid line) and for the remaining validation events (dashed line). In both methods the wrong tag fraction for the training sample is fitted with a polynomial of third order, the parameters are given in the top, right box.

For both Fisher analysis methods the distribution of the wrong tag fraction matches between the training sample and the validation sample. In Table 7.5 the two distributions of wrong tag fraction are compared by calculating their χ^2/ndf. In addition in this table the integrated probability $Q_{\chi^2,ndf}$ to measure this χ^2 or a larger value is shown. Values of $Q_{\chi^2,ndf} < 0.05$ correspond to a 95 % CL.

Despite the shape of the P_w distributions match between the training and validation sample, these results indicate that boosting of the input variables does not improve the results, but rather downgrade. Concluding, the Fisher method without re-weighting give a χ^2/ndf of 26.01/20 for $B_s^0 \to D_s^- \pi^+$ and of 27.81/20 for $B_s^0 \to D_s^- a_1^+$. Despite a small fluctuation at $v_{mva} = 0.2$ for $B_s^0 \to D_s^- a_1^+$, all data points of both, the training and validation sample, can be described by the fitted polynomial within the statistical error.

The results for the second method, the boosted decision tree, are illustrated in Figure 7.14. While the training and validation distributions of v_{mva} for $B_s^0 \to D_s^- \pi^+$ match each other, for $B_s^0 \to D_s^- a_1^+$ this does not hold. This fact is reflected in the distribution of the wrong tag fraction, where for most values of v_{mva} the wrong tag fraction of the validation sample lie above the P_w value of the training sample. This difference in the shape is compensated by a small difference in the range $0.30 < v_{mva} < 0.35$.

Quantitatively shown in Table 7.5, for the decay channel $B_s^0 \to D_s^- \pi^+$ the training and validation sample match, but for $B_s^0 \to D_s^- a_1^+$ with $\chi^2/ndf = 58.43/10$ the boosted decision tree by far cannot match these two samples.

MVA-Method	$B_s^0 \to D_s^- \pi^+$		$B_s^0 \to D_s^- a_1^+$	
	χ^2/ndf	$Q_{\chi^2,ndf}$	χ^2/ndf	$Q_{\chi^2,ndf}$
Fisher	26.01/20	0.165	27.81/20	0.114
Boosted Fisher	30.90/18	0.030	34.42/17	0.011
AdaBoost BDT	6.05/11	0.870	58.43/10	0
Multi Layer Perceptron	54.44/11	0	67.01/12	0
Clermont-Ferrand	8.85/11	0.636	12.75/11	0.3099

Table 7.5: Comparison of the validation sample against the training sample in the distributions of P_w by calculating χ^2 (see Figure 7.12-7.16). For each distribution and each method χ^2/ndf and the probability $Q_{\chi^2,ndf}$ are displayed.

In a final step, the multivariate analysis is performed with the two ANN, the ROOT multilayered perceptron in Figure 7.15, and the Clermont-Ferrand ANN in Figure 7.16.

Regarding the MLP, for both decay channels the distributions of v_{mva} do not match between training and validation sample. As shown in the right figures, apart from a small region around $v_{mva} \approx 0.85$ and at low values of v_{mva} the distribution of the validation samples lies well above the other. Comparing the two distributions by means of χ^2/ndf in Table 7.5, $Q_{\chi^2,ndf}$ is approximately zero for both decay channels.

Using the Clermont-Ferrand neural network, the distributions of training and validation sample well fit each other. Furthermore, the distributions of P_w perfectly match in the regime of $v_{mva} > 0.7$. Regarding the whole v_{mva} region, the trained neural network can reproduce the wrong tag fraction dependence in the validation sample. In terms of χ^2/ndf the Clermont-Ferrand ANN shows the best performance with 8.85/11 (12.75/11) for $B_s^0 \to D_s^- \pi^+$ ($B_s^0 \to D_s^- a_1^+$), as shown in Table 7.5.

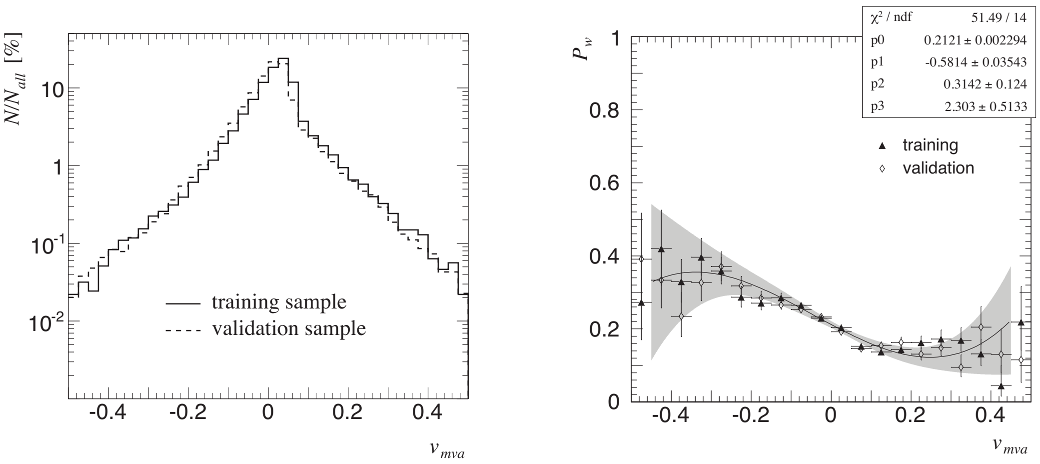

$B_s^0 \to D_s^- \pi^+$

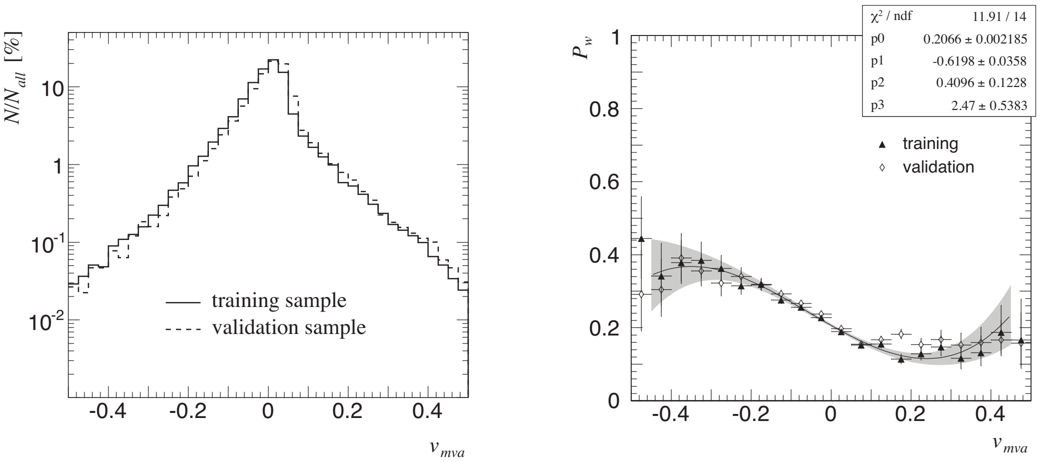

$B_s^0 \to D_s^- a_1^+$

Figure 7.12: Left, the distribution of training and validation events as a function of v_{mva}, where v_{mva} has been trained by using the TMVA method of *Fisher Discriminants*. Right, the wrong tag fraction P_w as a function of v_{mva}. At the top these dependencies are shown for the decay channel $B_s^0 \to D_s^- \pi^+$, at the bottom for $B_s^0 \to D_s^- a_1^+$. In both channels the training sample consists of 45 000 events, the remaining events are used as validation sample. The wrong tag results of the training sample are fitted with a polynomial of third order (solid line), the grey shaded areas display the statistical error of the fit. The fit parameters are in the top right box.

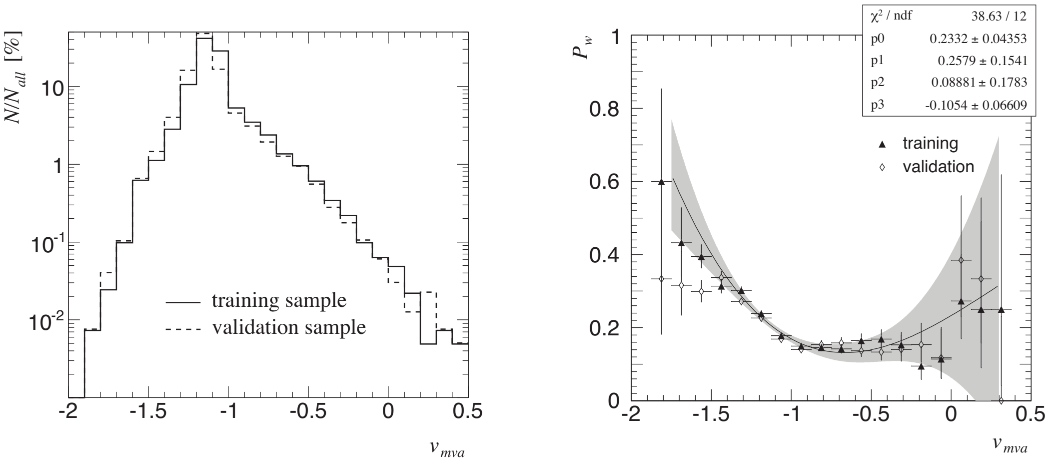

$B_s^0 \to D_s^- \pi^+$

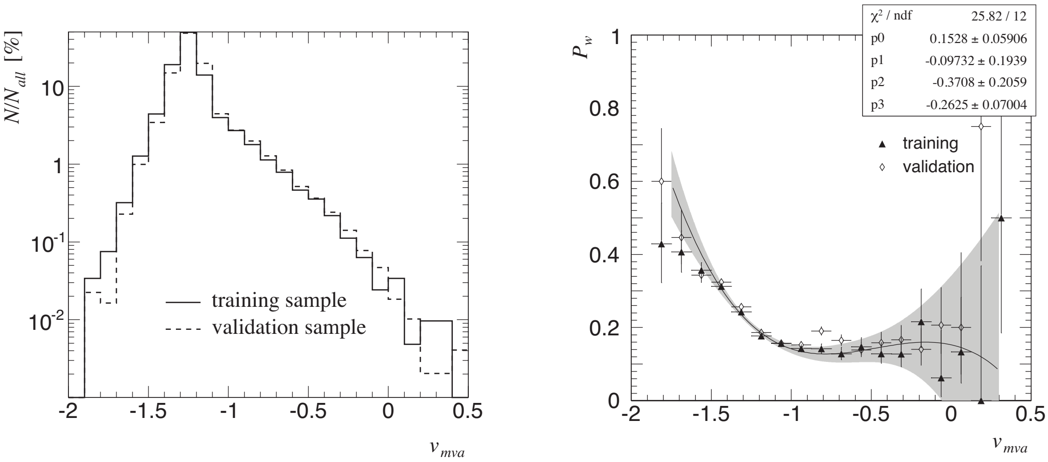

$B_s^0 \to D_s^- a_1^+$

Figure 7.13: Left, the distribution of training and validation events as a function of v_{mva}, where v_{mva} has been trained by using the TMVA method of *Fisher Discriminants* [86] boosted with ADABOOST [88]. Right, the wrong tag fraction P_w as a function of v_{mva}. At the top these dependencies are shown for the decay channel $B_s^0 \to D_s^- \pi^+$, at the bottom for $B_s^0 \to D_s^- a_1^+$. In both channels the training sample consists of 45 000 events, the remaining events are used as validation sample. The wrong tag results of the training sample are fitted with a polynomial of third order (solid line), the grey shaded areas display the statistical error of the fit. The fit parameters are in the top right box.

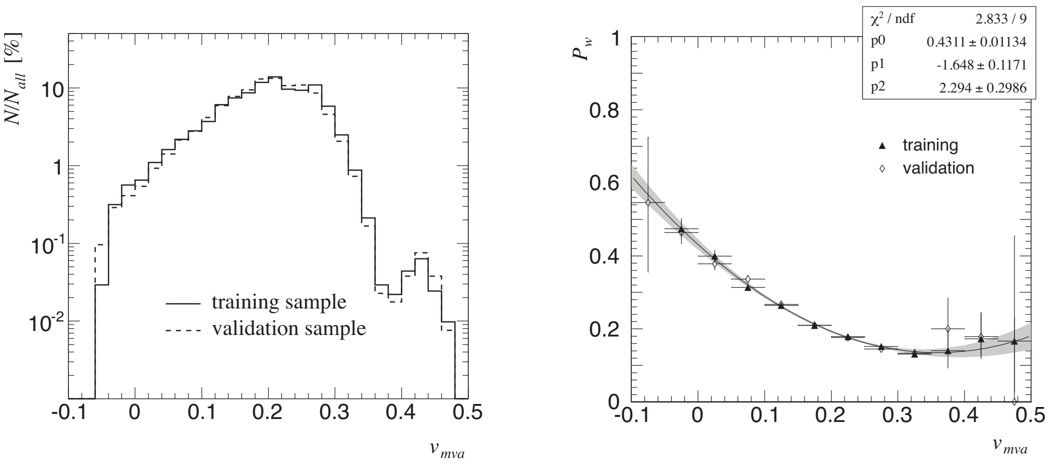

$B_s^0 \to D_s^- \pi^+$

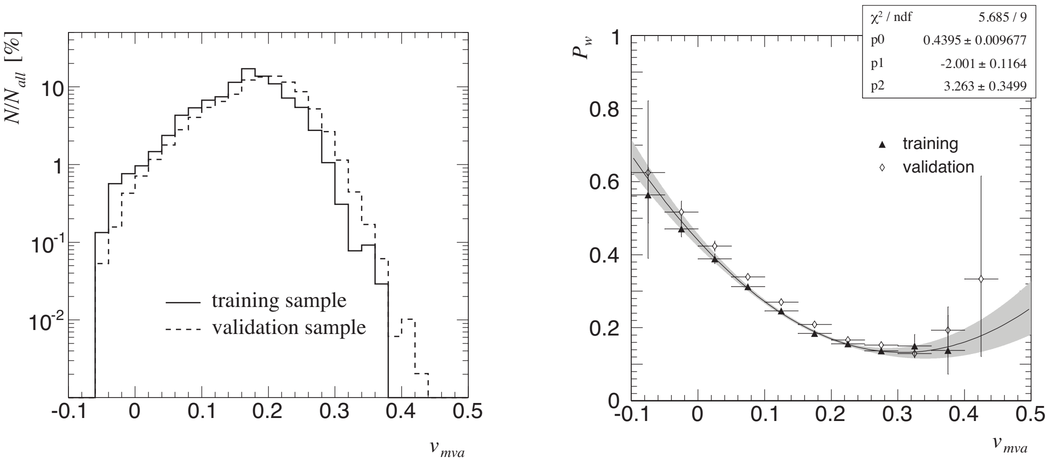

$B_s^0 \to D_s^- a_1^+$

Figure 7.14: Left, the distribution of training and validation events as a function of v_{mva}, where v_{mva} has been trained by using a decision tree, boosted with AdaBoost [88]. Right, the wrong tag fraction P_w as a function of v_{mva}. At the top these dependencies are shown for the decay channel $B_s^0 \to D_s^- \pi^+$, at the bottom for $B_s^0 \to D_s^- a_1^+$. In both channels the training sample consists of 45 000 events, the remaining events are used as validation sample. The wrong tag results of the training sample are fitted with a polynomial of third order (solid line), the grey shaded areas display the statistical error of the fit. The fit parameters are in the top right box.

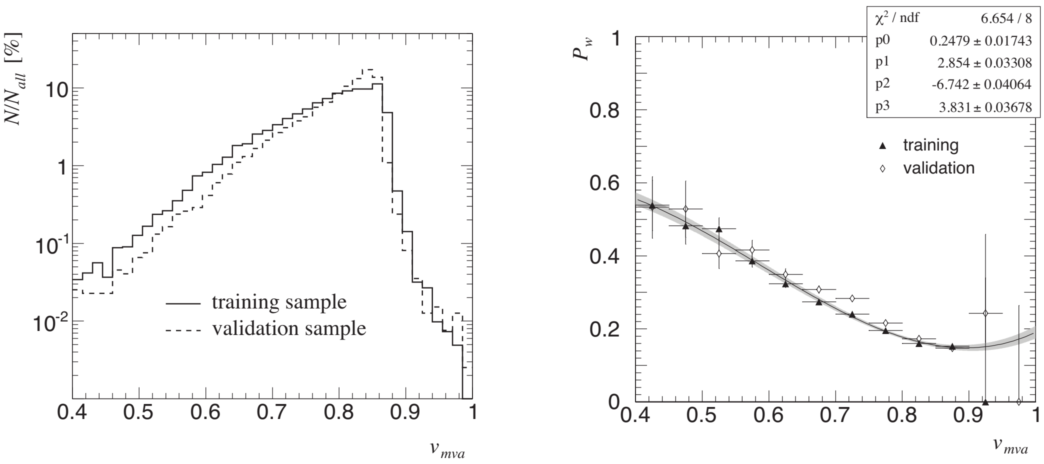

$B_s^0 \to D_s^- \pi^+$

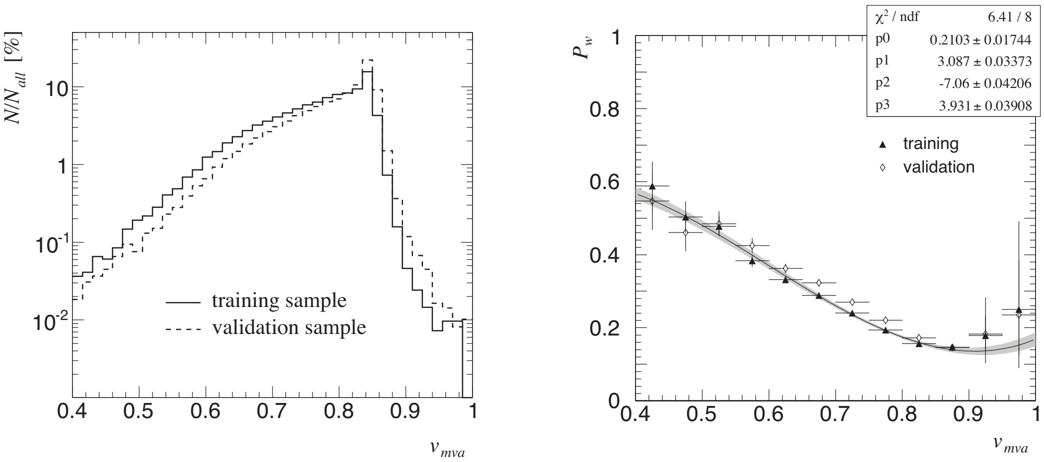

$B_s^0 \to D_s^- a_1^+$

Figure 7.15: Left, the distribution of training and validation events as a function of v_{mva}, where v_{mva} has been trained by using a Multi-Layered Perceptron, boosted with AdaBoost [88]. Right, the wrong tag fraction P_w as a function of v_{mva}. At the top these dependencies are shown for the decay channel $B_s^0 \to D_s^- \pi^+$, at the bottom for $B_s^0 \to D_s^- a_1^+$. In both channels the training sample consists of 45 000 events, the remaining events are used as validation sample. The wrong tag results of the training sample are fitted with a polynomial of third order (solid line), the grey shaded areas display the statistical error of the fit. The fit parameters are in the top right box.

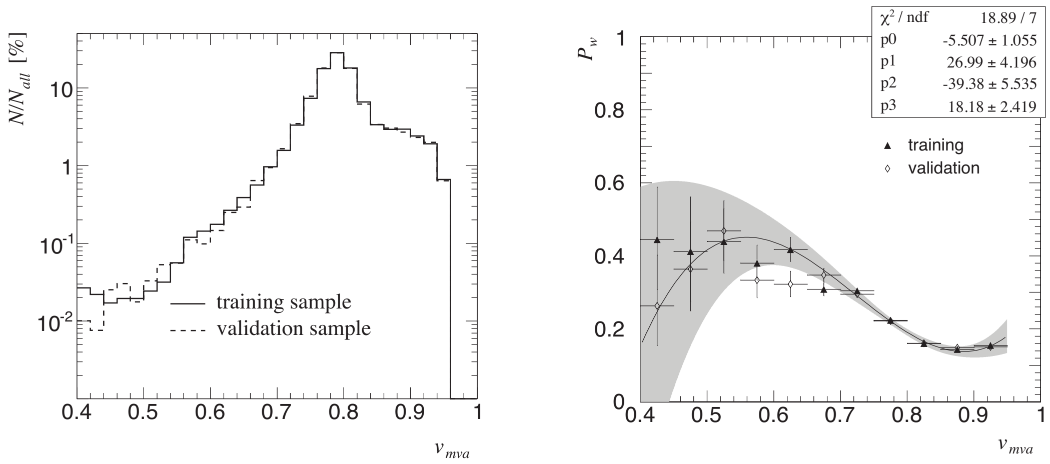

$B_s^0 \to D_s^- \pi^+$

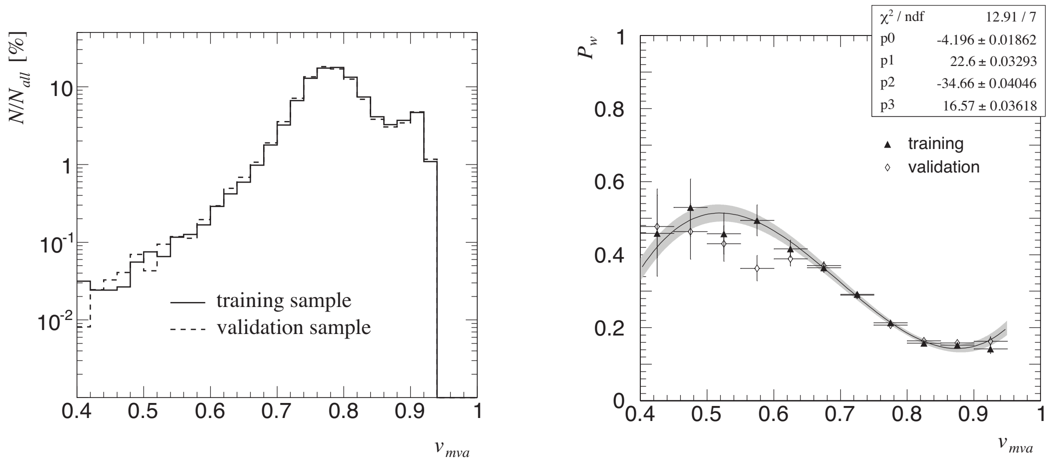

$B_s^0 \to D_s^- a_1^+$

Figure 7.16: Left, the distribution of training and validation events as a function of v_{mva}, where v_{mva} has been trained by using a Clermont-Ferrand neural network [101]. Right, the wrong tag fraction P_w as a function of v_{mva}. At the top these dependencies are shown for the decay channel $B_s^0 \to D_s^- \pi^+$, at the bottom for $B_s^0 \to D_s^- a_1^+$. In both channels the training sample consists of 45 000 events, the remaining events are used as validation sample. The wrong tag results of the training sample are fitted with a polynomial of third order (solid line), the grey shaded areas display the statistical error of the fit. The fit parameters are in the top right box.

CHAPTER

EIGHT

Summary and Conclusions

A full description of the electroweak interaction requires a precise measurement of the elements of the Cabibbo-Kobayashi-Maskawa matrix. Testing the unitarity of the CKM matrix is regarded as one possible path to unravel discrepancies within the Standard Model of Particle Physics. The precise determination of $\mathcal{CP}$ violation in heavy flavour B decays and the measurement of possible deviations from the Standard Model state a prominent candidate for the discovery of physics beyond the Standard Model.

In the ATLAS experiment various measurements of heavy flavour B_s^0 decays aim at the determination of the weak mixing phase ϕ_s, measured by a fit involving eight parameters. The main decay channel used in this analysis is $B_s^0 \to J/\psi(\mu^+\mu^-)\phi(K^+K^-)$. One crucial parameter in this analysis is the B_s^0 oscillation frequency Δm_s which will be measured in ATLAS using the hadronic decay channels $B_s^0 \to D_s^-(\phi\pi^-)\pi^+$ and $B_s^0 \to D_s^-(\phi\pi^-)a_1^+$.

The measurement of Δm_s can be separated into three important parts: the measurement of the B_s^0 decay time, the identification of the B_s^0 flavour at decay time and the measurement of the B_s^0 flavour at production time. While the first two items are covered by the reconstruction of the exclusive decay channels, the latter measurement is covered by methods of flavour tagging. In this thesis various aspects of flavour tagging of hadronic B decay channels are explored in detail.

As the ATLAS detector has a limited kaon/pion separation, flavour tagging methods like the reconstruction of the opposite side B decay or kaon tagging have a very limited performance. The method of same side jet charge tagging has shown a good performance in $B_s^0 \to J/\psi(\mu^+\mu^-)\phi(K^+K^-)$. However, due to the trigger strategy used for the identification of hadronic B_s^0 decays, the method of opposite side soft muon flavour tagging is by far the most promising method in the measurement of Δm_s and consequently proposed as the primary method.

In view of the increasing luminosity, trigger strategies will have to be adapted in order not to go beyond the scope of the trigger bandwidth assigned to the B physics working group. The possible sources of muons in B events have been explored in detail. The influence of trigger strategies with varying thresholds on the trigger muon p_T have been explored in detail as well as multi-muon and muon-electron trigger scenarios. This work has been performed on Monte Carlo generated events without reconstruction of the signal decay channel. Trigger efficiency, wrong tag fraction and tagging power have been studied in this thesis. In single muon trigger scenarios an increasing threshold on the muon transverse momentum has been found to improve the wrong tag fraction. Increasing thresholds in di-muon and muon-lepton trigger scenarios have a limiting impact on the tagging power.

In this thesis a flavour tagging algorithm has been developed and implemented within the ATLAS software framework. The flavour tagging algorithm has been applied to fully simulated events of the two decay channels exclusive $B_s^0 \to D_s^-\pi^+$ and $B_s^0 \to D_s^-a_1^+$ with $D_s^- \to \phi(K^+K^-)\pi^-$ and $a_1^+ \to \rho(\pi^+\pi^-)\pi^+$. Tagging efficiency, wrong tag fraction and tagging power have been analysed. The tagging power for the opposite side soft muon lepton tagging has been found to be 0.303 ± 0.005 for $B_s^0 \to D_s^-\pi^+$ and 0.281 ± 0.005 for $B_s^0 \to D_s^-a_1^+$. The sources of wrong tag fractions have been identified as wrong tags due to oscillations of the opposite side B meson, muons from chain decays of the type $b \to c \to \mu$, additional $c\bar{c}$ and $b\bar{b}$ pairs and muons e.g. from J/ψ and ρ mesons. In terms of tagging muon p_T, signal B_s^0 p_T and the tagging muon transverse momentum relative to the closest jet p_T^{rel} the differential behaviour of these sources and their interplay have been explored in detail.

For the measurement of the oscillation frequency Δm_s a method for a per-event wrong tag fraction based on a multivariate analysis has been developed. A multivariate analysis using unbiased data samples without any cut makes the flavour tagging algorithm independent of the muon trigger p_T threshold. Based on the Toolkit for Multivariate Data Analysis TMVA a program has been written in order to test various multivariate techniques. The combination of $p_T(\mu_{tag})$, $p_T(B_s^0)$ and p_T^{rel} into one single variable has been investigated by using two kinds of Fisher discrimination, a boosted decision tree and two different artificial neural network for both decay channels $B_s^0 \to D_s^- \pi^+$ and $B_s^0 \to D_s^- a_1^+$. The quality of the multivariate methods has been validated by comparing the results of the training sample with a validation sample. The usage of a Clermont-Ferrand neural network has shown a good performance and the validation- and training sample are compatible with each other with 95 % CL. In addition, this neural network shows a good discrimination of events in terms of wrong tag fraction. The usage of the Clermont-Ferrand neural network for the calculation of a per-event wrong tag fraction has been validated and therefore is proposed for the usage in the measurement of the B_s^0 oscillation frequency Δm_s.

Within this year, the flavour tagging algorithm as well as the multivariate analysis will be calibrated using the non-oscillating exclusive decay channel $B^+ \to J/\psi(\mu^+\mu^-)K^+$. The flavour tagging algorithm developed in this thesis is ready to be implemented into all kinds of precision measurements involving oscillating B^0 mesons, as e.g. the measurement of the B_s^0 oscillation frequency Δm_s.

APPENDIX

A

Some Calculations with the CKM Matrix in Wolfenstein Parametrisation in higher Orders

In section 2.3.1.2 the CKM matrix in the Wolfenstein parametrisation has been introduced in with the definitions

$$
\begin{aligned}
&\sin\Theta_{12} = \lambda \\
&\sin\Theta_{23} = A\lambda^2 \\
&\sin\Theta_{13}e^{-i\delta} = A\lambda^3(\rho - i\eta)
\end{aligned}
\tag{A.1}
$$

where the current fitted values by UTFit collaboration [55] are

$$
\begin{aligned}
&\rho = 0.135 \pm 0.021 \\
&\eta = 0.367 \pm 0.013 \\
&A = 0.8095 \pm 0.0095 \\
&\lambda = 0.22545 \pm 0.00065.
\end{aligned}
\tag{A.2}
$$

The CKM matrix, expanded as a series in powers of λ up to $\mathcal{O}(\lambda^3)$ already is shown in Equation (2.49), in this appendix the matrix elements of the CKM matrix are written up to an order of $\mathcal{O}(\lambda^5)$:

$$\begin{pmatrix} 1-\frac{\lambda^2}{2}-\frac{\lambda^4}{8} & \lambda & A\lambda^3(-i\eta+\rho) \\ -\lambda+\frac{1}{2}A^2\lambda^5(1-2(i\eta+\rho)) & 1-\frac{\lambda^2}{2}-\frac{1}{8}\left(1+4A^2\right)\lambda^4 & A\lambda^2 \\ A\lambda^3\left(1-\left(1-\lambda^2\right)(i\eta+\rho)\right) & -A\lambda^2+\frac{1}{2}A\lambda^4(1-2(i\eta+\rho)) & 1-\frac{A^2\lambda^4}{2} \end{pmatrix} \tag{A.3}$$

In the following, the six orthogonality relations (2.51-2.56) and their deviations from zero are calculated.

Triangle $V_{ud}V_{ub}{}^* + V_{cd}V_{cb}{}^* + V_{td}V_{tb}{}^* = 0$

$$\begin{aligned} V_{ud}V_{ub}{}^* &= \lambda^5 A\left(-\frac{1}{2}i\eta-\frac{\rho}{2}\right)+\lambda^7 A\left(-\frac{1}{8}i\eta-\frac{\rho}{8}\right)+\lambda^3 A(i\eta+\rho) \\ V_{cd}V_{cb}{}^* &= -\lambda^3 A+\lambda^7 A^3\left(\frac{1}{2}-i\eta-\rho\right) \\ V_{td}V_{tb}{}^* &= \lambda^3 A(1-i\eta-\rho)+\lambda^5 A(i\eta+\rho)+\lambda^7 A^3\left(-\frac{1}{2}+\frac{1}{2}i\eta+\frac{\rho}{2}\right) \end{aligned} \tag{A.4}$$

$$\begin{aligned} & V_{ud}V_{ub}{}^* + V_{cd}V_{cb}{}^* + V_{td}V_{tb}{}^* = \\ &= \left(\frac{i\eta}{2}+\frac{\rho}{2}\right)A\lambda^5-\frac{1}{8}\left((1+4A^2)(i\eta+\rho)\right)A\lambda^7+\mathcal{O}(\lambda^9) \end{aligned} \tag{A.5}$$

Triangle $V_{ud}V_{us}{}^* + V_{cd}V_{cs}{}^* + V_{td}V_{ts}{}^* = 0$

$$\begin{aligned} V_{ud}V_{us}{}^* &= \lambda-\frac{\lambda^3}{2}-\frac{\lambda^5}{8} \\ V_{cd}V_{cs}{}^* &= -\lambda+\frac{\lambda^3}{2}+\lambda^5\left(\frac{1}{8}+A^2(1-i\eta-\rho\right)+\lambda^7 A^2\left(-\frac{1}{4}+\frac{1}{2}i\eta+\frac{\rho}{2}\right) \\ V_{td}V_{ts}{}^* &= \lambda^5 A^2\left(-1+i\eta+\rho\right)+\frac{\lambda^7 A^2}{2}\left(1-i\eta+2\eta^2-5\rho+2\rho^2\right) \end{aligned} \tag{A.6}$$

$$\begin{aligned} & V_{ud}V_{us}{}^* + V_{cd}V_{cs}{}^* + V_{td}V_{ts}{}^* = \\ &= \left(\frac{1}{4}+\eta^2-2\rho+\rho^2\right)A^2\lambda^7+\mathcal{O}(\lambda^9) \end{aligned} \tag{A.7}$$

Triangle $V_{us}V_{ub}{}^* + V_{cs}V_{cb}{}^* + V_{ts}V_{tb}{}^* = 0$

$$\begin{aligned}
V_{us}V_{ub}{}^* &= \lambda^4 A(i\eta + \rho) \\
V_{cs}V_{cb}{}^* &= \lambda^2 A - \frac{\lambda^4 A}{2} + \lambda^6\left(-\frac{A}{8} - \frac{A^3}{2}\right) \\
V_{ts}V_{tb}{}^* &= -\lambda^2 A + \frac{\lambda^6 A^3}{2} + \lambda^4 A\left(\frac{1}{2} - i\eta - \rho\right)
\end{aligned} \tag{A.8}$$

$$\begin{gathered}
V_{us}V_{ub}{}^* + V_{cs}V_{cb}{}^* + V_{ts}V_{tb}{}^* = \\
-\frac{A\lambda^6}{8} + \left(-\frac{1}{4} + \frac{1}{2}i\eta + \frac{\rho}{2}\right)A^3\lambda^8 + \mathcal{O}(\lambda^9)
\end{gathered} \tag{A.9}$$

Triangle $V_{ud}{}^*V_{cd} + V_{us}{}^*V_{cs} + V_{ub}{}^*V_{cb} = 0$

$$\begin{aligned}
V_{ud}{}^*V_{cd} &= -\lambda + \frac{\lambda^3}{2} + \lambda^5\left(\frac{1}{8} + \frac{A^2}{2} - iA^2\eta - A^2\rho\right) + \lambda^7\left(-\frac{A^2}{4} + \frac{1}{2}iA^2\eta + \frac{A^2\rho}{2}\right) \\
V_{us}{}^*V_{cs} &= \lambda - \frac{\lambda^3}{2} + \left(-\frac{1}{8} - \frac{A^2}{2}\right)\lambda^5 \\
V_{ub}{}^*V_{cb} &= \lambda^5 A^2\left(i\eta + \rho\right)
\end{aligned} \tag{A.10}$$

$$\begin{gathered}
V_{ud}{}^*V_{cd} + V_{us}{}^*V_{cs} + V_{ub}{}^*V_{cb} = \\
= \left(-\frac{1}{4} + \frac{1}{2}i\eta + \frac{\rho}{2}\right)A^2\lambda^7 + \mathcal{O}(\lambda^9)
\end{gathered} \tag{A.11}$$

Triangle $V_{ud}{}^*V_{td} + V_{us}{}^*V_{ts} + V_{ub}{}^*V_{tb}$

$$\begin{aligned}
V_{ud}{}^*V_{td} &= \lambda^3 A(1 - i\eta - \rho) + \lambda^7 A\left(-\frac{1}{8} - \frac{3i\eta}{8} - \frac{3\rho}{8}\right) + \lambda^5 A\left(-\frac{1}{2} + \frac{3i\eta}{2} + \frac{3\rho}{2}\right) \\
V_{us}{}^*V_{ts} &= -A\lambda^3 + \lambda^5 A\left(\frac{1}{2} - i\eta - \rho\right) \\
V_{ub}{}^*V_{tb} &= \lambda^3 A(i\eta + \rho) + \lambda^7 A^3\left(-\frac{1}{2}i\eta - \frac{\rho}{2}\right)
\end{aligned} \tag{A.12}$$

$$\begin{gathered}
V_{ud}{}^*V_{td} + V_{us}{}^*V_{ts} + V_{ub}{}^*V_{tb} = \\
= \left(\frac{i\eta}{2} + \frac{\rho}{2}\right)A\lambda^5 - \left(\frac{A}{8}(1 + 3i\eta + 3\rho) + \frac{A^3}{2}(i\eta + \rho)\right)\lambda^7 + \mathcal{O}(\lambda^9)
\end{gathered} \tag{A.13}$$

Triangle $V_{cd}{}^* V_{td} + V_{cs}{}^* V_{ts} + V_{cb}{}^* V_{tb} = 0$

$$
\begin{aligned}
V_{cd}{}^* V_{td} &= \lambda^6 A(-i\eta - \rho) + \lambda^4 A(-1 + i\eta + \rho) \\
V_{cs}{}^* V_{ts} &= -\lambda^2 A + \lambda^4 A(1 - i\eta - \rho) + \frac{\lambda^6 A}{8}\left(-1 + 4A^2 + 4i\eta + 4\rho\right) \\
V_{cb}{}^* V_{tb} &= \lambda^2 A - \frac{\lambda^6 A^3}{2}
\end{aligned}
\tag{A.14}
$$

$$
\begin{aligned}
V_{cd}{}^* V_{td} + V_{cs}{}^* V_{ts} + V_{cb}{}^* V_{tb} = \left(-\frac{1}{8} - \frac{i\eta}{2} - \frac{\rho}{2}\right) A\lambda^6 + \\
+ \left(\frac{A}{8}(i\eta + \rho - 2) + A^3\left(\frac{1}{4} + i\eta + \rho + \eta^2 + \rho^2\right)\right)\lambda^8 + \mathcal{O}(\lambda^9)
\end{aligned}
\tag{A.15}
$$

In summary, adding more orders in λ up to $\mathcal{O}(\lambda^5)$, in the unitary relations the deviation from zero is of order $\mathcal{O}(A\lambda^5) \sim 4 \cdot 10^{-4}$ in (A.5) and (A.13), the two triangles with side length of the same order. The squashed triangles (A.9) and (A.15) deviate of order $\mathcal{O}(A\lambda^6) \sim 10^{-4}$, (A.7) and (A.11) of order $\mathcal{O}(A\lambda^7) \sim 2 \cdot 10^{-5}$.

APPENDIX

B

Treatment of Asymmetric Errors

Regarding efficiencies or wrong tag fractions close to $\varepsilon \gtrsim 0$ or $\varepsilon \lesssim 1$, the Binomial error calculation is not working for the error calculations used in this thesis. Assuming k events selected out of n and the efficiency or wrong tag fraction is denoted as $p = k/n$, the the expectation value ε and variance $\mathrm{Var}(\varepsilon)$ are given by

$$\varepsilon = n \cdot p \qquad \mathrm{Var}(\varepsilon) = n \cdot p \cdot (1 - p) \tag{B.1}$$

therefore in the limit $k \to 0$ and $k \to n$ the varianced is equal to zero, independent of the number of events. The Binomial error calculation is valid for efficiencies away from the limits. As in this thesis expectation values close to the problematic limits have to be regarded, an alternative method has been used throughout this work. A method based on Bayes Theorem has been shown in detail in [146]. In this chapter the main steps and the implementation within this thesis will be discussed briefly.

For a given efficiency ε measured in a sample consisting of n events by selecting k of those, the Binomial distribution is given by

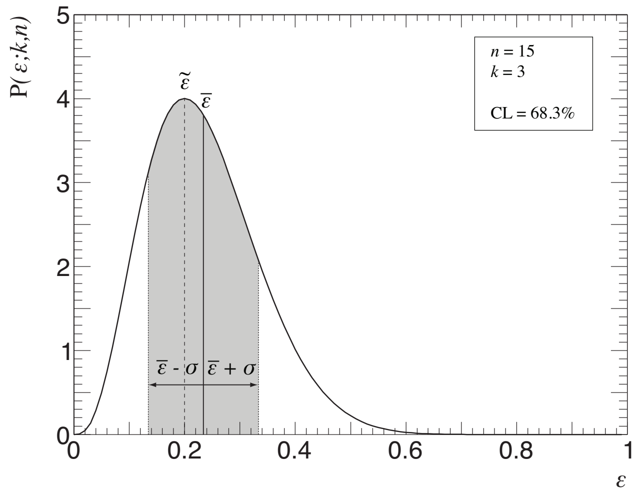

Figure B.1: Efficiency probability density function for $\mathrm{P}(\varepsilon; 3, 15)$. The dashed line shows the mode $\tilde{\varepsilon}$, the continuous line the mean value $\bar{\varepsilon}$ and the shaded area corresponds to the $\bar{\varepsilon} \pm \sigma$ area (CL = 68.3%).

$$\mathrm{P}(k; \varepsilon, n) = \begin{pmatrix} n \\ k \end{pmatrix} \varepsilon^k (1-\varepsilon)^{n-k}. \tag{B.2}$$

The Binomial estimator for the efficiency, $\bar{\varepsilon} = k/n$, has a variance of $\mathrm{Var}(\bar{\varepsilon}) = k(n-k)n^3$, resulting in absurd results vor $k = 0$ and $k = n$.

The proper error of ε with the knowledge of our data, n and k, has to be calculated by the probability density function $\mathrm{P}(\varepsilon; k, n)$. Using the Bayesian theorem, this distribution can be written as the Ansatz

$$\mathrm{P}(\varepsilon; k, n) = \frac{\mathrm{P}(k; \varepsilon, n)\mathrm{P}(\varepsilon; n)}{C} \tag{B.3}$$

where C is a normalisation constant and $\mathrm{P}(\varepsilon; n)$ describes the fact, that we require the efficiency to have a value between zero and one. Reasonably we can set $\mathrm{P}(\varepsilon; n) = 1$ if $0 \leq \varepsilon \leq 1$ and $\mathrm{P}(\varepsilon; n) = 0$ otherwise.

As shown in [146], by the calculation of the normalisation constant $C = 1/(n+1)$ one can recalculate the distribution (B.3), it becomes

$$\mathrm{P}(\varepsilon; k, n) = (n+1)\begin{pmatrix} n \\ k \end{pmatrix} \varepsilon^k (1-\varepsilon)^{n-k}. \tag{B.4}$$

Consequently, as showed in [146], calculating the estimator $\bar{\varepsilon}$ and its variance $\mathrm{Var}(\bar{\varepsilon})$ results in

$$\bar{\varepsilon} = \frac{k+1}{n+2}, \quad \mathrm{Var}(\bar{\varepsilon}) = \frac{(k+1)(k+2)}{(n+2)(n+3)} - \frac{(k+1)^2}{(n+2)^2} \tag{B.5}$$

whereas the maximum of $\mathrm{Max}(\varepsilon) = \tilde{\varepsilon} = k/n$ is identical to the Binomial estimator. In Figure B.1 the probability distribution from Equation (B.4) is shown for $n = 15$ and $k = 3$, the shaded area shows the region $\varepsilon \pm \sigma$ ($\sigma = \sqrt{\mathrm{Var}(\bar{\varepsilon})}$ from Equation (B.5)) corresponding to a CL of 68.3%. Note that the mean value is shifted from the usual Binomial mean value.

Using $\bar{\varepsilon}$ and $\mathrm{Var}(\bar{\varepsilon})$ from (B.5), one can prove for all $k \geq 0$ and $n \geq k$

$$\begin{aligned}
\bar{\varepsilon} + \mathrm{Var}(\bar{\varepsilon}) &= \frac{k+1}{n+2}\left(1 + \frac{k+2}{n+3} - \frac{k+1}{n+2}\right) < \\
&< \frac{k+1}{n+2}\left(1 + \frac{k+2}{n+3} - \frac{k+1}{n+3}\right) = \\
&= \frac{k+1}{n+2}\,\frac{n+4}{n+3} < \\
&= \frac{k+1}{n+2}\,\frac{n+2}{n+1} = \frac{k+1}{n+1} \leq 1
\end{aligned} \tag{B.6}$$

that the efficiency plus its variation always is smaller than one. In the same way it can be proven that $\bar{\varepsilon} - \mathrm{Var}(\bar{\varepsilon}) > 0$ for small values of $k \geq 0$ and $n \geq k$. Furthermore, as calculated in [146], for the values $k = 0$ and $k = 0$ one finds $\mathrm{Var}(\bar{\varepsilon}) > 0$. For small and large values of k no unphysical efficiencies occur.

However, $\mathrm{P}(\varepsilon; k, n)$ is not symmetric and the integral is not analytic. Therefore, within this thesis numerical calculations analogue to the calculations before (detailed in [128]) have been used to calculate the asymmetric errors. The calculations are integrated into ROOT as the class `TGraphAsymmErrors`[7]. As central value this class returns the $\tilde{\varepsilon}$, introducing an asymmetric error around this value. The asymmetry is large for efficiencies

[7]More information about the functionality of the ROOT class, the underlying calculations and access to the source code on `http://root.cern.ch/root/html/TGraphAsymmErrors.html`

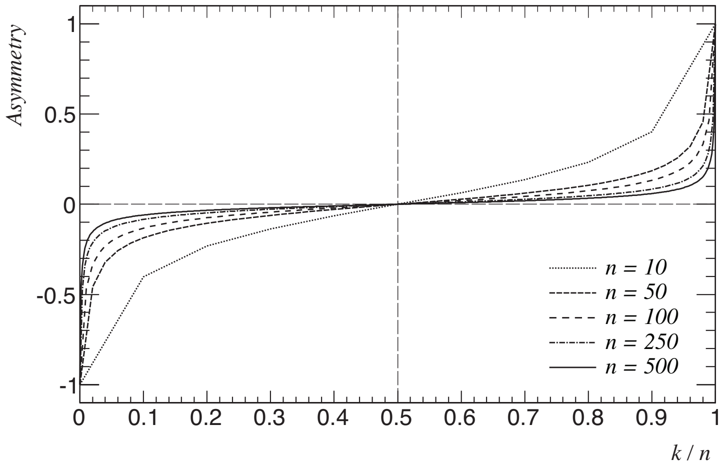

Figure B.2: Asymmetry $(\sigma_- - \sigma_+)/(\sigma_- + \sigma_+)$ of the asymmetric errors produced by `TGraphAsymmErrors` for different values of n and $1 \leq k \leq n$, where σ_- denotes the negative error and σ_+ the positve.

close to zero and one, for an efficiency of $\varepsilon = 50\%$ the error is symmetric, as shown in Figure B.2.

List of Figures

List of Tables

Abbreviations and Glossary

ALEPH **A**pparatus for **LEP PH**ysics at CERN

ALFA **A**bsolute **L**uminosity **F**or **A**TLAS

ALICE **A** **L**arge **I**on **C**ollider **E**xperiment

AMI **A**TLAS **M**etadata **I**nterface [37]

ANN **A**rtificial **N**eural **N**etwork

AOD **A**nalysis **O**bject **D**ata

ARGUS **A** **R**ussian-**G**erman-**U**nited States-**S**wedish Collaboration

ATHENA computing framework ATLAS based on Gaudi

ATLAS **A** **t**oroidal **L**HC **A**peratus

ATLFAST **Atl**as **Fast** Simulation

BaBar **B** **and** **B**-**bar**, B-factory at the PEP-II collider at SLAC

Belle B-factory at the KEK collider in Tsukuba, Japan

BT **B**arrel **T**oroid

CASTOR **C**ERN **A**dvanced **STOR**age Manager

CDF **C**ollider **D**etector at **F**ermilab

CERN European Organization for Nuclear Research,

(**C**onseil **E**uropéen pour la **R**echerche **N**ucléaire)

CESR	**C**ornell **E**lectron **S**torage **R**ing, 10 GeV synchrotron
CKM	**C**abibbo-**K**obayashi-**M**askawa matrix
CL	**C**onfidence **L**evel
CLEO	short for Cleopatra, particle detector at the CESR
CMS	**C**ompact **M**uon **S**ollenoid
CP	**C**harge **P**arity Symmetry
CPT	**C**harge **P**arity **T**ime Symmetry
CS	**C**entral **S**olenoid
CSC	**C**athode **S**trip **C**hamber
CTP	**C**entral **T**rigger **P**rocessor
DØ	One of two major experiments at Tevatron
DCS	**D**etector **C**ontrol **S**ystem
DELPHI	**DE**tector with **L**epton, **P**hoton and **H**adron **I**dentification
DIS	**D**eep **I**nelastic **S**cattering
DPD	**D**erived **P**hysics **D**ata
DQ2	**D**on **Q**uijote 2
ECT	**E**nd-**C**ap **T**oroid
EF	**E**vent **F**ilter
EMEC	LAr **E**lectro**m**agnetic **E**nd-**C**ap
ESD	**E**vent **S**ummary **D**ata
FATRAS	**Fa**st **AT**LAS **Tra**ck **S**imulation
FCal	**F**orward **Cal**orimeter
FCNC	**F**lavour **C**hanging **N**eutral **C**urrent
FS	**F**ull **S**can
FSR	**F**inal **S**tate **R**adiation
Ganga	distributed analysis tool [123]
GAUDI	Data processing applications framework, developed by and shared with the LHCb experiment.
Geant4	**Ge**ometry **an**d **T**racking
HEC	LAr **H**adronic **E**nd-**C**ap
HepMC	**H**igh **E**nergy **P**hysics **M**onte **C**arlo

HFAG	**H**eavy **F**lavour **A**veraging **G**roup
HLT	**H**igh **L**evel **T**rigger
ISR	**I**nitial **S**tate **R**adiation
KEK	**k**o-**e**nerugi **k**asokuki kenkyu-kiko, electron-positron collider in Tsukuba, Japan
LAr	**L**iquid **Ar**gon
LEP	**L**arge **E**lectron-**P**ositron collider
LHC	**L**arge **H**adron **C**ollider
LHCb	**L**arge **H**adron **C**ollider **b**eauty
LHCf	**L**arge **H**adron **C**ollider **f**orward
LINAC	**LIN**ear **AC**celerator
LUCID	**LU**minosity measurement using **C**erenkov **I**ntegrating **D**etector
LVL1	**L**e**v**e**l** **1** trigger
LVL2	**L**e**v**e**l** **2** trigger
MI	**M**ultiple **I**nteractions
MDT	**M**onitored **D**rift **T**ube
MSTW	**M**artin-**S**tirling-**T**horne-**W**att PDF
MOORE	**M**uon **O**bject **O**riented **RE**construction
NLO	**N**ext to **L**eading **O**rder
pAthena	**P**anda **Athena**, distributed analysis tool [74]
PDF	**P**arton **D**istribution **F**unction
PDG	**P**article **D**ata **G**roup, see `http://pdg.lbl.gov` [125]
POOL	**P**ool **O**f persistent **O**bjects for **L**HC [78]
PS	**P**roton **S**ynchrotron
PSB	**P**roton **S**ynchrotron **B**ooster
PYTHIA	A Monte Carlo program for the generation of high-energy physics events.
QCD	**Q**uantum **C**hromo**D**ynamics
QED	**Q**uantum **E**lectro**D**ynamics
RAW	**Raw** data file
RoI	**R**egion **o**f **I**nterest

ROOT	Data analysis software developed at CERN [58]
RPC	**R**esistive **P**late **C**hamber
SCT	**S**emi**c**onductor **T**racker
SLAC	**S**tanford **L**inear **A**ccelerator **C**enter
SPS	**S**uper **P**roton **S**ynchrotron
TAG	Event-level metadata
Tevatron	$p\bar{p}$ synchrotron with energies up to $\sqrt{s} = 1.96$ TeV at Fermilab
TGC	**T**hin **G**ap **C**hamber
TMVA	**T**oolkit for **M**ulti**V**ariate Data **A**nalysis [101]
TOTEM	**TOT**al **E**lastic and diffractive cross section **M**easurement
TRT	**T**ransition **R**adiation **T**racker
WLCG	**W**orldwide **L**HC **C**omputing **G**rid
ZDC	**Z**ero **D**egree **C**alorimeter

Bibliography

[1] G. Aad et al., *ATLAS pixel detector electronics and sensors*, J. Instrum. **3** (2008) P07007.

[2] E. Abat et al., *The ATLAS Transition Radiation Tracker (TRT) proportional drift tube: design and performance*, J. Instrum. **3** (2008) P02013.

[3] E. Abat et al., *The ATLAS TRT Barrel Detector*, J. Instrum. **3** (2008) P02014.

[4] E. Abat et al., *The ATLAS TRT end-cap detectors*, J. Instrum. **3** (2008) P10003.

[5] A. Abdesselam and T. Akimoto, *The barrel modules of the ATLAS semiconductor tracker*, Nucl. Instrum. Methods Phys. Res. A **568** (2006) 642 – 671.

[6] A. Abdesselam and T. Akimoto, *The ATLAS semiconductor tracker end-cap module*, Nucl. Instrum. Methods Phys. Res. A **575** (2007) 353–389.

[7] D. Adams et al., *Track reconstruction in the ATLAS Muon Spectrometer with MOORE*, ATL-SOFT-2003-007 (2003) 37 p. `http://cdsweb.cern.ch/record/685500`.

[8] P. Adragna, *Testbeam studies of production modules of the ATLAS Tile Calorimeter*, Nucl. Instrum. Methods Phys. Res. A **606** (2009) 362–394.

[9] S. Agostinelliae, J. Allisonas, K. Amakoe, et al., GEANT4 - *a simulation toolkit*, Nucl. Instrum. Methods Phys. Res. A **506** (2003) 3, 250–303.

[10] M. Aharrouche et al., *Energy Linearity and Resolution of the ATLAS Electromagnetic Barrel Calorimeter in an Electron Test-Beam*, Nucl. Instrum. Methods Phys. Res. A **568** (2006) 601–623.

[11] A. Akeroyd et al., *Physics at Super B Factory*, Belle, 2009. `http://arxiv.org/abs/1002.5012`. `http://belle2.kek.jp/physics.html`.

[12] T. Åkesson et al., *Electron identification with a prototype of the Transition Radiation Tracker for the ATLAS experiment*, Nucl. Instrum. Methods Phys. Res. A **412** (1998) 200–215.

[13] T. Åkesson et al., *Tracking performance of the transition radiation tracker prototype for the ATLAS experiment*, Nucl. Instrum. Methods Phys. Res. A **485** (2002) 298–310.

[14] ALEPH, DELPHI, L3, OPAL, and SLD Collaborations, *Precision electroweak measurements on the Z resonance*, Phys. Rep. **427** (2006) 5-6, 257–454.

[15] ALEPH Collaboration, *Test of the flavour independence of* α_s, Phys. Lett. B **355** (1995) 381–393.

[16] ALICE Collaboration, *The ALICE experiment at the CERN LHC*, J. Instrum. **3** (2008) S08002, 259 p.

[17] B. Andersson, G. Gustafson, G. Ingelman, and T. Sjöstrand, *Parton fragmentation and string dynamics*, Phys. Rep. **97** (1983) 2-3, 31–145.

[18] J. P. Archambault et al., *Energy calibration of the ATLAS Liquid Argon Forward Calorimeter*, J. Instrum. **3** (2008) P02002.

[19] ARGUS Collaboration, *Observation of* B^0 $\bar{B}^0$ *mixing*, Phys. Lett. B **192** (1987) 1-2, 245–252.

[20] ATLAS Collaboration, *ATLAS Public Results TWiki*. `https://twiki.cern.ch/twiki/bin/view/AtlasPublic`.

[21] ATLAS Collaboration, *ATLAS calorimeter performance : Technical Design Report*, ATLAS-TDR-001, CERN-LHCC-96-040 of *Technical Design Report ATLAS*, CERN, Geneva, 1996. http://cdsweb.cern.ch/record/331059.

[22] ATLAS Collaboration, *ATLAS liquid-argon calorimeter : Technical Design Report*, ATLAS-TDR-002, CERN-LHCC-96-041 of *Technical Design Report ATLAS*, CERN, Geneva, 1996. http://cdsweb.cern.ch/record/331061.

[23] ATLAS Collaboration, *ATLAS tile calorimeter : Technical Design Report*, ATLAS-TDR-003, CERN-LHCC-96-042 of *Technical Design Report ATLAS*, CERN, Geneva, 1996. http://cdsweb.cern.ch/record/331062.

[24] ATLAS Collaboration, *ATLAS central solenoid: Technical Design Report*, ATLAS-TDR-009, CERN-LHCC-97-021 of *Technical Design Report ATLAS*, CERN, Geneva, 1997. http://cdsweb.cern.ch/record/331067.

[25] ATLAS Collaboration, *ATLAS end-cap toroids: Technical Design Report*, ATLAS-TDR-008, CERN-LHCC-97-020 of *Technical Design Report ATLAS*, CERN, Geneva, 1997. http://cdsweb.cern.ch/record/331066.

[26] ATLAS Collaboration, *ATLAS Inner Detector: Technical Design Report, Volume 1*, ATLAS-TDR-004, CERN-LHCC-97-16 of *Technical Design Report ATLAS*, CERN, Geneva, 1997. http://cdsweb.cern.ch/record/331063.

[27] ATLAS Collaboration, *ATLAS Inner Detector: Technical Design Report, Volume 2*, ATLAS-TDR-005, CERN-LHCC-97-17 of *Technical Design Report ATLAS*, CERN, Geneva, 1997. http://cdsweb.cern.ch/record/331064.

[28] ATLAS Collaboration, *ATLAS muon spectrometer : Technical Design Report*, ATLAS-TDR-010, CERN-LHCC-97-022 of *Technical Design Report ATLAS*, CERN, Geneva, 1997. http://cdsweb.cern.ch/record/331068.

[29] ATLAS Collaboration, *ATLAS level-1 trigger: Technical Design Report*, ATLAS-TDR-012, CERN-LHCC-98-014 of *Technical Design Report ATLAS*, CERN, Geneva, 1998. http://cdsweb.cern.ch/record/381429.

[30] ATLAS Collaboration, *ATLAS detector and physics performance - Technical Design Report 1*, ATLAS-TDR-014, CERN-LHCC-99-014 of *Technical Design Report ATLAS*, CERN, Geneva, 1999. http://cdsweb.cern.ch/record/391176.

[31] ATLAS Collaboration, *ATLAS detector and physics performance - Technical Design Report 2*, ATLAS-TDR-015, CERN-LHCC-99-015 of *Technical Design Report ATLAS*, CERN, Geneva, 1999. http://cdsweb.cern.ch/record/391177.

[32] ATLAS Collaboration, *ATLAS computing: Technical Design Report*, ATLAS-TDR-017, CERN-LHCC-2005-022 of *Technical Design Report ATLAS*, CERN, Geneva, 2005. http://cdsweb.cern.ch/record/837738.

[33] ATLAS Collaboration, *The ATLAS Experiment at the CERN Large Hadron Collider*, J. Instrum. **3** (2008) S08003.

[34] ATLAS Collaboration, *Expected performance of the ATLAS experiment: detector, trigger and physics*, CERN-OPEN-2008-020, CERN, Geneva, 2009. arXiv:0901.0512. http://cdsweb.cern.ch/record/1125884.

[35] ATLAS Collaboration, *$D^{(*)}$ mesons reconstruction in pp collisions at $\sqrt{s} = 7$ TeV*, ICHEP 2010 (2010) ATLAS-CONF-2010-034, 7 p. http://cdsweb.cern.ch/record/1277669.

[36] ATLAS Collaboration, *Measurement of the centrality dependence of J/ψ yields and observation of Z production in lead-lead collisions with the ATLAS detector at the LHC*, Submitted to Physics Letters B (2010) , arXiv:1012.5419v1.

[37] Atlas Metadata Interface team, *AMI Homepage*. http://ami.in2p3.fr.

[38] BaBar Collaboration, *Observation of $\mathcal{CP}$ Violation in the B^0 Meson System*, Phys. Rev. Lett. **87** (2001) 091801, 8 p.

[39] BaBar Collaboration, *The BaBar detector*, Nucl. Instrum. Methods Phys. Res. A **479** (2002) 1, 1–116, arXiv:hep-ex/0105044.

[40] BaBar Collaboration, *Direct $\mathcal{CP}$ Violating Asymmetry in $B^0 \to K^{+-}$ Decays*, Phys. Rev. Lett. **93** (2004) 131801, 7 p.

[41] BaBar Collaboration, *Evidence for $D^0 - \bar{D}^0$ Mixing*, Phys. Lett. **98** (2007) 211802, 7 p.

[42] J. P. Badiou, J. Beltramelli, J. M. Maze, and J. Belorgey, *ATLAS barrel toroid: Technical Design Report*, ATLAS-TDR-007, CERN-LHCC-97-019 of *Technical Design Report ATLAS*, CERN, Geneva, 1997. http://cdsweb.cern.ch/record/331065.

[43] J. T. M. Baines, H. Drevermann, Emeliyanov, et al., *Fast Tracking for the ATLAS LVL2 Trigger*, Computing in High Energy Physics and Nuclear Physics 2004, Interlaken, Switzerland (2005) ATL-DAQ-CONF-2005-001 ATL-COM-DAQ-2004-028, 246. http://cdsweb.cern.ch/record/803143.

[44] E. Barberio et al., *Averages of b-hadron and c-hadron Properties at the End of 2007*, Heavy Flavour Averaging Group, 2008. arXiv:0808.1297v3. http://www.slac.stanford.edu/xorg/hfag/index.html.

[45] R. J. Barlow, *Statistics*. John Wiley and Sons, 1989.

[46] G. Barrand et al., *GAUDI: The software architecture and framework for building LHCb data processing applications*, Comp. Phys. Commun. **140** (2001) 1-2, 45–55. http://cdsweb.cern.ch/record/467678.

[47] P. Bartlett, Y. Freund, W. Lee, and R. Shapire, *Boosting the margin: a new explanation for the effectiveness of voting methods*, Ann. Statist. **26** (1998) 5, 1651–1686.

[48] Belle Collaboration, *Observation of Large $\mathcal{CP}$ Violation in the Neutral B Meson System*, Phys. Rev. Lett. **87** (2001) 091802, 7 p.

[49] Belle Collaboration, *The Belle Detector*, Nucl. Instrum. Methods Phys. Res. A **479** (2002) 1, 117–232.

[50] Belle Collaboration, *Evidence for Direct $\mathcal{CP}$ Violation in $B^0 \to K^{+-}$ Decays*, Phys. Rev. Lett. **93** (2004) 131802, 6 p.

[51] Belle Collaboration, *Evidence for $D^0 - \bar{D}^0$ Mixing*, Phys. Lett. **98** (2007) 211803, 6 p.

[52] M. Benedikt, P. Collier, V. Mertens, J. Poole, and K. Schindl, *LHC Design Report - The LHC Injector Chain*, CERN-2004-003-V-3, CERN, Geneva, 2004. http://cdsweb.cern.ch/record/823808.

[53] S. Bethke, *The 2009 World Average of α_s*, Eur.Phys.J. **C64** (2009) 689–703, arXiv:0908.1135v2.

[54] A. Bettini, *Introduction to Elementary Particle Physics*. Cambridge University Press, UK, 2008. http://www.cambridge.org/9780521880213.

[55] UTFit Collaboration, M. Bona et al., *The 2004 UTfit Collaboration Report on the Status of the Unitarity Triangle in the Standard Model*, J. High Energy Phys. **507** (2005) 32 p., arXiv:hep-ph/0501199v2. Updated results available at: http://www.utfit.org/UTfit/WebHome.

[56] M. Branco et al., *Managing ATLAS data on a petabyte-scale with DQ2*, J. Phys. Conf. Ser. **119** (2008) 062017, http://cdsweb.cern.ch/record/1177372.

[57] S. Brandt, *Datenanalyse*, 4. Auflage. Spektrum Akad. Verl., Heidelberg · Berlin, 1999.

[58] R. Brun and F. Rademakers, ROOT - *An Object Oriented Data Analysis Framework*, Nucl. Instrum. Methods Phys. Res. A **389** (1997) 1-2, 81–86. http://root.cern.ch/.

[59] O. S. Brüning, P. Collier, P. Lebrun, S. Myers, R. Ostojic, J. Poole, and P. Proudlock, *LHC Design Report - The LHC Infrastructure and General Services*, CERN-2004-003-V-2, CERN, Geneva, 2004. http://cdsweb.cern.ch/record/815187.

[60] O. S. Brüning, P. Collier, P. Lebrun, S. Myers, R. Ostojic, J. Poole, and P. Proudlock, *LHC Design Report - The main ring*, CERN-2004-003-V-1, CERN, Geneva, 2004. http://cdsweb.cern.ch/record/782076.

[61] N. Cabibbo, *Unitary Symmetry and Leptonic Decays*, Phys. Rev. Lett. **10** (1963) 531–533.

[62] J. Campbell, J. W. Huston, and W. J. Stirling, *Hard interactions of quarks and gluons: a primer for LHC physics*, Rep. Prog. Phys. **70** (2007) 89–193, `hep-ph/0611148v1`.

[63] S. Catani, M. Dittmar, D. Soper, W. J. Stirling, T. S, et al., *QCD*, 1999 CERN Workshop on SM physics (and more) at the LHC (2000) 115 p., `hep-ph/0005025v1`.

[64] CDF Collaboration, *Measurement of the average time-integrated mixing probability of b-flavored hadrons produced at the Fermilab Tevatron*, Phys. Rev. D **69** (2004) 012002, 16 p.

[65] CDF Collaboration, *Observation of B_s^0-$\bar{B}_s^0$ Oscillations*, Phys. Rev. **97** (2006) 242003, 8 p.

[66] J. Charles et al., *CP Violation and the CKM Matrix: Assessing the Impact of the Asymmetric B Factories*, Eur. Phys. J. C **41** (2004) 1–131. 178 p, `hep-ph/0406184`.

[67] CKMFitter Group, J. Charles et al., *CP Violation and the CKM Matrix: Assessing the Impact of the Asymmetric B Factories*, Eur. Phys. J. C **41** (2005) 131 p., `arXiv:hep-ph/0406184v3`.

[68] J. Charles, A. Höcker, H. Lacker, S. Laplace, F. R. Le Diberder, J. Malclés, J. Ocariz, M. Pivk, and L. Roos, *CP violation and the CKM matrix: assessing the impact of the asymmetric B factories*, Eur. Phys. J. C **41** (2005) 1, 131. updated results and plots available at: `http://ckmfitter.in2p3.fr`.

[69] L.-L. Chau and K. W.-Y., *Comments on the Parametrization of the Kobayashi-Maskawa Matrix*, Phys. Rev. Lett. **53** (1984) 19, 1802–1805.

[70] J. H. Christenson, J. W. Cronin, V. L. Fitch, and R. Turlay, *Evidence for the 2π decay of the K_2^0 meson*, Phys. Rev. Lett. **13** (1964) 138–140.

[71] CMS Collaboration, *The CMS experiment at the CERN LHC*, J. Instrum. **3** (2008) S08004.

[72] T. Cornelissen, M. Elsing, I. Gavrilenko, W. Liebig, E. Moyse, and A. Salzburger, *The new ATLAS track reconstruction (NEWT)*, J. Phys.: Conf. Ser. **119** (2008) 032014.

[73] G. Cowan, *Statistical Data Analysis.* Oxford University Press, 1998. http://www.pp.rhul.ac.uk/~cowan/sda/.

[74] K. Cranmer, *The ATLAS Analysis Architecture*, Nucl. Phys. B Proc. Supple **177-178** (2008) 126–130, http://cdsweb.cern.ch/record/1047631.

[75] D0 Collaboration, *Measurement of the CP-violation parameter of B_0 mixing and decay with $p\bar{p} \to \mu\mu X$ data*, Phys. Rev. D **74** (2006) 092001, 12 p.

[76] B. Dowler et al., *Performance of the ATLAS hadronic end-cap calorimeter in beam tests*, Nucl. Instrum. Methods Phys. Res. A **482** (2009) 94–124.

[77] R. Duda, P. Hart, and D. Stork, *Pattern Classification*, 2nd edition. John Wiley and Sons, 2001.

[78] D. Duellmann, *The LCG POOL Project – General Overview and Project Structure*, in *Conference on Computing in High Energy and Nuclear Physics in San Diego (CHEP03)*. 2003. physics/0306129.

[79] I. Dunietz, R. Fleischer, and U. Nierste, *In Pursuit of New Physics with B_s Decays*, Phys. Rev. D **63** (2001) 114015, 31 p., arXiv:hep-ph/0012219v2.

[80] K. Edmonds, S. Fleischmann, T. Lenz, C. Magass, J. Mechnich, and A. Salzburger, *The Fast ATLAS Track Simulation (FATRAS)*, ATL-SOFT-PUB-2008-001 (2008) 48 p., http://cdsweb.cern.ch/record/1091969.

[81] F. Englert and R. Brout, *Broken Symmetry and the Mass of Gauge Vector Mesons*, Phys. Rev. Lett. **13** (1964) 9, 321–323.

[82] B. Epp, V. M. Ghete, and A. Nairz, *Prospects for the measurement of B_s oscillations with the ATLAS detector at LHC.*, EPJ Direct **4** (2002) SN-ATLAS-2002-015. ATL-COM-PHYS-2001-031, N3, hep-ph/0202192.

[83] B. Epp, E. Kneringer, H. Duer, and P. Jussel, *Performance of the $B_s^0 \to D_s^-(\phi\pi^-)\pi^+$ channel with the ATLAS detector and prospects for the measurement of B_s^0 oscillations using Rome Monte Carlo simulation*, CERN, Geneva, Jun, 2006. http://cdsweb.cern.ch/record/967484.

[84] B. Epp, E. Kneringer, H. Duer, and P. Jussel, *Prospects of the measurement of B_s^0 oscillations with the ATLAS detector at LHC*, 26th International Symposium on Physics in Collision in Búzios, Brazil (2006) 4 p., hep-ex/0609044. http://cdsweb.cern.ch/record/985638.

[85] L. R. Evans and P. Bryant, *LHC Machine*, J. Instrum. **3** (2008) S08001. 164 p.

[86] R. Fisher, *The use of multiple measurements in taxonomic problems*, Annals of Eugenics **7** (1936) 179–188.

[87] A. Formica, *Design, implementation and deployment of the Saclay muon reconstruction algorithms (Muonbox/y) in the Athena software framework of the ATLAS experiment*, in *Conference on Computing in High Energy and Nuclear Physics in San Diego (CHEP03)*. 2003. arXiv:cs/0306105v1.

[88] Y. Freund and R. Shapire, *A Decision-Theoretic Generalization of On-Line Learning and an Application to Boosting*, J. Computer and System Sciences **55** (1997) 1, 119–139.

[89] D. Froidevaux, L. Poggioli, and E. Richter-Was, *ATLFAST 1.0 A package for particle-level analysis*, ATL-PHYS-96-079 (1996) 46 p., http://cdsweb.cern.ch/record/682460.

[90] R. Frühworth, *Application of Kalman filtering to track and vertex fitting*, Nucl. Instrum. Methods Phys. Res. A **262** (1987) 2-3, 444–450.

[91] Geant4 collaboration, *Geant4 Homepage*. http://geant4.web.cern.ch/geant4/.

[92] S. L. Glashow, *Partial-symmetries of weak interactions*, Nucl. Phys. **22** (1961) 4, 579–588.

[93] S. L. Glashow, J. Iliopulos, and L. Maiani, *Weak Interactions with Lepton-Hadron Symmetry*, Phys. Rev. D **2** (1970) 7, 1285–1292.

[94] J. Goldstone, A. Salam, and S. Weinberg, *Broken Symmetries*, Phys. Rev. **127** (1962) 3, 965–970.

[95] D. G. Gross and F. Wilczek, *Ultraviolet Behavior of Non-Abelian Gauge Theories*, Phys. Rev. Lett. **30** (1973) 26, 1343–1346.

[96] F. Halzen and A. D. Martin, *Quarks and Leptons: An Introductory Course in Modern Particle Physics*. John Wiley and Sons, USA, 1984.

[97] S. Hassani, L. Chevalier, E. Lançon, J.-F. Laporte, and A. Ouraou, *A muon identification and combined reconstruction procedure for the ATLAS detector at the LHC using the (MUONBOY, STACO, MuTag) reconstruction packages*, Nucl. Instrum. Methods Phys. Res. A **572** (2007) 1, 77–79.

[98] P. W. Higgs, *Broken Symmetries, massless particles and gauge fields*, Phys. Lett. **12** (1964) 2, 132–133.

[99] P. W. Higgs, *Spontaneous Symmetry Breakdown without Massless Bosons*, Phys. Rev. **145** (1966) 4, 1156–1163.

[100] A. Höcker and Z. Ligeti, *CP violation and the CKM matrix*, Annu. Rev. Nucl. Part. Sci. **56** (2006) 501–567, `hep-ph/0605217`.

[101] A. Hoecker, P. Speckmayer, J. Stelzer, J. Therhaag, E. von Toerne, and H. Voss, *TMVA: Toolkit for Multivariate Data Analysis*, PoS **ACAT** (2007) 040, `arXiv:physics/0703039`. `http://tmva.sourceforge.net/`.

[102] F. Hoyle, *Concluding Remarks*, Proc. R. Soc. A **301** (1967) 171.

[103] C. Jarlskog, *Commutator of the Quark Mass Matrices in the Standard Electroweak Model and a Measure of Maximal CP Nonconservation*, Phys. Rev. Lett. **55** (1985) 10, 1039–1042.

[104] C. Jarlskog and R. Storab, *Unitarity polygons and CP violation areas and phases in the standard electroweak model*, Phys. Lett. B **208** (1988) 2, 268–274.

[105] P. Jenni, M. Nessi, M. Nordberg, and K. Smith, *ATLAS high-level trigger, data-acquisition and controls: Technical Design Report*, ATLAS-TDR-016, CERN-LHCC-2003-022 of *Technical Design Report ATLAS*, CERN, Geneva, 2003. http://cdsweb.cern.ch/record/616089.

[106] P. Jenni, M. Nordberg, M. Nessi, and K. Jon-And, *ATLAS Forward Detectors for Measurement of Elastic Scattering and Luminosity*, CERN-LHCC-2008-004 of *Technical Design Report*, CERN, Geneva, 2008. http://cdsweb.cern.ch/record/1095847.

[107] P. Jussel, T. Stahl, B. Epp, E. Kneringer, and W. Walkowiak, *Study of muon trigger scenarios for the measurement of B_s^0 oscillations in the channels $B_s^0 \to D_s^- \pi^+$ and $B_s^0 \to D_s^- a_1^+$*, ATL-PHYS-PUB-2007-003, ATL-COM-PHYS-2006-091 (2006) 9 p. http://cdsweb.cern.ch/record/1005811.

[108] D. Kirkby, *Modeling data with per-event error observables*, Private Comm., 2011.

[109] D. Kirkby and Y. Nir, *Review on $\mathcal{CP}$ Violation in Meson Decays*, J. Phys. G **37** (2010) 154–163.

[110] J. Knobloch et al., *LHC computing Grid: Technical Design Report. Version 1.06 (20 Jun 2005)*, CERN-LHCC-2005-024 of *Technical Design Report LCG*, CERN, Geneva, 2005. http://cdsweb.cern.ch/record/840543.

[111] M. Kobayashi and T. Maskawa, *CP-Violation in the Renormalizable Theory of Weak Interaction*, Prog. Theor. Phys. **49** (1973) .

[112] F. Krauss, *QCD and Monte Carlo Tools*, in *2nd CERN-Fermilab Hadron Collider Physics Summer School Lectures*. CERN, June, 2007. http://cdsweb.cern.ch/record/993673.

[113] KTeV Collaboration, *Observation of Direct $\mathcal{CP}$ Violation in $K_{S,L} \to \pi\pi$ Decays*, Phys. Rev. Lett. **83** (1999) 22–27.

[114] T. Lagouri et al., *A muon identification and combined reconstruction procedure for the ATLAS detector at the LHC at CERN*, IEEE Trans. Nucl. Sci. **51** (2004) 6, 3030–3033. http://cdsweb.cern.ch/record/681410.

[115] T. Lee and C. Yang, *Question of Parity Conservation in Weak Interactions*, Phys. Rev. (1956) 104, 254–258.

[116] A. Lenz and U. Nierste, *Theoretical update of $B_s - \bar{B}_s$ mixing*, J. High Energy Phys. **06** (2007) 072, 40 p.

[117] LEP Collaboration, *LEP design report*, CERN-LEP-84-01, CERN, Geneva, 1984. http://cdsweb.cern.ch/record/102083.

[118] LHCb Collaboration, *The LHCb Detector at the LHC*, J. Instrum. **3** (2008) S08005.

[119] LHCf Collaboration, *The LHCf detector at the CERN Large Hadron Collider*, J. Instrum. **3** (2008) S08006.

[120] E. Lohrmann, *Hochenergiephysik*, 4. Auflage. Teubner Studienbücher, Stuttgard, 1992.

[121] A. Martin, W. J. Stirling, R. Thorne, and G. Watt, *Parton distributions for the LHC*, Eur.Phys.J. **C63** (2009) 189–285, arXiv:0901.0002v3.

[122] B. Martin and G. P. Shaw, *Particle Physics*, 3rd Edition. John Wiley and Sons, Manchester, 2008.

[123] J. T. Moscicki et al., *Ganga: a tool for computational-task management and easy access to Grid resources*, Comput. Phys. Commun. **180** (2009) 11, 2303–2316, arXiv:0902.2685v2. http://ganga.web.cern.ch/ganga/.

[124] NA48 Collaboration, *A new measurement of direct CP violation in two pion decays of the neutral kaon*, Phys. Lett. B **465** (1999) 335–348, arXiv:hep-ex/9909022v1.

[125] Particle Data Group, K. Nakamura et al., *Review of particle physics*, J. Phys. G **37** (2010) . Updated results available at: http://pdg.lbl.gov.

[126] P. Nason, G. Ridolfi, O. Schneider, F. Tartarelli, P. Vikas, et al., *Bottom Production*, 1999 CERN Workshop on SM physics (and more) at the LHC (2000) 74 p., hep-ph/0003142.

[127] K. Nikolopoulos, D. Fassouliotis, C. Kourkoumelis, and A. Poppleton, *Event-by-Event Estimate of Muon Energy Loss in ATLAS*, IEEE Trans. Nucl. Sci. **54** (2007) 5, 1792–1796.

[128] M. Paterno, *Calculating Efficiencies and Their Uncertainties*, DØ-note-2861 (1996) 3 p. `http://home.fnal.gov/~paterno/images/effic.pdf`. Updated Version 2004.

[129] D. H. Perkins, *Introduction to High Energy Physics*, 4th Edition. Cambridge University Press, 2000.

[130] T. S. Pettersson and P. Lefèvre, *The Large Hadron Collider: conceptual design*, CERN-AC-95-05 LHC, CERN, Geneva, Oct, 1995. `http://cdsweb.cern.ch/record/291782`.

[131] A. Pich, *Aspects of Quantum Chromodynamics*, in *Lectures given at the ICTP Summer School in Particle Physics*, IFIC/00-5, FTUV/00-5, p. 50 p. Trieste, 1999. `arXiv:hep-ph/0001118v1`.

[132] A. Pich, *Aspects of Quantum Chromodynamics*, in *Lectures given at the 2006 European School of High Energy Physics*, IFIC/07-27, FTUV/07-0529. 2006. `arXiv:0705.4264v1`.

[133] E. Ritsch, *Fast Simulation of Punch Through Particles into the Muon System at the ATLAS Experiment*, Master's thesis, Leopold Franzens Universität Innsbruck, 2010, t.b.p.

[134] A. Salam and J. Ward, *Electromagnetic and weak interactions*, Phys. Lett. **13** (1964) 2, 168–171.

[135] S. Schlenker et al., *The detector control system of the ATLAS experiment*, J. Instrum. **3** (2008) P05006.

[136] O. Schneider, *Review on $B^0 - \bar{B}^0$ mixing in Review of Particle Physics*, J. Phys. G **37** (2010) 973–980.

[137] T. Sjöstrand, *Pythia Homepage*. `http://home.thep.lu.se/~torbjorn/Pythia.html`.

[138] T. Sjöstrand, *Monte Carlo Generators*, in *Lectures given at the 2006 European School of High-Energy Physics*, CERN-LCGAPP-2006-06. Aronsborg, 2006. hep-ph/0611247.

[139] T. Sjöstrand, S. Mrenna, and P. Skands, *PYTHIA 6.4 Physics and Manual*, J. High Energy Phys. **05** (2006) 026, 570 p., hep-ph/0603175.

[140] T. Sjöstrand and M. v. Zijl, *A multiple-interaction model for the event structure in hadron collisions*, Phys. Rev. D **37** (1987) 7, 2019–2041.

[141] M. Smizanska, *PythiaB an interface to Pythia6 dedicated to simulation of beauty events*, ATL-COM-PHYS-2003-038 (restricted access), 2003.

[142] T. Stahl, *Prospects for Measuring the B_s^0 Mixing Parameter Δm_s Using the Decay Channel $B_s^0 \to D_s^- a_1^+$ with the ATLAS Detector.* PhD thesis, Siegen, University of Siegen, Siegen, 2008.

[143] S. Tarem, Z. Tarem, N. Panikashvili, and O. Belkind, *MuGirl - Muon identification in the ATLAS detector from the inside out*, Nucl. Sci. Symp. Conf. Rec. IEEE **1** (2006) 617–621.

[144] TOTEM Collaboration, *The TOTEM Experiment at the CERN Large Hadron Collider*, J. Instrum. **3** (2008) S08007.

[145] UA1 Collaboration, *Search for B^0 - $\bar{B}^0$ oscillations at the CERN proton-antiproton collider*, Phys. Lett. B **186** (1986) 2, 247–254.

[146] T. Ullrich and Z. Xu, *Treatment of Errors in Efficiency Calculations*, Data Analysis, Statistics and Probability (physics.data-an) (2007) , arXiv:physics/0701199v1.

[147] W. Verkerke and D. Kirkby, *RooFit Users Manual v2.91*, Online manual, 2008. http://root.cern.ch/download/doc/RooFit_Users_Manual_2.91-33.pdf.

[148] G. Viehauser, *CLEO III Operation*, Nucl. Instrum. Methods Phys. Res. A **462** (2001) 1-2, 146–151.

[149] S. Weinberg, *A Model of Leptons*, Phys. Rev. Lett. **19** (1967) 21, 1264–1266.

[150] N. Wermes and G. Hallewel, *ATLAS pixel detector: Technical Design Report*, ATLAS-TDR-011, CERN-LHCC-98-013 of *Technical Design Report ATLAS*, CERN, Geneva, 1998. http://cdsweb.cern.ch/record/381263.

[151] L. Wolfenstein, *Parametrization of the Kobayashi-Maskawa Matrix*, Phys. Rev. Lett. **51** (1983) 1945–1947.

[152] C. Wu, E. Ambler, R. Hayward, D. Hoppes, and R. Hudson, *Experimental Test of Parity Conservation in Beta Decay*, Phys. Rev. (1957) 105, 1413–1415.

[153] A. Yamamoto, Y. Makida, R. Ruber, et al., *The ATLAS Central Solenoid*, Nucl. Instrum. Methods Phys. Res. A **584** (2008) 53–74.

[154] G. Ybeles Smit, *Asymmetries in the decay of beauty.* PhD thesis, Amsterdam, Amsterdam U., 2010. http://cdsweb.cern.ch/record/1255877.

Acknowledgements

At first place I would like to thank Prof. Dr. Emmerich Kneringer for his excellent supervision and advice in the recent years. A lot of fruitful discussions resulted in many new insights and I got aware of several ideas new to me.

Further I would like to thank Prof. Dr. Dietmar Kuhn for his large efforts to financially support my work. His support gave me the opportunity to work for the ATLAS collaboration.

Of course this work would have been not possible without the advise of Dr. Maria Smizanska. I followed many of her brilliant ideas. Thanks for your excellent help. Thanks to Dr. Brigitte Epp for her constant help at work and good friendship. It was a great opportunity to work with you. Thanks to Dr. James Catmore for the many times he instantly had the right answer to all of my questions regarding the ATLAS software. Last, but definitely not least I would like to thank our close colleagues from the University of Siegen, Dr. Wolfgang Walkowiak and Dr. Thorsten Stahl.

Thanks a lot also to the group members of the Innsbruck ATLAS group, the people from the Grid group and my friends and colleagues in my office and the institute. Also thanks to the people from the ATLAS B Physics working group and all my colleagues and friends from the ATLAS collaboration.

Natürlich geht mein herzlichster Dank an meinen Schatz Sandra, meine Schwester Babsi und meine Eltern.